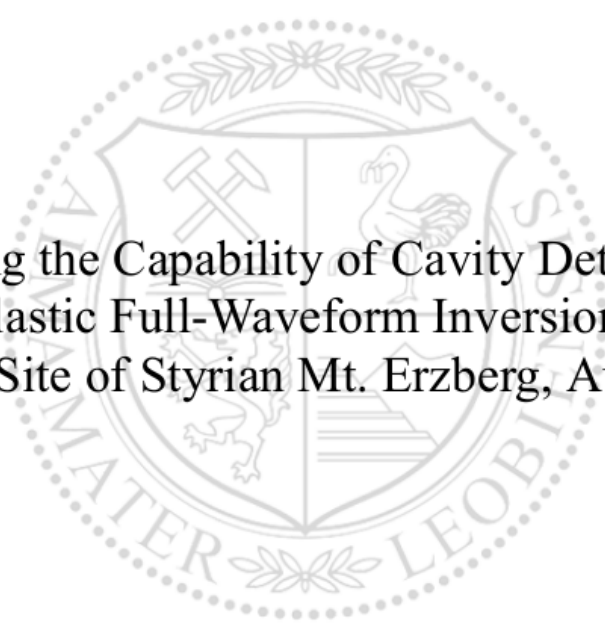Chair of Applied Geophysics

Doctoral Thesis

Testing the Capability of Cavity Detection with elastic Full-Waveform Inversion at the Test Site of Styrian Mt. Erzberg, Austria

Katrin Peters-Poethke, M.Sc.

November 2020

MONTANUNIVERSITÄT LEOBEN
www.unileoben.ac.at

EIDESSTATTLICHE ERKLÄRUNG

I declare on oath that I wrote this thesis independently, did not use other than the specified sources and aids, and did not otherwise use any unauthorized aids.

I declare that I have read, understood, and complied with the guidelines of the senate of the Montanuniversität Leoben for "Good Scientific Practice".

Furthermore, I declare that the electronic and printed version of the submitted thesis are identical, both, formally and with regard to content.

Datum 25.11.2020

Signature Author
Katrin Peters-Poethke

Abstract

This thesis deals with the theory and application of full-waveform inversion. In the first part of this thesis the full-waveform inversion is mathematically described. Thereby the forward problem is explained, including a short discussion about numerical stability and dispersion. Following that, the inversion theory is given, once in the time-domain and once in the frequency-domain. The emphasis of the formulations lays here on the theory implemented in a newly developed inversion algorithm. This novel code is then tested by applying the inversion schemes to a simple cross-hole configuration. The inversion is carried out for Vp, Vs and Vp and Vs, simultaneously. The velocity anomalies were once placed at the same position and once at different positions, additionally showing different sign of perturbation. This cross-hole configuration is also applied to another 2-dimensional inversion code developed by the Institute of Technology in Karlsruhe (KIT). Both inversion algorithms could reliably reconstruct the velocity anomaly in terms of position, shape, size and sign of perturbation. The inversion converge very fast and the data misfit could be minimised in few iteration steps. In the second part of this thesis, the survey area is introduced, which is located in a closed down part of Mt. Erzberg. Old mine maps indicate an abandon tunnel in $25\,\mathrm{m}$ depth and with a diameter of $4\,\mathrm{m}$. Two surveys were conducted, using two different sources for wave excitation. The first survey in 2016 used hammer strikes on a prismatic wedge. This kind of source was chosen in order to generate high-frequency signals and S-waves. The profile was $138\,\mathrm{m}$ long and 80 3-component receivers were deployed with a receiver spacing of 2 and $1\,\mathrm{m}$, respectively. The data processing includes data quality control, normalisation routines, stacking, rotation and finally a velocity and spectral analysis. The signal-to-noise ratio is not satisfactory at all, wherefore a second survey with a different kind of source was repeated. The second survey in 2018 used small explosives with a so called Buffalo-Gun as source. The profile was $128\,\mathrm{m}$ long and therefore $10\,\mathrm{m}$ shorter than in the previous measurements. That is due to the ongoing construction works for the nearby Zentrum am Berg. Nevertheless 75 3-component receivers could be deployed with the same receiver spacing as in the previous measurement and a shot spacing of $8\,\mathrm{m}$. The data processing again included a data quality control and a spectral analysis, showing improved signal-to-noise ratio. The data from the second survey are considered for a first-arrival travel-time tomography. Two starting models are designed, which possess gradually increasing velocities with depth, but different velocity values. Both inverted models were averaged to determine a sophisticated starting model for the tomography. The then inverted model serves as the initial model for the following synthetic study and the inversion of elastic parameters. The synthetic studies allow a characterization of wavefield behaviour in the presence of a subsurface cavity. Initially a comparable source wavelet is determined by transforming the amplitude spectra of the field data into the time-domain. Afterwards several forward simulations are done with different quality factors. The comparison of the amplitude spectra of measured field data and synthetically modelled data allows a determination of a reasonable Q-factor of 5. Now

the simulations based on the tomography model without and with an implemented cavity are executed, allowing a comparison and development of inversion strategies. Three main strategies are considered, strategy A includes a trace killing without any filtering, strategy B includes a trace killing and a LP-filtering of the data and strategy C includes an offset mute until 50 m, a filtering and a time-windowing of the data for P-waves and Surface-waves. Those inversion strategies are applied to two different starting models in order to recreate the implemented cavity. The first model is the travel-time tomography model and the second one is a perturbed version of the travel-time tomography model. The synthetic inversion results show a good and reliable reconstruction of the cavity in nearly all inversion approaches and parameters. The implemented cavity can undoubtedly be reconstructed. With that knowledge at hand, finally the inversion strategies are applied to the measured field data. Here the cavity could not be reliably and undoubtedly resolved. The suspected cavity is not as well and clearly reconstructed as in the synthetic study. Considering all inversion approaches and the a priori knowledge of the cavity, it might be argued that the cavity is indicated.

Zusammenfassung

Diese Arbeit beschäftigt sich mit der Theorie und Anwendung der vollen Wellenforminversion. Dabei wird im ersten Teil der Arbeit die Wellenforminversion mathematisch beschrieben. Hierbei wird das Vorwärtsproblem erläutert, inklusive einer Diskussion über das numerische Stabilitäts- und Dispersionsverhalten. Anschließend wird auf das Inversionsproblem eingegangen, wobei zwischen der Inversion im Zeitbereich und im Frequenzbereich unterschieden wird. Die mathematischen Formulierungen beziehen sich dabei auf die implementieren Routinen in einem neu programmierten Inversionscode. Anschließend wird die Implementierung dieser Inversionsroutinen an einem einfachen cross-hole Modell getestet. Hierbei wird für die P-Wellen-, S-Wellen- und die P- und S-Wellengeschwindigkeit invertiert. Die Geschwindigkeitsanomalien befinden sich dabei an gleicher Position und an unterschiedlichen Positionen mit unterschiedlicher Richtung der Geschwindigkeitsperturbation. Dieses einfache cross-hole Modell wird mit einem weiteren 2-dimensionalen Inversionscode vom Intitute of Technology Karlsruhe (KIT) invertiert. Beide Inversionsalgorithmen können die Anomalien sehr gut rekonstruieren was ihre Position, Form, Größe und Vorzeichen der Perturbation betrifft. Die Inversionen konvergieren schnell und können den Datenunterschied nach wenigen Iterationen wesentlich minimieren. Im zweiten Teil der Arbeit wird das Untersuchungsgebiet vorgestellt, welches sich in einem stillgelegten Teil des Erzbergs befindet. Alte Karten verweisen auf einen offengelassenen Tunnel in 25 m Tiefe und einem Durchmesser von 4 m, welcher durch die Inversion mit seismischen Daten abgebildet werden soll. Zwei Messungen wurden durchgeführt, wobei zwei unterschiedliche Quellen zum Einsatz kamen. Für die erste Messung 2016 wurden Hammerschläge auf eine prismatische Metallhaube verwendet. Diese Art der Quelle sollte hohe Frequenzen und S-Wellen generieren. Das Profil war 138 m lang, wobei 80 3-Komponentengeophone mit einem Abstand von 2, bzw. 1 m verwendet wurden. Die Datenprozessierung beinhaltet eine Qualitätskontrolle, ein Normalisierungsprozedere, das Aufsummieren der Daten, eine Rotation und abschließend eine Geschwindigkeits- und Spektralanalyse. Das Signal-Rausch-Verhältnis ist nicht zufriedenstellend, weshalb eine zweite Messung mit Verwendung einer anderen Quelle 2018 wiederholt wurde. Die gewählt Quelle waren dabei Explosionen mit einer sogenannten Buffalo-Gun. Das Profil war bei der zweiten Messung 10 m kürzer, da die Ebene für Bauarbeiten am darunterliegenden Zentrum am Berg verkürzt werden musste. Dennoch konnten 75 3-Komponentengeophone mit dem gleiche Abstand wie bei der ersten Messung ausgelegt werden. Der Schussabstand betrug 8 m. Die Datenprozessierung beinhaltet eine Qualitätskontrolle und eine Spektralanalyse, welche auf ein verbessertes Signal-Rausch-Verhältnis hindeutet. Die Daten der zweiten Messung werden für eine P-Wellenlaufzeittomographie verwendet. Als Startmodell werden zwei Modelle mit graduellem Geschwindigkeitsanstieg mit der Tiefe verwendet und invertiert. Beide unterscheiden sich durch die gewählten Startgeschwindigkeiten. Die invertierten Modelle werden dann gemittelt und als eigentliches Startmodell genutzt. Das Tomographiemodell wird weiterhin als Startmodell für die folgenden synthetischen Studien und die elastische

Parameterinversion verwendet. Die synthetischen Studien erlauben eine Einschätzung des Verhalten des Wellenfeldes im Falle eines Hohlraums im Untergrund. Zunächst wird aus dem Amplitudenspektrum der gemessenen Felddaten ein adäquates Quellwavelet ermittelt. Danach werden verschiedene Vorwärtssimulationen auf Grundlage des Tomographiemodells durchgeführt, welche unterschiedliche Qualitäts-Faktoren berücksichtigen. Durch den Vergleich der Amplitudenspektren der im Feld gemessenen und der simulierten Daten kann ein geeigneter Q-Faktor von 5 ermittelt werden. Nun werden Simulationen ohne und mit implementierten Hohlraum durchgeführt und die Wellenfelder verglichen, wobei drei Inversionsstrategien erntwickelt werden. Strategie A beinhaltet eine Löschung quellnaher Spuren, aber kein Filtern. Strategie B beinhaltet eine Löschung quellnaher Spuren und ein Filtern der Daten und Strategie C beinhaltet die Löschung aller Spuren innerhalb eines Quellabstandes von 50 m, eine Filterung der Daten und die Anwendung eines geeigneten Zeitfensters für die P-Welle und die Oberflächenwellen. Diese Inversionsstrategien werden im synthetischen Fall angewendet und auf ihre Eignung zur Hohlraumdetektierung getestet. Für die Inversion synthetischer Daten werden zwei Startmodelle berücksichtigt, einmal das Tomographiemodell und eine perturbierte Version des Tomographiemodells. Die Inversion beider Startmodelle unter Anwendung der Inversionsstrategien zeigt eine gute Rekonstruktion des implementierten Hohlraums. Dieser kann in fast allen Inversionsdurchläufen und Parametern unzweifelhaft abgebildet werden. Die ermittelten und getesteten Inversionsstrategien werden letztendlich auf die im Feld gemessenen Daten angewendet. Die Ergebnisse zeigen keinen eindeutigen Hohlraum, sondern lediglich eine Andeutung dessen. Unter Verwendung aller Inversionsergebnisse und dem a priori Wissens eines Hohlraums in der Lage und der Tiefe könnte eine Lokalisation eben dessen argumentiert werden.

Contents

II Real Data Application

8 Conclusion and Outlook   **129**

9 Acknowledgement   **131**

List of Figures

List of Tables

Nomenclature

Symbol	Description
R	relaxation function
G	Green's function
J	Jacobian
H	Hessian
$\theta(t)$	Heaviside function
b_k	base function
$\mathcal{C}$	Courant number
x_r, x'	receiver and source position
r	source receiver offset
t	travel time
nx, nz	grid points in x- and z-direction
x, z	model length in x- and z-direction
dx	grid spacing
dt	time step
T_{max}	maximum modelling time
ntr	number of traces
nsp	number of time samples
f, f_{dom}	frequency, dominant frequency
E	objective function
m	model
m^{true}, m^{inv}	true and inverted model
d	data
δu	data residuals
k	iteration step
α	step length
G	inversion kernel
U, V, S	matrix of data space, model space and singular values
si	singular value
W_d, W_m	data and model weighting matrices
R_m, R_d	model and data resolution matrix
λ	damping factor
P	preconditioning factor
β	Polak-Ribiére weighting factor
η, f_k, w_k	specific weighting factors
d_{lk}, s_{lk}	observed and synthetic Fourier coefficients
ϵ	water level
F	body force

$\sigma,\ \epsilon$	stress and strain history
M_R	relaxation modulus
$\tau_{\epsilon l},\ \tau_{\sigma l}$	stress and strain relaxation times
p	pressure
r_l	memory variable
s	source term
σ_{ij}	stress tensor components
$\pi,\ \mu$	relaxation moduli
$V_p,\ V_s$	P-wave and S-wave velocity
u	particle displacement
ω	angular frequency
ρ	density
$\lambda,\ \mu$	Lamé constants
L	forward operator
Ψ	wave field
sc	scaling factor per trace
SF	scaling factor per triplet
OSF	global scaling factor
$D^V,\ D^H$	vertically and horizontally rotated data
$D^S,\ D^N$	South and North directed data
ϕ	angle of hammer blow
S/N	Signal-to-Noise ratio
A	Amplitude
Q	quality factor
λ	wave length
d	width of Fresnel zone
l	length of ray path
i, k, N	counting variables
∂	partial derivation
$\Re,\ \Im$	real and imaginary part
Δ	Laplace operator
$\mathcal{O}$	terms of higher order
$\underline{\square}$	rotated matrix
$\square^{-g}$	generalized inverse
TTT model	travel-time tomography model
TTT perturbed	perturbed travel-time tomography model
initial data	data calculated with starting model
observed data	data calculated with true model
real data	data measured in the field

Chapter 1

Introduction

1.1 Motivation

The detection, and mapping, of subsurface cavities is an important task, primarily because the potential collapse of a cavity poses a hazard to infrastructure and residents. Cavities can either be human-induced or created naturally. Natural cavities form through chemical erosion. Acidic rainwater or groundwater dissolve soil underlying limestones, dolomites, carbonate rocks, salt beds or naturally dissoluble rocks and leave small voids, which can expand to cavities of several centimetres or even meters in diameter. Man-made cavities include tunnels from abandoned mining, old basement structures from demolished buildings, tunnels created for illegal activities, and cavities produced through a nuclear weapon test.

The collapse of a cavity, meaning the migration of these cavities to the surface, causes sinkholes, which often causes devastating consequences. In the US-states Florida, Texas, Alabama, Missouri, Kentucky, Tennessee and Pennsylvania naturally formed cavities in the subsurface cause the generation of sinkholes quite frequently (Galloway et al. (1999), USGS (2000)). In the Chinese province of Shandong 20 million square meters of land per year are devoured by sinkholes due to excessive coal mining (Quanyuan et al. (2009), Xiao et al. (2014)). In the Russian cities Solikamsk and Berezniki huge sinkholes are caused by the combination of human-induced cavities, due to potash mining and naturally flowing groundwater, which expands the region of collapse only further (Andreichuk et al. (2000), Whyatt and Varley (2008)). These few examples only confirm the necessity of confidently detecting and mapping subsurface cavities, already in an early stage. Whether filled with air or water, the material contrast of a cavity to the surrounding rock or soil, is typically strong enough to provide a significant signal in many geophysical measurements. Miller and Steeples (1991) did seismic reflection studies to detect water-filled cavities in 0.6 m thick coal seams in 7 m depth in Kansas (USA), which where left open after subsurface mining. The voids produced a trace-to-trace lack of reflection energy and showed an increase of the dominant frequency within the stacked sections. Grandjean and Leparoux (2004) even built a suited test site in order to test geophysical methods for the detection of cavities. They

buried a polystyrene cylinder of 0.4 m diameter in 0.2 to 0.4 m depth and used a dropping mass to generate seismic waves. They found a first-break in arrival times of P-waves and significant slope changes in the Rayleigh wave move out. Cardarelli et al. (2009) applied a seismic refraction tomography to detect cavities in 9 m depth with diameters of 2-5 m in Rome (Italy), which could be reliably be reconstructed, but showed wave speeds of the cavity that are higher than they theoretically should be. Another study in Italy was carried out by Fiore et al. (2013), who used high resolution seismic reflection methods to detect tuff-cavities, that are in 10-19 m depth and posses an extent of 6 m vertically and 6x10 m horizontally. The cavity caused diffraction hyperbolas and appeared as perturbations on strong reflections. Sloan et al. (2013) used also seismic refraction tomography and additionally conducted a multichannel surface wave analysis to detect man-made tunnels in the USA and Afghanistan. The tunnels have a sizes of 1x1, 1.25x1.25 and 1.5x1.2 m, respectively, and are located in 3 to 9 m depth. They saw a Vp and Vs decrease at the void position in a ray-coverage plot. The multichannel analysis of surface waves showed a high-velocity zone above the tunnel, which is explained by the stress increase due to the material removal and therefore an increased load borne by the roof and side walls. Driad and Piwakowski (2014) used high resolution seismic reflection (HRSR) to detect 2 m big and 7-20 m deep cavities in south France. The wave propagation through these cavities cause a delay in arrival times and introduced a masking effect on the underlying reflector. Combined geophysical measurements were used by Giorgi and Leucci (2014) at the Ionian coast of Salento peninsula in south Italy. A clear low-velocity zone with P-wave velocities of about 300-400 m/s was induced by cavities in 1 m depth that are 15 m wide and 4 m high. Peterie and Miller (2015) used P-to-S diffraction imaging methods to detect a man-made tunnel in 5-10 m deep granite. The tunnel, with the size of 7x5 m, caused diffraction hyperbolas with low amplitudes and a polarity reversal at the apex. Shao et al. (2016) calculated the generalized S-transform of Rayleigh waves and detected a 1 m deep, 6 m high and 6 m wide tunnel in Kansas, USA. The challenge of cavity detection lies in the size-to-depth-ratio of most tunnels or voids, which is at, or below, the resolution capacity of most geophysical methods. Fig. 1.1.1 shows the relationship between size and depth of the cavities and tunnels detected in the previously mentioned studies. The size-to-depth ratio of the cavity, which we try to reconstruct in this study is plotted as well. Even though the diameter of our cavity is not as small or big as other detected tunnels and voids, the depth of our target is way deeper than in any other study presented here. Therefore this study serves as a capability test of cavity detection with elastic full-waveform inversion with that given specifications.

1.2 Structure of this Thesis

This thesis is organised in two more or less independent parts, where the first part includes the mathematical theory of the newly developed *visleawie2d code*, as well as a synthetic cross-hole
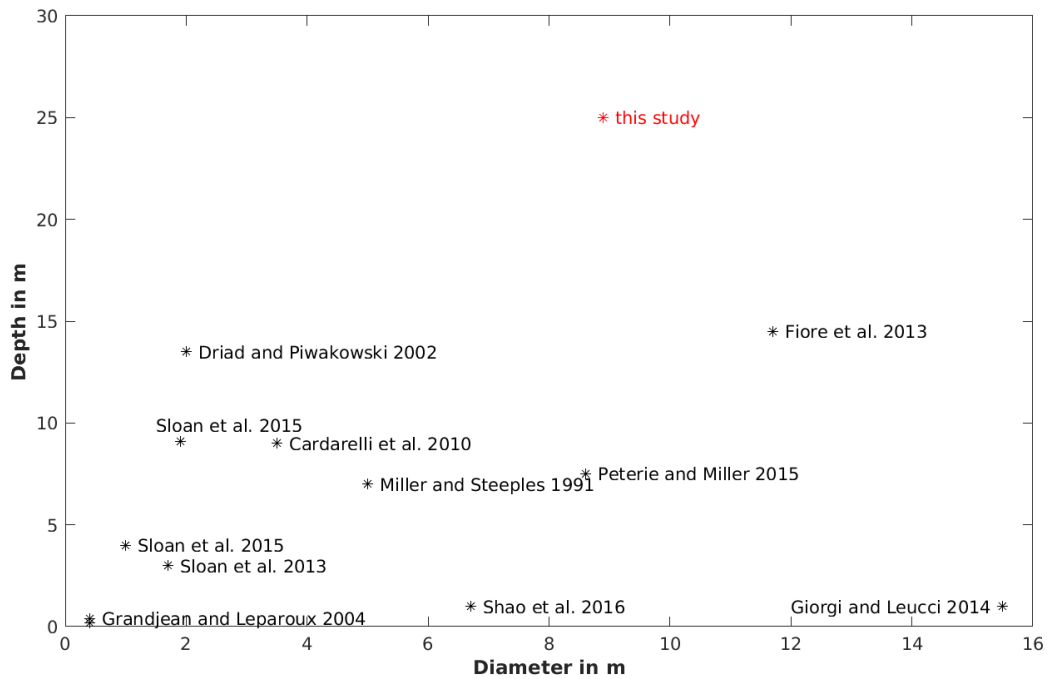
Figure 1.1.1: Size to depth ratios for previous studies on cavity detection

study. The second part is dedicated to the real data acquisition, travel time tomography and the inversion studies, synthetically and of the real data.

Chapter 2 Chapter two gives an overall overview of the state of the art of full-waveform (FWI) inversion and the developments of the last three decades. The theory of the forward problem, including a shot discussion on stability and dispersion, is explained with the emphasis on the FD code developed by Robertsson et al. (1994) and Robertsson (1996). Afterwards the inversion theory for time-domain and frequency-domain data is outlined, again with the emphasis on the implemented routines in the novel *visleawie2d code* (**VIS**co-**ELA**stic **W**aveform **I**nversion). The theory of the mathematical approach used for this code was largely gathered and implemented by Dr. Marco Paschke. Further code organisation was performed by Dr. Jean Kormann and Dipl.-Geophys. Jens Zeiß.

Chapter 3 In chapter three the algorithms implemented in *viselawi2d* are tested with a simple cross-hole configuration, in which velocity anomalies are located at coinciding or at different positions. The elastic parameter inversion was carried out for P-wave, S-wave and P- and S-waves, respectively. Also different frequencies and inversion strategies were tested. The later used inversion code *IFOS2D* was also applied to the cross-hole model, in order to somehow benchmark the inversion parameters provided to IFSO2D. The results are similar and the velocity perturbation could be recovered very well by both inversion codes. The shape, size, position and magnitude of the anomaly could be resolved without doubt. Both algorithms show very good and fast convergence.

Chapter 4   Chapter four is dedicated to the real data acquisition and data processing. First, the test site at Mount Erzberg is introduced by giving a short overview about the local geology. Two surveys were performed in June 2016 and October 2018, respectively, using two different sources for excitation, namely hammer blows and explosives. The data from the first survey were quality controlled, a proper normalisation and stacking procedure was determined and a rotation of the data was performed to better separate the wave fields in order to improve the signal-to-noise ratio. Afterwards a velocity and spectral analysis was conducted, resulting in unsatisfying signal-to-noise quality and the decision for another survey and a more powerful (explosion) source. The data from the second survey were also quality controlled and a spectral analysis shows a good signal-to-noise ratio. That is why the data from the second survey were taken to perform a travel-time tomography of first arrivals.

Chapter 5   Within chapter five a first-arrival travel-time tomography based on the data from the second survey is performed. The brief theory of travel-time tomography is given. Afterwards a determination of a reasonable starting model is done, by averaging the velocities of two inverted models based on a very fast and rather slow starting model. The inversion results gained from the first-arrivals are interpreted and serve as a sophisticated model for the following synthetic studies and later full-waveform inversion.

Chapter 6   Chapter six includes synthetic studies on how a subsurface cavity influences the wavefield. A source wavelet for the calculations was derived by a Fourier transformation of the amplitude spectra of the real data. Different forward calculations with different attenuation factors were carried out and the comparison of amplitude spectra of the synthetic and real data allowed the determination of a Q-factor. By setting these preconditions a forward modelling based on the travel-time tomography model without and with a cavity allows a realistic comparison of data and therefore the analysis of influences by the cavity. The phase spectra of the difference seismograms of initial and observed data were calculated and show a reasonable phase shift larger than 30° at higher frequencies and larger offsets. Additionally the phase shifts were further examine in the time-domain, allowing a specific selection of shots, offset ranges and time-windows in which the phase shift is apparent. This synthetic study also serves for the determination of inversion strategies that were applied to the synthetic data. After several synthetic inversion runs in order to yield an effective taper function, two different starting models for the synthetic inversion were considered. First, the travel-time tomography model and second a perturbed velocity model. Three inversion strategies are tested on those models, namely strategy A (trace killing, no filtering), strategy B (trace killing, low-pass filtering) and strategy C (offset muting, time-windowing, low-pass filtering). The inversion runs are shown and discussed.

Chapter 7   In chapter seven the inversion strategies derived and tested in the previous chapter are applied to the measured field data. Additionally a fourth strategy is introduced,

strategy D which includes a trace killing and a BP-filtering. The inversion results are shown and summarized. Finally the inversion outcomes are discussed in terms of reliability, with a special focus on the inversion of density.

Chapter 8   Finally in chapter eight the results of this thesis are once again summarized and some ideas for an improved inversion of subsurface cavities are given.

Part I

Mathematical Theory, Implementation and Testing

Chapter 2

Theory

In this chapter the overall state of the art of full-waveform inversion (FWI) as well as the mathematical theory of the forward and inverse problem are outlined. The emphasis of the theory section lays on the implemented routines of the newly developed *viselawi2d* code, but also includes the mathematical approaches used in the *IFOS2D* code, which is used later on. A short discussion about numerical stability and dispersion as well as the physics of the implemented sources is given. The inversion theory shortly explains the inverse problem in the time-domain and more detailed in the frequency-domain.

2.1   State of the Art of FWI

Tarantola (1984a,b) was the first one to describe and introduce the needed mathematics for the inversion of reflection seismic data. He found that the linearization of the forward problem is dependent on the reference medium used: in homogeneous reference media it leads to an inverse solution strongly related to the Kirchhoff migration whereas in heterogeneous media it leads to an inverse algorithm based on imaging principles. At the same time Berkhout (1984) worked out that each linear inversion step consists of a prestack migration and prestack modelling step. The described theory needed the first computational implementations to solve the forward and inverse problem numerically. Even though Kelly et al. (1976) were the first one to compute the forward problem with a finite-difference approach by solving the wave equation, Virieux (1984) was the one who computed the forward problem with a finite-difference approach by solving the equation for the stress relation and Newton's Law alternating. This was a big advantage because it cut down computational costs. Gauthier et al. (1986) followed up with the theoretical mathematics introduced by Tarantola (1984a,b) and invented an iterative algorithm by solving the forward and inverse problem numerically by using a gradient method to minimize the misfit function and computed the first numerical examples. Now the computation of the full-waveform inversion was born as a novel approach to resolve subsurface models with greater detail, but due to the numerical nature of this method, some problems became visible. One big issue is the efficiency of inversion algorithms.

Tarantola (1986) draw the attention to the choice of inversion parameters, which is not neural. He stated that the parametrization defines a hierarchical problem and that an inadequate choice of parameters leads to an inefficient algorithm. He proposed to first invert for P-wave velocity and impedance, then for S-wave velocity and impedance and finally for density. Another important step to increase the efficiency of iterative algorithms was introduced by conjugate gradient algorithms, which was first discussed by Mora (1987). Furthermore Mora (1988) examined the influence of different wave types on the inversion results and found out, that different wave types resolve different components of the model, namely reflection data resolve high wave numbers and transmission data resolve low wave numbers.

The core of the inversion process is to minimize the difference between the synthetic data, generated by solving the forward problem, and the observed data. This difference is quantified by the misfit function. Usually this misfit function is defined as a least-squares problem. Crase et al. (1990) examined the robustness of other criteria, such as the L1-norm, the L2-norm, the Cauchy and sech criterion. He found out that the latter two are superior to the first two for the inversion of noise-free and noise-added data. Also Shin and Min (2006) introduced a new approach of defining the misfit function. They used the ordinary least-squares approach, but they did not minimize the residuals of the synthetic and observed data, but the difference between the amplitudes, phases or both, amplitudes and phases of the data. This was realized by using the logarithmic of the wavefield, which allows to separate the data into amplitude-only, phase-only or both. One of the main cornerstones in FWI was the transformation of the wave equation into the frequency-domain and moreover, the introduction of a 2-dimensional finite-difference method to solve the forward problem and the inversion problem in the frequency domain. This was done by Pratt and Worthington (1990); Pratt (1990) and following working groups used the frequency-domain approach to solve the inversion problem. This was a big advantage because it cut down computational costs. Sirgue and Pratt (2004) found out that only a selection of frequencies is required for the inversion when a wide range of offsets is available, or in other words, the larger the range of offsets the fewer frequencies are needed. The choice of frequencies and how to invert them was now a new issue that had to be examined. Brossier et al. (2009) implemented a parallel full-waveform inversion by using a limited-memory quasi-Newton algorithm and inverted a selection of increasing frequencies sequentially and successively and found that it is necessary to invert for more than just one frequency at the beginning of the inversion process. Also Shin et al. (2010) did some frequency analysis and introduced another novel approach of how to invert the data. They did the inversion in the Laplace- and Laplace-Fourier domain and showed the robustness of the inversion algorithm in the Laplace-Fourier domain.

When inverting data with a gradient-based method one faces the problem of convergence into a 'false' minima. If the algorithm converges it does not necessarily mean that the algorithm converges into the global minima. It could be possible that the algorithm converges into a local minimal and is trapped there, this is particularly possible if the starting model is

far from the true model. Bunks et al. (1995) suggested a multigrid method to improve performance of iterative inversions by decomposing the problem by scale. He first inverted for large scales and with each iteration decreased the scale length which ensures the algorithm to converge into the global minima. Another approach to decrease computational capacities was introduces by Krebs et al. (2009) who reduced the cost of FWI by using data that were formed by encoding and summing of data from individual sources. Here all the data which are generated by different sources with different source signatures and are recorded by different receivers are encoded and summed and form a single gather.

The application of FWI to real data became serious in the 90s, e.g. Crase et al. (1990) and Igel et al. (1996). Operto et al. (2004) and Bleibinhaus et al. (2009) did acoustic FWI for reflection seismic data and showed the improvement in resolution of the starting model derived by traveltime tomography. Further Bleibinhaus and Rondenay (2009) showed that neglecting the free-surface rather than the structure of the surface results in deteriorating influences. FWI is also a mighty tool to resolve gas clouds or CO_2 plumes in the subsurface, which can be useful in the oil and gas exploration or in monitoring reservoirs (Warner et al. (2013); Romdhane and Querendez (2014)). Nevertheless a lot of energy was put into the development of FWI in the past 30 years, FWI has not reached its limits in terms of resolution and (computational) efficiency yet.

The newly developed code presented in this study takes the forward modelling routines developed by Robertsson et al. (1994) and Robertsson (1996). The elastic parameter inversion is realised by using the Gauß-Newton method including Tikhonov's 0th order regularisation of weighted model updates. Advantages of this code include the incorporation of topography, the consideration of attenuation and the explicit computation of Jacobian matrices which give resolution matrices. Furthermore, the forward modelling is performed in the time-domain, whereas the parameter inversion is executed in the frequency-domain. That reduces computational costs and an explicit muting of undesired surface waves can be done, which would deteriorate the inversion due to their high amplitudes but limited penetration depths.

2.2 Forward Modelling

2.2.1 Solving the Wave Equation

Solving the forward problem means solving the wave equation at each point of the considered model. Therefore a large number of numerical approaches have been developed over the years, which exhibit their most significant distinction in the spatial discretisation used. The spatial discretisation transforms the exact spatial derivatives in the wave equation into an algebraic system. Most common used numerical approaches are the *finite-difference method, finite-element method, spectral-element method* or some mixtures of those. All of these methods have their eligibility and come with advantages, but also with disadvantages that

have to be considered and weighted in the matter of a specific application. Basically what all algorithms do is to solve the wave equation, meaning describing the wave propagation in a general elastic medium. This is mathematically described by the following equation

$$\rho \frac{\partial^2 u_i}{\partial t^2} = \frac{\partial \sigma_{ij}}{\partial x_j} + F_i \tag{2.2.1}$$

with u_i the particle displacement, t the travel time, σ_{ij} the stress tensor and F_i a generic body force. The material specific properties that describe the material's reaction in case a body force is applied can be formulated by a linear stress-strain relationship as

$$\sigma_{ij} = \lambda \Theta \delta_{ij} + 2\mu \epsilon_{ij} \tag{2.2.2}$$

$$\epsilon_{ij} = \frac{1}{2} \left(\frac{\partial u_i}{\partial x_j} + \frac{\partial u_j}{\partial x_i} \right) \tag{2.2.3}$$

with λ and μ the Lamé constants, δ_{ij} the Kronecker delta, Θ the dilatation (sum of all three stress components) and ϵ_{ij} the strain tensor. Eq. 2.2.3 account for isotropic, elastic media and together with Eq. 2.2.1 are called the *stress-displacement formulation*. To solve these equations numerically they have to be discretized in space and time on a grid, meaning that the Lamé constants, particle velocities and stresses have to be defined at discrete coordinates and discrete times and must be calculated throughout the whole model at every grid point and at each time step.

The forward modelling implemented in the *viselawi2d code* is performed in the time-domain and is based on a visco-elastic Finite-Difference (FD) algorithm that also accounts for topography by using the image method (Robertsson et al. (1994), Robertsson (1996)). This FD-modelling has an accuracy of second-order in time and fourth-order in space, since it was tested to be superior to second-order or fourth-order in time and in space (Robertsson et al. (1994)). The model is based on the hypothesis that the current value of the stress tensor depends on the strain tensor's history. To transform the strain history into the stress history, a transform function is needed, the so called *relaxation function*. Mathematically this relation can be described for the 1-dimensional, isotropic and homogeneous case as follows

$$\sigma = R * \dot{\epsilon} = \dot{R} * \epsilon \tag{2.2.4}$$

where σ and ϵ are the stress and strain histories, respectively, R is the relaxation function and the asterisk $*$ denotes the convolution in time. The relaxation function is of special interest, it determines the behaviour of the material and is defined as

$$R(t) = M_R \left(1 - \sum_{l=1}^{L} \left(1 - \frac{\tau_{\epsilon l}}{\tau_{\sigma l}} \right) e^{\frac{-t}{\tau_{\sigma l}}} \right) \theta(t) \tag{2.2.5}$$

with M_R and $\theta(t)$ as relaxation modulus and Heaviside function, respectively, and $\tau_{\epsilon l}$ and $\tau_{\sigma l}$ as stress and strain relaxation times (Robertsson et al. (1994)). By taking the time derivative of equation (2.2.4), substituting the definitions for the pressure $\sigma = -p$ and dilatation $\dot{\epsilon} = v_x$ (1-dimensional case) one can derive the formula

$$-\dot{p} = M_R \left(1 - \sum_{l=1}^{L} \left(1 - \frac{\tau_{\epsilon l}}{\tau_{\sigma l}} \right) \right) v_x + \sum_{l=1}^{L} \underbrace{M_R \left(\frac{1}{\tau_{\sigma l}} \left(1 - \frac{\tau_{\epsilon l}}{\tau_{\sigma l}} \right) e^{\frac{-t}{\tau_{\sigma l}}} \right) \theta(t) * v_x}_{r_l} \qquad (2.2.6)$$

where the sum of the second term of the right hand-side is called *memory variable* r_l (Robertsson et al. (1994)). The time derivative of r_l gives

$$\dot{r}_l = -\frac{1}{\tau_{\sigma l}} r_l + M_R \frac{1}{\tau_{\sigma l}} \left(1 - \frac{\tau_{\epsilon l}}{\tau_{\sigma l}} \right) v_x. \qquad (2.2.7)$$

For the complete description of the wave propagation Newton's second law is needed (Robertsson et al. (1994))

$$\rho \dot{v} = -p_x. \qquad (2.2.8)$$

Now equations (2.2.6) till (2.2.8) construct a first-order linear differential system of 1-dimensional wave propagation in a visco-elastic medium and have to be extended for the 2-dimensional case and both wave types (P- and SV-waves). This gives a set of eight equations needed for the calculation of the time derivatives of stress tensors, velocities and memory variables with respect to the x- and y-direction. The forward operator in the time-domain looks like the following

$$\frac{\partial \sigma_{xz}}{\partial t} = \mu \frac{\tau_\epsilon^s}{\tau_\sigma} \left(\frac{\partial v_x}{\partial z} + \frac{\partial v_z}{\partial x} \right) + r_{xz} + s_{\sigma_{xz}}$$

$$\frac{\partial \sigma_{xx}}{\partial t} = \pi \frac{\tau_\epsilon^p}{\tau_\sigma} \left(\frac{\partial v_x}{\partial x} + \frac{\partial v_z}{\partial z} \right) - 2\mu \frac{\tau_\epsilon^s}{\tau_\sigma} \frac{\partial v_z}{\partial z} + r_{xx} + s_{\sigma_{xx}}$$

$$\frac{\partial \sigma_{zz}}{\partial t} = \pi \frac{\tau_\epsilon^p}{\tau_\sigma} \left(\frac{\partial v_x}{\partial x} + \frac{\partial v_z}{\partial z} \right) - 2\mu \frac{\tau_\epsilon^s}{\tau_\sigma} \frac{\partial v_x}{\partial x} + r_{zz} + s_{\sigma_{zz}}$$

$$\frac{\partial v_x}{\partial t} = \frac{1}{\rho} \left(\frac{\partial \sigma_{xx}}{\partial x} + \frac{\partial \sigma_{xz}}{\partial z} \right) + s_{v_x}$$

$$\frac{\partial v_z}{\partial t} = \frac{1}{\rho} \left(\frac{\partial \sigma_{xz}}{\partial x} + \frac{\partial \sigma_{zz}}{\partial z} \right) + s_{v_z} \qquad (2.2.9)$$

$$\frac{\partial r_{xz}}{\partial t} = -\frac{1}{\tau_\sigma} \left[r_{xz} + \mu \left(\frac{\tau_\epsilon^s}{\tau_\sigma} - 1 \right) \left(\frac{\partial v_x}{\partial z} + \frac{\partial v_z}{\partial x} \right) \right]$$

$$\frac{\partial r_{xx}}{\partial t} = -\frac{1}{\tau_\sigma} \left[r_{xx} + \pi \left(\frac{\tau_\epsilon^p}{\tau_\sigma} - 1 \right) \left(\frac{\partial v_x}{\partial x} + \frac{\partial v_z}{\partial z} \right) - 2\mu \left(\frac{\tau_\epsilon^s}{\tau_\sigma} - 1 \right) \frac{\partial v_z}{\partial z} \right]$$

$$\frac{\partial r_{yy}}{\partial t} = -\frac{1}{\tau_\sigma} \left[r_{yy} + \pi \left(\frac{\tau_\epsilon^p}{\tau_\sigma} - 1 \right) \left(\frac{\partial v_x}{\partial x} + \frac{\partial v_z}{\partial x} \right) - 2\mu \left(\frac{\tau_\epsilon^s}{\tau_\sigma} - 1 \right) \frac{\partial v_x}{\partial x} \right]$$

with $\mathbf{s}$ source terms, π, μ relaxation moduli and v_i velocity. Since the inversion is done in the frequency-domain the equations must be transformed in the frequency-domain, too. Therefore the time-dependent deviations are replaced by $i\omega$ and to reduce the number of equations, the memory variables can be substituted into the stresses. Reorganizing the equations with respect to the relaxation moduli yields (Paschke (2016))

$$i\omega\sigma_{xx} = \pi \left(\frac{\partial v_x}{\partial x} + \frac{\partial v_z}{\partial z} \right) \left(\frac{\tau_\epsilon^p}{\tau_\sigma} - \frac{1}{i\omega\tau_\sigma + 1} \left(\frac{\tau_\epsilon^p}{\tau_\sigma} - 1 \right) \right) - 2\mu \frac{\partial v_z}{\partial z} \left(\frac{\tau_\epsilon^s}{\tau_\sigma} - \frac{1}{i\omega\tau_\sigma + 1} \left(\frac{\tau_\epsilon^s}{\tau_\sigma} - 1 \right) \right) + s_{\sigma_{xx}}$$

$$i\omega\sigma_{zz} = \pi \left(\frac{\partial v_x}{\partial x} + \frac{\partial v_z}{\partial z} \right) \left(\frac{\tau_\epsilon^p}{\tau_\sigma} - \frac{1}{i\omega\tau_\sigma + 1} \left(\frac{\tau_\epsilon^p}{\tau_\sigma} - 1 \right) \right) - 2\mu \frac{\partial v_x}{\partial x} \left(\frac{\tau_\epsilon^s}{\tau_\sigma} - \frac{1}{i\omega\tau_\sigma + 1} \left(\frac{\tau_\epsilon^s}{\tau_\sigma} - 1 \right) \right) + s_{\sigma_{zz}}$$

$$i\omega\sigma_{xz} = \mu \left(\frac{\partial v_x}{\partial z} + \frac{\partial v_z}{\partial x} \right) \left(\frac{\tau_\epsilon^s}{\tau_\sigma} - \frac{1}{i\omega\tau_\sigma + 1} \left(\frac{\tau_\epsilon^s}{\tau_\sigma} - 1 \right) \right) + s_{\sigma_{xz}}$$

$$i\omega v_x = \frac{1}{\rho} \left(\frac{\partial \sigma_{xx}}{\partial x} + \frac{\partial \sigma_{xz}}{\partial z} \right) + s_{v_x}$$

$$i\omega v_z = \frac{1}{\rho} \left(\frac{\partial \sigma_{xz}}{\partial x} + \frac{\partial \sigma_{zz}}{\partial z} \right) + s_{v_z}.$$

$$(2.2.10)$$

A parametrisation of V_p, V_s and ρ demands a substitution of the relaxation moduli in eq.

2.2.10 with

$$
\pi = \lambda + 2\mu = \frac{V_p^2(1+\omega^2\tau_\sigma^2)^2\rho}{(1+\omega^2\tau_\sigma\tau_{\epsilon_p})^2}
$$
$$
\mu = \frac{V_s^2(1+\omega^2\tau_\sigma^2)^2\rho}{(1+\omega^2\tau_\sigma\tau_{\epsilon_s})^2}
$$

(2.2.11)

and changes eq. 2.2.10 to

$$
\begin{aligned}
i\omega\sigma_{xx} &= \frac{V_p^2(1+\omega_0^2\tau_\sigma^2)^2\rho}{(1+\omega_0^2\tau_\sigma\tau_{\epsilon_p}^2)} \left(\frac{\partial v_x}{\partial x} + \frac{\partial v_z}{\partial z}\right)\left(\frac{\tau_\epsilon^p}{\tau_\sigma} - \frac{1}{i\omega\tau_\sigma+1}\left(\frac{\tau_\epsilon^p}{\tau_\sigma}-1\right)\right) \\
&\quad - 2\frac{V_s^2(1+\omega_0^2\tau_\sigma^2)^2\rho}{(1+\omega_0^2\tau_\sigma\tau_{\epsilon_s})^2}\frac{\partial v_z}{\partial z}\left(\frac{\tau_\epsilon^p}{\tau_\sigma} - \frac{1}{i\omega\tau_\sigma+1}\left(\frac{\tau_\epsilon^s}{\tau_\sigma}-1\right)\right) + s_{\sigma_{xx}} \\
i\omega\sigma_{zz} &= \frac{V_p^2(1+\omega_0^2\tau_\sigma^2)^2\rho}{(1+\omega_0^2\tau_\sigma\tau_{\epsilon_p}^2)} \left(\frac{\partial v_x}{\partial x} + \frac{\partial v_z}{\partial z}\right)\left(\frac{\tau_\epsilon^p}{\tau_\sigma} - \frac{1}{i\omega\tau_\sigma+1}\left(\frac{\tau_\epsilon^p}{\tau_\sigma}-1\right)\right) \\
&\quad - 2\frac{V_s^2(1+\omega_0^2\tau_\sigma^2)^2\rho}{(1+\omega_0^2\tau_\sigma\tau_{\epsilon_s})^2}\frac{\partial v_x}{\partial x}\left(\frac{\tau_\epsilon^p}{\tau_\sigma} - \frac{1}{i\omega\tau_\sigma+1}\left(\frac{\tau_\epsilon^s}{\tau_\sigma}-1\right)\right) + s_{\sigma_{zz}} \\
i\omega\sigma_{xz} &= \frac{V_s^2(1+\omega_0^2\tau_\sigma^2)^2\rho}{(1+\omega_0^2\tau_\sigma\tau_{\epsilon_s}^2)} \left(\frac{\partial v_x}{\partial z} + \frac{\partial v_z}{\partial x}\right)\left(\frac{\tau_\epsilon^s}{\tau_\sigma} - \frac{1}{i\omega\tau_\sigma+1}\left(\frac{\tau_\epsilon^s}{\tau_\sigma}-1\right)\right) + s_{\sigma_{xz}} \\
i\omega v_x &= \frac{1}{\rho}\left(\frac{\partial\sigma_{xx}}{\partial x} + \frac{\partial\sigma_{xz}}{\partial z}\right) + s_{v_x} \\
i\omega v_z &= \frac{1}{\rho}\left(\frac{\partial\sigma_{xz}}{\partial x} + \frac{\partial\sigma_{zz}}{\partial z}\right) + s_{v_z}
\end{aligned}
$$

(2.2.12)

Now with the substitution

$$
\begin{aligned}
\tilde{V}_p(\omega) &= \frac{(1+\omega_0^2\tau_\sigma^2)^2}{(1+\omega_0^2\tau_\sigma\tau_{\epsilon_p})^2}\left(\frac{\tau_\epsilon^p}{\tau_\sigma} - \frac{1}{i\omega\tau_\sigma+1}\left(\frac{\tau_\epsilon^p}{\tau_\sigma}-1\right)\right) \\
\tilde{V}_s(\omega) &= \frac{(1+\omega_0^2\tau_\sigma^2)^2}{(1+\omega_0^2\tau_\sigma\tau_{\epsilon_s})^2}\left(\frac{\tau_\epsilon^s}{\tau_\sigma} - \frac{1}{i\omega\tau_\sigma+1}\left(\frac{\tau_\epsilon^s}{\tau_\sigma}-1\right)\right)
\end{aligned}
$$

(2.2.13)

one finally gets (Paschke (2016))

$$
\begin{aligned}
s_{\sigma_{xx}} &= i\omega\sigma_{xx} - V_p^2\rho\tilde{V}_p(\omega)\left(\frac{\partial v_x}{\partial x} + \frac{\partial v_z}{\partial z}\right) + 2V_s^2\rho\tilde{V}_s(\omega_0)\frac{\partial v_z}{\partial z} \\
s_{\sigma_{zz}} &= i\omega\sigma_{zz} - V_p^2\rho\tilde{V}_p(\omega)\left(\frac{\partial v_x}{\partial x} + \frac{\partial v_z}{\partial z}\right) + 2V_s^2\rho\tilde{V}_s(\omega_0)\frac{\partial v_x}{\partial x} \\
s_{\sigma_{xz}} &= i\omega\sigma_{xz} - 2V_s^2\rho\tilde{V}_s(\omega_0)\left(\frac{\partial v_x}{\partial z}\frac{\partial v_z}{\partial x}\right) \\
s_{v_x} &= i\omega v_x - \frac{1}{\rho}\left(\frac{\partial\sigma_{xx}}{\partial x} + \frac{\partial\sigma_{xz}}{\partial z}\right) \\
s_{v_z} &= i\omega v_x - \frac{1}{\rho}\left(\frac{\partial\sigma_{xz}}{\partial x} + \frac{\partial\sigma_{zz}}{\partial z}\right)
\end{aligned}
$$

(2.2.14)

The set of equations (2.2.14) can be written in matrix-vector form and would look like this

$$
\underbrace{\begin{bmatrix} s_{\sigma_{xx}} \\ s_{\sigma_{zz}} \\ s_{\sigma_{xz}} \\ s_{v_x} \\ s_{v_z} \end{bmatrix}}_{\mathbf{s}} = \underbrace{\begin{bmatrix} i\omega & 0 & 0 & -V_p^2\rho\tilde{V}_p(\omega)\frac{\partial}{\partial x} & \rho(-V_p^2\tilde{V}_p(\omega)+2V_s^2\tilde{V}_s(\omega))\frac{\partial}{\partial z} \\ 0 & i\omega & 0 & \rho(-V_p^2\tilde{V}_p(\omega)+2V_s^2\tilde{V}_s(\omega))\frac{\partial}{\partial z} & -V_p^2\rho\tilde{V}_p(\omega)\frac{\partial}{\partial z} \\ 0 & 0 & i\omega & -V_s^2\rho\tilde{V}_s(\omega)\frac{\partial}{\partial z} & -V_s^2\rho\tilde{V}_s(\omega)\frac{\partial}{\partial x} \\ \frac{-1}{\rho}\frac{\partial}{\partial x} & 0 & \frac{-1}{\rho}\frac{\partial}{\partial z} & i\omega & 0 \\ 0 & \frac{-1}{\rho}\frac{\partial}{\partial z} & \frac{-1}{\rho}\frac{\partial}{\partial x} & 0 & i\omega \end{bmatrix}}_{\mathbf{L}} \underbrace{\begin{bmatrix} \sigma_{xx} \\ \sigma_{zz} \\ \sigma_{xz} \\ v_x \\ v_z \end{bmatrix}}_{\boldsymbol{\Psi}}
$$

$$(2.2.15)$$

where $\mathbf{L}$ is the simplified forward operator and $\boldsymbol{\Psi}$ the wave field that should be calculated during the forward modelling. The wave field $\boldsymbol{\Psi}$ can be written by using the Green's tensor

$$\boldsymbol{\Psi}(x_r, \omega) = \mathbf{G}(x_r, x', \omega)\mathbf{s}(x', \omega) \tag{2.2.16}$$

where x_r represents the receiver position, x' the source position and ω a certain frequency. The whole Green's tensor looks like the following (Paschke et al. (2016))

$$
\mathbf{G}(x, x', \omega) = \begin{bmatrix} G_{\sigma_{xx},\sigma_{xx}} & G_{\sigma_{xx},\sigma_{zz}} & G_{\sigma_{xx},\sigma_{xz}} & G_{\sigma_{xx},v_x} & G_{\sigma_{xx},v_z} \\ G_{\sigma_{zz},\sigma_{xx}} & G_{\sigma_{zz},\sigma_{zz}} & G_{\sigma_{zz},\sigma_{xz}} & G_{\sigma_{zz},v_x} & G_{\sigma_{zz},v_z} \\ G_{\sigma_{xz},\sigma_{xx}} & G_{\sigma_{xz},\sigma_{zz}} & G_{\sigma_{xz},\sigma_{xz}} & G_{\sigma_{xz},v_x} & G_{\sigma_{xz},v_z} \\ G_{v_x,\sigma_{xx}} & G_{v_x,\sigma_{zz}} & G_{v_x,\sigma_{xz}} & G_{v_x,v_x} & G_{v_x,v_z} \\ G_{v_z,\sigma_{xx}} & G_{v_z,\sigma_{zz}} & G_{v_z,\sigma_{xz}} & G_{v_z,v_x} & G_{v_z,v_z} \end{bmatrix} (x, x', \omega) \tag{2.2.17}
$$

The forward modelling within the *IFOS2D code* is a little different to that described previously, but uses also finite-differences and discretizes the elastic wave equation on a grid. Here a staggered grid (Virieux (1986), Levander (1988)) is used, meaning that not all spatial derivatives of the wavefield variables are located at the same grid point, but are staggered by a half of the distance between two grid points and are then averaged harmonically and arithmetically. The partial wavefield variables are estimated by a Taylor series and, depending on the truncation of the Taylor series, of different order. For a more detailed mathematically description, the reader is referred to Köhn (2011b).

2.2.2 Stability and Dispersion Criteria

The numerical nature of solving the forward problem demands for a discretisation in time and space. The temporal discretisation has to full fill numerical stability criteria of the following

$$dt \leq \frac{\mathcal{C} \cdot dx_{min}}{v_{max}} \tag{2.2.18}$$

where dt is the time step, $\mathcal{C}$ is a constant called Courant number, dx_{min} the minimum grid spacing and v_{max} the maximum velocity within the model. This maximum velocity should be conservatively determined, since the velocity might increase over iterations. Eq. 2.2.18

is also called *CFL condition* named after Courant, Friedrichs and Lewy (Courant et al. (1928)). If one fails to meet this stability criterion the numerical calculation will fail and, depending on the implementation, end with no reasonable outcome. What happens if the CFL condition is violated is shown schematically in Fig. 2.2.1. In this example, taken from Fichtner (2011), the minimum grid spacing is dx=1 km, $\mathcal{C}$=2 and the maximum propagation velocity is v_{max}=5 km/s. According to Eq. 2.2.18, the maximum time step should not exceed a value of 0.4 s. The forward modelling was performed twice, once with a time step of dt=0.39 s that met the condition and once where the time step of dt=0.41 s slightly exceeds the condition. For the first case, the modelling shows a stable solution (Fig. 2.2.1, upper panel), whereas for the latter case the solution of the calculation grows indefinitely. The value of the Courant number $\mathcal{C}$ depends on the stencil used.
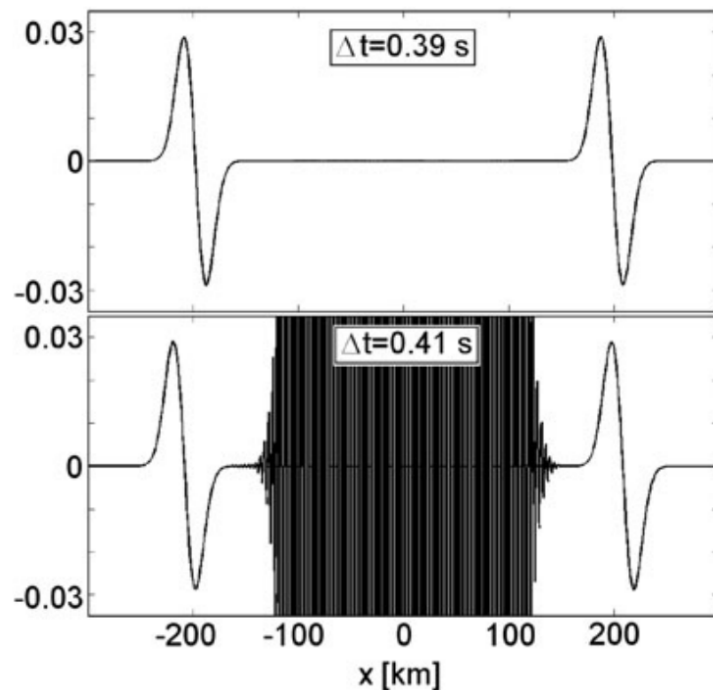
Figure 2.2.1: Numerical Wavelet sampled with dt that satisfies the numerical stability criterion (upper panel) and that does not satisfy the stability criterion (lower panel) from Fichtner (2011)

Comparing the analytical solution to the numerical solution shows an effect, which must be considered when modelling longer propagation times. This effect is shown schematically in Fig. 2.2.2 taken from Fichtner (2011). Here the numerical and analytical solutions for a modelled wave are shown at different time steps. At first, both solutions coincide and cannot be distinguished. However, with increasing time and therefore increasing number of propagated wavelengths, the solutions show more pronounced differences. Over time, the numerical errors increase and the numerical solution disperses. The analytical solution remains exact for each propagation time since all frequencies travel at the same velocity and therefore show no dispersion. This is not the case for the numerical solution since high frequency components propagate slower. This effect is called numerical dispersion. The

solution will become more and more inaccurate for longer propagation times.
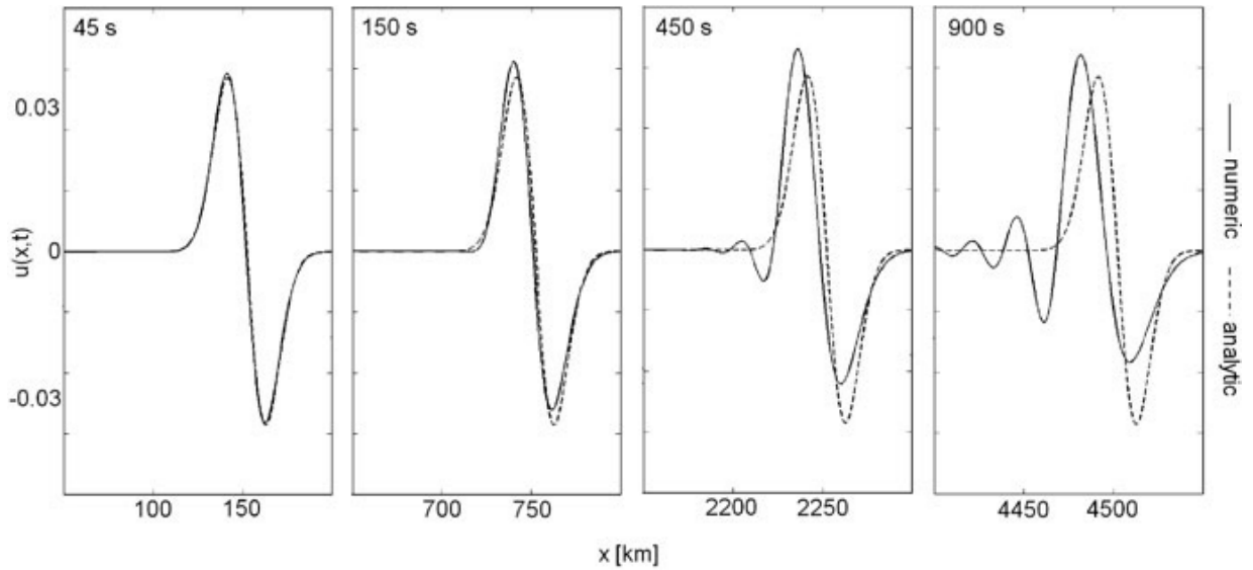
Figure 2.2.2: Numerical (solid line) and analytical (dashed line) solutions after different times (indicated in upper left corner) from Fichtner (2011)

2.3 Physics of Sources

2.3.1 Source Excitation

There are two source types implemented in the viselawi2d code, stress sources and velocity sources. In the first case one can excite three stress components, S_{xx}, S_{zz} and/or S_{xz}. In the latter case two excitation directions are possible, Vx and/or Vz. The physics of both source implementations acting on the wavefield is different as it is exemplary shown in Fig. 2.3.1. If a stress component source is applied the first motion direction is depending on what side of the source the receiver is situated. In this case, the first motion direction will be in direction of the stress direction and thus the excitation is acting in opposite directions. If now two stress components in x- and z-directions are excited this would simulate an explosion source. In case of a velocity source, the position of the receiver referred to the source is unimportant, since the first motion direction will always be in the direction of the velocity component. Exciting two velocity source components in x- and z-direction would not simulate an explosion, but some kind of shear component velocity source.

2.3.2 Source Components

In this subsection the set-up of source components are closer examined. The aim of this test was to check if the waveforms do look the same if single source components like the normal stresses S_{xx}, S_{zz} and combined source components of these two are used for the forward

16
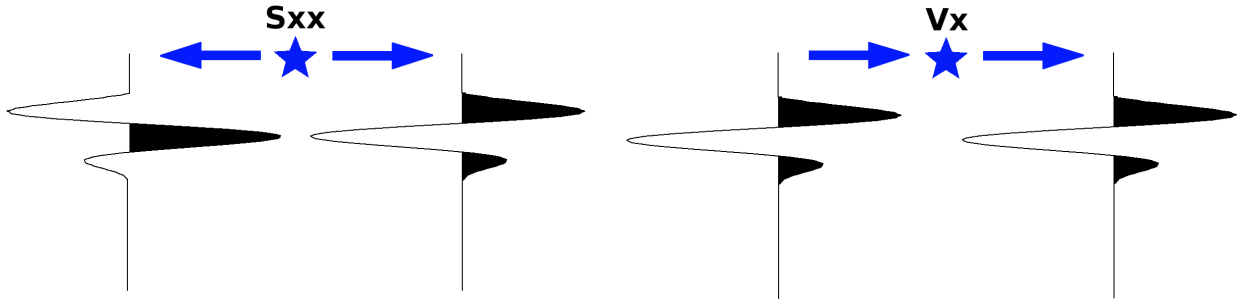
Figure 2.3.1: Physics of the source excitation of a stress component in x-direction (left) and of a velocity component in x-direction (right); blue stars mark source position; arrow mark first motion direction

modelling. The same was done by using the velocity source components Vx and Vz. Fig. 2.3.2 displays the model for this test, which is a simple homogeneous velocity model, one source and 38 receivers. These two vertical receiver lines were chosen in a distance of near field (offset does not exceeds minimum wavelength) and far field conditions (offset larger than roughly three times the minimum wavelength). The following table 2.3.1 summarises the modelling parameters.

Table 2.3.1: Summary of FWD parameters

Model size (x/z) [m]	Time step [s]	Samples	max. Freq. [Hz]	Grid size [m]
36/32	$2.5 \cdot 10^{-5}$	1201	600	0.4
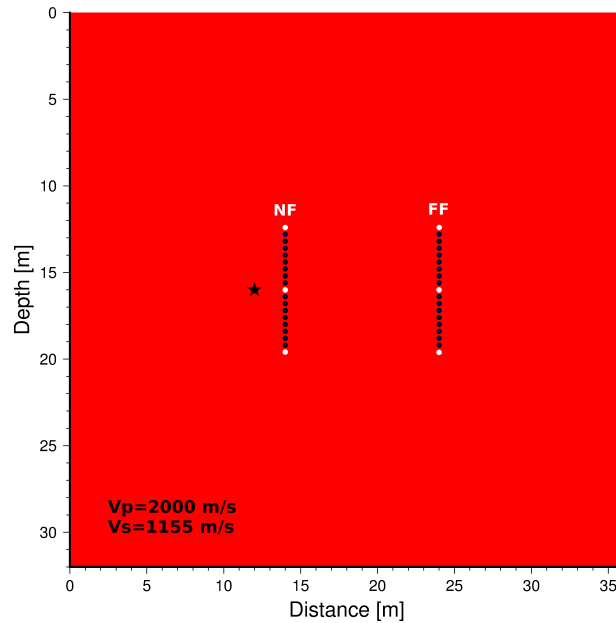
Figure 2.3.2: Velocity model used for source component tests; black star marks source; blue circles mark receivers; white circles mark receivers for which seismograms are shown; P- and S-velocities are indicated in the left lower corner; NF near field; FF far field

The work flow was now to do a FWD modelling for S_{xx} source component, a modelling for S_{zz} source component and one modelling for S_{xx} and S_{zz} source components combined.

The seismograms generated with the single-component source were then added (stacked without division) and compared to the seismograms generated with the double-component source. This work flow was repeated with the velocity source components. Since the outcome for both source types are the same, only the results for the stress component source are shown. Looking at Fig. 2.3.3 it becomes clear that the waveforms are the same, which is the expected and desired outcome. This means that the source physics for the forward modelling is correctly implemented.
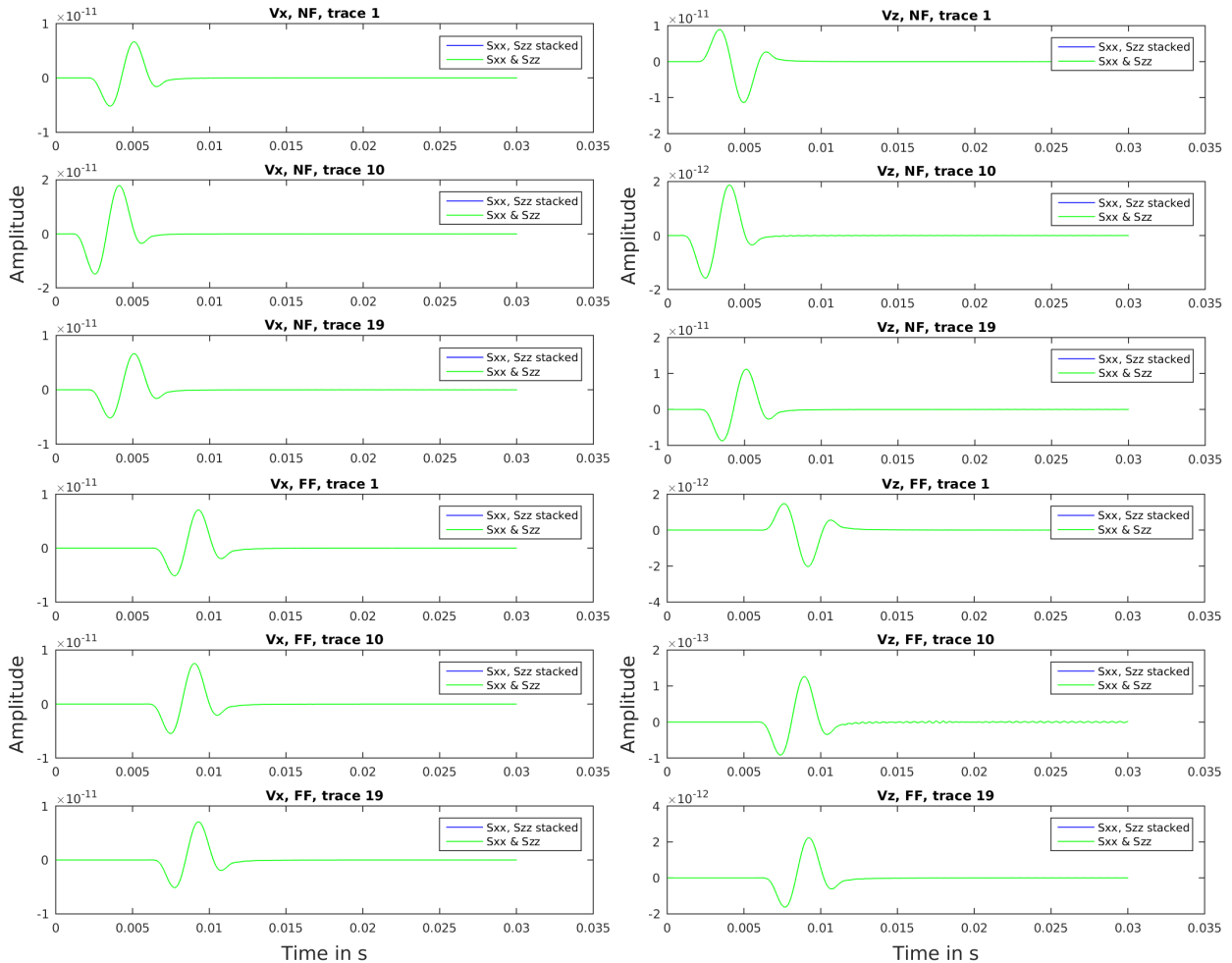
Figure 2.3.3: Trace comparison of modelled seismograms recorded at x-component receivers (left panel) and z-component receivers (right panel) in the near field (upper three panels) and the far field (lower three panels)

2.4 Elastic Parameter Inversion

2.4.1 Inversion in the Time-Domain

The seismic full waveform inversion (FWI) is basically the physically meaningful quantification of the difference between synthetic seismograms $\mathbf{d}^{syn}$ and the observed data $\mathbf{d}^{obs}$, and moreover the minimisation of this quantification which is expressed as some kind of misfit function to

estimate the model parameters of the subsurface $\mathbf{m}$. This misfit function depends non-linearly on the assumed model and the overall aim is to find an optimal Earth model that minimises this misfit function. An often used misfit function is described as the L2-norm of the kind

$$E(\mathbf{m}) = \frac{1}{2}\delta\mathbf{d}^t \cdot \delta\mathbf{d} \tag{2.4.1}$$

where $\delta\mathbf{d}$ represents the difference between observed and synthetic data. There are other misfit functions, often referred to as *objective functions*, e.g. the L1-norm, the Cauchy norm or the Sech norm (Crase et al. (1990)). To minimise the misfit function, it is firstly linearised by a Taylor series expansion and further the derivative is calculated, which must be zero, yielding

$$\frac{\partial E(\mathbf{m})}{\partial\mathbf{m}} = \frac{\partial E(\mathbf{m_0})}{\partial\mathbf{m}} + \frac{\partial^2 E(\mathbf{m_0})}{\partial\mathbf{m}^2}\delta\mathbf{m} = 0. \tag{2.4.2}$$

Now the first derivative of Eq. 2.4.1 gives

$$\frac{\partial E(\mathbf{m_0})}{\partial\mathbf{m}} = \left(\frac{\partial\mathbf{d}^{syn}(\mathbf{m_0})}{\partial\mathbf{m}}\right)^t (\mathbf{d}^{syn}(\mathbf{m_0}) - \mathbf{d}^{obs}) = \mathbf{J}_0^t\delta\mathbf{d} \tag{2.4.3}$$

where $\mathbf{J}$ denotes the Jacobian matrix and is also known as Fréchet derivative matrix (The calculation of this matrix is described in more detail in the following section 2.4.2.2). This method is called *gradient method*. By taking the second derivative of the misfit function 2.4.2 the *Newton method* is defined

$$\frac{\partial^2 E(\mathbf{m_0})}{\partial\mathbf{m}^2} = \mathbf{J}_0^t\mathbf{J}_0 + \left(\frac{\partial\mathbf{J}_0}{\partial\mathbf{m}}\right)^t \delta\mathbf{d} \tag{2.4.4}$$

The whole term of Eq. 2.4.4 is also known as the Hessian matrix. Since the Hessian is a very large matrix, which is computationally expensive to calculate, the more common *Gauss-Newton method* is considered (Schuster (2017)), which uses an approximation of the Hessian of the kind $\mathbf{H}_{approx} = \mathbf{J}^t\mathbf{J}$. The model updates of the described methods are as follows:

$$\mathbf{m}_{n+1} = \mathbf{m}_n - \mathbf{H}_n^{-1}\left(\frac{\partial E}{\partial\mathbf{m}}\right)_n \qquad \text{Newton method} \tag{2.4.5}$$

$$\mathbf{m}_{n+1} = \mathbf{m}_n - (\mathbf{H}_{approx}^{-1})_n\left(\frac{\partial E}{\partial\mathbf{m}}\right)_n \qquad \text{Gauss-Newton method} \tag{2.4.6}$$

$$\mathbf{m}_{n+1} = \mathbf{m}_n - \alpha_n\left(\frac{\partial E}{\partial\mathbf{m}}\right)_n \qquad \text{steepest decent method} \tag{2.4.7}$$

where the steepest decent method is basically the same as the Newton method, just that the Hessian matrix is replaced by the step length α. The search for an appropriate step length is a crucial part in the inversion process, since too large step length could lead the to

a failure of convergence, meaning that the algorithm does not find a global minima, whereas too small step lengths could drastically slow down the convergence rate. To increase and stabilise the convergence of the gradient method, a so called *conjugate gradient method* can be applied, which preconditions the gradient with a factor P leading to a preconditioned model perturbation $\delta \mathbf{m_n^p} = P \delta \mathbf{m_n}$ as well as the conjugate gradient direction for each iteration

$$\delta \mathbf{c}_n = \delta \mathbf{m}_n^p + \beta \delta \mathbf{c}_{n-1} \tag{2.4.8}$$

where $\delta \mathbf{c}_1 = \delta \mathbf{m}^p$. The weighting factor β can be defined by different approaches, e.g. the Flechter-Reeves method or the Hestenes-Stiefel method (Köhn (2011b)), but the algorithm applied to the data uses the Polak-Ribiére method:

$$\beta^{PR} = \delta \mathbf{m}_n^p \frac{\delta \mathbf{m}_n^p - \delta \mathbf{m}_{n-1}^p}{\delta \mathbf{m}_{n-1}^p \delta \mathbf{m}_{n-1}^p}, \qquad \beta = max[\beta^{PR}, 0]. \tag{2.4.9}$$

The model update can then be calculated with

$$\mathbf{m}_{n+1} = \mathbf{m}_n - \alpha_n \delta \mathbf{c}_n \tag{2.4.10}$$

where the step length α is determined by a 3-point hyperbola fitting (Kurzmann et al. (2008)).

2.4.2 Inversion in the Frequency-Domain

The elastic parameter inversion and the source inversion of viselawi2d are performed in the frequency-domain minimizing the L2-norm of data residuals. The elastic parameter inversion uses the Gauß-Newton method including the Tikhonov's 0th order regularization of weighted model updates. Thereby the Jacobian matrix is build by explicitly calculated sensitivity kernels. With this Jacobian matrix the resolution matrix is provided.

2.4.2.1 From Misfit Function to damped least-square Solution

To minimise the misfit between two geophysical quantities, different norms can be used, all of them showing their advantages and also disadvantages (Crase et al. (1990)). In this approach, an L2-norm for the misfit function was considered of the kind

$$E(\mathbf{m}, \omega) = \delta \mathbf{d^t}(\omega) \cdot \delta \mathbf{d^*}(\omega) \tag{2.4.11}$$

where $\mathbf{m}$ contains the model parameters, ω is a certain frequency and $\mathbf{d}$ contains the data. The derivative of the objective function 2.4.11 with respect to the model parameter yields now

$$\nabla_m E(\mathbf{m}, \omega) = \Re\{\mathbf{J}^t(\mathbf{m}, \omega) \cdot \delta \mathbf{d}^*\} \tag{2.4.12}$$

the gradient of the objective function with the Fréchet derivative matrix $\mathbf{J}$. A general solution in a gradient method would be of the kind

$$\mathbf{m}_{k+1} = \mathbf{m}_k - \alpha_k \nabla_m E(\mathbf{m}, \omega) \tag{2.4.13}$$

where k is the iteration step and α the step length. In a gradient method solution as it is displayed in eq. 2.4.13 the gradient at the source and receiver positions would be the largest. This would only result in model updates in this regions, but the rest of the model would not be updated (Tarantola (2005)). To overcome this effect a preconditioning can be implemented, that could be a tapering of sources and receivers, or the use of the Hessian matrix as it is done in the *Newton method*. If a preconditioning with the Hessian is used, the misfit function is developed by a Taylor series expansion (Aster et al. (2013))(comp. Eq. 2.4.2)

$$E(\mathbf{m} + \delta\mathbf{m}, \omega) = E(\mathbf{m}, \omega) + \delta\mathbf{m}^t \nabla_m E(\mathbf{m}, \omega) + \frac{1}{2}\delta\mathbf{m}^t \mathbf{H}(\mathbf{m}, \omega)\delta\mathbf{m} + \mathcal{O}(\|\delta\mathbf{m}^3\|) \tag{2.4.14}$$

with the Hessian (comp. Eq. 2.4.4)

$$\mathbf{H}(\mathbf{m}, \omega) = \frac{\partial^2 E(\mathbf{m}, \omega)}{\partial m_i m_j}. \tag{2.4.15}$$

Now the preconditioned solution of eq. 2.4.13 would look like

$$\delta\mathbf{m} = -\mathbf{H}(\mathbf{m}, \omega)^{-1} \cdot \nabla_m E(\mathbf{m}, \omega) \tag{2.4.16}$$

where the first part of the right hand side is the Hessian and the second part the gradient. As already mentioned the computation of the Hessian matrix is quite expensive and therefore it is approximated by the multiplication of the Fréchet derivative matrix (*Gauß-Newton method*) (Schuster (2017)). Eq. 2.4.16 would then transform to

$$\delta\mathbf{m} = -(\Re\{\mathbf{J}^t(\mathbf{m}, \omega)\mathbf{J}^*(\mathbf{m}, \omega)\})^{-1}\Re\{\mathbf{J}^t(\mathbf{m}, \omega)\delta\mathbf{d}^*\} \tag{2.4.17}$$

In order to stabilise the inversion, a damping factor λ can be introduced, which leads to the final approximated preconditioned damped least-square solution

$$\delta\mathbf{m} = -(\Re\{\mathbf{J}^t(\mathbf{m}, \omega)\mathbf{J}^*(\mathbf{m}, \omega)\} + \mathbf{I}\lambda)^{-1}\Re\{\mathbf{J}^t(\mathbf{m}, \omega)\delta\mathbf{d}^*\}. \tag{2.4.18}$$

2.4.2.2 Calculation of the Fréchet Derivative Matrix

The Fréchet derivative matrix can be determined with two different approaches, the *Born approximation* or the *adjoint method*. The latter one can be further subdivided into the explicit adjoint method or implicit adjoint method.

The Born approximation states the dependency for one source and all receivers from one model parameter. It means that the wavefield is propagated from a certain model parameter position to the receiver by using the recorded wavefield from the source (pers. comm. Paschke (2016), Fig. 2.4.1, a).

$$
\frac{\partial \mathbf{\Psi}(\mathbf{x},\omega)}{\partial m_k} = \underbrace{\mathbf{G}(x,x_m,\omega)}_{\text{Green's fct.}} \left(\underbrace{\frac{-\partial \mathbf{L}(x_m,\omega)}{\partial m_k}}_{\text{derivative of FWD operator}} \cdot \underbrace{\Psi(x_m,\omega)}_{\text{propagated source wavefield}} \right) \underbrace{b_k(x_m)}_{\text{base fct.}} \qquad (2.4.19)
$$

The base function is an interpolation scheme and is needed, when the spacing of the model parameters are coarser than the grid spacing. x_m and x are the model parameter position or a general position, respectively.

The adjoint method states, that all model parameters for one source-receiver pair can be inverted by multiplying the propagated source wavefield with the wavefield propagated from the receiver (Fig. 2.4.1, b). If the back-propagating from the receiver is done for one source-receiver pair, it is called explicit and the Fréchet derivative matrix would be calculated like

$$
\frac{\partial \mathbf{\Psi}(\mathbf{x_r},\omega)}{\partial m(x_m)} = \mathbf{G}(x_m,x_r,\omega) \left(\frac{-\partial \mathbf{L}(x_m,\omega)}{\partial m(x_m)} \Psi(x_m,\omega) \right) \qquad (2.4.20)
$$

with x_r the receiver position (pers. comm. Paschke (2016)). However, if the back-propagating is done simultaneously from all the receivers, it is called implicit adjoint method and yields (pers. comm. Paschke (2016))

$$
\nabla_{m_k} E(\mathbf{m},\omega) = \sum_{i=1}^{N} \Re \left\{ \left(\frac{-\partial \mathbf{L}(x_k,\omega)}{\partial m(x_k)} \mathbf{\Psi}(x_k,\omega) \right)^t \cdot \underbrace{\mathbf{G}^t(x_k,x_r,\omega)(\delta \mathbf{d}^*)_i}_{\text{simultaneously propagated data residual from receivers}} \right\}
$$
$$
(2.4.21)
$$
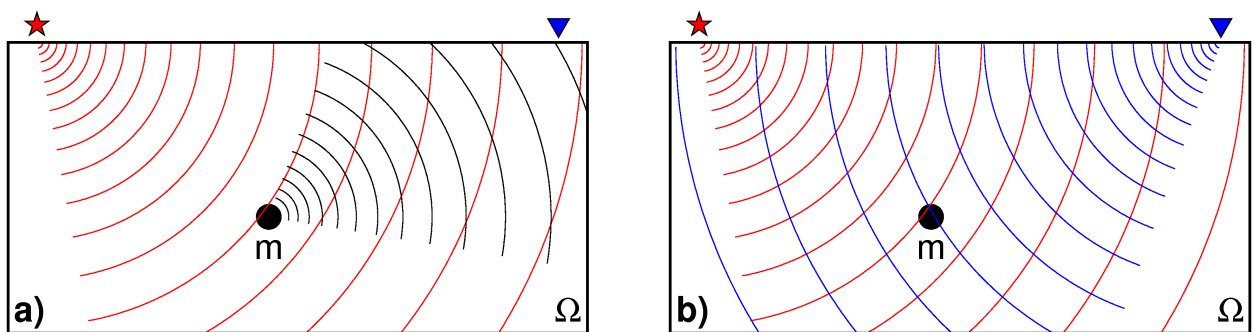
Figure 2.4.1: Scheme of Born approximation (a) and adjoint method (b) taken from Paschke (2016); red, black and blue lines indicate wave fronts propagated from the source, the model parameter position and receiver, respectively; m marks an arbitrary model position

2.4.2.3 Singular Value Decomposition

Coming back to the misfit function of eq. 2.4.11. This equation can be further extended to a weighted, damped least-square misfit function of the kind

$$E(\omega) = \delta\mathbf{d}^T\mathbf{W}_d\delta\mathbf{d} + \lambda\delta\mathbf{m}^T\mathbf{W}_m\delta\mathbf{m} \tag{2.4.22}$$

where $\mathbf{W}_d$ and $\mathbf{W}_m = \mathbf{D}^T\mathbf{D}$ are the data and model weighting matrices, respectively (Menke (2012a)). The claim $\frac{\partial E}{\partial\mathbf{m}} = 0$ yields for the model update the *weighted damped least-squares solution*

$$\mathbf{m}^{est} = \left[\mathbf{G}^T\mathbf{W}_d\mathbf{G} + \lambda^2\mathbf{W}_m\right]^{-1}\mathbf{G}^T\mathbf{W}_d\delta\mathbf{d} \tag{2.4.23}$$

If now the coordinate system is rotated in a proper way, the weighting matrices vanish (indeed they are included in the data residuals and model perturbations (Menke (2012b))).

$$E(\omega) = \underline{\delta\mathbf{d}}^T\underline{\delta\mathbf{d}} + \lambda\underline{\delta\mathbf{m}}^T\underline{\delta\mathbf{m}} \tag{2.4.24}$$

$\underline{\delta\mathbf{d}}$ and $\underline{\delta\mathbf{m}}$ are the rotated data residuals and rotated model perturbations, respectively. And the model update transforms to

$$\underline{\mathbf{m}}^{est} = \left[\underline{\mathbf{G}}^T\underline{\mathbf{G}} + \lambda^2\mathbf{I}\right]^{-1}\underline{\mathbf{G}}^T\underline{\delta\mathbf{d}} = \underline{\mathbf{G}}^{-g}\underline{\delta\mathbf{d}} \tag{2.4.25}$$

with the generalised inverse

$$\underline{\mathbf{G}}^{-g} = \left[\underline{\mathbf{G}}^T\underline{\mathbf{G}} + \lambda^2\mathbf{I}\right]^{-1}\underline{\mathbf{G}}^T. \tag{2.4.26}$$

Now any matrix can be decomposed into orthonormal matrices, which is called *singular value decomposition*, short SVD.

$$\underline{\mathbf{G}} = \mathbf{U}\mathbf{S}\mathbf{V}^T \tag{2.4.27}$$

where the columns of the $m \times m$ **U** matrix span the data space, the columns of the $n \times n$ **V** matrix span the model space and **S** contains the singular values and is a diagonal matrix (Aster et al. (2013)). If now eq. 2.4.27 is substituted into eq. 2.4.26 yields (Menke (2012b))

$$\underline{\mathbf{G}}^{-g} = \left[\mathbf{V}\mathbf{S}\mathbf{U}^T\mathbf{U}\mathbf{S}\mathbf{V}^T + \lambda^2\mathbf{I}\right]^{-1}\mathbf{V}\mathbf{S}\mathbf{U}^T \tag{2.4.28}$$

$$= \mathbf{V}\left[\mathbf{S}^2 + \lambda^2\mathbf{I}\right]^{-1}\mathbf{S}\mathbf{U}^T \tag{2.4.29}$$

$$\underline{G_{ij}}^{-g} = \sum_{k=1}^{mini} V_{ik}\frac{si_k}{si_k^2 + \lambda^2}U_{kj} \tag{2.4.30}$$

The non-rotated model update then can be calculated with

$$\delta \mathbf{m} = \mathbf{D}^{-1} \underline{\mathbf{G}}^{-g} \underline{\delta \mathbf{d}} \tag{2.4.31}$$

With the generalised inverse the model and data resolution matrix can be explicitly calculated with

$$\mathbf{R}_m = \mathbf{G}^{-g} \cdot \mathbf{G} \qquad \text{and} \qquad \mathbf{R}_d = \mathbf{G} \cdot \mathbf{G}^{-g}. \tag{2.4.32}$$

Chapter 3

Cross-hole Model Application

Since the viselawi2d inversion algorithm is newly developed and implemented the elastic parameter inversion should be tested on a quite simple model. As such a model a cross-hole design was chosen where the sources and receivers are opposite of each other in a vertical alignment. As a starting model, a simple homogeneous velocity model without any perturbation was created (Fig. 3.0.1, left). The seismic velocities of P-waves are $2000\,\mathrm{m/s}$ and for S-waves $1155\,\mathrm{m/s}$. For the true model, a circular velocity anomaly with a diameter of $7\,\mathrm{m}$ in the middle of the model was introduced, with decreased velocities of $1800\,\mathrm{m/s}$ for P-waves and $1040\,\mathrm{m/s}$ for S-waves (Fig. 3.0.1, right). In the following sections these models were used for the synthetic inversion study to test the viselawi2d code, but also the IFOS2D algorithm. An explosion was used for the source mechanism, meaning that the stress components S_{xx} and S_{zz} were seized with a Küpper wavelet (Fig. 3.0.2), having a dominant frequency of $200\,\mathrm{Hz}$. Finally the inversion outcomes of both algorithms are compared and discussed.
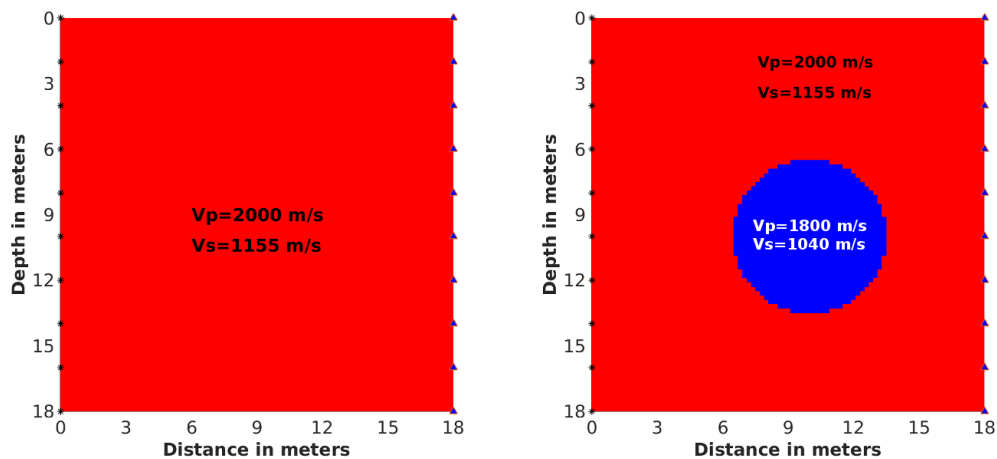
Figure 3.0.1: Cross-hole velocity starting (left) and true (right) model for synthetic inversion study; black stars mark the source positions; blue triangles mark the receiver positions
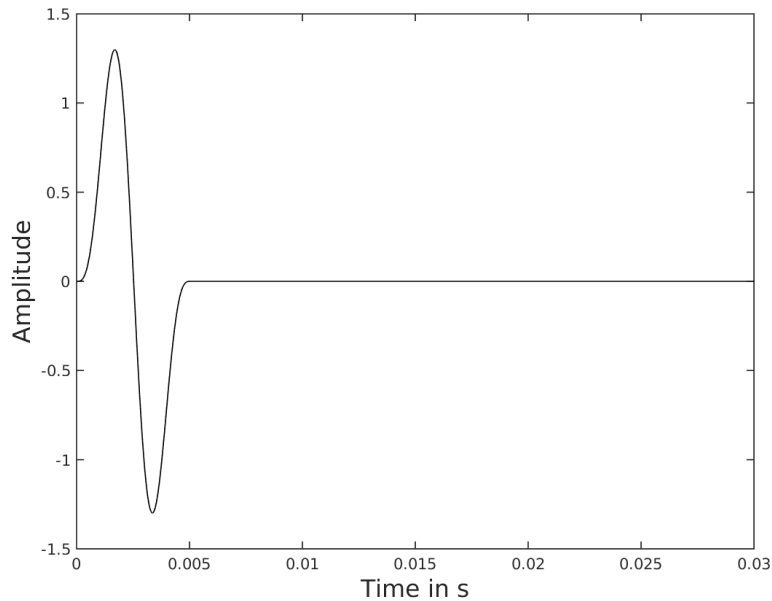
Figure 3.0.2: One component source time function used as source wavelet for the synthetic cross-hole study

3.1 P-wave Inversion

The first test was the inversion of P-waves only. For that purpose, the velocity anomaly was only implemented in the true P-velocity model, the S-velocity models were kept homogeneous. The inversion parameters are summarised in Tab. 3.1.1. Ten iterations were performed.

Table 3.1.1: Summary of inversion parameters for P-wave cross-hole inversion

Grid size [m]	Inversion Freq. [Hz]	Damping values
0.24	233.33/266.67/299.99	$[20/10/5/2.5/1.25/0.625/0.312] \cdot 10^3$

The inversion results of that test after the first, second and fourth iteration are summarised in Fig. 3.1.1. The velocity inside the circle is further decreased. The true P-wave velocity inside the circle of $1800\,\mathrm{m/s}$ is not reached yet and a difference of approx. $90\,\mathrm{m/s}$ remains. In contrast the velocity above and under the velocity anomaly is slightly increased after the second iteration. The shape of the anomaly focuses more and more, but still possesses a lateral extend, which is due to the long P-wavelengths. Looking at the misfit curve displayed in Fig. 3.1.2 indicates that the global minimum for this approach is reached after the fourth iteration. After that, the curve does not decrease any further and the misfit does not change for the last five iterations. However, these preliminary results are quite satisfying and justify to broaden the synthetic inversion tests.
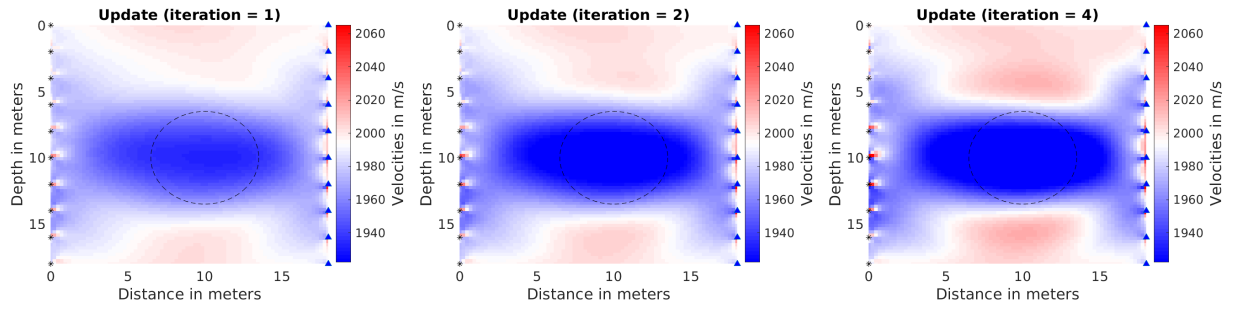
Figure 3.1.1: Inverted P-wave velocity models after first (left), second (middle) and fourth (right) iteration; black stars mark source positions; blue triangles mark receivers; dashed circle marks position of the velocity anomaly

Figure 3.1.2: Misfit curve for Vp inversion

3.2 S-wave Inversion

3.2.1 Inversion for higher Frequencies

In this section, the same inversion test was done as in section 3.1 for P-waves, just that now the inversion was carried out for S-waves exclusively. The approach is the same as explained above. The velocity anomaly was implemented in the true S-velocity model and both P-velocity models were kept homogeneous. As one can see in Tab. 3.2.1, the inversion parameters were slightly changed. That is due to the different physics of S-waves compared to P-waves. This concerns on the one hand the grid size, which was decreased since S-wavelengths are shorter than P-wavelengths and on the other hand the damping values, where the range was increased to avoid stability failures.

Table 3.2.1: Summary of inversion parameters for S-wave cross-hole inversion and higher frequencies

Grid size [m]	Inversion Freq. [Hz]	Damping values
0.2	233.33/266.67/299.99	$[40/20/10/5/2.5/1.25/0.625/0.312/0.156/0.078] \cdot 10^3$

The inversion results are displayed in Fig. 3.2.1. The S-velocity inside the anomaly is decreased, but does not reach its true value of 1040 m/s. Nevertheless, the circular geometry

is finer resolved than in the P-wave inversion and does not have a lateral extend, which is natural due to the shorter wavelengths of S-waves. Going from the velocity anomaly towards the model boundaries, it seems that there are two halos of first increased and second decreased background velocities compared to the true velocity of $1155\,\mathrm{m/s}$. Right at the edges of the model, the background velocity recovers to that true value. Again the smallest misfit is reached after the third iteration (Fig. 3.2.2) and does not change much after that.
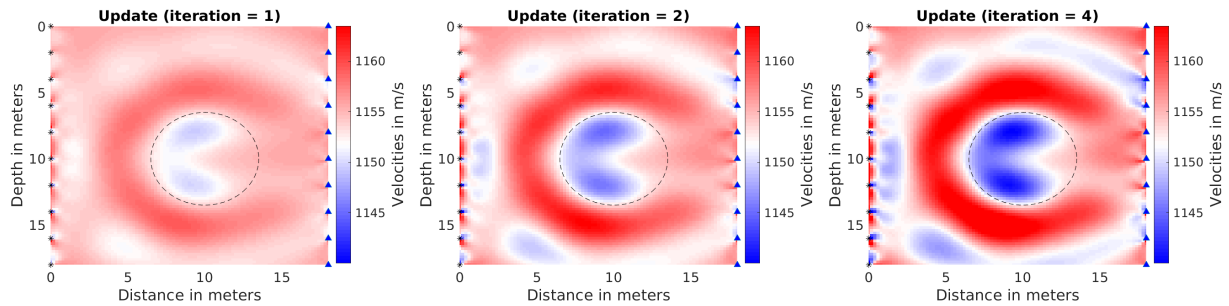
Figure 3.2.1: Inverted S-wave velocity models after first (left), second (middle) and fourth (right) iteration; black stars mark source positions; blue triangles mark receivers; dashed circle marks position of the velocity anomaly

Figure 3.2.2: Misfit curve for Vs inversion of higher frequencies

3.2.2 Inversion for lower Frequencies

The S-wave inversion test was once again repeated, but with lower inversion frequencies (see Tab. 3.2.2).

Table 3.2.2: Summary of inversion parameters S-wave cross-hole inversion and lower frequencies

Grid size [m]	Inversion Freq. [Hz]	Damping values
0.2	100/200	$[5/2.5/1.25/0.625/0.312] \cdot 10^3$

Differently to the previous inversion test the velocity inside the anomaly is much more decreased and reaches nearly its true value of $1040\,\mathrm{m/s}$. However, the same issue of falsely

corrected background velocity remains and is increased around the anomaly of about 30-40 m/s The minimum misfit is here not reached after the third iteration as in the previous inversion approach, but after the ninth iteration.
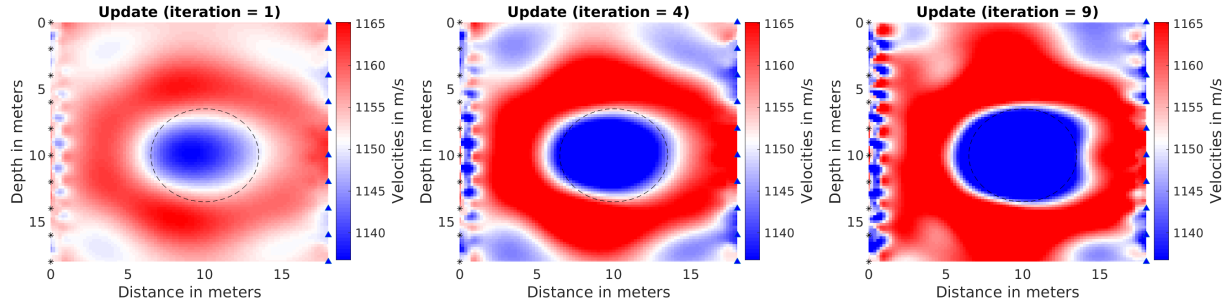
Figure 3.2.3: Inverted S-wave velocity models after first (left), fourth (middle) and ninth (right) iteration; black stars mark source positions; blue triangles mark receivers; dashed circle marks position of the velocity anomaly

Figure 3.2.4: Misfit curve for Vs inversion for lower frequencies

3.3 P- and S-wave Inversion

3.3.1 Same anomaly position

3.3.1.1 Same damping for P- and S-wave

Since the inversion results for P- and S-waves were quite satisfying now both velocities were inverted simultaneously. This means that the anomaly of decreased velocities is present in both true models. Again ten iterations were performed, the input parameters for the inversion are gathered in Tab. 3.3.1.

The P-wave inversion results displayed in Fig. 3.3.1 look quite similar to the results obtained by single P-wave inversions. The velocities around the anomaly are locally a little bit shifted upwards and are falsely corrected. This difference comes to approx. 20 m/s. In case of S-wave it seems that the algorithm decreases the velocity inside the anomaly and outside of the

Table 3.3.1: Summary of inversion parameters for P- and S-wave inversion of coinciding anomaly position

Grid size [m]	Inversion Freq. [Hz]	Damping values
0.2	100/200	$[40/20/10/5/2.5/1.25/0.625/0.312/0.156/0.078] \cdot 10^3$

halo around the anomaly within the first several iterations. The halo of increased velocity around the cavity increases in extent over iterations, whereas the velocity decrease inside the anomaly becomes bigger. However, the anomaly itself is very well resolved in terms of position and geometry. The differences to the true decreased velocities inside the anomaly is not greater than $100\,\mathrm{m/s}$ for Vp and $70\,\mathrm{m/s}$ for Vs. The smeared appearance of the circular anomaly in the P-wave inversion model is due to the bigger wavelength of P-waves. Looking at the misfit curve (Fig. 3.3.2) one can see that the misfit was decreased by a factor of about 5 and seems to reach its minimum after the sixth iteration.

Figure 3.3.1: Inverted P- (upper panel) and S-wave (lower panel) velocity models after first (left), fourth (middle) and ninth (right) iteration; black stars mark source positions; blue triangles mark receivers; dashed circle marks position of the velocity anomaly
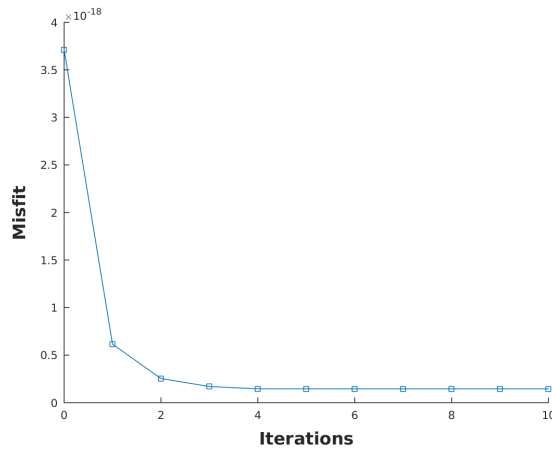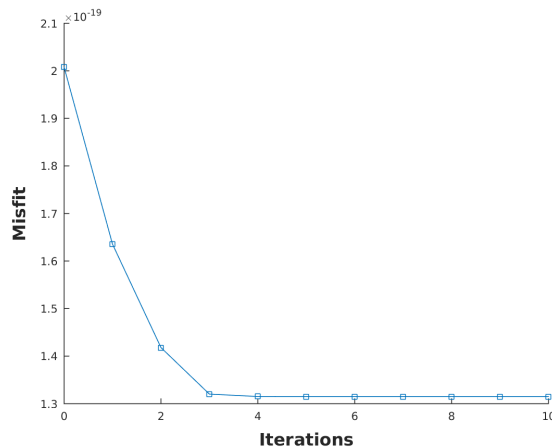
Figure 3.3.2: Misfit curve for Vp and Vs inversion and same damping

3.3.1.2 Different damping for P- and S-wave

In the previous section, the P- and S-wave inversion for the decreased velocity perturbation was carried out simultaneously. For the inversion a variety of damping values were given and a damping test was performed with each damping value at each iteration. All the damping values were applied to both models, to P-wave model and to the S-wave model even though the quantities of both seismic velocities are different. What was actually varied during each iteration was the λ within the objective function (eq. 2.4.22), but W_m was a unity matrix and therefore kept constant. In this subsection a different damping of P-wave and S-wave models was applied in order to test the influence and if the results can be improved. In the initial and starting model the velocities are chosen so that the Vp-Vs-ratio is 1.7 and therefore this factor was also introduced in W_m, meaning that the damping of Vp is 1.7-times bigger than for Vs. Apart from that all inversion parameters are the same as in the previous test (see Tab. 3.3.1).

A comparison of the inversion results derived by a constant damping for both seismic velocities (Fig. 3.3.1) and the results obtained by a differently applied damping (Fig. 3.3.3) shows no big difference at first sight. In Tab. 3.3.2 the velocities for the P- and S-wave inversions are summarised. Now it becomes visible that the velocity recoverey is slightly better when different damping values are applied for P- and S-waves, respectively. For the P-wave, the background velocity is less increased in case of an adapted damping by $10\,\mathrm{m/s}$. Also the perturbation velocity is nearer to the true perturbation velocity, but only of $3\,\mathrm{m/s}$. Looking at the S-wave inversion results, the background velocity is slightly more increased than in case of a constant damping ($2\,\mathrm{m/s}$). However, the low-velocity zone is here again nearer to the true one in case of an adapted damping of about $9\,\mathrm{m/s}$.

The comparison of misfit curves displayed in Fig. 3.3.4 shows that the misfit for the inversion with constantly applied damping (green) is bigger than that when the damping is adapted (blue) to the seismic quantities, but become nearly the same after the fifth iteration.

Table 3.3.2: Velocity recovery for same and different damping

	$\mathbf{v_{max}[m/s]}$	$\mathbf{\Delta_{true}[m/s]}$	$\mathbf{v_{min}[m/s]}$	$\mathbf{\Delta_{true}[m/s]}$
Same damping				
P-wave	2035	35	1894	94
S-wave	1194	39	1104	64
Diff. damping				
P-wave	2025	25	1891	91
S-wave	1196	41	1095	55

Figure 3.3.3: Inverted P- (upper panel) and S-wave (lower panel) velocity models after first (left), fourth (middle) and ninth (right) iteration and different damping for P- and S-wave model; black stars mark source positions; blue triangles mark receivers; dashed circle marks position of the velocity anomaly
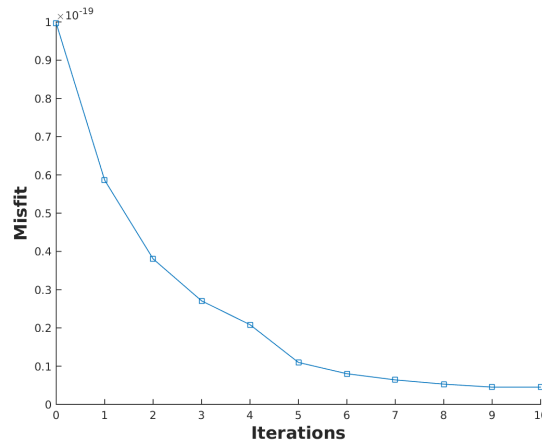

Figure 3.3.4: Misfit curves for Vp and Vs inversion for the same damping values (blue) and for a different damping (green)

3.3.1.3 Multi-scale approach

In order to increase the resolution for the previous inversion run with a constant damping a multi-scale approach was applied. The idea of multi-scale inversion is to start the inversion with low frequencies and then increase the inversion frequency with each inversion run to mitigate the inherent non-linearity. This approach helps to avoid cycle-skipping, which might occur when too high frequencies were used at the beginning of the inversion process. Since the inversion is performed in the frequency-domain, it is easy to just pick a desired frequency, or frequency range, for which one should invert for. In this case the first low frequencies were 100 Hz and 200 Hz, now the inversion frequencies are increased to 250 Hz and 300 Hz. As starting models the models obtained after the ninth iteration displayed in Fig. 3.3.1 (right column) are given. Again ten iterations were performed. The results are shown in Fig. 3.3.5.
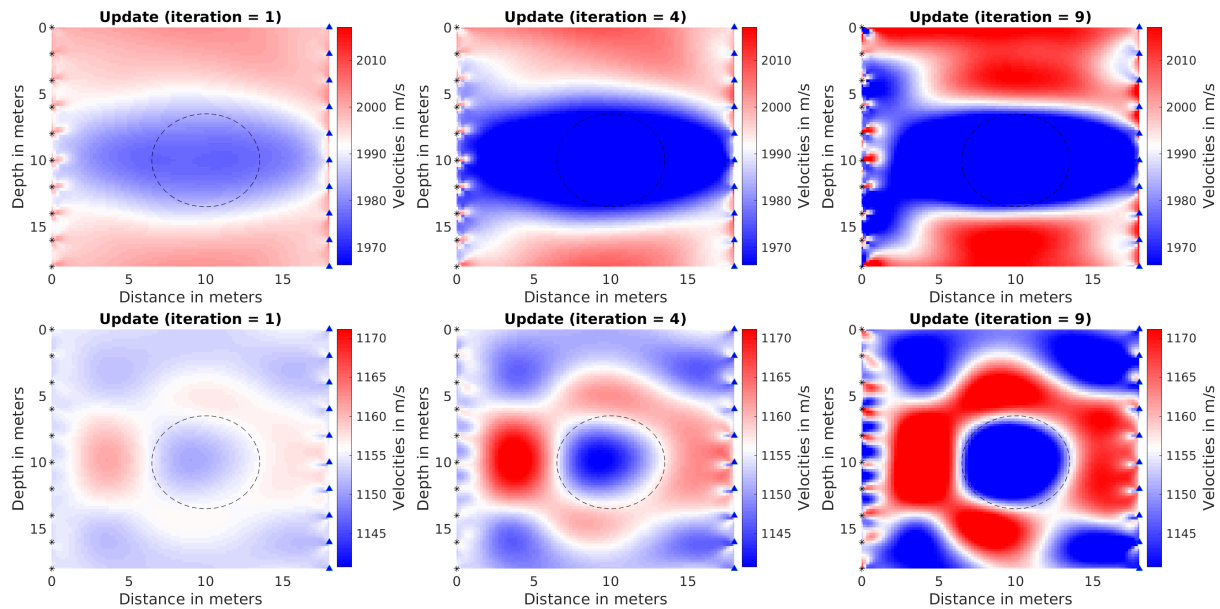

Figure 3.3.5: Inverted P- (upper panel) and S-wave (lower panel) velocity models after first (left), fourth (middle) and ninth (right) iteration, using a multi-scale approach; black stars mark source positions; blue triangles mark receivers; dashed circle marks position of the velocity anomaly

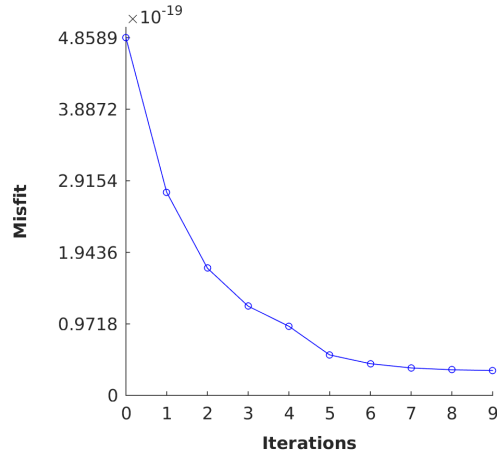**Figure 3.3.6: Misfit curves for Vp- and Vs-inversion using the multi-scale approach**

For the S-wave there is no further change. The velocities are nearly the same as in the previous run ($v_{s_{max}}$=1194 m/s and $v_{s_{max}}$=1192 m/s; $v_{s_{min}}$=1104 m/s and $v_{s_{min}}$=1104 m/s). But for Vp there is a big change regarding the velocity perturbation. Here the velocity is further decreased to 1866 m/s instead of only 1894 m/s, making a difference of 28 m/s and therefore coming closer to the true model. Also the lateral extend of the P-wave anomaly is better defined, which is due to the additional higher frequencies and therefore shorter wavelengths. The resolution capacity is increased, allowing a sharper reconstruction of the anomaly.

3.3.2   Different anomaly position

The above described synthetic inversion tests showed some promising results and so the complexity of the model set-up was increased. The overall geometry of a cross-hole approach remained, but now the velocity anomalies have a different position, size and direction of velocity change. The P-wave anomaly was kept the same and just shifted towards the left lower corner of the model (Fig. 3.3.7, left). The S-wave anomaly on the contrary was shifted into the right upper corner, decreased to a diameter of 5 m and the velocity was increased to 1300 m/s compared to the background velocity (Fig. 3.3.7, right). The positions and sizes of the anomalies were chosen so that they do not touch or interfere each other. Now the algorithm must resolve two differently signed velocity anomalies at different positions.
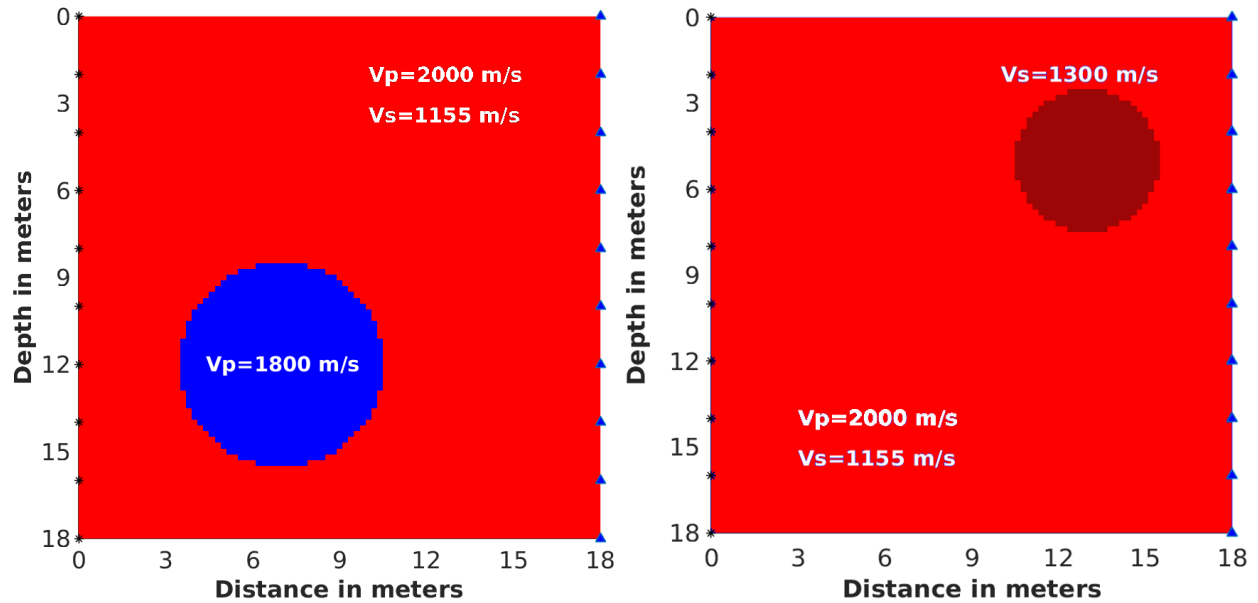
Figure 3.3.7: True velocity model for P-wave (left) and S-waves (right); black stars mark source positions; blue triangles mark receiver positions

Table 3.3.3: Summary of inversion parameters for P- and S-wave inversion of differently placed anomaly position

Grid size [m]	Inversion Freq. [Hz]	Damping values
0.2	100/200	$[10/5/2.5/1.25/0.625/0.312] \cdot 10^3$

The inversion results gathered in Fig. 3.3.8 show that the algorithm reconstructs the position, geometry and direction of velocity difference of the anomaly, but also falsely projects velocity perturbations into the model at the position of the velocity perturbation of the other parameter, meaning that in Vp a low-velocity zone is introduced at the position of the Vs anomaly and vice versa. For the P-wave anomaly the velocity is decreased to 1880 m/s leaving a difference of 80 m/s to the true low-velocity inside the perturbation. The background velocity is slightly increased of about 40 m/s compared to the starting background velocity of 2000 m/s, except for the position of the S-wave perturbation. Here, the background velocity is also decreased. The inversion for S-waves shows, that a velocity anomaly of increased velocities is introduced in the lower left corner of the model, which is not true. In fact the position of the falsely introduced perturbation coincides with the P-wave anomaly, but is different in direction of velocity change. The actual S-wave perturbation is increased to 1220 m/s with a remaining difference of 80 m/s to the true velocity inside the perturbation of 1300 m/s. The rest of the background S-wave velocity is slightly decreased to 1120 m/s. It seems that the algorithm tries to compensate the increase in velocity of the perturbation by decreasing the background velocity and vice versa.
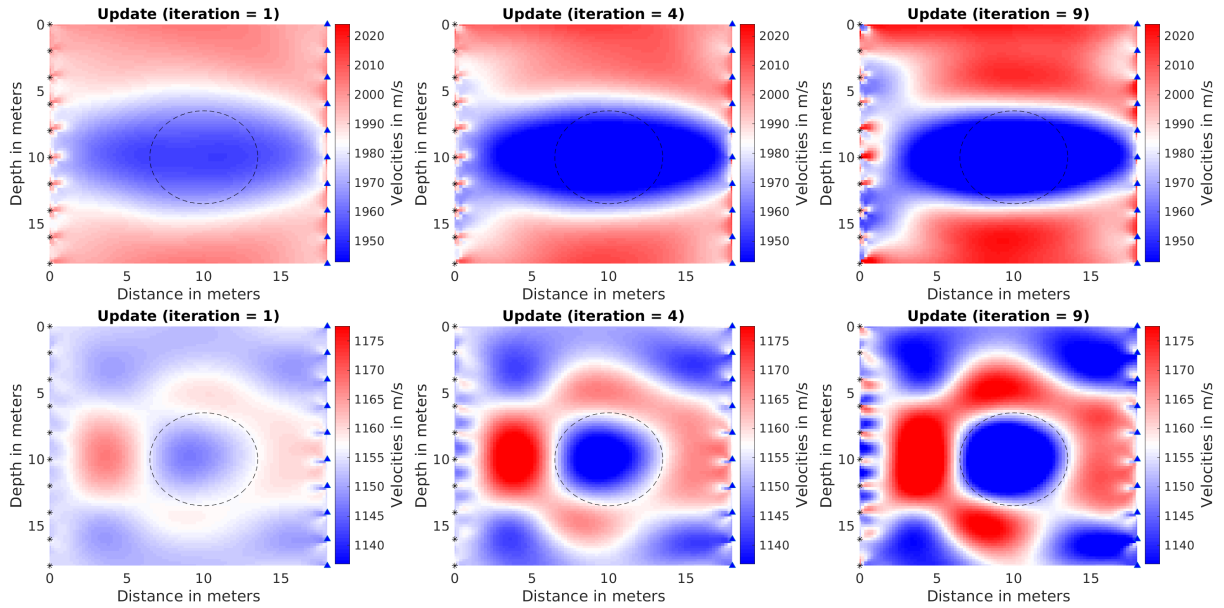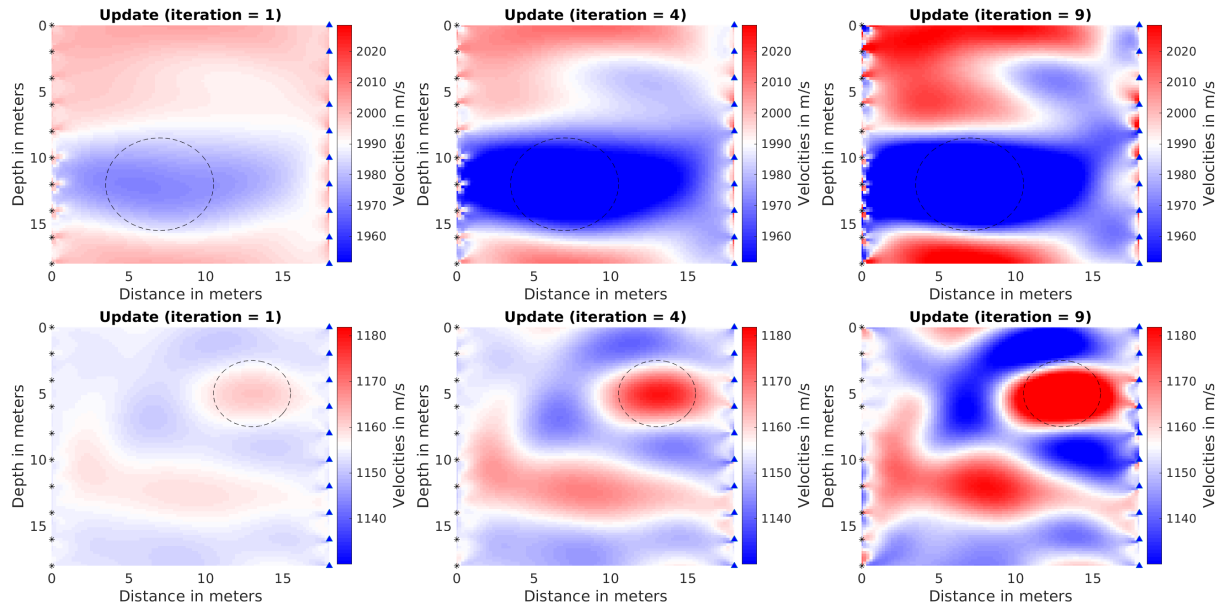
Figure 3.3.8: Inverted P- (upper panel) and S-wave (lower panel) velocity models after first (left), fourth (middle) and ninth (right) iteration; black stars mark source positions; blue triangles mark receivers; dashed circle marks position of the velocity anomaly
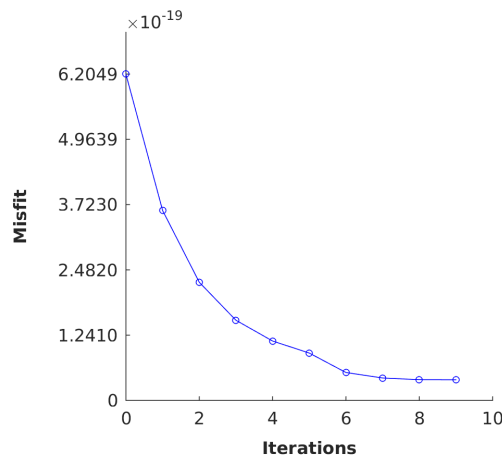
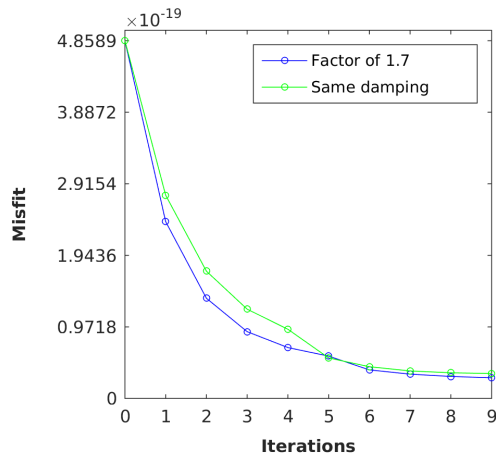**Figure 3.3.9:** Misfit curve for Vp- and Vs-inversion

3.3.2.1 Multi-scale approach

For this previously described inversion run a multi-scale approach was conducted, too. The frequencies were increased to 250 Hz and 300 Hz. As an input, the models derived from the previous inversion were taken (Fig. 3.3.8, right column). After the seventh iteration the numerical stability of the code exceeded and the calculation was dumped. To continue further, e.g. a smaller dt has to be used, but since the misfit was not decreasing any further (see Fig. 3.3.11) this should be enough.
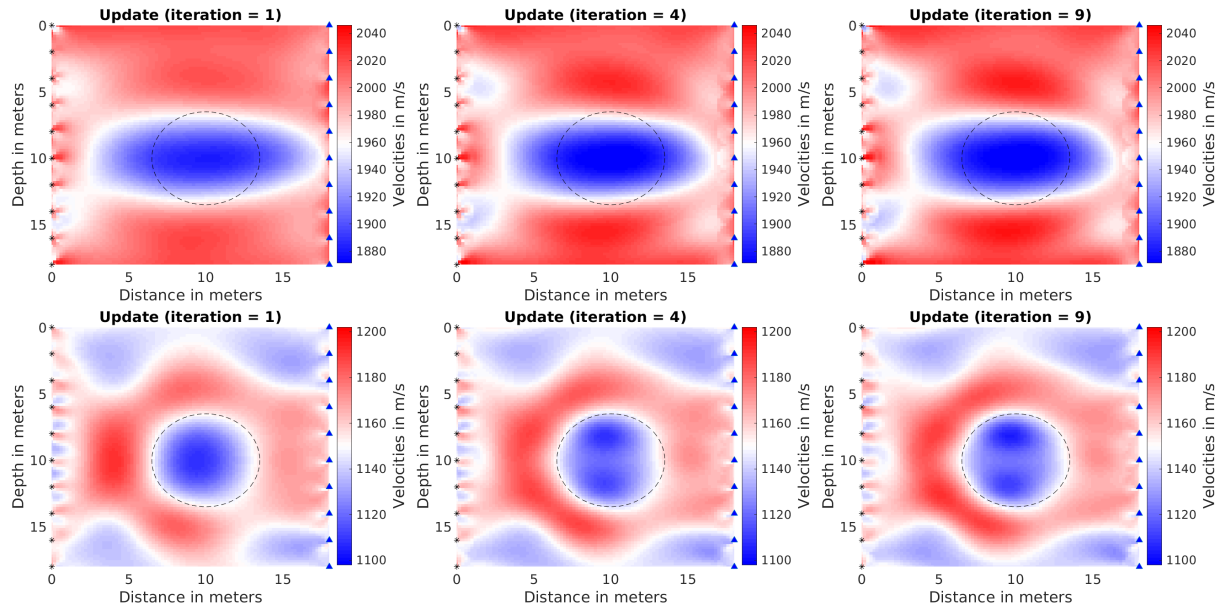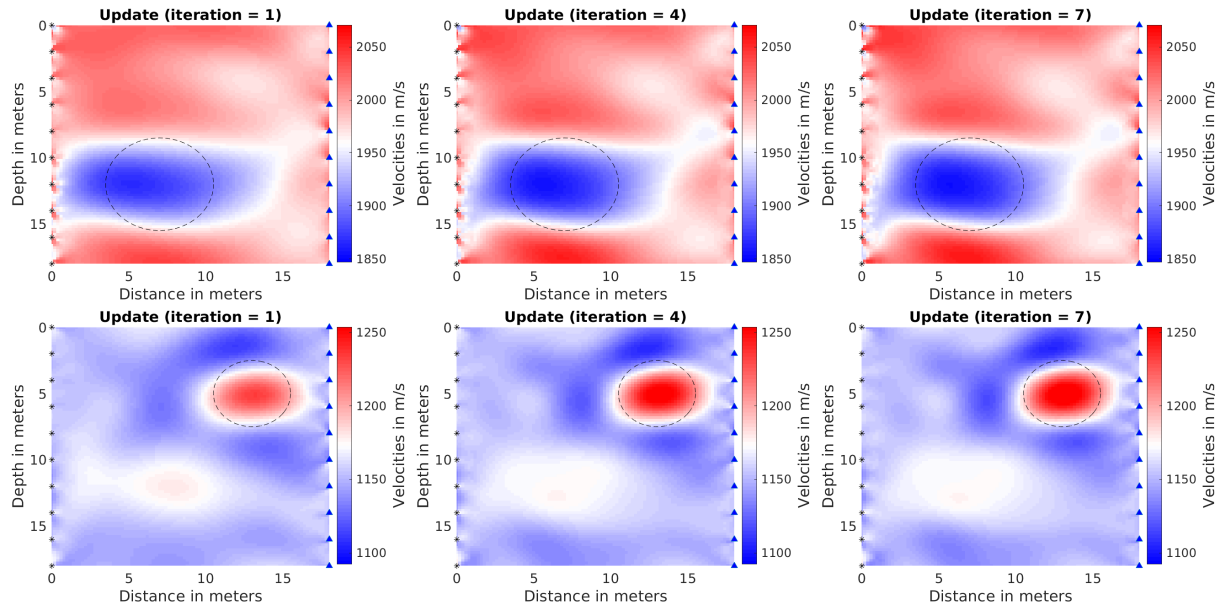
Figure 3.3.10: Inverted P- (upper panel) and S-wave (lower panel) velocity models after first (left), fourth (middle) and seventh (right) iteration using a multi-scale approach; black stars mark source positions; blue triangles mark receivers; dashed circle marks position of the velocity anomaly
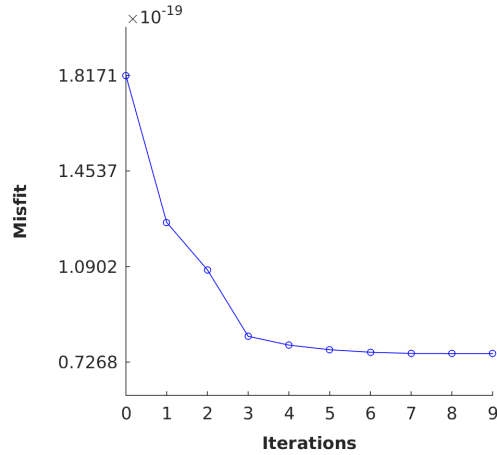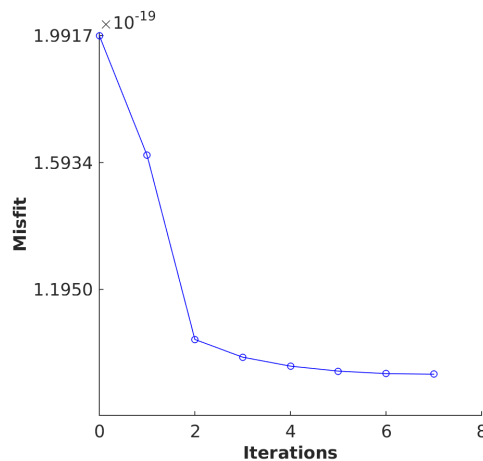

Figure 3.3.11: Misfit curve for multi-scale Vp- and Vs-inversion

The velocity anomalies in both models are laterally more sharpened (Fig. 3.3.10) as in the previous case, which is not surprising due to the overall shorter wavelengths and therefore the increased resolution capacity. Again the S-wave perturbation looks much nicer and defined than the P-wave perturbation, but this is also due to the much shorter wavelengths of S-waves. The velocity comparison of this and the previous inversion run are summarised in Tab. 3.3.4. The correction of the background velocities becomes worse, they are farther away from the true model. On the other hand, the velocity recovery of the perturbation is much better in both models. Here the mismatch is reduced of about $20\,\text{m/s}$ for the P-wave anomaly and $40\,\text{m/s}$ for S-wave anomaly. Overall it seems, that the algorithm wants to compensate the big velocity change inside the perturbation by "over-correcting" and changing the background velocity in the other direction.

Table 3.3.4: Velocity recovery for multi-scale approach

	$\mathbf{v_{max}}[\mathbf{m/s}]$	$\mathbf{\Delta_{true}}[\mathbf{m/s}]$	$\mathbf{v_{min}}[\mathbf{m/s}]$	$\mathbf{\Delta_{true}}[\mathbf{m/s}]$
Frequencies $100, 200\,Hz$				
P-wave	2051	51	1872	72
S-wave	1227	73	1114	41
Frequencies $250, 300\,Hz$				
P-wave	2060	60	1854	54
S-wave	1267	33	1105	50

3.4 Comparison of Cross-hole Models with IFOS2D

For the following subsection the synthetic modelling and inversion is performed with another 2-dimensional elastic waveform inversion code called IFOS2D (Köhn (2011a)) from the University of Karlsruhe. Before using these routines, the code was tested by inverting the same cross-hole model as in the previous sections. Both configurations, the velocity anomaly is placed at the same position for P- and S-waves and the anomaly is placed at different locations, are tested. This test is necessary to get to know the code and ensure the right application of input parameters. In the next subsections the inversion results for the cross-hole model from sections 3.3.1 and 3.3.2 are shown.

To compare the results derived by viselawi2d and IFOS2D, the model input parameters are chosen to be similar if possible. Since both codes possess different mathematical approaches, it was necessary to slightly change some parameters (e.g. a different time step and therefore a different spatial discretisation), but the overall framework was kept very similar (e.g. velocity models, geometry, source type). To maintain as much input parameters as possible is essential for a meaningful comparison between both inversion results. The number of iterations was terminated by the program when the last two misfits were decreased by less than one percent. For the viselawi2d program this threshold was reached after the 12th and 11th iteration for the model with coinciding velocity anomalies and differently placed velocity anomalies, respectively. The IFOS2D program reached those thresholds after much more iterations. The individual inversion outcomes are shown and discussed in the following sections.

3.4.1 Same Anomaly Position

As it was tested previously with the viselawi2d program in section 3.3.1, a simple crosshole geometry as an inversion setup was chosen. The inversion was carried out for P- and S-wave velocities simultaneously and the decreased velocity anomaly was similar in position, size and direction of velocity change for both geophysical quantities (see Fig. 3.4.1, A). The inversion was terminated when the change of the misfit of two consecutive iterations was less than one percent. As it was done for the previous test the inversion with the IFOS2D program was carried out for two low-pass frequencies of $100\,\mathrm{Hz}$ and $200\,\mathrm{Hz}$. The outcomes for this inversion test is displayed in Fig. 3.4.1.
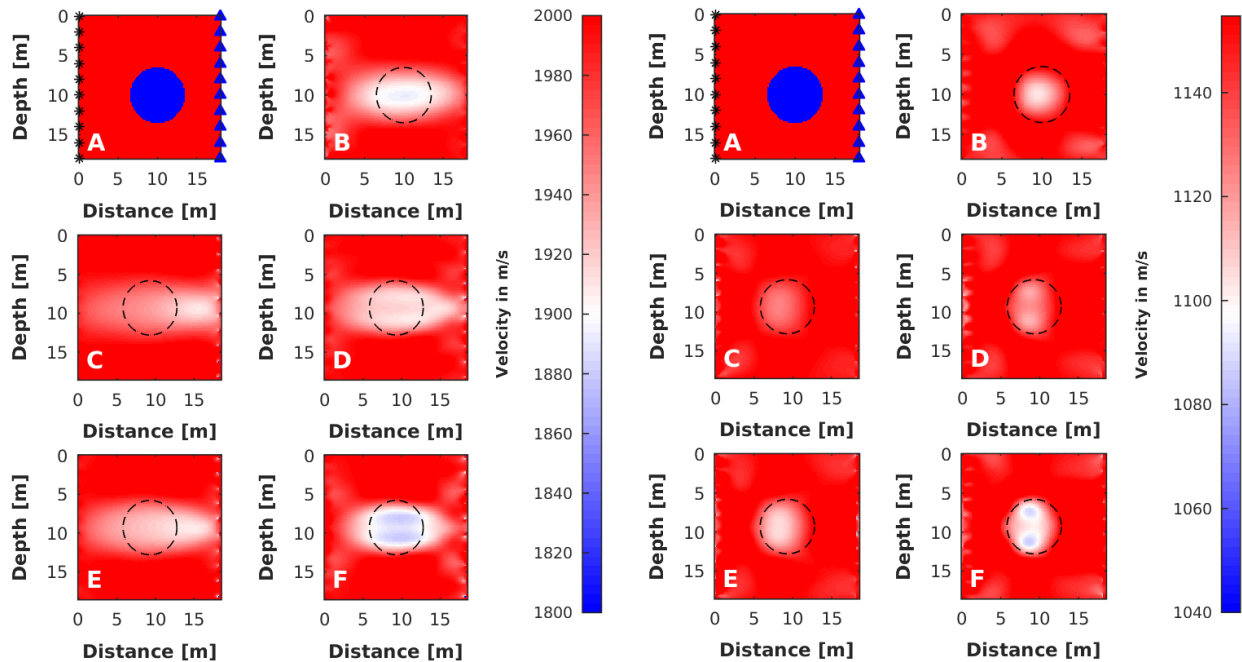
Figure 3.4.1: Inversion results for P-wave (left) and S-wave (right) velocities; A: true models; B: (last) iteration 12 of viselawi2d algorithm; C: 12th iteration of IFOS2D code for 100 Hz; D: 12th iteration of IFOS2D code for 200 Hz; E: (last) iteration 26 of IFOS2D code for 100 Hz; F: (last) iteration 44 of IFOS2D code for 200 Hz; black stars mark source positions, blue triangles mark receiver positions, the dashed line marks the position of the anomaly

The last iteration received by the viselawi2d program are shown in Fig. 3.4.1 and are marked with the letter B. After the 12th iteration viselawi2d reached the abortion criteria and the misfit was no longer decreased. The middle panel of Fig. 3.4.1 shows the inversion results for the IFOS2D algorithm after the 12th iteration. Here the algorithm has not reached the abortion criteria yet and further iterations were performed. The lower panel of Fig. 3.4.1 shows the final inversion results achieved with IFOS2D. In both P- and S-wave inversion both codes show the exact position of the anomaly and correct the velocity in the right direction. However, the P-wave anomaly is well defined in the vertical direction, but seems to be smeared in horizontal direction. The boundaries of the anomaly are not as sharp defined as for the S-wave velocity anomaly, since P-waves have longer wavelengths at the same frequency range as S-waves. To quantify the inversion outcomes qualitatively the Euclidean distance L between the inverted and true models were calculated with

$$L = \sqrt{\frac{(\mathbf{m}^{true} - \mathbf{m}^{inv})^2}{nx \cdot nz}} \tag{3.4.1}$$

where m_{true} and m_{inv} are the true and inverted models, respectively, and nx and nz are the grid points in x- and z-direction, respectively. Fig. 3.4.2 shows the decrease of the Euclidean distance with each iteration.
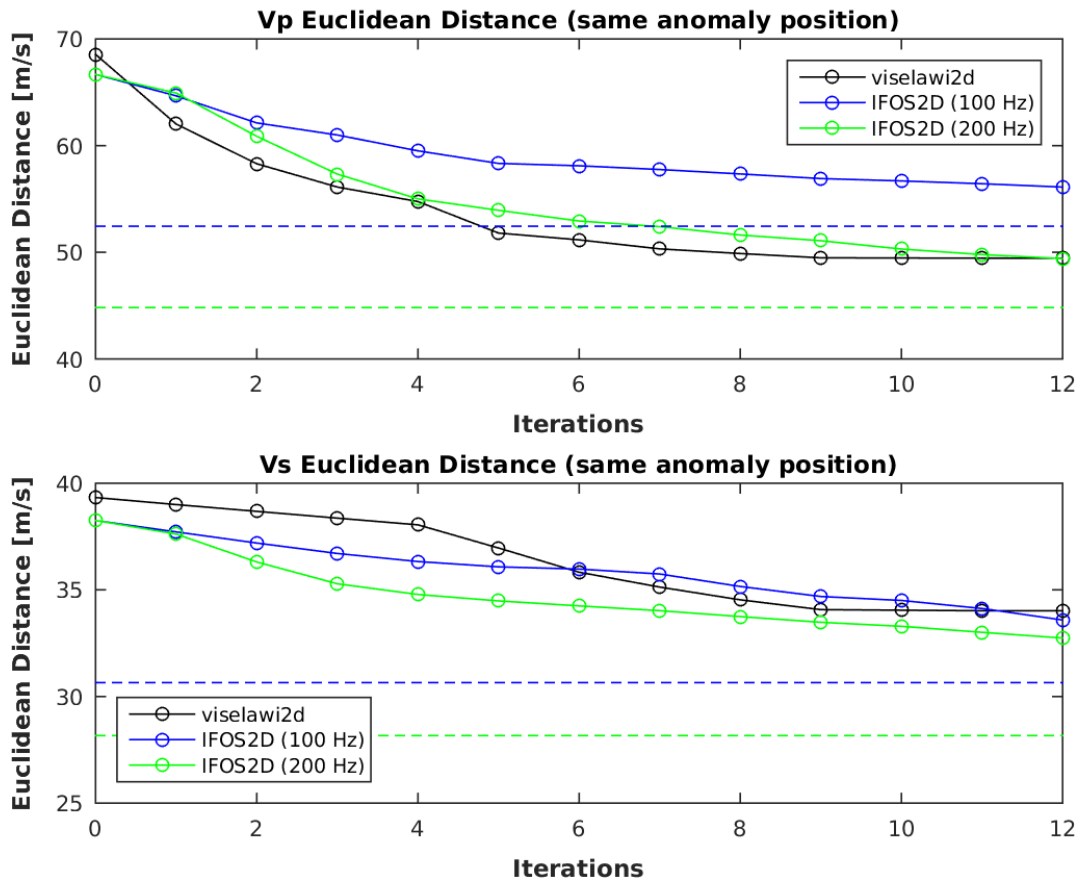
Figure 3.4.2: Euclidean distance for iterations 1 to 12 done with viselawi2d (black) and IFOS 100 Hz (blue) and 200 Hz (green); dashed lines indicate the final Euclidean distance of models E and F in Fig. 3.4.1; upper panel shows P-wave inversion, lower panel S-wave inversion

The Euclidean distance should be a measure of how close the inverted models come to the true models within the whole model space and not only inside the anomaly. The outcome for the P-wave inversion shows, the viselawi2d reaches a smaller Euclidean distance after 12 iterations than IFOS for 100 Hz and 26 iterations. Nevertheless, the IFOS inversion result for 200 Hz reduces the velocity differences even further and is therefore the best inversion result for this model setup. Concerning the S-wave inversion, the final distance of viselawi2d is higher compared to IFOS, but again the inversion for 200 Hz shows the best outcome.

3.4.2 Different Anomaly Position

The same inversion test was also done with the crosshole model where the velocity anomalies are placed at different locations in the model and also show different sign of anomaly. The procedure was kept the same and the inversion results are displayed in Fig. 3.4.3. Again viselawi2d reached its abortion criteria after the 11th iteration (Fig. 3.4.3, B), whereas IFOS2D reached its final inverted model after 53 and 59 iterations, respectively (Fig. 3.4.3, E and F). Both algorithms recover the anomalies at the right positions and with the right sign of velocity. However the S-wave anomaly recovered with the IFOS2D code and low-pass

200 Hz seems very well defined in shape and even in the magnitude of velocity increase, whereas in the viselawi2d code the anomaly seems to be implied at best. Again the Euclidean distances were calculated and are plotted in Fig. 3.4.4. The vieselawi2d code shows the same good results as the IFOS2D code for the P-wave inversion and at 200 Hz. Both algorithms decrease the Euclidean distance to the true model in the same range. One advantage of the viselawi2d code here is the fast convergence rate. However looking at the S-wave inversion results, the IFOS2D code shows its supremacy compared to viselawi2d. It decreases the Euclidean distance much further and is therefore closer to the real model. Still the inversion results for viselawi2d and IFOS2D at 100 Hz look quite the same.
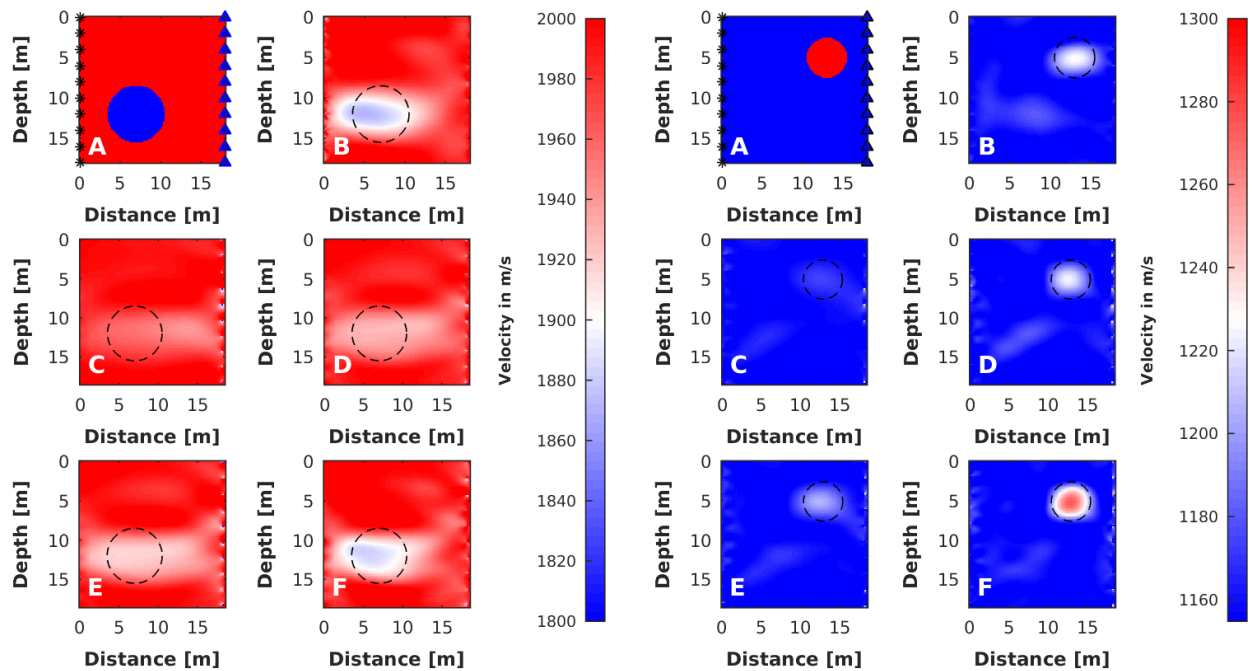
Figure 3.4.3: Inversion results for P-wave (left) and S-wave (right) velocities; A: true models; B: (last) iteration 11 of viselawi2d algorithm; C: 11th iteration of IFOS2D code for 100 Hz; D: 11th iteration of IFOS2D code for 200 Hz; E: (last) iteration 53 of IFOS2D code for 100 Hz; F: (last) iteration 59 of IFOS2D code for 200 Hz; black stars mark source positions, blue triangles mark receiver positions, the dashed line marks the position of the anomaly
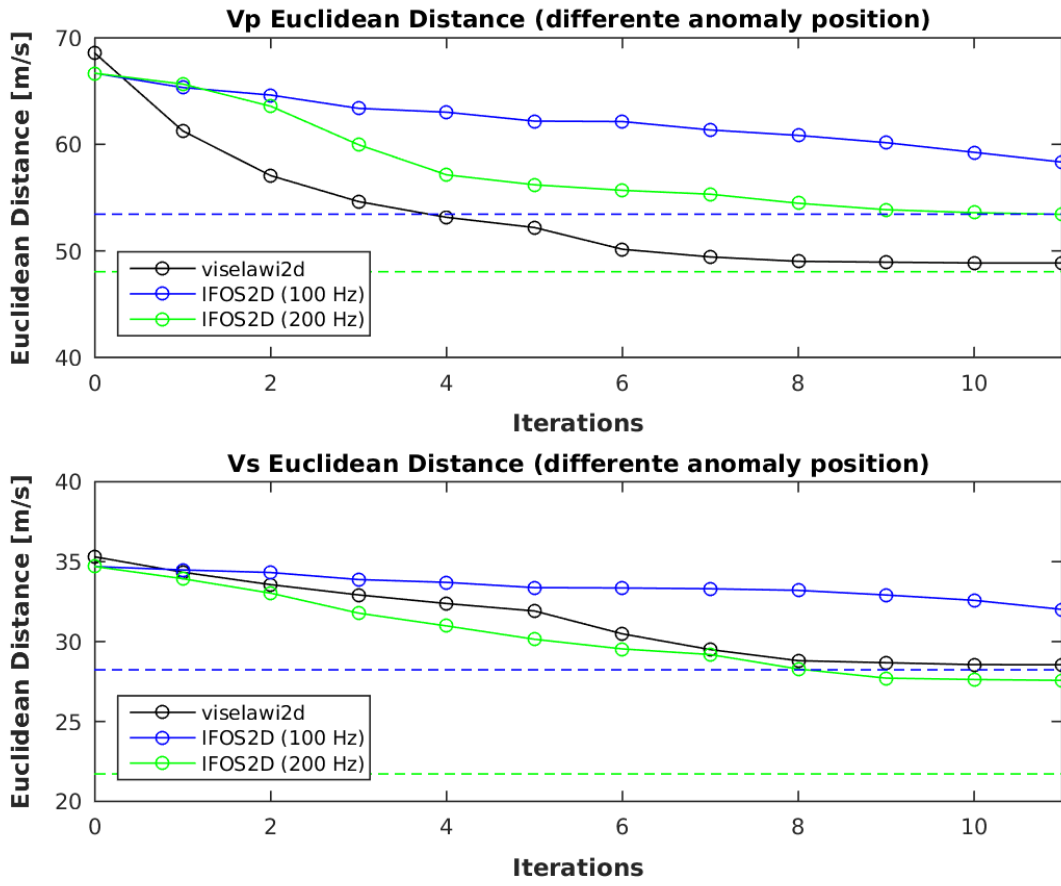
Figure 3.4.4: Euclidean distance for iterations 1 to 11 done with viselawi2d (black) and IFOS 100 Hz (blue) and 200 Hz (green); dashed lines indicate the final Euclidean distance of models E and F in Fig. 3.4.3; upper panel shows P-wave inversion, lower panel S-wave inversion

It is important to notice that this test was not meant to compare both algorithms in terms of convergence, applicability or supremacy. It is meant to show that the application of correctly chosen input parameters into IFOS2D yield the same results as viselawi2d and therefore deals as an application test before introducing more complex models as the one derived by the travel-time tomography.

3.5 Summary and Conclusion of Cross-hole Model Results

The inversion results shown and discussed in the previous sections show quit satisfying inversion outcomes for transmission seismic data. The velocity anomalies were correctly reconstructed in terms of position, geometry and type of anomaly. Both codes have no problems in recovering the velocity anomalies if they coincide or are positioned at different places within the model. Even the different sign of anomaly for P- and S-wave anomaly is no problem and could be reliably recovered. The convergence of the inversion is fast and the inversion results were received after only few iterations. Fig. 3.5.1 (same anomaly position)

and 3.5.2 (different anomaly position) show the inverted velocity models and velocity profiles for the best inversion outcomes of viselawi2d of sections 3.3.1.3 and 3.3.2.1, respectively. The velocities are significantly decreased or increased in the area of the velocity anomaly. However, the code tries to over-correct the velocity in- or decrease of the anomaly by changing the velocities outside of the anomaly in the opposite direction, which is not reasonable. Nevertheless the over-compensation is less of a magnitude than the velocity correction of the true anomaly. In general the synthetic tests show satisfying results and a confident inversion of transmission data.
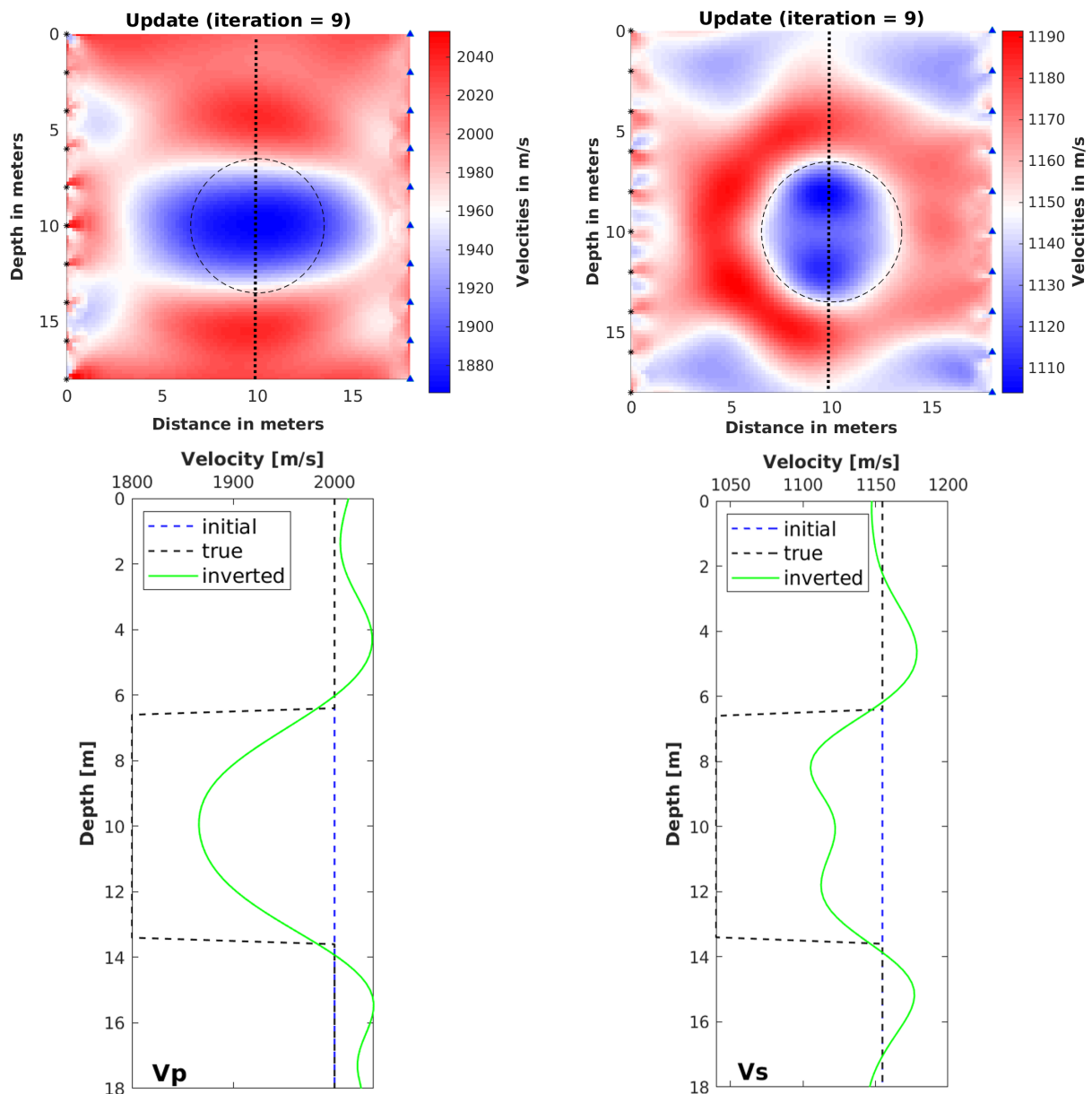
Figure 3.5.1: Inverted velocity models (upper panel, see Fig. 3.3.5) and velocity profiles (lower panel) through the velocity anomaly of coinciding velocity anomalies (black dotted line) for P-wave (left) and S-wave (right); blue dashed line indicates homogeneous initial velocity model, black dashed line indicates true velocity model with the velocity anomaly and green solid line indicates the inverted model
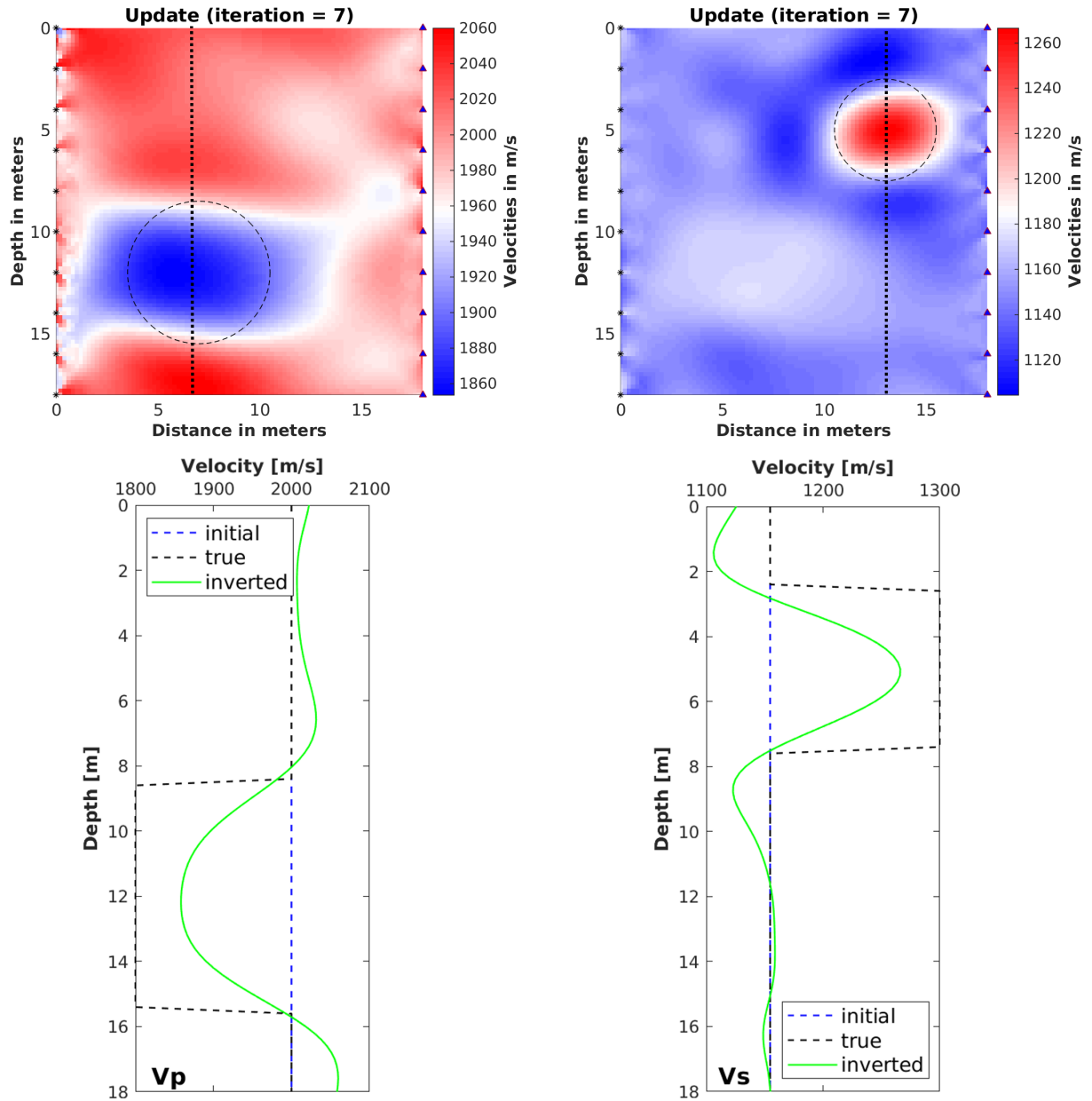
Figure 3.5.2: Inverted velocity models (upper panel, see Fig. 3.3.10) and velocity profiles (lower panel) through the velocity anomaly of non-coinciding velocity anomalies (black dotted line) for P-wave (left) and S-wave (right); blue dashed line indicates homogeneous initial velocity model, black dashed line indicates true velocity model with the velocity anomaly and green solid line indicates the inverted model

Part II

Real Data Application

Chapter 4

Data Acquisition

In this chapter the test site is introduced in terms of geology, lithology and tectonics. The first survey was conducted by hammer blows on a prismatic wedge. Therefore a special data processing is necessary including data quality control, rotation, normalisation and stacking and finally a spectral analysis and a rough velocity estimation is performed. Unfortunately the signal-to-noise ratio is not satisfactory wherefore a second survey with a Buffalo gun was repeated. Again the data are quality controlled and a spectral analysis was done.

4.1 Survey Area

4.1.1 Geology

4.1.1.1 Geological Overview

The Styrian Mt. Erzberg is the biggest open-cast ore mine in Central Europe and the largest siderite deposit in the world (Erzberg (2018b)). It is located in the North of Styria, Austria, roughly 85 km in north-west direction from Graz (see Fig. 4.1.1). It is 1465 m high and is situated at the north-eastern boundary of the Eisenerzer Alps within the northern greywacke zone of the Eastern Alps. The Eastern Alps proceed in north-east direction, descent in the Vienna Basin and reappear in the east as Carpathians. The greywacke zone forms the north-eastern alpine Palaeocene and separates the Central Alps from the Northern Calcareous Alps. It belongs to the Noric ceiling (Bryda et al. (2013)), which was sheared off and transported during the early alpine orogenesis. The alpine Noric thrust line separates the Noric ceiling (Zeiritzkampel nappe, Wildfeld nappe, Reiting nappe, scale zone and Noric zone) from the lower Veitscher nappe (Schönlaub (1982)). Mt. Erzberg is bordered by the spur of the Northern Calcareous Alps in the North, the Präbichlpass and Gerichtsgraben in the East, the Eisenerzer Alps in the South and the Krumpental in the West. Its stratigraphic sequences range from the Ordovician to the Carboniferous and are overlain by an erosion discordant superposition of permocytic sediments. The sequences were deformed by the Variscan and Alpine orogenesis (Schulz et al. (1997)).
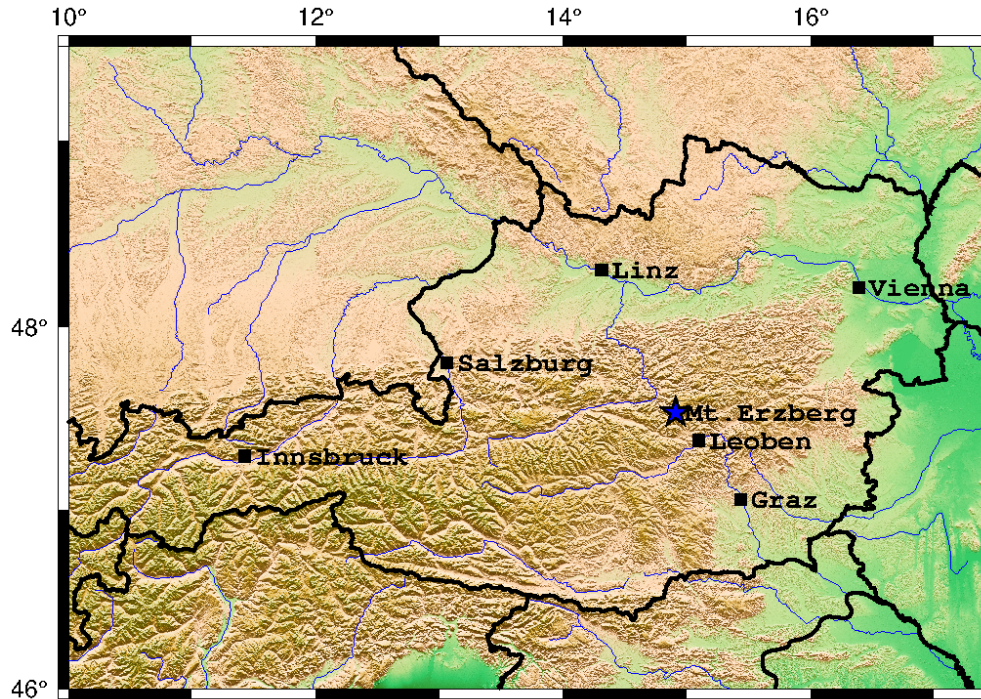
Figure 4.1.1: Overview map of Austria and Mt. Erzberg (blue star)

4.1.1.2 Lithologies

The main geological units can be distinguished in three parts, the porhyroid in the lower block serving as the basis, the ore-bearing formations, which are the actual deposit area and the Werfer layers in the upper block (Erzberg (2018b)). In this subsection the lithologies are mentioned in more detail, separated by age and from bottom to top. For a more detailed description and explanations of their deposition regime the reader is referred to the authors mentioned in the following section.

The main basis of the *Ordovician* is composed of the so called "Gerichtsgrabengruppe". That are different kind of slates, phyllitic greywacke slate, mica containing sandstones, sandy slate, greywacke, quartzitic slate, and carbonate bands of 400-500 m thickness (Flajs and Schönlaub (1976)). The Gerichtsgrabengruppe is followed by 400 m of Blasseneckporphyroids, which itself is in places overlain by a thin sequence (4-5 m) of fine-layered sericit-, calcite- and siderite quartzite that is often called "transition porphyroid" (Bryda et al. (2013)). The Ordovician sequence is closed by a 15 m thick layer of cystoid limestones (Schönlaub (1982)). The *Silurian* sequence consists of 50-80 m thick black-, siliceous- and alum shale, followed by 30 m of limestones with intercalated clay skins (Schönlaub et al. (1980), Schönlaub (1982)). The basis of the *Devonian* is marked by the so called "Schiefererz" (slate ore) and introduces the beginning of the ore mineralisation. The slate ore consists of 10 m thick phyllonitic metamorphic rock of sericit-, chlorite-, quartzite-, haematite- and limestone-, ankerite- and siderite phyllite with accessory pyrite, quartz and mica. On top of the slate ore follows lime slate (9 m), sericitic lime marble (9 m), siderite- and ankerite ore (45 m, in mining terminology often referred to as "Rohwand"), sericite marble (4-5 m) and 4 m of white marble which

forms the transition to the so called "Sauberger Kalke" (Schönlaub et al. (1980), Schulz et al. (1997)). The upper top of the Devonian sequence is formed by the Sauberger Kalke, ore bearing limestones, with porphyroid intercalation, haematite enrichment and tuff interlayer, of 115 m thickness (Schönlaub et al. (1980)).

The base of the *Carboniferous* is composed of 10 m of lime breccia and overlain by the 80-150 m thick "Eisenerzer Schichten", interslate, consisting of greyish black or colourful slate and phyllites (Schönlaub et al. (1980), Schulz et al. (1997), Bryda et al. (2013)).

The final sequence, the *Permian* sequence, is formed by 40 m breccia (Schulz et al. (1997)) and the Werfer slate, that is also called "Präbichl" sequences. The breccia in the lower block possesses devonian chalks, quartz, ore or Rohwand and in the upper block mica rich sandstones and silt slate (Schönlaub et al. (1980)). The Werfer slate shows authigenic gypsum together with greyish intermediate layer (Schulz et al. (1997)).

Fig. 4.1.2 shows a WNW-ESE trending cross-section through Mt. Erzberg with the main analysed stratigraphy. The blue bar marks the tier of the test site.

Figure 4.1.2: Cross-section through Mt. Erzberg indicating the most prominent stratigraphy taken from Schulz et al. (1997), the blue bar marks the position of the test site; translation: *Siderit-Erzkörper- und Lagen*: siderite ore bodies- and layers, *Ankerit-Körper*: ankerite bodies, *Eisenerzer-Schichten*: interslate, *Kalkschiefer, -phyllit, -marmor*: lime slate, -phyllite, -marble, *Permoskyth: Breccie, Sandstein, Schiefer, Phyllit*: permoscyth: breccia, sandstone, slate, phyllite, *Porphyroid* : porphyroid, *Tagbaustand*: status of surface mining progress, *Christof-Hauptverwurf*: Christof main fault

4.1.1.3 Tectonic Setting

The area of Mt. Erzberg experienced a polyphase tectogenesis. The east-west narrowing during the Variscan orogeny resulted in the over-thrusting of two neighbouring carbonate platforms, which was favoured by the Eisenerzer sequences serving as sliding surface (Hirzbauer et al. (1991)). This split the area into two main parts, the lower block of Ordovician to

Devonian sequences overlain by carbonate slates, and the upper block of Devonian chalks (Schönlaub (1982)). The further narrowing of the ongoing Variscan orogeny, now in north-south direction, resulted in a large fold relief with the major fault visible at Mt. Erzberg called the Christof main fault (Fig. 4.1.3). This fault possesses an inclination of 30° and a normal fault of 300 m in eastern direction (Schulz et al. (1997)). The Christof main fault was reactivated during the Alpine orogeny, which also caused the evolution of the trough shape and the different inclinations of the major deformation axis of the Eisenerzer syncline towards the North (Hirzbauer et al. (1991)).
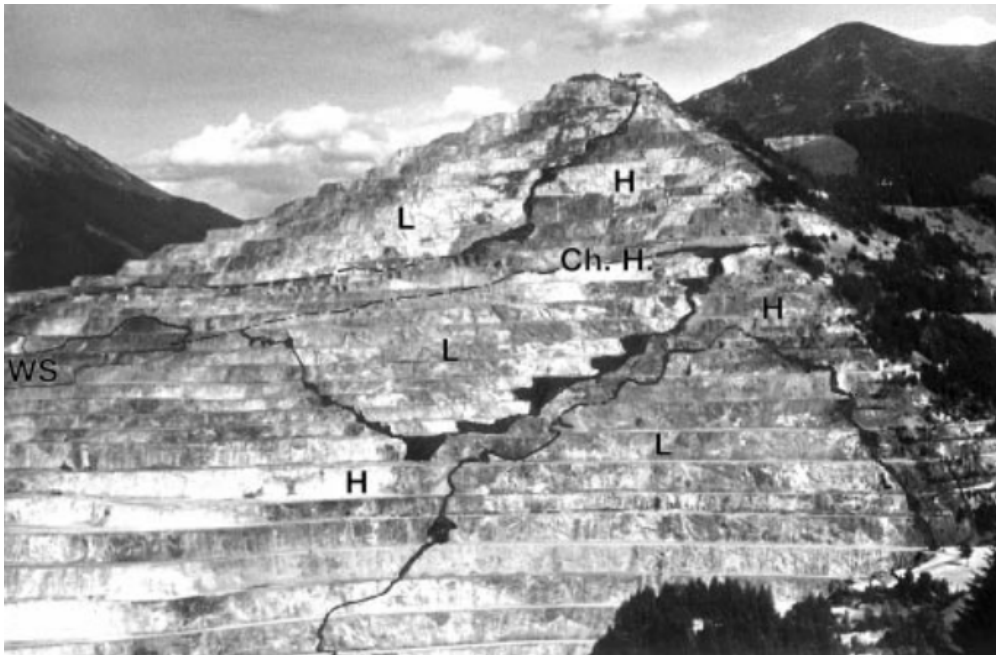
Figure 4.1.3: Mt. Erzberg with its major faults taken from Schulz et al. (1997) seen from WNW; L - lower block, H - upper block, CH. H. - Christof main fault, WS - Werfer slate

4.1.2 Test Site

At Mt. Erzberg it is assumed that iron ore is produced since Celtic-Roman times (Schulz et al. (1997)), but at the latest since the 3rd century A.D. (Erzberg (2018a)). This deposit is an important factor for the economy and policy in this region. Surface mining was replaced by subsurface mining since the 16th century A.D., but was resumed in 1986 (Erzberg (2018a)), giving the mountain its characteristic stepped appearance (Fig. 4.1.4, left). The study area is located in a closed down part of the Mt. Erzberg at the *Schuchardt tier*, which is bordered by the elevated *Hell tier* to the East and the next deeper tier *Dreikönige*. The whole tier is located 1116 m above the Adria and approximately 23-31 m above the tier *Dreikönige* (Sladky (2018)). In Fig. 4.1.4 (left) the red arrow marks the location of the test site. Old maps provided by the VA Erzberg GmbH show an abandon tunnel system of left open subsurface mining adits, which positions and diameters are quite well known. By knowing the approximate position of those cavities the specific geophysical measurement can be designed accordingly in order to resolve such cavities in the resulting subsurface model. Fig. 4.1.4

(right) shows a schematic map view of the tier with the abandoned tunnel system and the seismic profile indicated by the blue line.
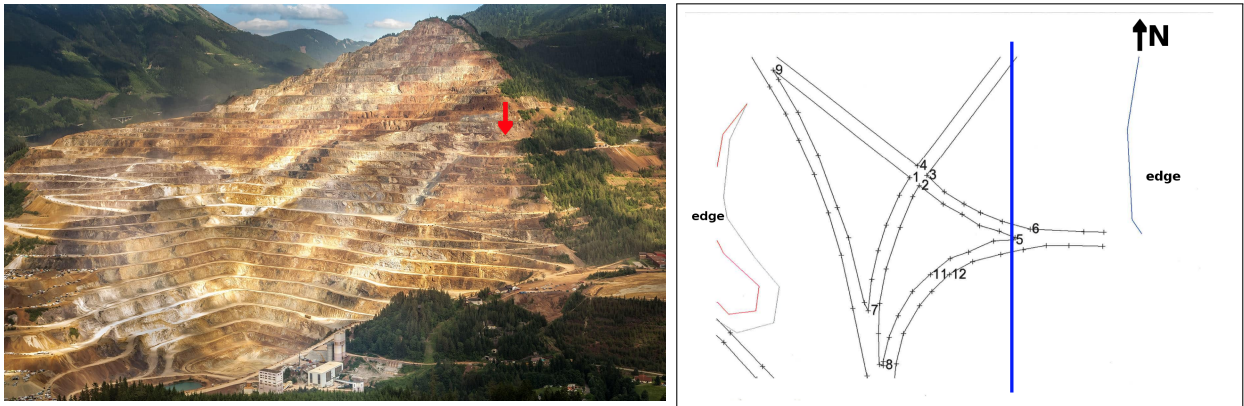
Figure 4.1.4: Right: Bird's eye view at Mt. Erzberg; red arrow marks position of the test site (modified after 1000things (2018)); Left: Map view of Schuchardt tier; blue line marks seismic profile, adit system expected in approximately 25 m depth (pers. comm. VA Erzberg)

Fig. 4.1.5 shows a map view of the tier including the seismic profile, which crosses an area with increased wetness between profile meters 20-30. To the West of the profile two big puddles can be seen, that remained there during the whole measurement. Also the soil in that area was squashy and wet, which made it easy to deploy the geophones there, but could lead to decreased surface velocities. In the South the profile heads into dense vegetation including trees and bushes. Except for those two areas the rest of the profile was located on hard ground, compacted gravel or even bed rock, so that a borer had to be used to drill holes for the geophone spikes. The rocks of the tier show fractures and faults, that can already be seen on the tier's side and also at the surface of the tier where cracks of various sizes are visible. This is not surprising since the rocks were heavily worked by surface and subsurface mining. Fig. 4.1.6 shows a photo of the side of the *Schuchardt tier* from the lower tier. One can clearly see cracks and fractures and also weathered slope rock which indicates erosion processes that also weakens the rock. In this Figure, the identified lithologies are also marked and labelled.

Sladky (2018) did some geophysical studies on that tier to investigate the detection of those cavities. He conducted a geomagnetic measurement, a geoelectric resistivity measurement and a ground penetrating radar (GPR) measurement. They were not able to detect the tunnel with the geomagnetic and geoelectric resistivity measurements, but the GPR measurement showed some indications of a tunnel in some of the measured profiles across the tunnel. However, the study did not reliably show the presence of a cavity in the suspected area, but confirmed the present lithologies in the subsurface as it was also suggested by the old mine plan provided by the VA Erzberg GmbH (not shown here, but in Sladky (2018)). In Fig. 4.1.7 one final geoelectric resistivity profile using the Wenner Alpha configuration is shown. The obtained resistivity model shows lateral and vertical heterogeneities in the ranges of 1580 to 6310 Ωm. The low resistivity area marked with 1 could be differently
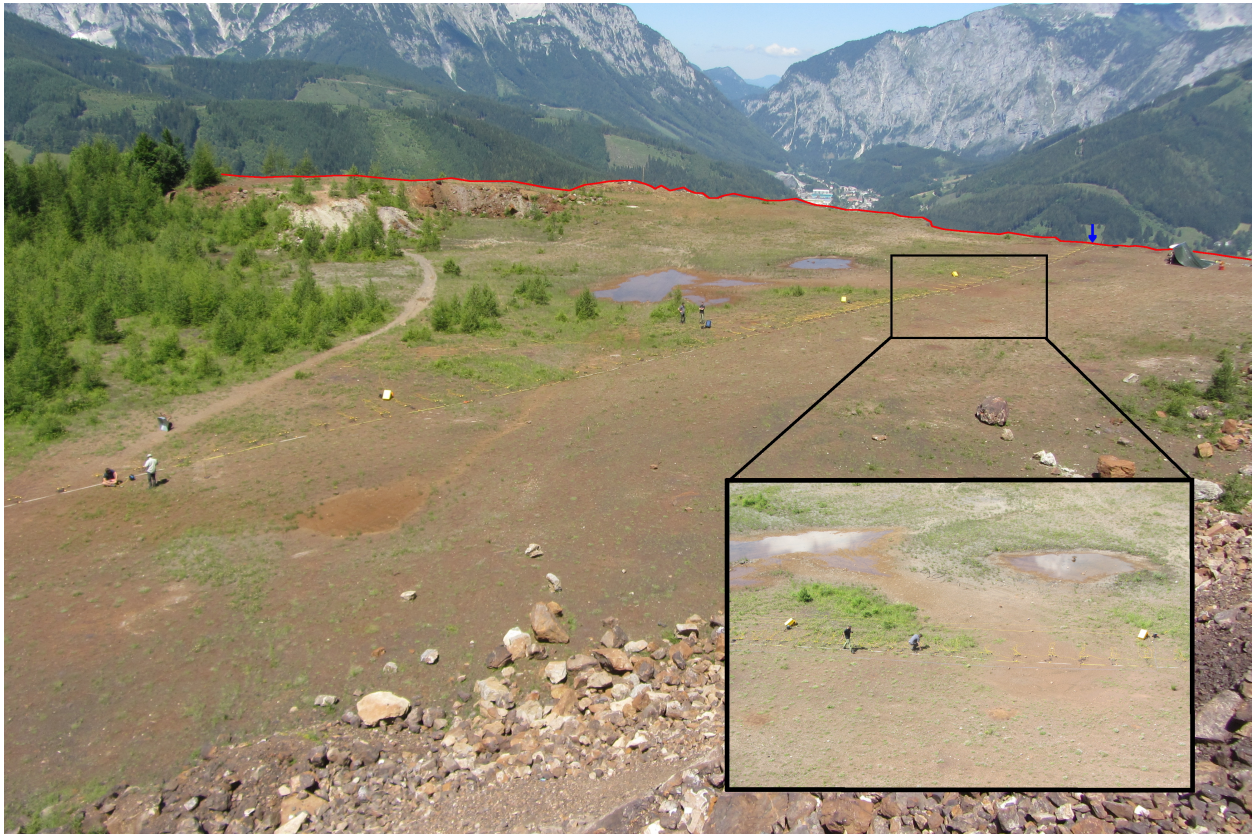
Figure 4.1.5: Map view from *Hell tier* down at *Schuchardt tier* from the East; blue arrow marks the beginning of the profile in the North (0 m); red line marks the brim of the tier; inlay figure shows area of increased wetness

interpreted; it could be ionized potable groundwater, a heavily fractured and water-filled ore body or betwixt schist which functioned as nappes between ore bearing parts. The other low resistivity areas marked with 5 and 6 are interpreted as stained or water bearing rocks, respectively. Another hint for a water rich area in the very South of the profile would be the vegetation there. The high resistivity areas labelled with 3 and 4 are interpreted as carbonate sediments and high-resistive, less-fractured, dry ore bodies, respectively. The remaining low resistivity area marked with 2 is identified as dry, less-fractured bed rock, that functions as water-impermeable horizon causing a wet area at the surface characterized by a low resistive area between profile meters 20 to 40 and puddles on the surface, which are also visible in Fig. 4.1.5. Right at the surface unconsolidated rock fragments of Siderit, Ankerit, schists and carbonates are interpreted, that were used to flatten the tier. This was not only measured in the geoelectric resistivity survey, but also in the geomagnetic survey.
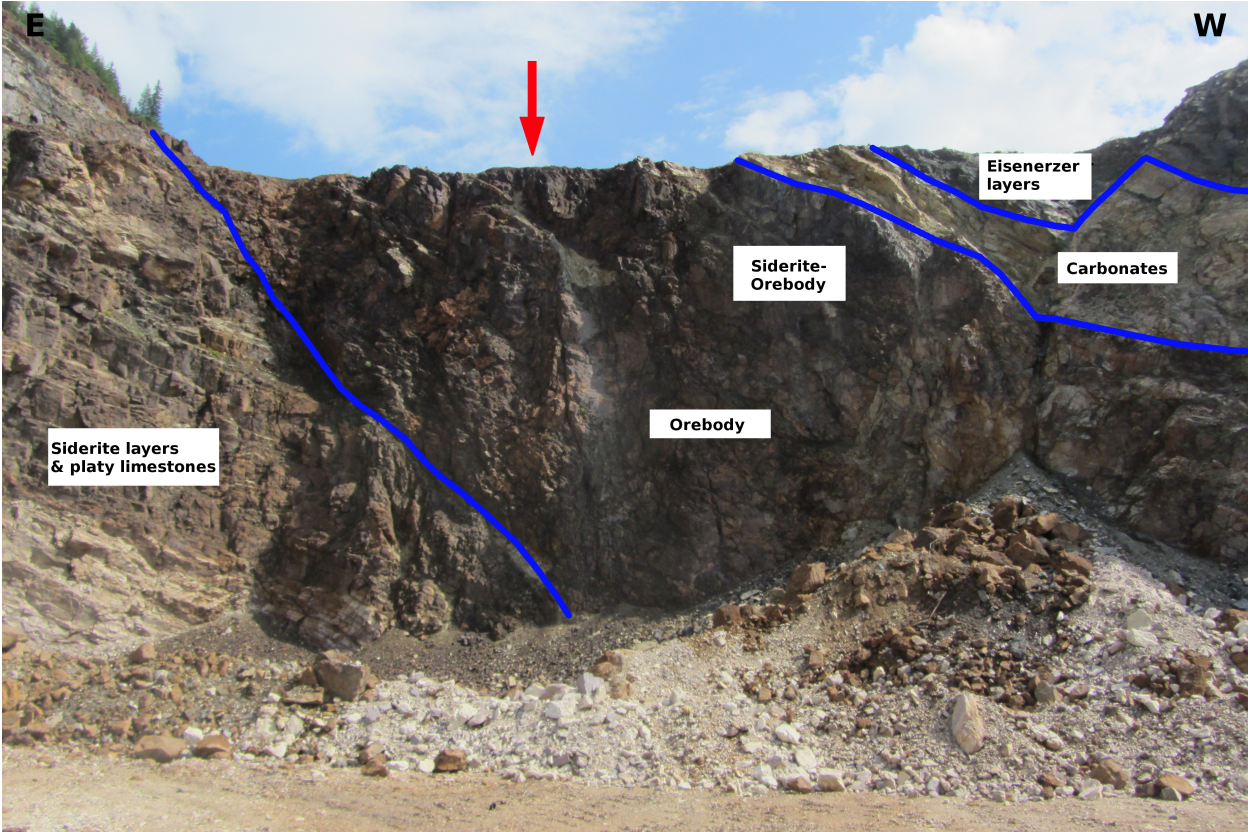
Figure 4.1.6: Side view of the Schuchardt tier from the North towards the South; blue lines mark lithological boundaries; red arrow marks beginning of the seismic profile
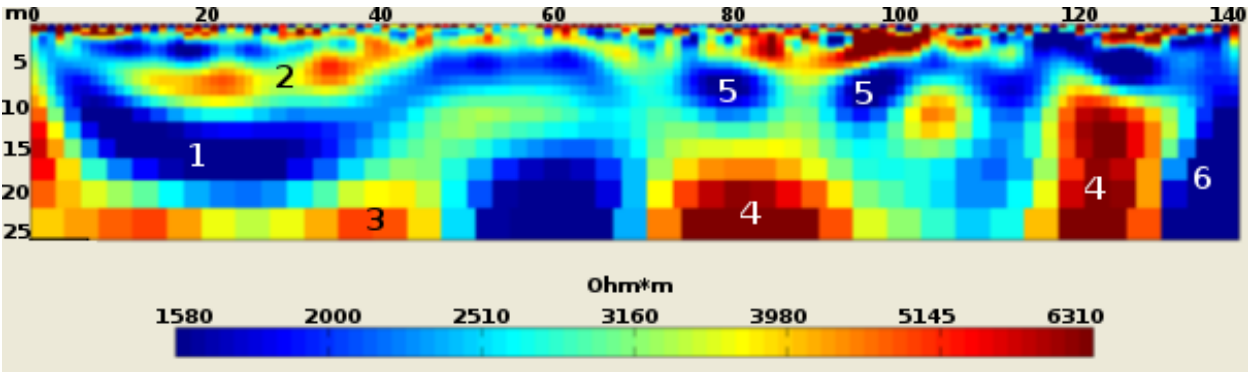
Figure 4.1.7: Geoelectric results obtained with Wenner Alpha configuration modified after Sladky (2018); white and black numbers mark interpreted geological features further explained in the text

The reason why the suspected tunnels could not be resolved in the geoelectric resistivity measurements is not a lack of eligibility of this method, but the experimental set-up in general. The tunnels, suspected in approximately 25 m depth, are too deep for the length of the geoelectric profile. This is shown by Fig. 4.1.8, where the resistivity data are once again inverted as they are (lower panel) and when two tunnels are forced into the model (upper panel). The overall model does not change, only the RMS slightly increases from 5.33 % to 5.6 %. To increase the length of the profile is not possible as both profile ends reached the edges of the tier already. For refraction seismic measurements a rule of thumb says, that the

profile length should be five times the target depth, meaning the target depth is 25 m the seismic profile should be at least 125 m. In this study the profile length is 136 m for the first survey and 128 m for the second, which is already close to the threshold. In case the tunnels are deeper, there is also no chance to reach the tunnels with the seismic measurement.
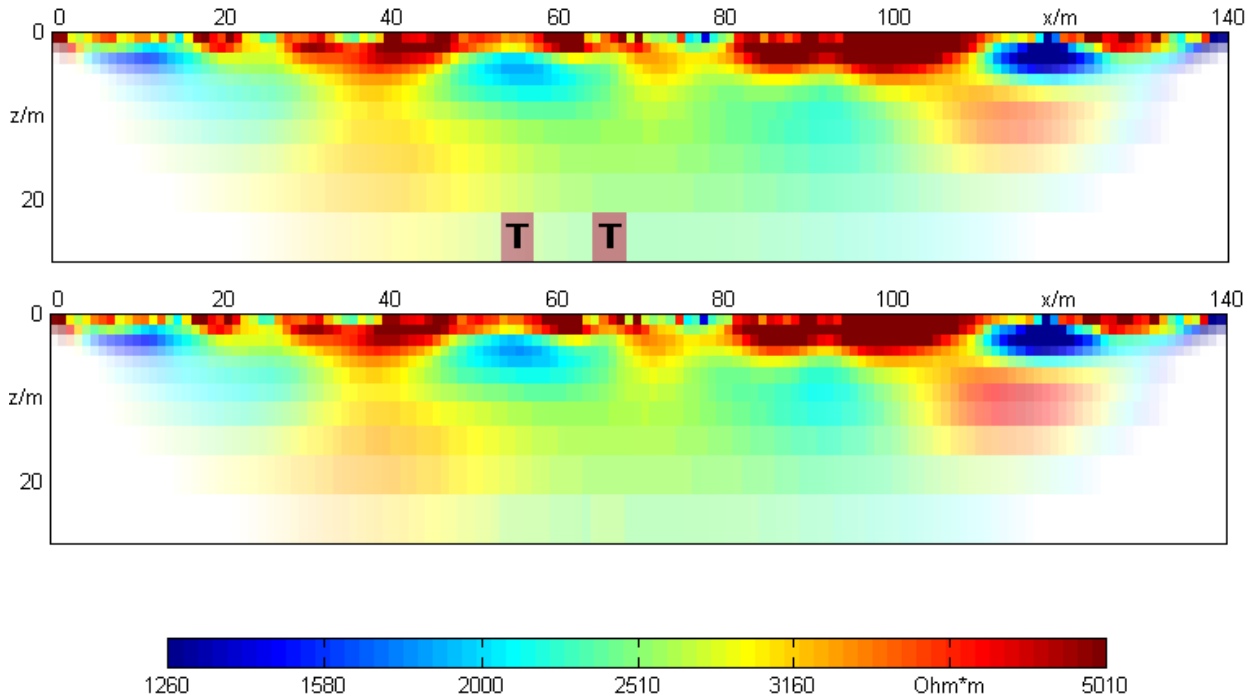
Figure 4.1.8: Geoelectric resistivity inversion models for the Wenner Alpha configuration as used by Sladky (2018) (lower panel) and when two tunnels (marked by T) are forced into the model (upper panel)

4.2 Survey 1: Hammer Blows

4.2.1 Field Measurements: Hammer Blows

Reflection and refraction seismic measurements were conducted on Saturday 9.7. and Sunday 10.7.2016 at the *Schuchardt tier* at Mt. Erzberg, Austria. The profile was 136 m long, with a receiver spacing of 2 m and a densely spaced receiver area of 1 m spacing between profile meter 42 to 64 m. The first geophone and therefore profile meter 0 was located very close to the edge (see Fig. 4.2.1, left). 80 3-component geophones were used (Fig. 4.2.1, middle). The shot spacing was 1 m. The expected cavity should cross the profile perpendicular at profile meter 53 in approximately 25 m depth. At this position the tunnel is branching into two adits, generating an efficient width of approximately 8 m (one single adit is assumed to be 3-4 m wide) (see Fig. 4.1.4, right). As a source a prismatic wedge with 45° inclined sides and hammer strikes normal to the wedge's sides were used (Fig. 4.2.1, right). This kind of source should generate higher frequencies and S-wave phases to better resolve the rather small extent of the cavity compared to its depth. The deployed system was the Summit X One from DMT.
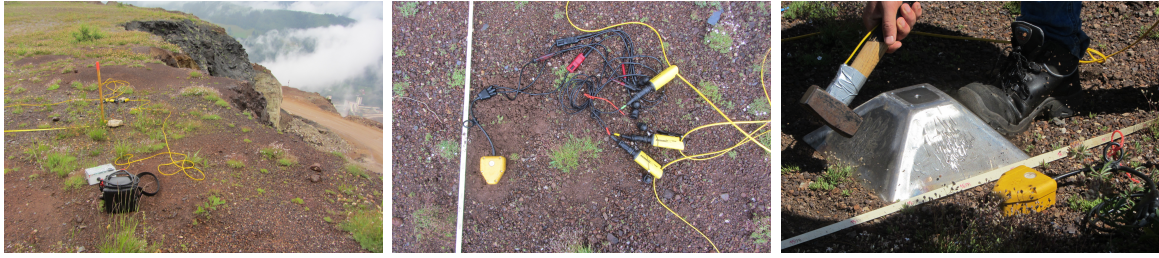
Figure 4.2.1: Measurement impressions; left: profile meter 0 was located near the edge; middle: 3 component geophone and connected remote units (RU); right: prismatic wedge with normal hammer blows on inclined side

4.2.2   Data Quality Control

To assure data quality of measured data is one of the essential steps in data processing. A critical part of this processing step is to maintain the reproducibility by simultaneously improving the data quality without excessively beautifying or adulterating them. In this survey, the reflection and refraction seismic data were collected at two days, Saturday and Sunday. The overall noise level is different, even though some noise sources were present on both days. Noise created by mine workers and big haulys should have the same level on both days. Nevertheless the data quality of the Sunday data is much better, due to several reasons. On Sunday the geophones and remote unites were carefully tested considering their "standard" noise level before the actual measurement started, which was not done on Saturday. Geophones or remote units showing a high noise level before the measurements were exchanged. A further improvement of data quality is achieved by a greater number of hammer strikes, namely 3 instead of 2.

Another investigation of the data revealed that some traces show a reverse polarity than the other traces. This could have different reasons. On the one hand, this could be due to conversions from one phase into another, but this would only affect several phases and not the whole trace.

Another, more likely, reason would be the incorrect installation of geophones and their connection to the remote units. Here it could be possible, that components were mixed up. If this is the case, such polarity flip of one trace compared to all other traces, should be visible in all shots. After a spot check of nearly 40 shot sections, such erroneous polarity flip could only be identified at geophone 8. Figure 4.2.2 shows exemplary the reversed trace at geophone 8 (left) and the corrected trace at geophone 8 (right). Other traces showing such flipped polarity were also investigated, but were not reversed because their erroneous polarity could not be discovered in all shots. In the following processing steps the traces recorded at geophone 8 were flipped.
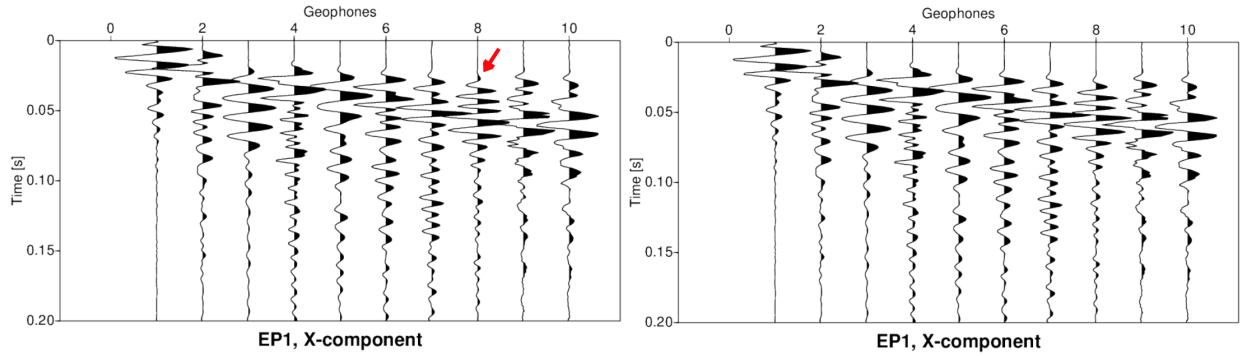
Figure 4.2.2: Example of one shot and first few traces; left: reversed trace at geophone 8 marked by red arrow; right: flipped trace at geophone 8

4.2.3 Normalisation & Stacking

The collected seismic data were normalised by applying a normalisation procedure. Three inclined hammer strikes compose one single shot and should therefore be equal in magnitude before stacking them. First, all three conjugate traces are normalised with respect to every first hammer strike. This gives three scaling factors for each receiver (one for every first, second and third trace, respectively), whereas every first trace is scaled by 1 to maintain its amplitudes. Equation 4.2.1 shows the computation of these scaling factors with ntr number of traces (here 80) and sc_i scaling factor per trace.

$$SF_k = \frac{\sum\limits_{i=1}^{ntr} sc_i}{ntr} \qquad \text{with } k = 1, 2, 3 \tag{4.2.1}$$

After applying equation 4.2.1 to the data, the traces are scaled by the scaling factors SF_{1-3} and then diversity stacked. In theory, real seismic signals are considered to be coherent and noise is considered to be arbitrary. Therefore coherent signals should be added, whereas arbitrary noise should cancel out, or at least should be minimised. Stacking is a processing tool to enhance coherent signals of any kind, in which all amplitudes of all considered traces are added. Differently to the normal data stacking, where the seismic traces are summed and then divided by the number of non-zero stacked samples (or just plainly summed without division) (Stockwell (2016)), the diversity stacking algorithm first scales each trace by the inverse of its average power

$$S = \left(\frac{\sum\limits_{i=1}^{nsp} x_i^2}{nsp} \right)^{-1} \tag{4.2.2}$$

where x_i is the ith sample and nsp is the amount of all samples in one trace. After the scaling the traces are stacked and normalised by dividing the stacked traces by the sum of used scalers (here three scalers are used) (Stockwell (2016)). The reason to apply diversity stacking instead of normal stacking is to overcome the influence of differently strong hammer strikes or get rid

of noise "outbursts" (Sheriff and Geldart (1995)). Such outbursts, e.g. caused by someone walking along the profile, have large amplitudes and would add up constructively during the stacking. Generally, the diversity stacking algorithm down-weights big and up-weights small amplitudes, therefore an amplitude normalisation should be applied before the stacking. Now, by the introduced normalisation the scaling of every second and third trace is dependent on every first trace of a triplet. Therefore, after the stacking an overall scaling factor must again be applied to each stacked trace to diminish the dependency of the choice of the first trace as reference. The overall scaling factor is computed by

$$OSF_i = \frac{3^2}{\sum_{k=1}^{3} sc_k} \qquad \text{with } i = 1, 2, ..., ntr. \qquad (4.2.3)$$

A beneficial data normalisation before the stacking helps to increase the signal-to-noise ratio and ensures a coherent signal throughout the whole seismic section. Figure 4.2.3 show the comparison between data that were normalised prior to the diversity stacking and data that were not normalised before the diversity stacking. It becomes obvious that the previously normalised data show an increased amplitude throughout the whole seismic section, especially in the z-component data (Fig. 4.2.3) between traces 30 and 40 (0.07-0.12 s) this processing strategy shows its strength compared to the other strategy. Here, the amplitudes become only visible because of the normalisation before the stacking.

4.2.4   Rotation

One shot consists of two or three inclined hammer strikes normal to the wedge's sides. Because of the inclination of the sides of the wedge the generated motions have a vertical and horizontal component. Translating this into wave characteristics, the excited wave has a P-wave (vertical) and S-wave (horizontal) component right from the beginning of excitation. To separate the wave field into pure P- and pure S-wave energy a rotation of the data was performed as it was suggested by Schmelzbach et al. (2016). Therefore two opposing inclined hammer strikes were rotated under the angle ϕ into one vertical and one horizontal hammer strike (Fig. 4.2.4).
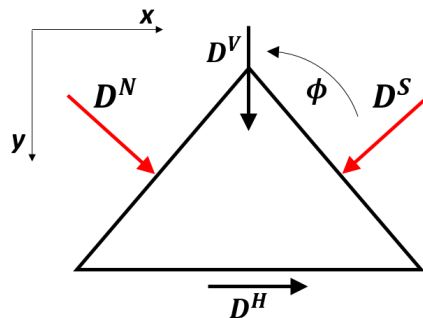
Figure 4.2.4: Rotation of two opposing inclined hammer strikes in North (D^N) and South (D^S) direction into vertical (D^V) and horizontal (D^H) direction

Figure 4.2.3: Comparison of non-normalised diversity stacked data (blue) and normalised diversity stacked data (black) for EP 1 and z-component

The data can be rotated with the rotational matrix of the kind

$$\begin{bmatrix} D^V \\ D^H \end{bmatrix} = \begin{bmatrix} \cos\phi & \sin\phi \\ -\sin\phi & \cos\phi \end{bmatrix} \begin{bmatrix} D^S \\ D^N \end{bmatrix} \tag{4.2.4}$$

where D^V and D^H are the vertically and horizontally rotated data and D^S and D^N are the inclined data in South and North direction, leading to a set of equations as

$$D^V = \cos\phi \cdot D^N + \sin\phi \cdot D^S \tag{4.2.5}$$

$$D^H = -\sin\phi \cdot D^N + \cos\phi \cdot D^S \tag{4.2.6}$$

The angle ϕ is 45° and therefore $\cos(45°) = \sin(45°) = 1/\sqrt{2}$, resulting in a simple scaling of the data D^N and D^S of the kind

$$D^V = 1/\sqrt{2} \cdot D^N + 1/\sqrt{2} \cdot D^S = 1/\sqrt{2} \cdot \left(D^N + D^S \right) \tag{4.2.7}$$

$$D^H = -1/\sqrt{2} \cdot D^N + 1/\sqrt{2} \cdot D^S = 1/\sqrt{2} \cdot \left(D^S - D^N \right) \tag{4.2.8}$$

Now, following the theory, the addition of data enhances P-waves and suppresses S-waves and

vice versa, the subtraction of data enhances S-waves and suppresses P-waves. Concerning the theory, P-wave energy dominates the vertically rotated data and S-wave energy the horizontally rotated data. The overall result of the rotation should be the separation of wavefields, meaning that mostly all of the P-wave energy should be concentrated on the vertical component, SV-wave energy on the inline horizontal component and SH-wave energy on the crossline horizontal component. This effect is expressed by increased and decreased amplitudes. Generally an amplitude decrease after the rotation means that this phase was dominated by another component beforehand and vice versa for an amplitude increase.

In Fig. 4.2.5 one example of shot point 1 is shown, non-rotated and rotated. The source was an 45° inclined hammer strike on the prismatic wedge's side in profile direction (inline), x- and z-components are the recorded receiver components, respectively. After the rotation, the source excitation direction should be purely vertical or horizontal. The comparison of non-rotated and rotated data shows differences in the seismogram sections, which can be summarised with amplitude increase or decrease. The increase of amplitudes boosts the coherency of phases or the separation of two merged and overlaid phases to two more distinct ones. This increased amplitudes can be clearly seen in the z-component data. Especially the first arrivals benefit from the rotation, but not only. E.g. the phase between 80 to 120 m and 0.12 to 0.19 s seems to be more coherent and pronounced than before the rotation. The phase below (from 0.19 to 0.2 s) becomes "leaner", maybe due to the separation of merged phases to one coherent phases. However, the x-component data seem to benefit less from the rotation than the z-component data, but nevertheless show also differences when compared with each other. Here not only increased amplitudes can be discovered, but also phases that "vanish" after the rotation, e.g. between 40 to 60 m and at approx. 0.15 s and between 65 to 100 m and at approx. 0.11 s. Maybe these phases were influenced by P-phases before the rotation that are now diminished. Hence, the rotation of data promises a better, incipient separation of wavefields and is therefore included in the data preparation work flow.

4.2.5   Spectral Analysis

An important step in data preparation is the spectral analysis of the data and noise to determine the signal-to-noise ratio and which offsets should be considered for the inversion later on. First, all data are separated into four offset bins (1-10 m, 10-30 m, 30-70 m and 70-140 m), resulting in 477 traces in range 1, 817 traces in range 2, 1228 traces in range 3 and 638 traces in range 4. All these traces were individually Fourier transformed into the frequency domain, yielding the amplitude spectra for each trace. Then the mean amplitude spectra for each frequency interval ($\Delta f \approx 2\,Hz$) was calculated as shown in Fig. 4.2.6 (upper panel). To determine the noise level, normally the noise before the first arrival is considered. However, during our survey 5 noise records distributed over the day were recorded only for the purpose of noise estimation. Since the study area is located in an active pit mine those noise measurements are reasonable. Now there are two ways of how to proceed with those

noise records. The first option is to simply transform each trace into the frequency domain and calculate the mean amplitude spectra how it was done with the signal data (Fig. 4.2.6 (upper panel, black dashed line)). Another more reasonable way is to treat the noise as the signals, thus applying all processing steps to the noise records (Fig. 4.2.6 (upper panel, black dash-dotted line)). In this second approach, only three noise records (from beginning, middle and end of the day) were considered. They were normalised with respect to every first trace of the triplet, diversity stacked and then again overall scaled as it was done with the data explained in the previous sections. The only thing that is not necessary is the rotation, since the noise was not excited in any specific direction. To perform such kind of processing to the noise makes sense, because during the data processing not only the signals are normalised and stacked, but also the noise content in the data. Thus, to compare signals and noise it is just naturally to apply the same processing to the noise as to the data. In order to determine the signal-to-noise ratio, the mean amplitude spectra for each offset bin was divided by the mean amplitude spectra of noise for each frequency bin, following the equation

$$S/N = \frac{A_{i_{signal}}^2}{A_{i_{noise}}^2} \tag{4.2.9}$$

where $A_{i_{signal}}$ and $A_{i_{noise}}$ are the mean spectral amplitudes of the ith frequency interval of the signal and noise, respectively.

Looking at the upper panel of Fig. 4.2.6 all mean amplitude spectra for the considered offset bins for each source-receiver combination important for this survey (P-zz, SV-xx, SH-yy) and both noise levels are plotted. In the lower panel of Fig. 4.2.6 the corresponding signal-to-noise ratios are shown. Ratios plotted with a solid line are calculated by using the unprocessed noise records, ratios plotted with a dashed line are determined by using the processed noise records for calculation. It is not surprising that the previously normalised noise level is a bit higher as the unprocessed noise level, due to the normalisation and therefore the increase of amplitudes before the stacking. This increased noise level leads consequently to an overall lower signal-to-noise ratio. However, in a frequency range of 30 to 155 Hz the mean signal amplitude spectra and the mean noise spectra are well separated, regardless for which noise level or offset bin. For frequencies higher than 155 Hz and offsets larger than 30 m the mean signal amplitude spectra converge to the mean noise spectra. This frequency range shows also the highest signal-to-noise ratios for all offsets (lower panel of Fig. 4.2.6). The Nyquist frequency of 500 Hz is given by the sampling rate of 1 ms that was set during the measurement, but actually no reasonable signal is recorded at more than 400 Hz, which is due to the technical properties of the recording system that is capable to sample the signal reliable to $0.8 \cdot$ Nyquist (DMT (2017)).

These results are not satisfying at all. The influence of the cavity should theoretically be significant at higher frequencies, because shorter wavelengths are needed to detect such a small anomaly. Lower frequencies cause long wavelengths that could have too low resolution

capacity. Also longer offsets are preferential, because of the deeper penetration depth. Signals within short offsets are not influenced by the subsurface cavity and therefore do not carry useful information for this study. Now that the noise-level is as high as the signal-level at higher frequencies and longer offsets, signals influenced by the cavity may be covered by noise. The used source may generate high-frequency signals, but those signals are too weak to significantly separate from noise. Nevertheless, the data acquired with this survey can be used to get a rough velocity estimate of the survey area in order to synthetically examine the influence of a cavity on the wavefield.
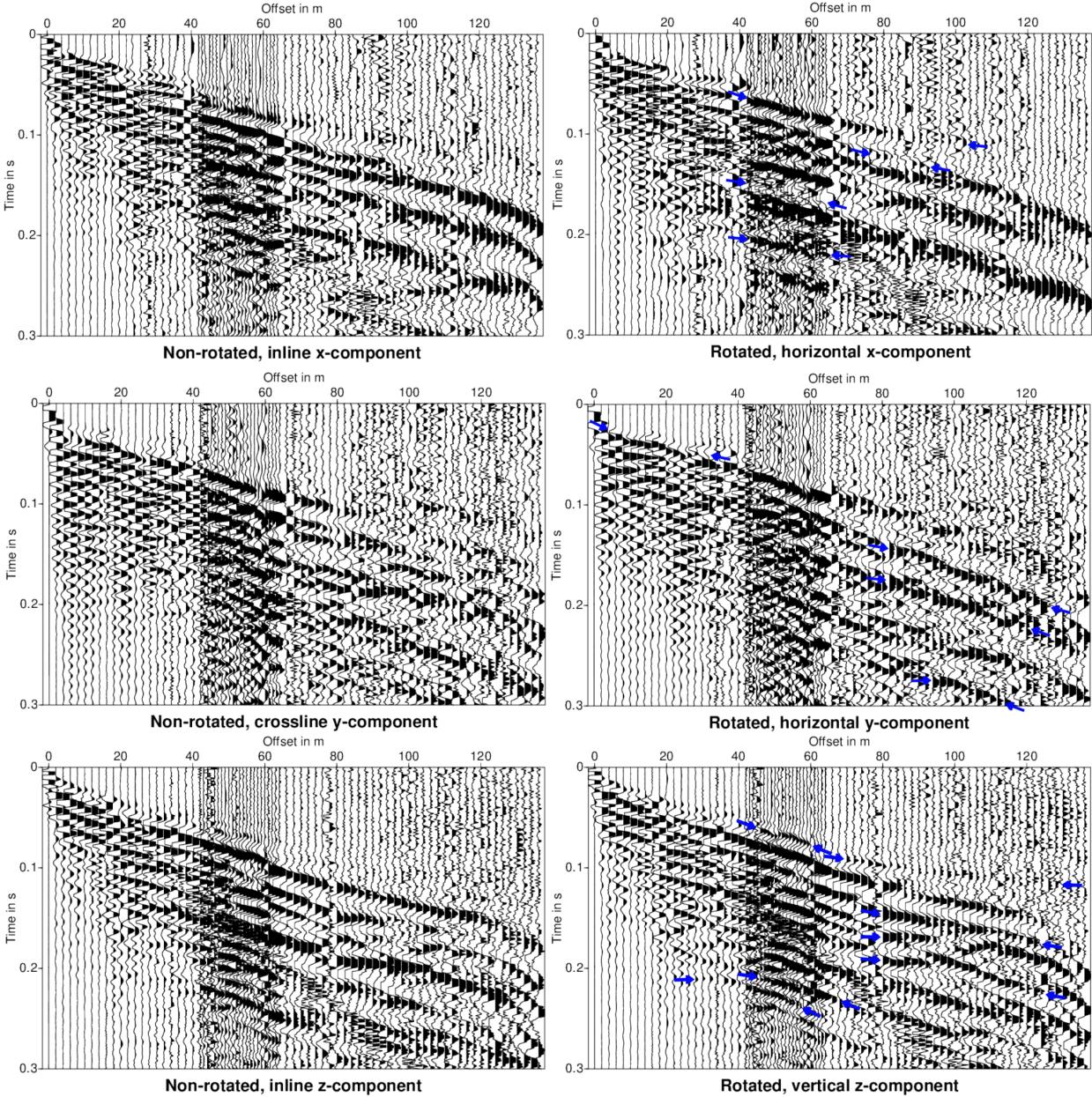
Figure 4.2.5: Comparison of non-rotated (left) and rotated (right) data for Shot point 1; x-receiver component (upper panel), y-receiver component (middle panel) and z-receiver component (lower panel); blue arrows mark beginning and end of phases that have been changed due to rotation; source excitation was $45°$ inline for x- and z-components and $45°$ crossline for y-components
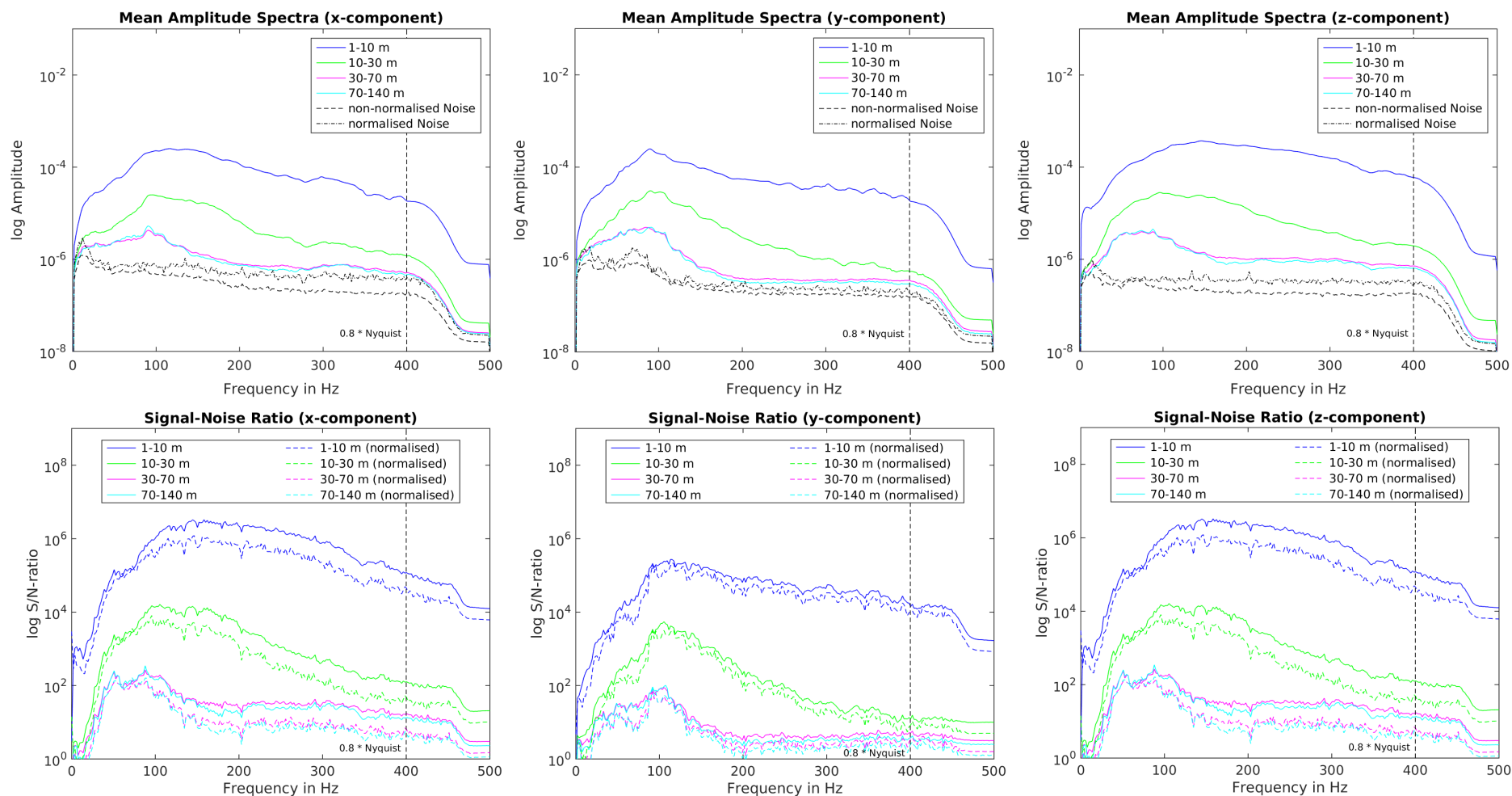
Figure 4.2.6: Upper panel: mean amplitude spectra of x-component (left), y-component (middle) and z-component (right) data; lower panel: signal-to-noise ratios for x-component (left), y-component (middle) and z-component (right) data; data are organised in offset bins of 1-10 m (blue), 10-30 m (green), 30-70 m (magenta) and 70-140 m (cyan), dashed black line is noise level, dash-dotted line is normalised noise level, dashed line marks the system's limitation of sampling frequency

4.2.6 Velocity Analysis

Another important physical property for the later performed modelling is the determination of velocities. There are two ways, of how the velocities in this chapter are determined. First, by literature research and second, by geophysical measurements. The first approach is very general, but serves as a good first guess. Therefore, the identified geological units from the geoelectrical resistivity measurements conducted by Sladky (2018) are linked to their seismic characteristics taken from literature (Tab. 4.2.1).

Table 4.2.1: P- and S-wave velocities for identified geological units from literature (Schön (2011))

Geological Unit	$v_p[m/s]$	$v_s[m/s]$
uncon. rock fragments, gravel	300-2000	100-300
betwixt schist		
parallel	4100-6250	2650-3680
perpendicular	3450-6080	1900-3450
ore body (Ankerit, Siderit)	6960	3590
Porphyroid (Rhyolith)	4200-5850	2600-3250
Limestone	3700-6250	2000-3700

The second approach is more sophisticated, but is characterized by the underlying uncertainties a geophysical measurement by nature possesses. Nevertheless this should serve also as a good initial guess to characterize the subsurface of the test site. In Fig. 4.2.7 three shots are shown that were taken for a first velocity estimate. The following table summarises the results.

Table 4.2.2: Summary of velocity estimates

	$v_1[m/s]$	$\bar{v}_2[m/s]$	$v_2[m/s]$	Depth [m]
EP 1	435	2222	1700	6.8
EP 25	680/730	1382/1303	-	1.6/1.8
EP 40	504	1875	1533	6.1

The true velocities and depths for the second layer were calculated between EP 1 and EP 25, and EP 25 and EP 40. Those velocities are too low for bed rocks and are more in the range of consolidated sediments. One explanation could be the fracturing of the rock (Schön (2011)), which is also sometimes visible at the surface where big cracks migrated to the surface. The heavy fracturing of the bed rock is not surprising since the tunnel excavation and the open pit mining weakened the rock. One can see, that the velocities for the first layer vary strongly laterally, with a very low velocity of 435 m/s in the North of the profile, intermediate velocities of 680 m/s to 730 m/s in the middle of the profile and again lower velocities of 504 m/s in the South of the profile. Those velocity variations can be expected, because the whole tier was flatten with unconsolidated rock fragments that may be differently

compacted. Also an area of increased wetness in the North was identified and clearly visible at the surface that could lead to those decreased velocities. The high velocities are also not surprising and are generated due to the bed rock that is exposed at the surface. The depth of 1.6 and 1.8 is in good accordance to the layer depth of unconsolidated rock fragments identified by Sladky (2018) in the geoelectric resistivity measurements. A layer depth of 6 m might indicate a second layer, because that is probably too thick for a layer of unconsolidated rock fragments just to flatten the tier.
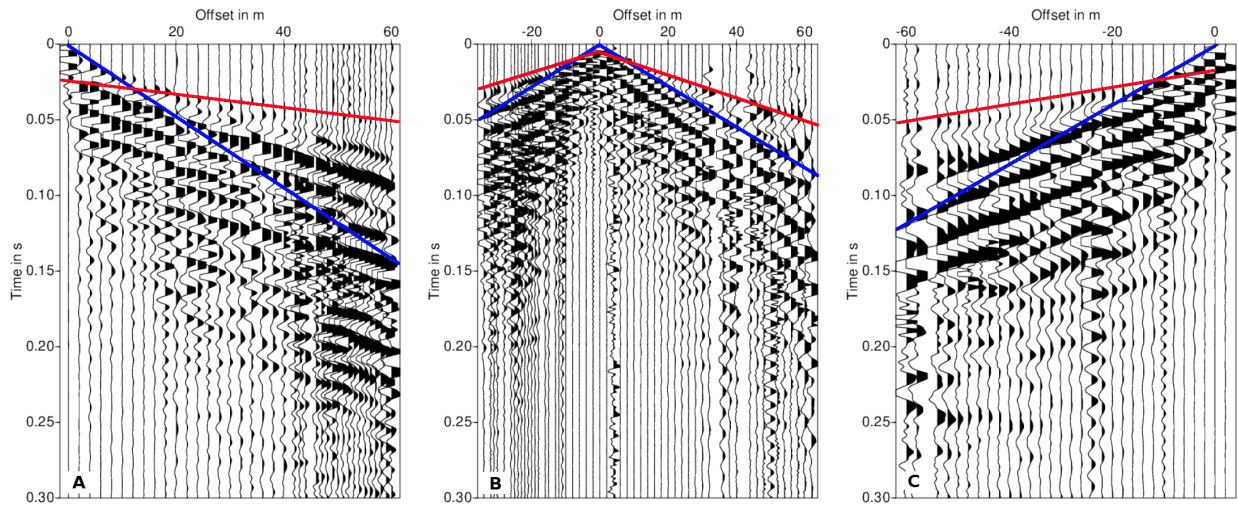
Figure 4.2.7: Three shots (vertical z-component) taken for velocity analysis; A) EP 1; B) EP 25; C) EP 40; blue lines mark direct phase, red lines mark refracted phase; EP 1 and 40 are 200 Hz LP-filtered

4.3   Survey 2: Explosives

4.3.1   Field Measurements: Explosives

Since the signal-to-noise ratio for greater offsets of the first survey is not satisfying at all (comp. Fig. 4.2.6) a second survey on Monday 15.10. and Tuesday 16.10.2018 with a different source was conducted. This time the source were small explosions (so called "Buffalo Gun" (Pullan and MacAulay (1987))). Two different systems were deployed along the profile, the Summit X One that was also used during the previous measurements and the Sercel 26 e-Unite. 75 vertical receivers for the Summit and 75 3-component receivers for the Sercel were installed with a receiver spacing of 2 m and a more densely spaced area of 1 m above the suspected cavity between profile meters 48 and 68. Shot positions were placed every 8 m. This time the whole profile was 128 m and therefore 8 m shorter than in the previous survey. This shortening of the profile length was due to the ongoing construction work for the "Zentrum am Berg" (ZAB) on the lower tier Dreikönige (Galler (2016)). During the construction the tier was shorten for several meters to introduce a supply floor between the Schuchardt tier and the Dreikönige tier. The construction work was also the dominant noise

source during the measurements, because dredgers and other heavy vehicles were driving around the tier. Fig. 4.3.1 shows the northern construction site from the Schuchardt tier. Since the installation of pure vertical receivers for the Summit X One acquisition system provides limited information due to its one-dimensionality, the data were just used to compare noise levels between both surveys in 2016 and 2018. For the following subsections the data from the Sercel 26 e-Unite acquisition system were used exclusively (see Appendix A).

Figure 4.3.1: View from the Schuchardt tier in northern direction down to the construction site at tier Dreikönige

For the explosive sources 60-80 cm deep boreholes had to be drilled. The borehole cuttings once again showed the strong lateral variation of lithologies. The cuttings showed three different colours, ranging from white, bright grey (Fig. 4.3.2, left) to reddish brown, ochre (Fig. 4.3.2, middle) to dark reddish brown (Fig. 4.3.2, right). Comparing these cuttings to the geology from the literature (comp. section 4.1.1.2) and the identified lithologies displayed in Fig. 4.1.6 the white, bright grey cuttings are carbonates, the reddish brown, ochre cuttings are from the ore body and the dark reddish brown cutting are from the siderite ore body.

4.3.2   Spectral and Noise Analysis

Both surveys, in 2016 and 2018, were conducted in an open pit mine where seismic noise was produced at each time of the day from heavy vehicles and mining activities. Even when the survey area was located in a closed down part of the mine, the noise coming from the mining activities was still strong enough to have an significant influence on the data and especially on the signal-to-noise ratio. During the second survey, not only these mining activities were present, but also the noise from the construction work for the near-by ZaB. A comparison of the noise levels for both surveys (Fig 4.3.3) show that the noise level from the second survey was higher than the noise level from the previous survey. This is true for frequencies of up to 250 Hz. For frequencies higher than that, the noise level was equally high and even a bit lower for the second survey for frequencies higher than 320 Hz. This comparison is quite

Figure 4.3.2: Borehole cuttings from the boreholes drilled for the explosive sources showing three different coloured lithologies ranging from white, bright grey (left) to reddish brown, ochre (middle) to dark reddish brown (right)

reasonable, since the noise produced from the mining activities during the first survey were farther away and therefore higher frequency noise was attenuated. During the second survey the source of noise was very near and produced strong low-frequency noise.
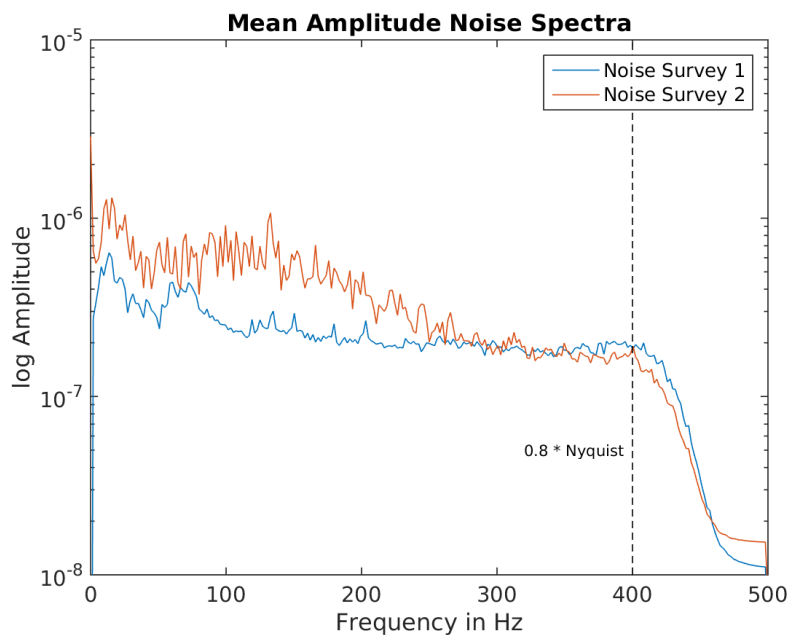
Figure 4.3.3: Noise level comparison of both surveys; used were z-component data measured with the Summit X One during the day

In order to evaluate the signal quality in the presence of noise from the construction site, the mean amplitude spectra for the explosive shots and noise records were calculated (Fig. 4.3.4). The shots were organised in five offset bins between 3-5 m, 6-15 m, 16-30 m, 31-70 m and 71-128 m, respectively. These offset bins become larger with farther offsets and were chosen in

that way to better capture the attenuation behaviour within the close vicinity of the sources. During the day several noise measurements were conducted. Care was taken to ensure that nobody was walking or working along the line to avoid noise peaks within the data and to record the ambient noise exclusively. Looking at Fig. 4.3.4 (upper panel) it becomes obvious that the x-component signal is very well separated from the noise for offsets until 30 m. For greater offsets, the signal-to-noise ratio becomes one for frequencies higher 200 Hz. However, the signals recorded at the z-component seem to be very well separated from the noise for all offset ranges and at all frequencies. Also all spectra show a maximum amplitude at roughly 45-50 Hz, which is the dominant frequency generated by the chosen source. For offset ranges greater than 16 m the amplitude decay with frequency is very dominant and indicates strong attenuation in the subsurface. In the following chapter the data were used to conduct a P-wave travel-time tomography to get a sophisticated underground model, which was then used as the initial model for the following synthetic studies. The synthetic studies help on the one hand to approximate an appropriate Q-factor, and therefore an estimation about the attenuation, and on the other hand to understand what phases of an underground cavity can be expected to be present in the real data.
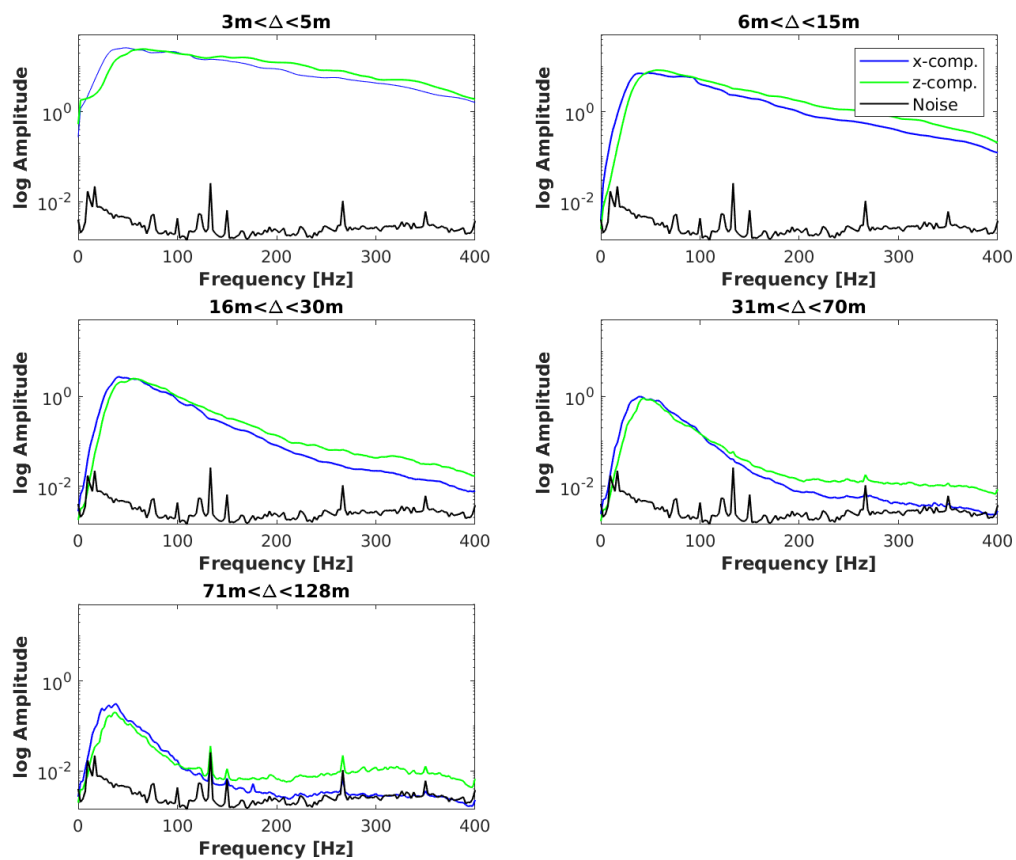

Figure 4.3.4: Mean amplitude spectra of the explosive shots for the x-component (blue graph) and z-component (green graph) and noise records (black graph) organised in offset bins; range 1: 3-5 m; range 2: 6-15 m; range 3: 16-30 m; range 4: 31-70 m; range 5: 71-128 m

Chapter 5

Travel-Time Tomography

In this chapter a first-arrival travel-time tomography is carried out with the explosive data collected during the second survey explained in the previous chapter. First a brief explanation of travel-time tomography is done, afterwards the tomography is carried out for two different starting models. Both models show gradual increasing velocities with depth, one with quite high velocities and one with rather low velocities. This approach serves the purpose of determining an appropriate starting model. Afterwards the inversion is repeated with the determined starting model. Finally the travel-time tomography-model is interpreted and used for the later synthetic studies and inversions.

5.1   Theory

Seismic tomography is a non-linear optimisation problem, since the seismic waves strongly depend on the interaction with the structures that are to be imaged (Evans et al. (1994)). Often the amount of rays covering the desired subsurface is less optimal, that could also lead to an ill-behaved tomography. The travel time tomography was performed with the *simulr16* program (Bleibinhaus (2014), Hole (1992)). The travel times of the forward synthetic wavefield are calculated with a finite-difference Eikonal solver that was first implemented by Vidale (1988, 1990) and further developed by Hole and Zelt (1995) to also account for large, sharp velocity contrasts. The residuals of the calculated and observed travel times are minimised in a damped least-square sense. The updated velocity model serves as the starting model for the next iteration.

5.2   Picking First Arrivals

For the explosion data recorded with the Sercel 26 e-Unite a travel time tomography was performed. Therefore, first arrivals were picked (see Tab. B1 in Appendix B). Previous to the picking of first-arrivals the data had to be time-shifted, because the onset does not coincide with zero-time (see Fig. 5.2.1, left). The reason for that lays in the technical approach of

the time triggering and the usage of the Buffalo Gun. The Sercel 26 e-Unite uses a so called GPS synchronizer that stores the GPS time when a shot is initiated. Since the Sercel records continuously, those time marks are later used by the program as starting times to cut out desired time series. The triggering starts when the electric circuit is closed, which in this case is the moment, when the hammer hits the upper metal pin of the gun. However, the actual detonation of the cartridge happens a bit later, since the metal pin needs some time to slide down, hit the trigger of the cartridge and therefore initiate the detonation. Those time delays would lead to an erroneous travel-time model and have to be corrected beforehand. To correct these time shifts, all shots were carefully inspected and manually shifted to their zero-onset times (5.2.1, right). Generally the time delays were in the range of 0.006-0.009 s. Since the manual picking is very objective, the blast times were inverted too. The inverted and manually picked arrival times were double checked and, if necessary, corrected again.
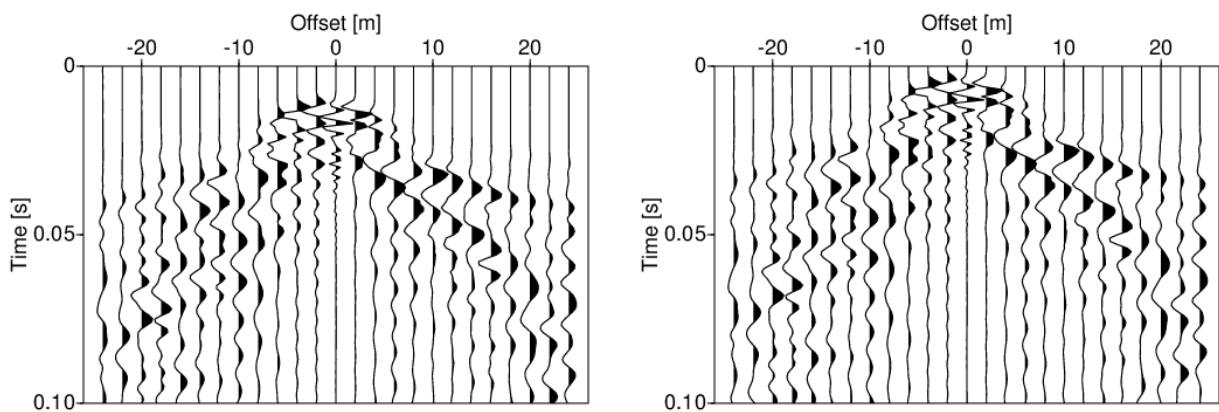
Figure 5.2.1: Uncorrceted EP 4 (left) and time corrected (right)

In total 1018 from 1350 traces were picked, yielding an average of roughly 57 traces per shot, or 75 % of all traces per shot (see Fig. 5.2.2). Also a weighting of offset depending first arrivals was considered. First arrivals within an offset of 70 m were weighted with 100 %, whereas first arrivals with offsets between 70 and 120 m were weighted with 50 %. This was done to reduce the impact of imprecise travel time picks due to the increasing noise level with increasing offset. Erroneously picked travel times influence the inversion result quite seriously, because linearised least-square problems are generally profoundly affected by large data errors (Evans et al. (1994)).
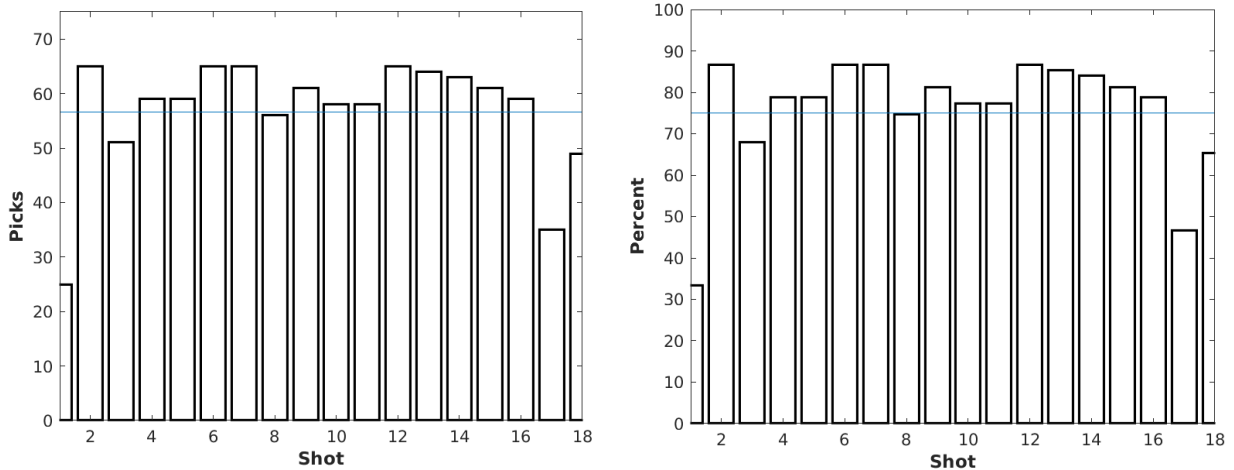
Figure 5.2.2: Pick statistic for first-arrival travel time picks; left: traces picked per shot; right: percent of picked traces; blue line marks average value

5.3 Starting Model Determination

A crucial part of every inversion algorithm is the proper choice of an adequate starting model. There are two approaches of how to determine a proper starting model. One approach would be to begin with a sparse parametrisation of the model, meaning using only few inversion nodes and increasing the number of nodes with each iteration. The second way, and how it was done in the following section, is to start with two, or more, different starting models and see if the inversion of each of the models culminates in one similar inverted model. Here two different starting models were designed, which are referred to as starting model fast and starting model slow in the following. Both starting models show a velocity increase with depth and have the same parametrisation. The difference of both models are the starting velocities. The velocities of the fast starting model range from 1000 m/s to 5000 m/s (Fig. 5.3.2, upper left), whereas the velocities for the slow starting model range from 600 m/s to 4200 m/s (Fig. 5.3.2, upper right). Before the inversion was preformed for each model a damping test was conducted. The corresponding damping curves, or L-curves, are displayed in Fig. 5.3.1. These kind of test helps to determine the correct damping value for the first iterations. A high damping value detains the inversion of big changes in the model, whereas a small damping value allows big model changes, but could also lead to an erroneous introduction of artefacts that could distort the whole inversion. A good choice of a damping value is to take the "knee" of the curve, meaning to chose a value that allows moderate model changes, but remains a relatively small data misfit. In this study, a starting damping value of 200 was chosen for the fast starting model and a value of 1000 for the slow starting model. As a stopping criterion a 95 % F-test was used, that calculates the quotient of normalised chi-squares of two consecutive iterations (Bleibinhaus (2014)).

71
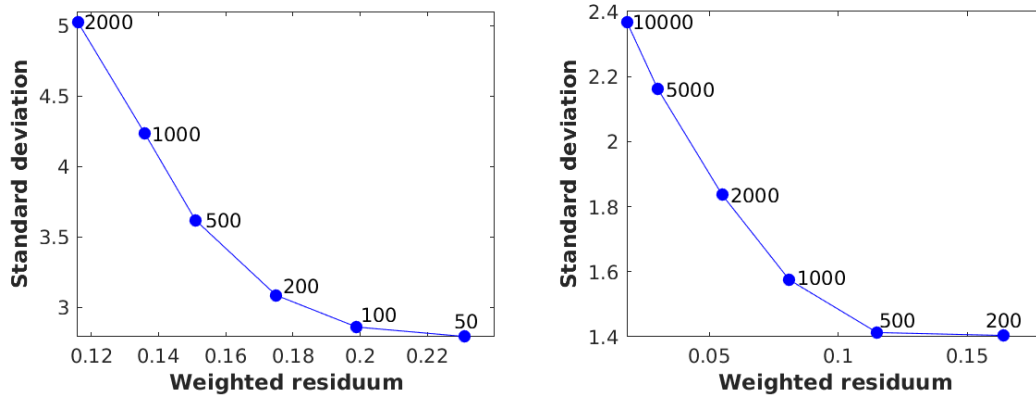
Figure 5.3.1: Damping curves for the fast (left) and slow (right) velocity starting model displayed in Fig. 5.3.2 (upper panel); numbers indicate damping values

The first set of iterations was done until the stopping criterion was reached. The generated model of the last iteration then served as the starting model for the next set of iterations where the damping value was further decreased to allow more model changes. This was repeated until no damping (damping factor 1) was needed. For the fast starting model, the first inversion run took six iterations with a damping of 200, the second run two iterations with a damping of 20 and the last run took one iteration without any damping. For the slow velocity starting model the first run took ten iterations with a damping of 1000, the second took five iterations with a damping of 100, the third took two iterations with a damping of 10 and the last run took one iteration without any damping. The starting and inverted intermediate models are displayed in Fig. 5.3.2. Beside the velocity distribution, another important aspect is the resolution of the inverted models. The resolution models are also display in Fig. 5.3.3. It becomes obvious that the inverted models are reliable until a depth of roughly 27 m and only in the middle of the model. Depths deeper than 27 m or close to the model boundary can not be reliably resolved. This is due to the ray coverage, which do not penetrate the model beyond a depth of 27 m.
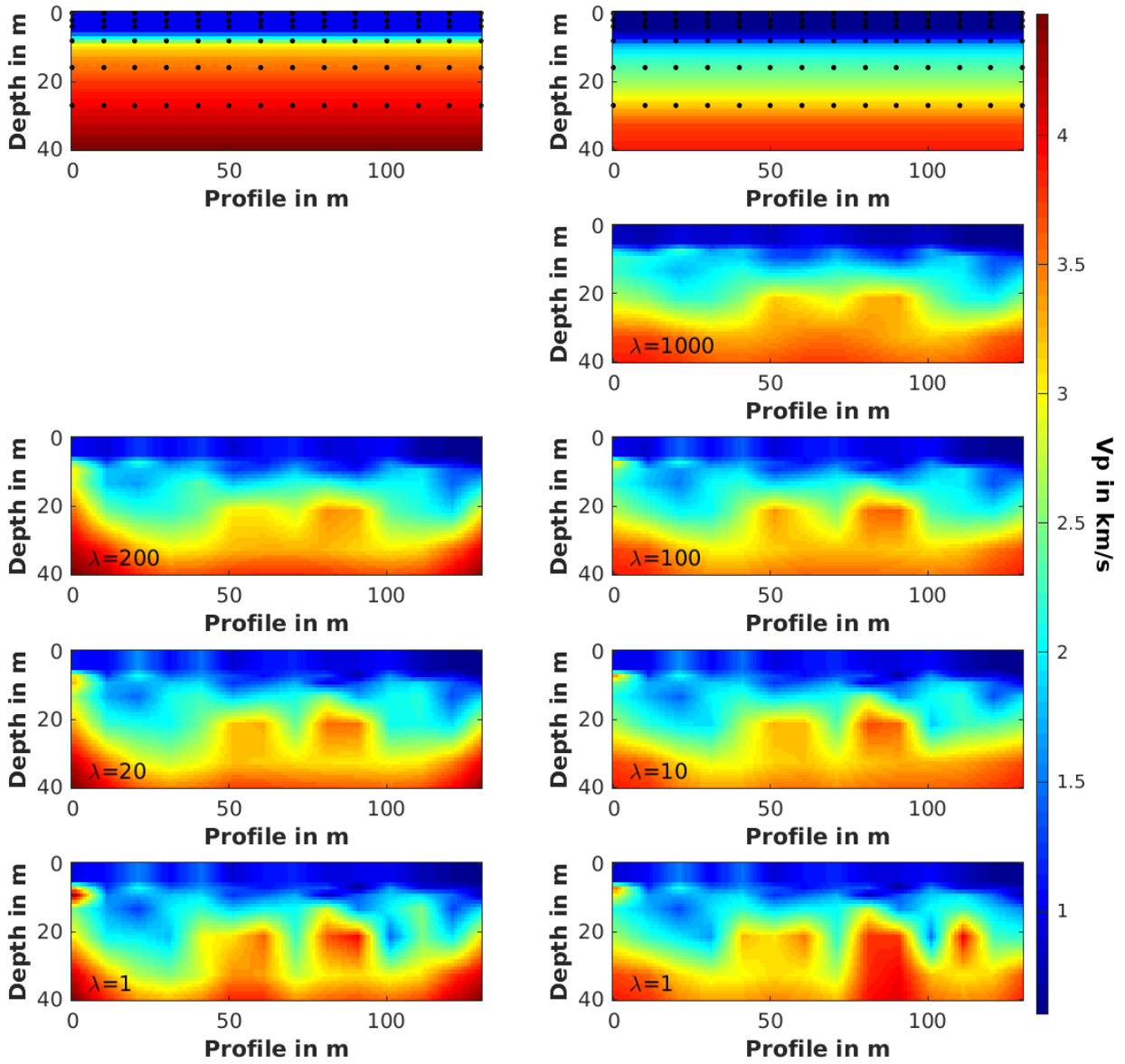
Figure 5.3.2: Starting (upper panel) and inverted models for fast (left) and slow (right) starting models; corresponding damping values are indicated in the left lower corner of each model
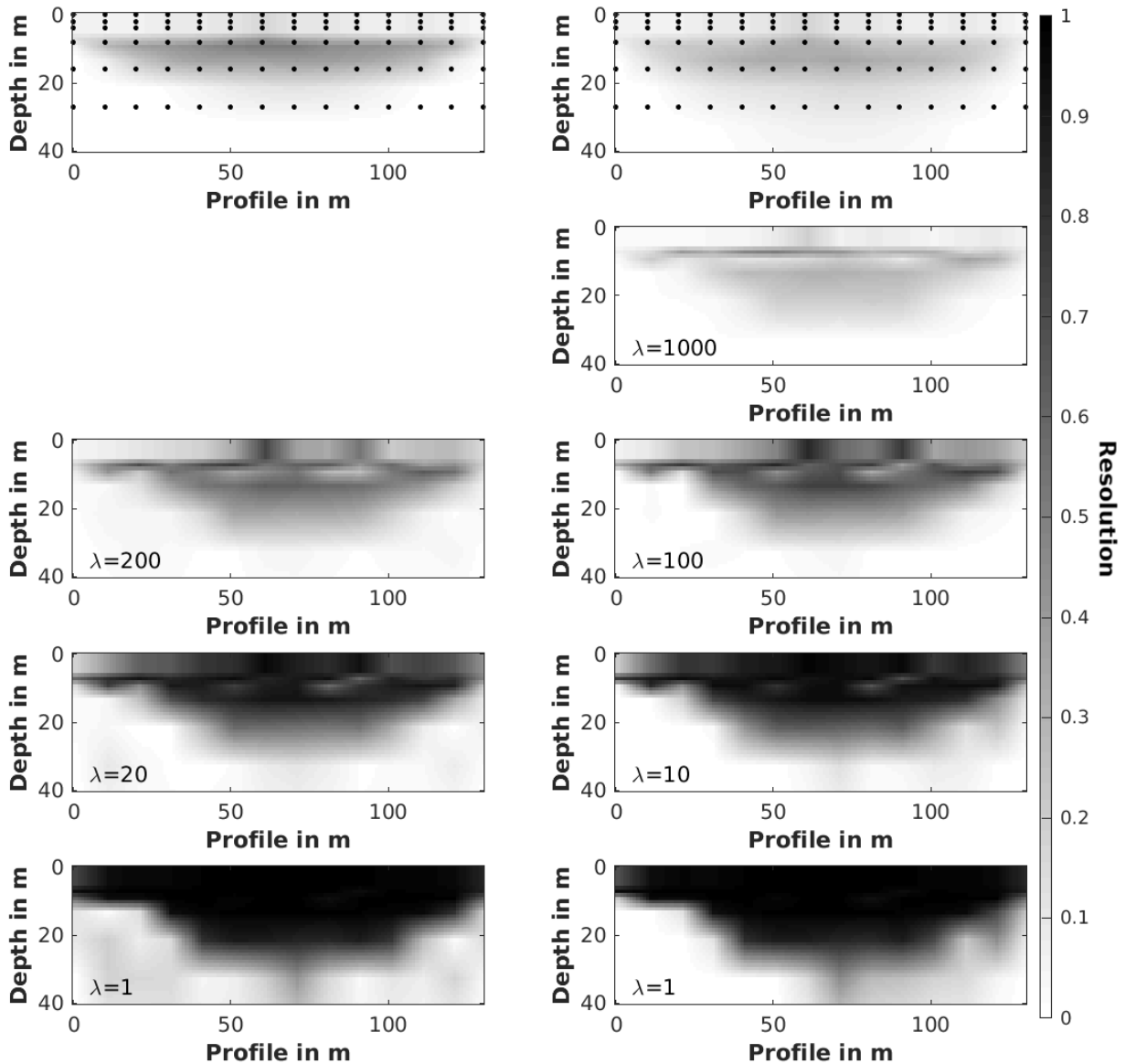
Figure 5.3.3: Resolution models for the starting and inverted models shown in Fig. 5.3.2; black dots mark inversion node positions

5.4   First-Arrival Inversion

For the determination of the best model the weighted data residuum was plotted against the standard deviation for each model (Fig. 5.4.1, green and blue graphs). The best model is a model that shows small model complexity but at the same time still a small data misfit. For the fast starting model, the best choice is the model with a damping value of 200, for the slow starting model, the model with a damping of 100 is the best choice. Comparing both models with each other show some similarities, e.g. the high velocity areas at profile meters 50 and 85 or the low velocity areas at the surface at the right-hand side of the profile, but they also show differences, e.g. the extend of the high velocity areas. In order to design a suitable starting model, the mean velocity of each depth slice of the best model choices ($\lambda = 200$ and

$\lambda = 100$) were calculated. Plotting the mean velocities with depth (Fig. 5.4.2) show nearly the same velocities until the resolution depth of 27 m. The inversion corrects both models to the right velocities, it drastically decreases the velocities from the fast starting model and adjusts the velocities of the slow starting model. This mean velocity distribution with depth (red line in Fig. 5.4.2) serves now as a well constructed starting model (Fig. 5.4.3, upper panel). Again a damping test was performed and different inversion runs with decreasing damping until no damping was needed. The results can be seen in Fig. 5.4.3.
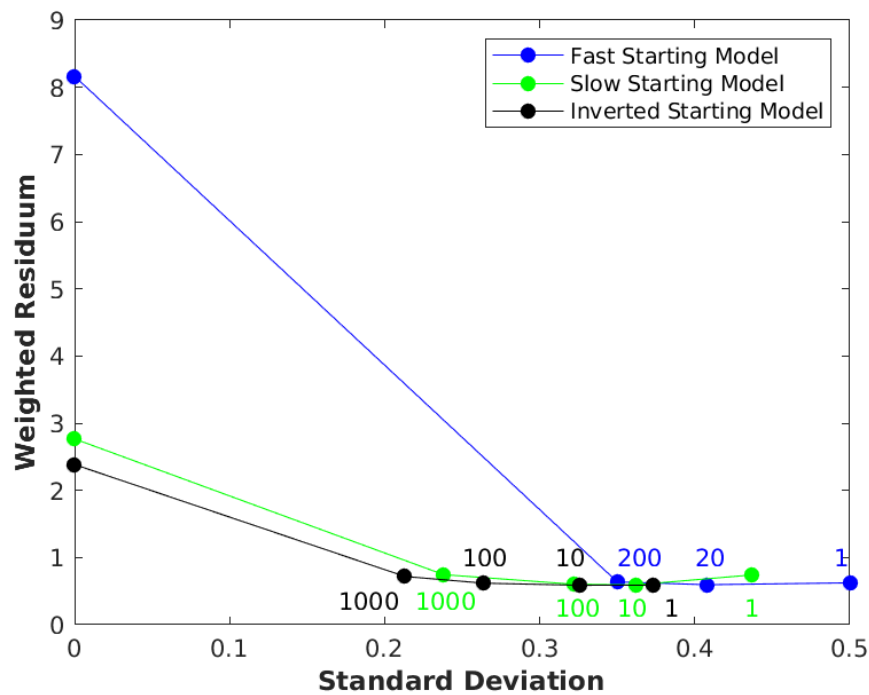
Figure 5.4.1: Model evaluation of inversion stages of the models shown in Fig. 5.3.2 (blue and green lines) and final starting model (black line) with corresponding damping values
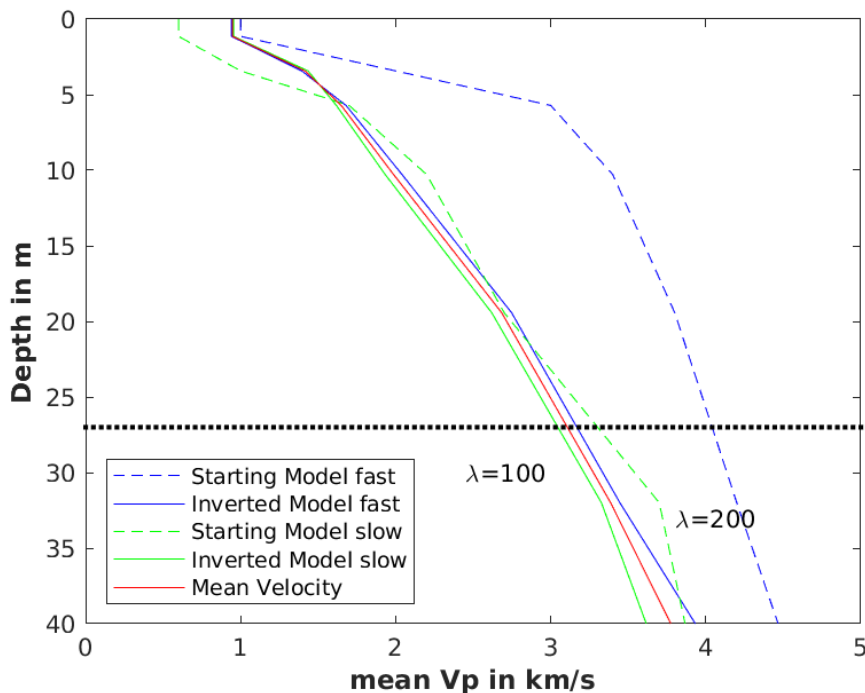
Figure 5.4.2: Mean velocity profiles for the starting models (dashed line, ref. Fig. 5.3.2, upper panel), inverted models (solid line, ref. Fig. 5.3.2) and their mean velocity profile (red); black dotted line marks maximum resolution depth of ray coverage

For the first inversion run seven iterations with a damping of 1000 were performed, for the second run two iterations with a damping of 100, for the third two iterations with a damping of 10 and for the last run one iteration without any damping was done. To determine the best final velocity model, the weighted data misfit was plotted against model complexity (Fig. 5.4.1, black graph). The models with a damping of 100 shows the smallest residuum at fairly low model complexity. Even though the model with a damping of 10 plots nearer to the considered models chosen for the starting model determination (200 blue and 100 green) the data misfit between these two is negligible and that is why the model with a smaller model complexity but nearly identical data misfit is chosen. The resolution capacity in depth is limited by the penetration depth of the rays and the coverage of rays in deeper parts of the model. In Fig. B1 (Appendix B) all shots with their corresponding ray paths are plotted. Except for shot two the ray paths are limited to a depth of approximately 25 m. Since the top of the cavity is expected to be at 25 m depth, this can be a problem in the later inversion for the cavity. However, the rays depicted here are first P-wave arrivals, for the elastic full-waveform inversion later on the whole wavefield is considered. Maybe the full amount of data will still lead to a reasonable inversion result with a distinct cavity.
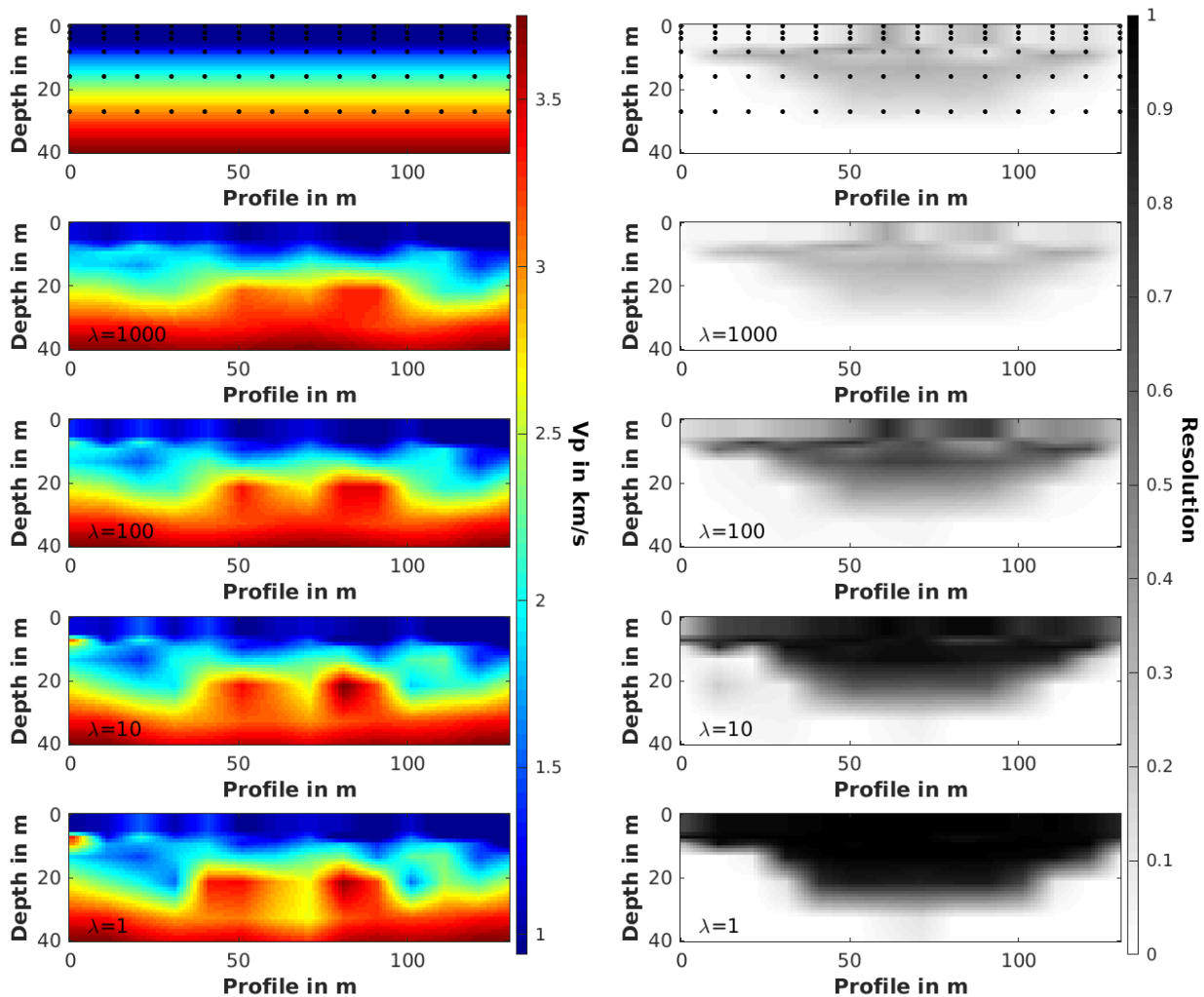
Figure 5.4.3: Starting (upper panel) and inverted velocity models (left panel) and corresponding resolution models (right panel); corresponding damping values are indicated in the lower left corner; black dots mark position of inversion nodes

5.5   Interpretation

The final tomography model depicted in Fig. 5.5.1 shows some structures, that were to be expected or were yet seen in the resistivity model (Fig. 4.1.7). The low-velocity zone at profile meter 10 corresponds to the area of increased wetness, where puddles were present during the first survey. The zone of low velocities from profile meter 110 to the end is due to the vegetation and therefore the unconsolidated soil. The shallow zone of increased velocity at the beginning of the profile corresponds to dry, less-fractured bedrock (comp. Fig. 4.1.7, labelled 2). One of the two high-velocity areas between 40 and 100 m, the right one, corresponds to a dry, less-fractured ore body (comp. Fig. 4.1.7, labelled 4). Generally the velocities are very low compared to what can be expected for ore bodies, carbonates or bed rocks (comp. Tab. 4.2.2). This decrease of velocity could once again be explained by the excavation processes during the mining period and the following weathering of the

rocks. Even though the heterogeneous structure of the subsurface seems to be reasonable, the velocities of these structures could be underestimated. This is a common issue in most tomographic techniques, and is due to the finite number of rays that are present. Therefore the velocities are a spatially averaged versions of the real structure velocities (Hole (1992)).
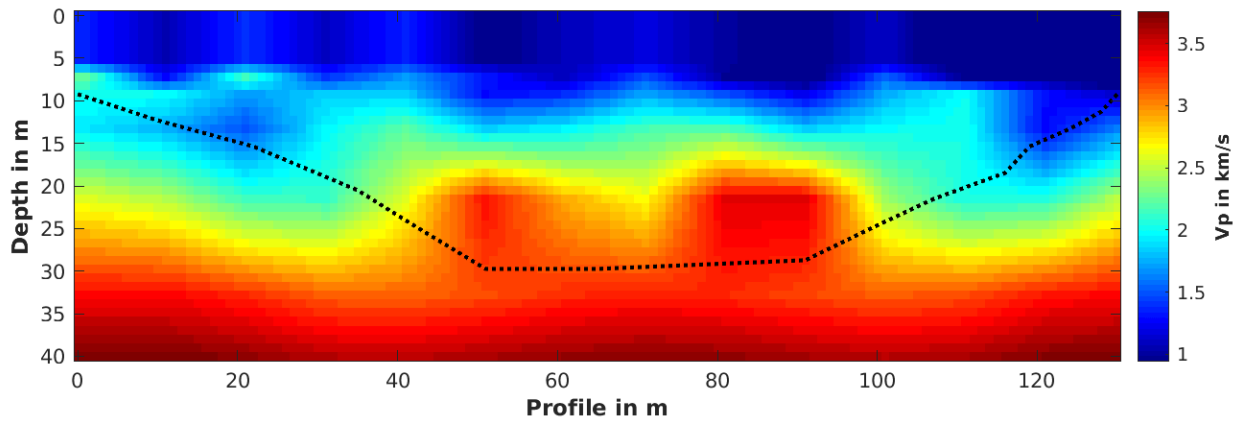
Figure 5.5.1: Final tomography model (comp. model L in Fig. 5.4.3); black dots mark depth of resolution

Chapter 6

Synthetic Studies

In order to evaluate the influence of a subsurface cavity on the data, the P-wave velocity model obtained by travel-time tomography is used as a sophisticated starting model for the following study. The introduction of a synthetic cavity into the model allows a direct comparison of phases that are generated by it. In order to make this comparison eligible, the first step is to determine a source wavelet, that is comparable to the true source. The second step is to match the amplitude spectra of observed and synthetic data, the third step is the introduction of a cavity and the comparison of synthetic data generated with and without the cavity. Finally the synthetic data sets are inverted by applying different inversion strategies that are derived from the synthetic forward study. Those inversion strategies are as follows: strategy A includes a trace killing but no filtering, strategy B includes a trace killing and a low-pass filtering after Bunks et al. (1995) and inversion strategy C includes an offset mute, a time-windowing and a LP-filtering. The inversion results are shown and discussed. The forward calculation as well as the inversions were done with the IFOS algorithm provided by the Karlsruhe Institute of Technology (KIT).

6.1 Forward Modelling of Synthetics with and without a Cavity

6.1.1 Parameters for the Forward Calculation

For the forward calculations the model derived by the travel-time tomography from the previous chapter is considered. In the following table (Tab. 6.1.1), all important parameters that were considered for the forward calculations are summarised.

The perfectly matched layer (PML) boundaries were implemented after Komatitsch and Martin (2007) and Martin and Komatitsch (2009).

Table 6.1.1: Parameter of model set-up and FWD modelling

x/z [m]	136/40
receiver/source	75/18
dx [m]	0.16
nx/nz	875/250
f_{dom} [Hz]	45
dt [s]	2.0E-5
T_{max} [s]	0.42
nsp	21000
Boundaries	free surface, PML

6.1.2 Source Wavelet and Q-Estimation
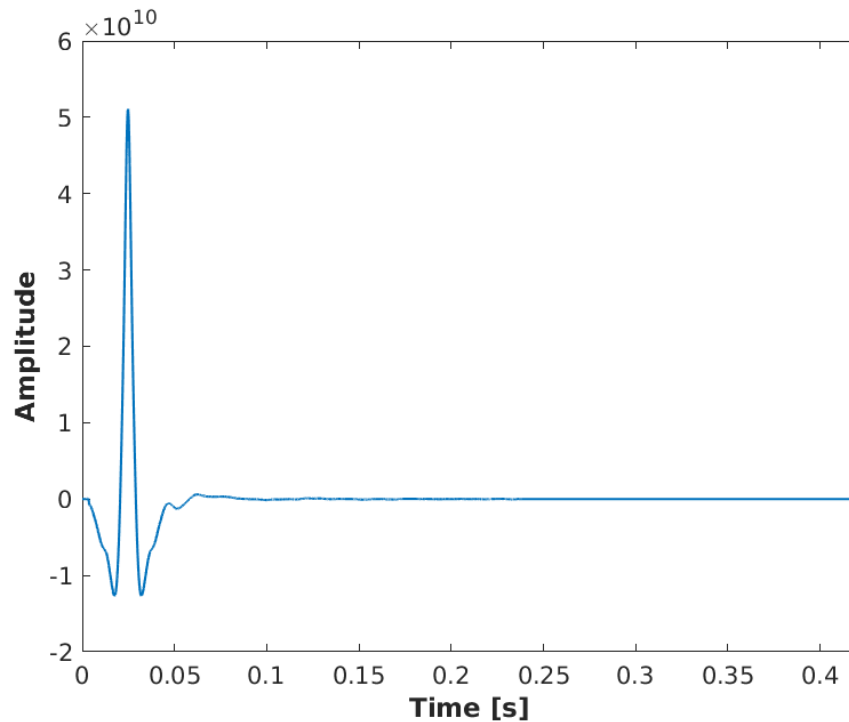
Figure 6.1.1: Determined source wavelet for the synthetic study

First, a proper source wavelet for the synthetic calculations has to be estimated. Therefore the amplitude spectra of the x-component of offset range 2 was Fourier transformed to obtain a wavelet in the time-domain (Fig. 6.1.1). The spectra of this offset range was chosen, because it looks most similar to all other spectra in terms of amplitude decay and maximum frequency. This obtained source wavelet is used as the synthetic explosion source for the forward modelling. The significant amplitude decay in the mean amplitude spectra shown in Fig. 4.3.4 indicates strong attenuation, which might be the effect of fracturing and weathering of the subsurface due to the mining and excavation process in the past.

Comparing the mean amplitude spectra of the real data and the calculated synthetic data based on the travel-time model without attenuation (Fig. 6.1.2) it becomes clear, that a

proper choice of Q is unavoidable. The maximum amplitude of the real data decays drastically with increasing offset, which is not the case for the attenuation-free synthetic data. Also the amplitude decay with increasing frequency is much stronger for the real data compared to the synthetic ones. In order to estimate an appropriate Q-value, different Q-models with a homogeneous Q distribution were taken into the forward modelling process. The Q-model which fits the amplitude decay of the real data best is Q=5. Fig. 6.1.3 shows the comparison of both amplitude spectra, but with the implementation of a proper attenuation. The maximum amplitude decay with increasing offset is still not perfect, but at least the decay with increasing frequency fits the real data nicely. This is the best approximation that can be obtained with a homogeneous Q model. Therefore a Q-value of 5 is considered for the following synthetic study.
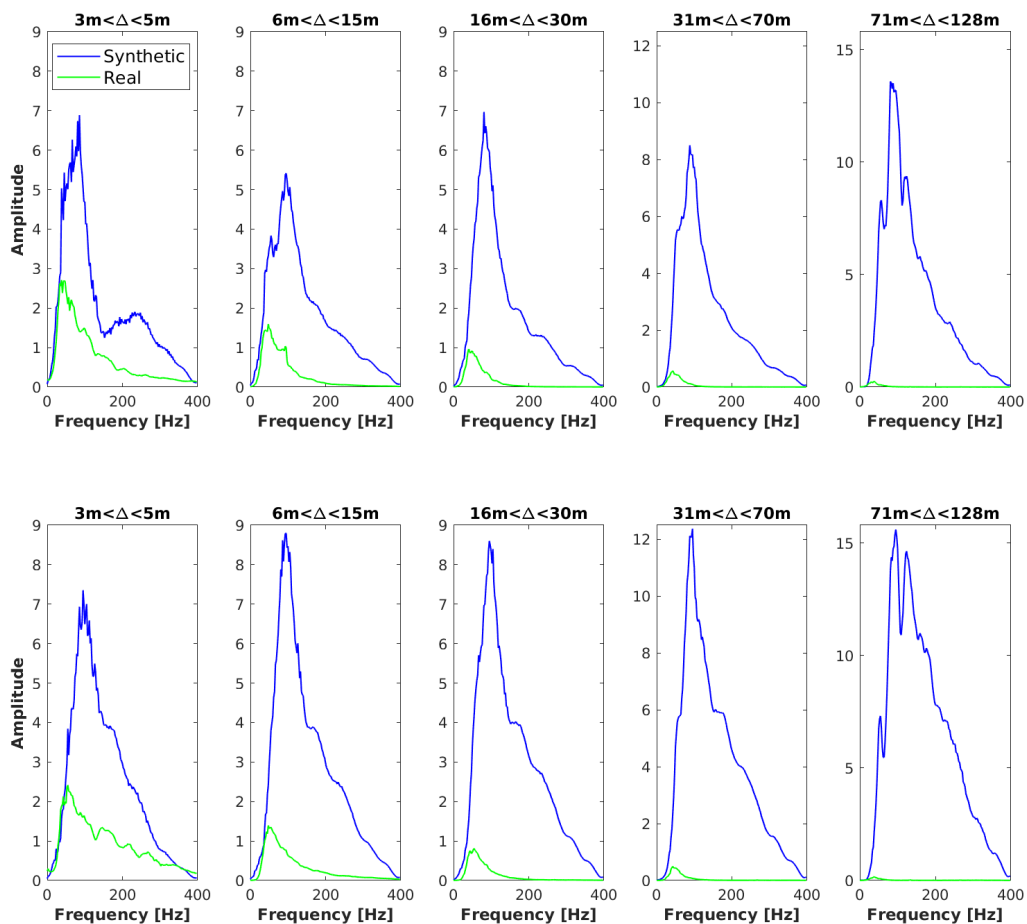
Figure 6.1.2: Mean amplitude spectra for x- (upper panel) and z-component (lower panel) real data (green) and synthetic data (blue) without attenuation, organised in five offset bins; range 1: 3-5 m; range 2: 6-15 m; range 3: 16-30 m; range 4: 31-70 m; range 5: 71-128 m
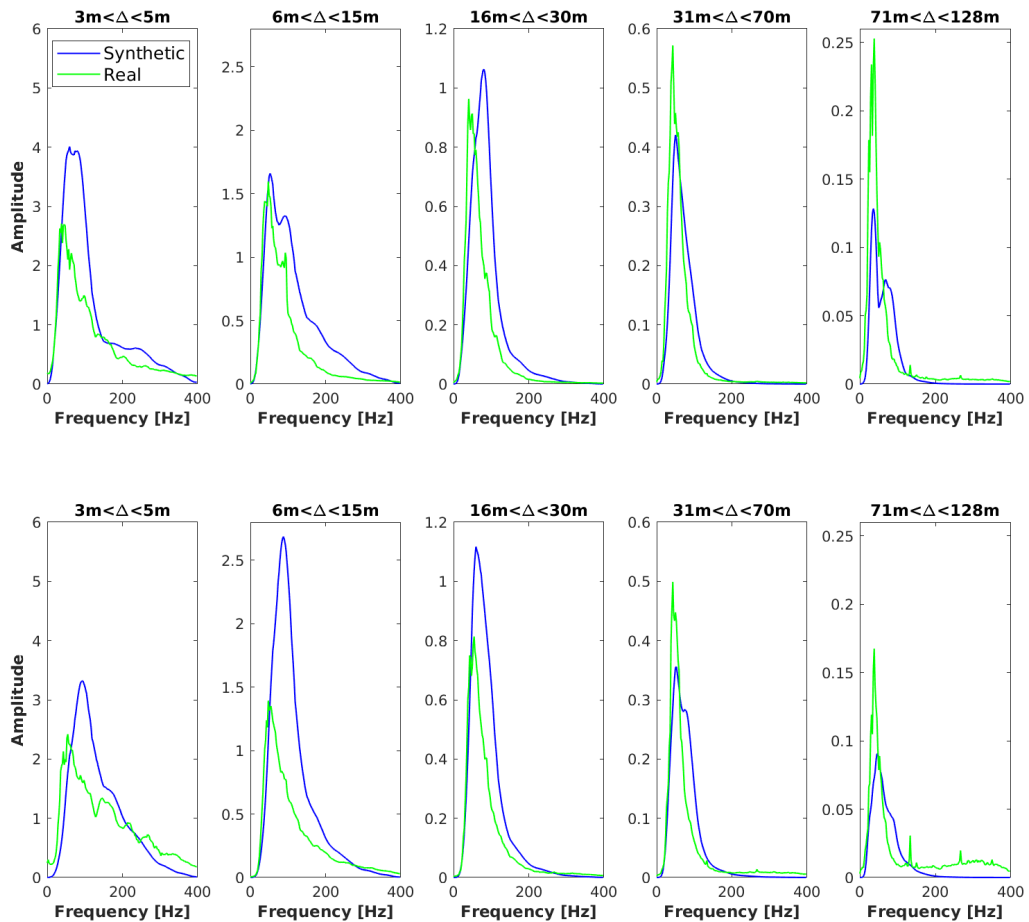
Figure 6.1.3: Mean amplitude spectra for x- (upper panel) and z-component (lower panel) real data (green) and synthetic data (blue) with attenuation (Q=5), organised in five offset bins; range 1: 3-5 m; range 2: 6-15 m; range 3: 16-30 m; range 4: 31-70 m; range 5: 71-128 m

6.1.3 Influence of a Cavity and Determination of Inversion Strategies

In order to evaluate the influence of a subsurface cavity, a synthetic velocity anomaly with the specifications of a (pseudo-) cavity was implemented into the P-wave model derived from the travel-time tomography. To implement a pseudo-cavity (Vs=330 m/s) rather than a true cavity is of pure numerical nature. Very small velocities demand a very small spatial discretisation of the model or the problem of grid dispersion arises. Also would a very small spatial discretisation lead to a small time step (compare Eq. 2.2.18) and therefore a lot of modelling steps that would lead to numerical inaccuracies due to the accumulation of numerical inaccuracies during each forward modelling step (compare Fig. 2.2.2). The comparison of synthetic data calculated without and with the cavity allows a basic understanding of the influence of the cavity on the wavefield. The main questions of this study are, how the cavity influences the wavefield, where become those influences visible and where are those influences

strongest.

Fig. 6.1.4 shows both models, without (left) and with (right) the implemented cavity. Underneath the corresponding synthetic seismograms for the second shot (marked by the black star) are plotted. The differences within the wavefields are hardly visible and here are indicated by the blue arrows. To make the differences more visible difference plots were calculated for all shots (Fig. C1 and C2 in appendix C). The differences caused by the cavity are concentrated and strongest in the area of denser receiver spacing and therefore also in the area of the implemented cavity. What actually cause the differences are the reflections and/or diffractions, respectively. Here those differences are clearly visibly, since the strong amplitudes caused by the explosion source and the ray path effects that are not influenced by the cavity are diminished by the subtraction of both noise-free synthetic wavefields. Also the seismograms are scaled by the biggest amplitude within the plot. Actually they exhibit a difference of one order of magnitude between the shots at the beginning and end of the profile compared to the shots in the centre of the line. The difference amplitudes are strongest for shot ranges 5 to 16.
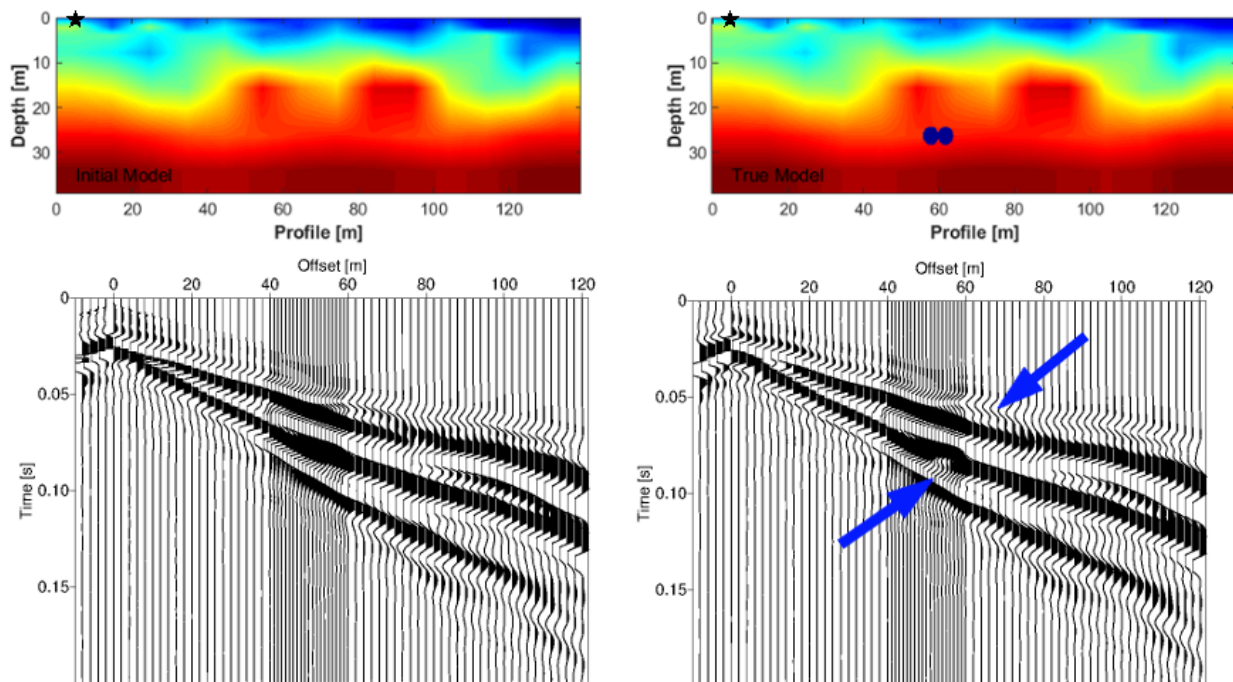
Figure 6.1.4: Upper panel: travel-time tomography model without (left) and with an implemented cavity (right, brown circles), black stars mark shot position; Lower panel: corresponding synthetic seismograms of EP 2, blue arrows mark differences within the wavefield

6.1.3.1   Strategy: Trace killing

To evaluate the differences compared to the complete initial wavefield (modelled without the cavity), the percentage of the differences with respect to the complete wavefield are calculated and shown for two example shots 1 and 10 in Fig. 6.1.5 (for all shots: Fig. C3 in appendix

C). The biggest difference amplitudes are approx. 25 % of the initial amplitudes. Generally the differences increase with increasing offsets. This is reasonable, since the wavefield is strongly dominated by the source amplitudes at and in the vicinity of the source position. In case of shot 10, looking at the difference seismograms, the amplitudes are strongest at offset 0 m and in the surrounding, but the percentage share is nearly zero for the same region. The strong source amplitudes mask the comparable small differences in that region, which become negligibly small. In view of the synthetic inversion, one strategy would be to neglect offsets for which the percentage share of the differences fall below a certain threshold.
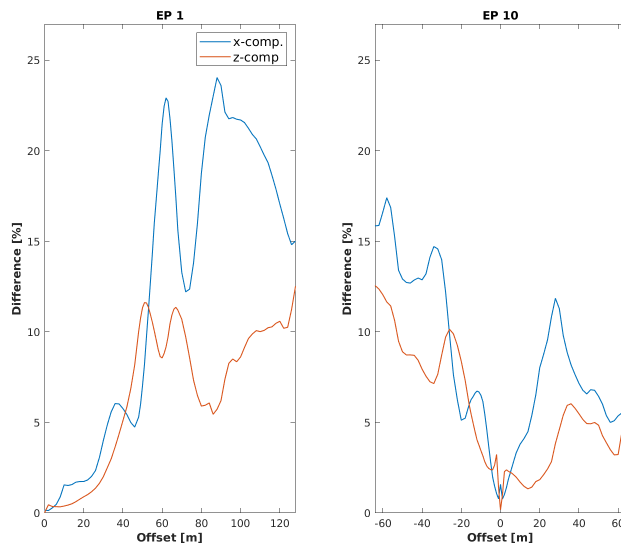
Figure 6.1.5: Percentage of difference amplitudes compared to complete initial wavefield for shots 1 (left) and 10 (right)

6.1.3.2 Strategy: Filtering

The synthetic study allows also an analysis in terms of frequencies. At what frequencies and offsets is the imprint of the cavity strongest? To answer that question gives another sophisticated strategy for the later inversion. Therefore the time-domain data were transformed into the frequency domain by a Fast-Fourier transformation. Afterwards, the difference phase spectra of the frequency-domain initial (data modelled without cavity) and observed data (data modelled with implemented cavity) are calculated. These difference phase spectra are divided into five offset bins, within each offset bin the standard deviation was calculated. The result is plotted in Fig. 6.1.6. A threshold of 30° is considered in order to categorize if a phase shift is significant or not.
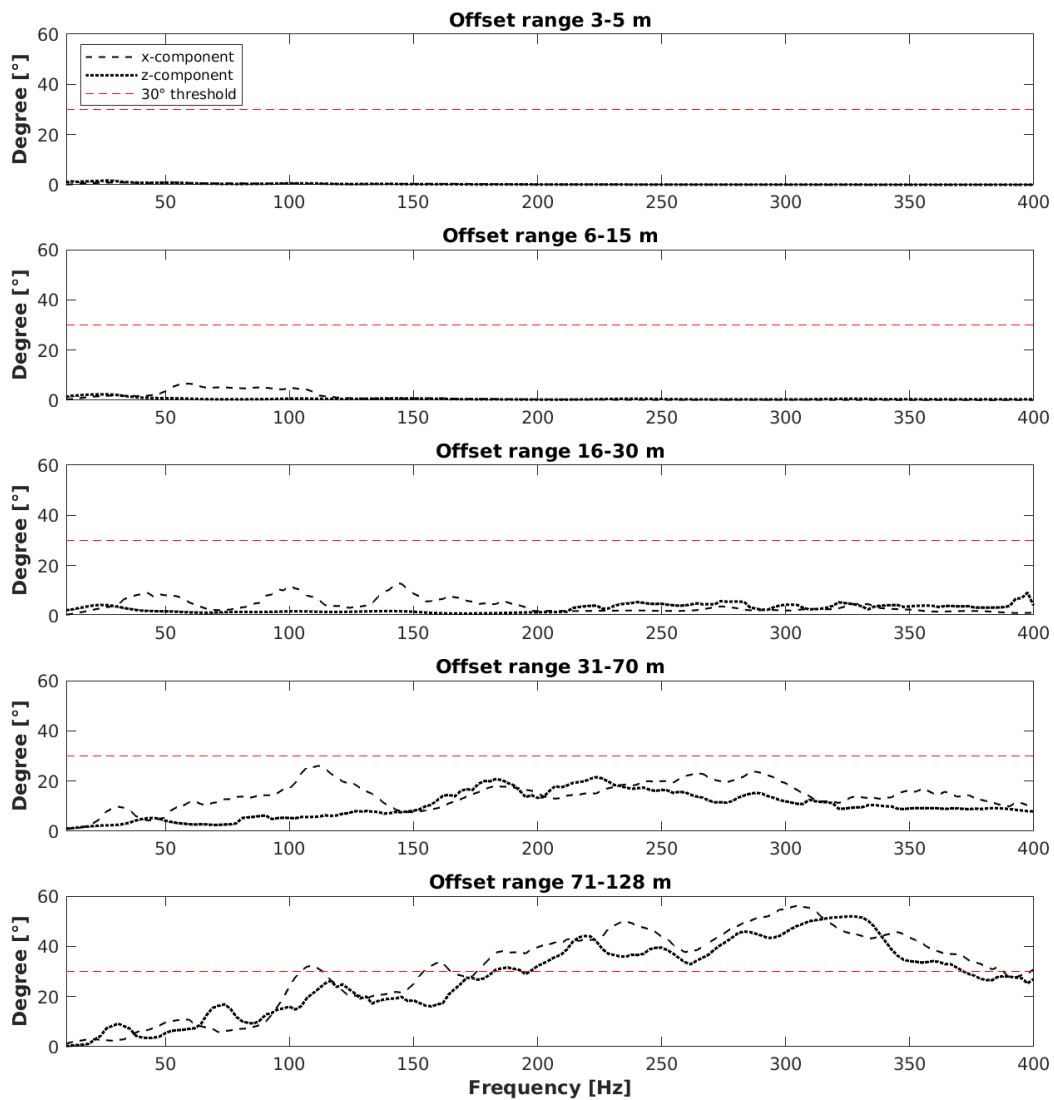
Figure 6.1.6: Phase shifts between initial and observed x-component (dashed line) and z-component data (dotted line); red line marks threshold of $30°$

For the first four offset ranges up to 70 m it is obvious that the cavity does not cause a significant phase shift. The phase differences between the synthetics without and with the cavity do not exceed the threshold of 30°. With increasing offsets, the phase shifts become stronger and more significant. Within the fifth offset range of 71-128 m, the cavity introduces a dominant phase shift of nearly 60° between 200 and 370 Hz in the z-component. This phase shift is already visible from 170 Hz within the x-component. Additionally two peaks are present which exceed the threshold at 110 Hz and 160 Hz, respectively. That the influence of the cavity in terms of a significant phase shift becomes apparent with greater offsets is quite logical, since the waves within that offset ranges have a deeper penetration depth and therefore interact with the deep cavity, whereas the waves within short offsets passes only

shallow penetration depths and do not reach the cavity at all. The fact that a significant phase shift appears only at higher frequencies is also quite consequential, since higher frequencies mean shorter wavelengths. Assuming a 10 m wide area around the cavity and calculating the mean P-wave and S-wave velocity within that area gives 3343 m/s and 1966 m/s, respectively. Since the wavelength λ is determined as

$$\lambda = \frac{v}{f} \tag{6.1.1}$$

with v the velocity and f the frequency, the mean wavelength for P- and S-waves with the specific frequency content derived from Fig. 6.1.6 can be estimated and gives

$$\lambda_{v_p}(f_1 = 350\,Hz) \approx 9.6\,m \qquad\qquad \lambda_{v_s}(f_1 = 350\,Hz) \approx 5.7\,m$$
$$\lambda_{v_p}(f_2 = 270\,Hz) \approx 12.4\,m \qquad\qquad \lambda_{v_s}(f_1 = 270\,Hz) \approx 7.4\,m.$$

Since the cavity possesses a lateral extend of 8 m and a vertical extend of 4 m and only a fourth of the wavelength is needed for an object to be detected, the wavelengths are short enough so that the cavity interfere with them. The horizontal resolution of seismic waves is derived by the Fresnel zone, which describes the region in which rays interfere constructively and where travel-time differences are smaller or equal than half of their period Schuster (2017). The width d of the Fresnel zone is determined by

$$d \approx \sqrt{l \cdot \lambda} = \sqrt{l \cdot \frac{v}{f}} \tag{6.1.2}$$

with l the length of the ray path. In this case, assuming an average length of the ray path of 100 m for offset range five, gives Fresnel zone widths of 28 m and 30 m for P-waves and 24 m and 27 m for S-waves.

6.1.3.3   Strategy: Time-Windowing

To evaluate which seismic phase is affected by the cavity, the phase shifts displayed in Fig. 6.1.6 are again calculated, but this time only within the P-wave or Surface-wave time-window. Therefore the seismic phases within the synthetic seismograms were determined and the data was muted accordingly. This means that all traces before the P-wave onset and after the S-wave onset are muted in case of the P-wave time window and all traces before the S-onset are muted in case of the Surface-wave time window. Afterwards the phase shift for these time windows was once more calculated the same way as previously described. Fig. 6.1.7 shows the result. Again no phase shifts for smaller offsets until 30 m are visible, but become bigger for offsets larger than 31 m. Nevertheless, the significant threshold of 30° is exceeded only for the farthest offset range between 71 to 128 m. Here the phase shift is mostly significant in the z-component data for the P-wave time window (left) and in the x-component data for the

Surface-wave time window (right). This is not surprising since the vertical z-component is predominantly dominated by P-waves, whereas the horizontal x-component is dominated by S-waves. The phase shift within the P-wave time window becomes significant for frequencies higher than 200 Hz and lower 350 Hz. In case of S-waves the significant phase shift becomes apparent between frequencies of 160 Hz to 300 Hz.
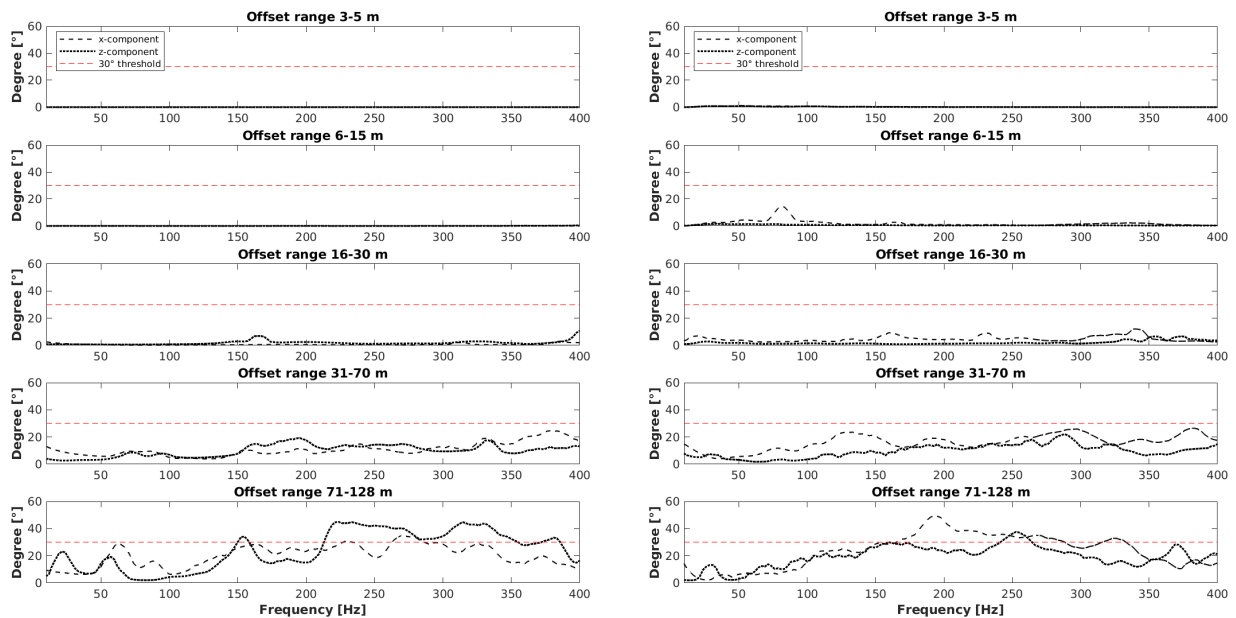
Figure 6.1.7: Phase shifts between initial and observed x-component (dashed line) and z-component data (dotted line) within the P-wave (left) and Surface-wave time window (right); red line marks threshold of $30°$

In order to evaluate the time shift within the time-domain, the initial and observed data were 200 Hz LP- and 200-400 Hz BP-filtered and plotted one upon each other. Fig. 6.1.8 shows the initial unfiltered data (upper panel) of shot 16 (right) and 17 (left) and the LP- and BP-filtered initial and observed data (second and third panel, respectively). The blue dots mark the picked P-wave arrivals (upper) and the onset of the S-wave arrivals (lower). For the LP-filtered seismograms of shot 16 and 17 no phase shift within the P-wave window is visible at all, which is already indicated by Fig. 6.1.7. In case of the BP-filtered data of shot 17 (left) in near offsets (up to roughly -65 m) and the most farthest offsets (farther roughly -100 m) the initial and observed data do not show any differences. Between -65 m and -100 m the seismograms exhibit a phase shift, that is only present within the P-wave time window. Those phase shifts can be observed in shots 1-6 and 13-18, which include large enough offsets for the waves to interact with the implemented cavity. Within the LP-filtered time-domain data the phase shift is visibly only after the S-onset (shot 16, right, enhanced figure in third panel) and disappears at higher frequencies (shot 16, right, enhanced figure in fourth panel).
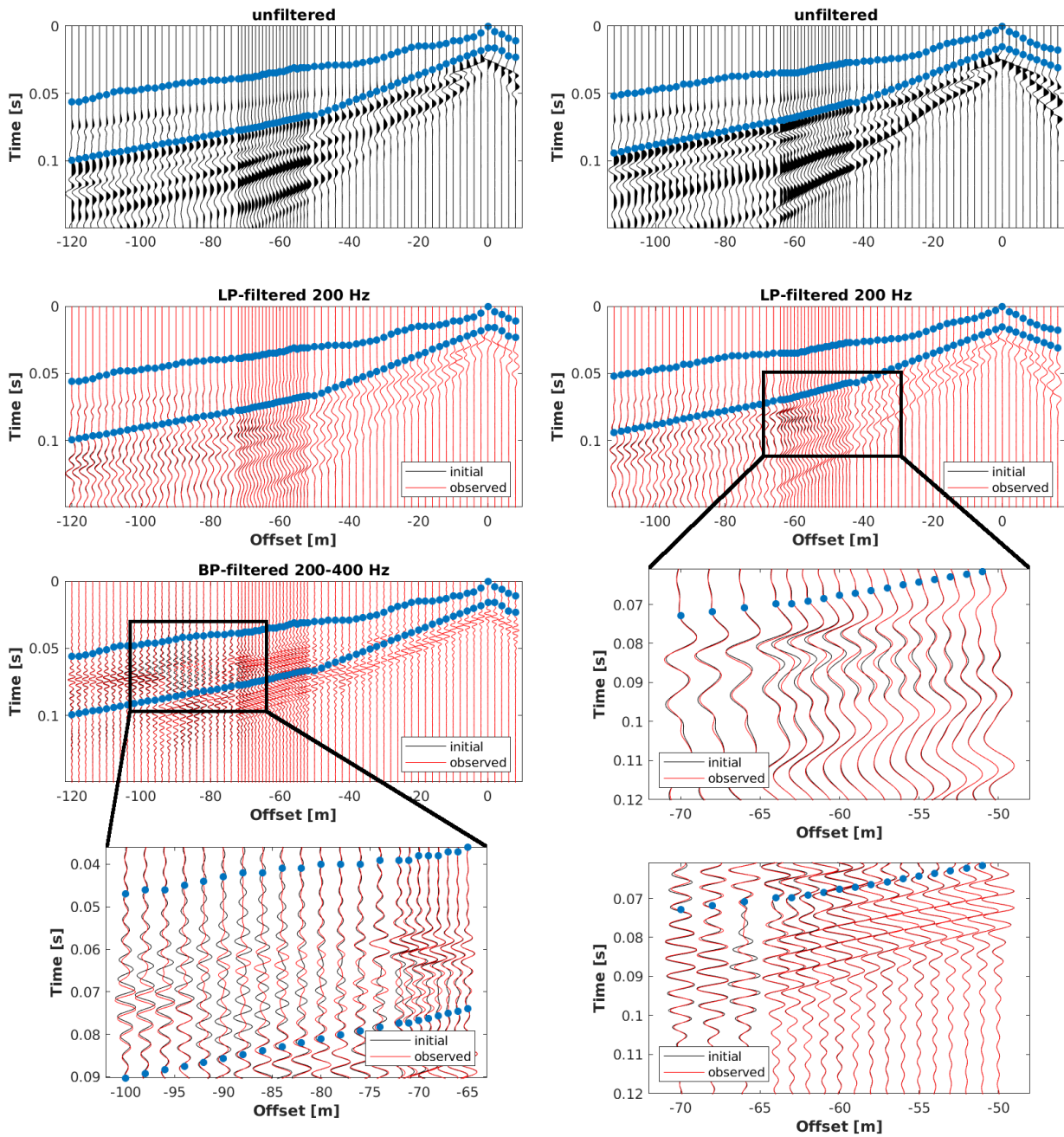
Figure 6.1.8: X-component data of example shot 17; upper panel: initial data; middle panel: LP-filtered 200 Hz initial (black) and observed data (red); second lower panel: BP-filtered 200-400 Hz initial (black) and observed data (red); lower panel: enhanced area; blue dots mark chosen time window for inversion

This examination of time shifts at different frequencies and in different time windows allows a selective inversion of those time windows and their corresponding frequencies.

6.2 Inversion of Synthetic Data

6.2.1 Models and Parameters

After a detailed examination of the synthetically forward modelled data and the influence of the cavity on the data, the next step is to do a synthetic inversion. In the following subsection different starting models are used, whereas the true model remains the same, which is the model obtained by the travel-time tomography with the implemented cavity. First, the travel-time tomography model (TTT model) is used to calibrate the inversion in terms of preconditioning and tapering. Afterwards different inversion results are shown for this model and inversion strategies. A second starting model is considered, a perturbed version of the TTT model (TTT pert). The different starting models are used to analyse the different parameters and how they effect the inversion. Also the synthetic inversions are used to determine if the cavity can be reconstructed at all. All inversion runs were terminated when the abort criterion was reached, which was less than 1% misfit reduction between two consecutive iterations. A preconditioned conjugate gradient method was used. Three main inversion strategies are applied to the models, that were derived from the previous synthetic analysis. These inversion strategies are summarized in the following table Tab. 6.2.1.

Table 6.2.1: Inversion strategies applied in the synthetic inversion

Strategy A	trace killing, no filtering
Strategy B	trace killing, LP-filtering (after Bunks et al. (1995))
Strategy C	offset mute, time windowing (P- or Surface-wave), LP-filtering

In the following the names of the inversion runs are a combination of the model used as the starting model and the strategy applied. For example the inversion run for strategy A and the TTT model used as starting model is named TTT.A, whereas the inversion for strategy B and the perturbed starting model is named PERT.B. In case of time-windowing and therefore in case of strategy C, the type of time window is indicated in brackets (e.g. TTT model with P-wave time-windowing is named TTT.C(P)). The data filtering was conducted by using a Butterworth filter of order 4 (strategy B) or 20 (strategy C).

6.2.2 Tapering and Precondition

Köhn (2011b) already showed in his PhD thesis the importance of a proper preconditioning and tapering of the data in order to get reasonable model updates also in the deeper part of the model. Without a proper tapering of the shot/receiver positions the main model updates would concentrate near to them, since the amplitudes are strongest near to the shots. Cylindrical tapers around the shots were introduced and the final gradients (summed gradients of each shot) were multiplied with this taper function. The taper functions are plotted in Fig. 6.2.1, whereas the three functions 1.1-1.3 (blueish dashed lines) are just

different in their extend, but not in their shape. The circular taper is zero at the shot position and increases to one at the edge of the taper. The taper applied in case 1.1 tapers a radius of 8 m around the shots, whereas the taper applied in case 1.2 and 1.3 tapers the data in a radius until the bottom of the model, respectively. Additionally, the taper in case 1.3 is zero for a depth of up to 6 m. The taper in case 2.1 (black dotted line) is a log-function, that tapers almost only the very shallow region of the model. Cases 3.1-3.2 (greenish dashed lines) show self-designed error-function tapers, that taper the shallow region of the model quite strongly.
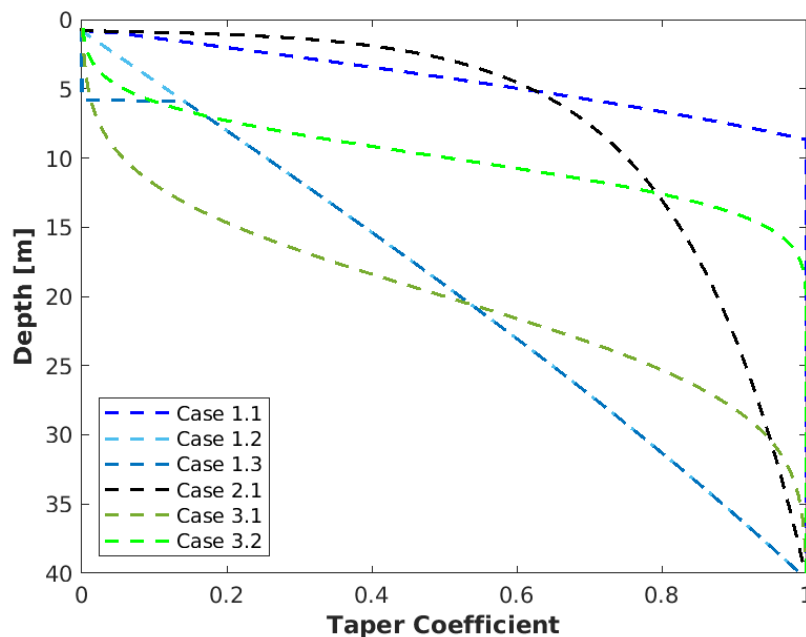
Figure 6.2.1: Different taper functions tested for inversion

The taper width has a big influence on the inversion results as shown in Fig. 6.2.2 (no trace killing or filtering is applied). Here the difference between the initial and inverted Vp (left) and Vs model (right) are plotted for the taper function cases 1.1 to 3.2. It is quite obvious that the choice of taper strongly influences the inversion results. For cases 1.1 and 2.1 the cavity is not reconstructed within the inverted Vp models. The model updates concentrate to the surface. The cavity is clearly visible in cases 1.2, 1.3 and 3.1, whereas the cavity is only indicated in case 3.2. The taper function of case 1.3 disqualifies, because the zero tapering around the sources until 6 m depth introduces a sharp discontinuity within the model which is not physical. For a synthetic case where the initial and the true background velocities and density are the same, a deep taper (case 3.1) is very sufficient, because the physical properties are already correct and do not need to be corrected. For starting models where the background velocities and densities are different from that of the true model, a deep taper would hinder the inversion to also correct for these shallow properties and therefore would forcefully falsify the inversion results. In case of the real data inversion, maybe a shallow taper would be more sufficient.

An additional preconditioning with the approximate Hessian leads not only to a faster convergence, but also "illuminates" the deeper part of the model. Therefore for the following inversions a preconditioning after Shin et al. (2001) was applied.
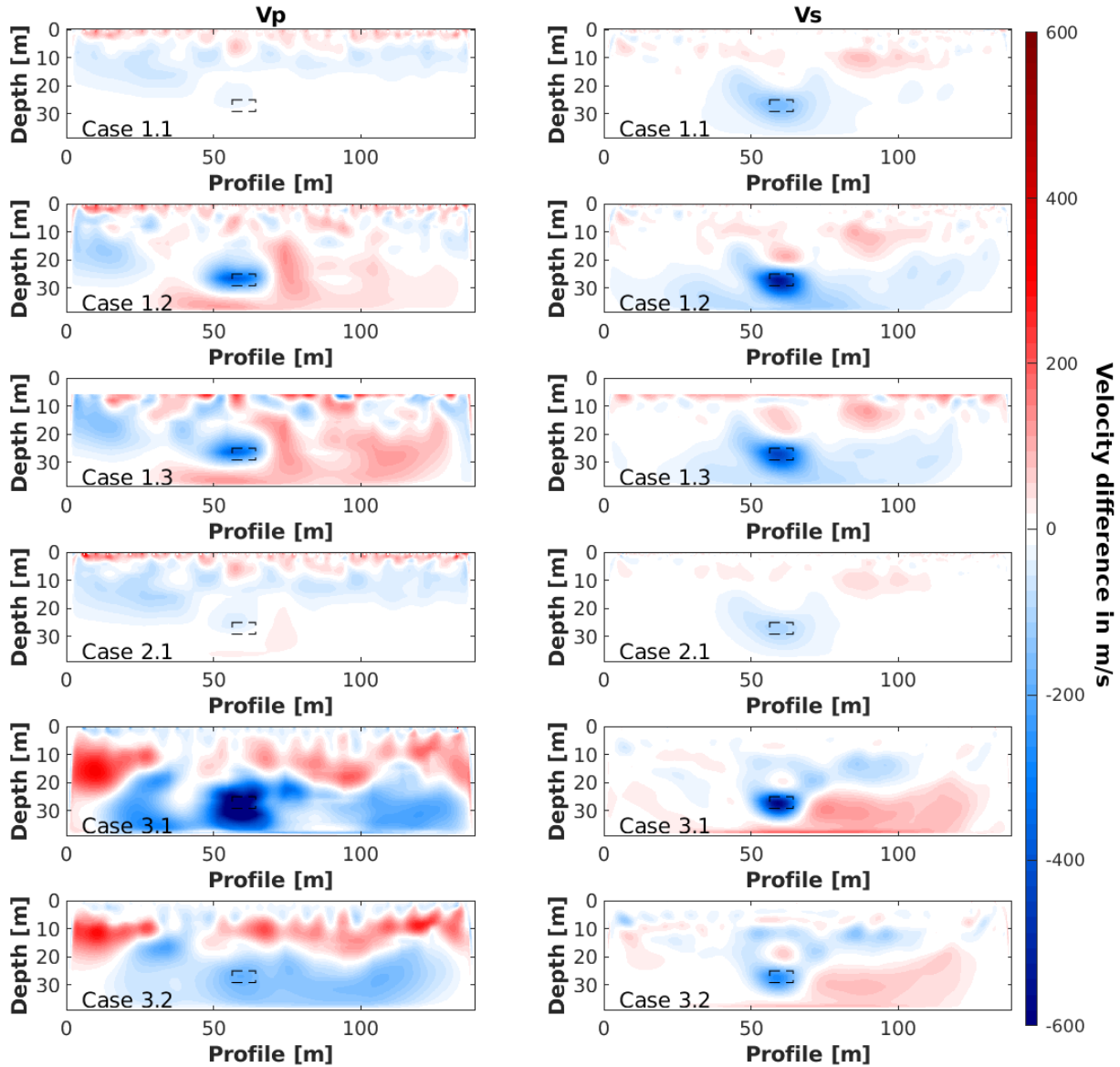
Figure 6.2.2: Different models for different taper functions; left: difference Vp models, right: difference Vs models

6.2.3   Travel-Time Tomography Model

In this section the model obtained by the travel-time tomography is used as the initial model, meaning that the only difference between the initial and true model is the implemented cavity. For a verification of how good the model describes the data, the first arrivals of two example shots (5 and 16) were picked for every fifth trace and compared to the first arrivals of the measured data. The plot of superimposed picked times is displayed in Fig. 6.2.3. The picked times for the measured data and the synthetic data fit very well for shot 5 (upper panel) and

shows a mean difference of half a millisecond. The mean deviation for shot 16 is in the range of two milliseconds, which is still satisfactory. Since the travel-time tomography gives P-wave velocities the initial model for S-waves was estimated by dividing Vp with a factor of $\sqrt{3}$. The values for density were obtained by Gardner's relation (Gardner et al. (1974))

$$\rho = 310 \cdot V_p^{0.25} \ [kg/m^3].\tag{6.2.1}$$
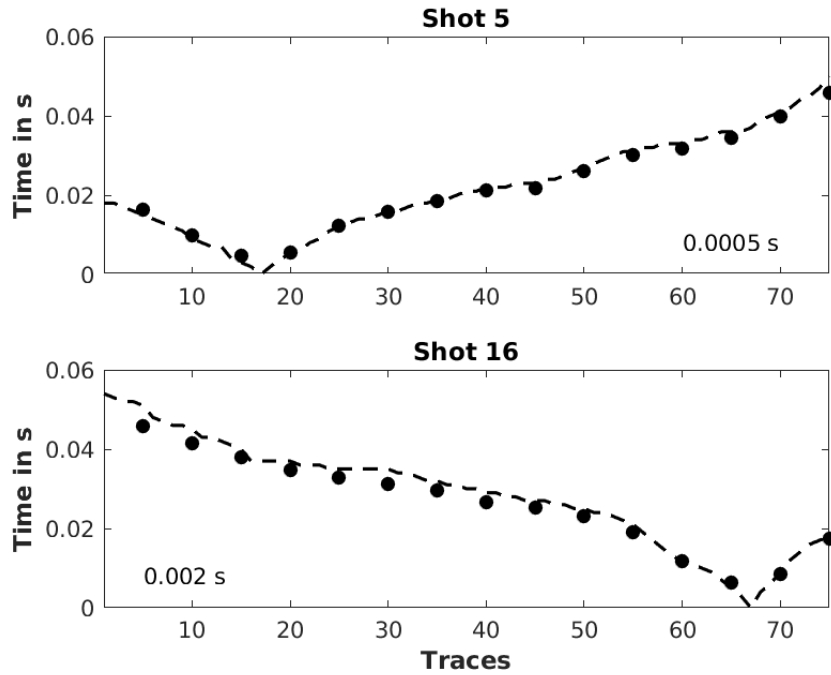
Figure 6.2.3: Picked first arrivals of measured data (dashed line) and synthetics (circles) for every fifth trace for shot 5 (upper panel) and shot 16 (lower) panel; the numbers in the lower corners indicate the mean difference between picked times

TTT.A   The first synthetic inversion tests were conducted using the model derived from the travel-time tomography shown in section 5 (Fig. 5.5.1) as the initial model. By implementing a cavity into the model a true model is obtained. Fig. 6.2.4 shows the initial model (upper left panel) and the true model (upper right panel). The parameters for the inversion run is summarised in Tab. 6.2.2.

Table 6.2.2: Parameter for inversion TTT.A

trace killing	yes
filtering	no
taper	case 3.1
time windowing	no
STF inversion	no

The trace killing was applied as it was described in section 6.1.3.1, meaning that all traces were neglected within offsets for which the percentage share of the differences between the

initial and observed seismograms fall below a threshold of 5 %. The inversion results after 31 iterations are displayed in Fig. 6.2.4 (upper black box, left panel), the differences between the initial and inverted model are displayed in the right panel. In the area of the implemented cavity the velocities and density are drastically reduced. In case of P-wave the velocity reduction is about 1000 m/s, for S-wave 600 m/s and the density reduction is even 1940 kg/m^3. In case of S-waves and density the circular shape of the cavity is nicely reconstructed. The depth profiles shown in Fig. 6.2.5 (left three panels) illustrate how the velocity and density reduction in the area of the cavity (solid lines) approaches the values of the cavity within the real model (dashed lines) and diverge from the initial model (dotted lines). Nevertheless the algorithm tries to also correct the background velocities and density, even though they are already correct and do not have to be changed. This causes an increase or decrease of velocities or density within the inverted model where it is not meaningful. In the left upper panel of Fig. 6.2.6 the changes of the Euclidean distances in percent (comp. Eq. 6.2.2) between the inverted and true model over the iterations are plotted. The initial distance is roughly 0.5 % and increases for all three properties over iterations. At the end of the inversion, after 31 iterations, the final Euclidean distance is three times higher for Vp (1.5 %), slightly higher for Vs (0.7 %), but more than ten times higher for density (5.5 %). Although the main target, namely the cavity, is very well reconstructed, the artefacts within the background models causes a divergence in model distances. To verify the model fit in the target area exclusively, the Euclidean distance around a 2 m radius around the cavity is calculated and plotted in the middle panel of Fig. 6.2.6. Here it becomes obvious that the algorithm worked well for the purpose of reconstructing the cavity. The initial model distance within the target area is roughly 40 to 50 % for all three parameters and decreases in case of P- and S-wave velocities to under 20 % and for density even under 1 %. The lower panel of Fig. 6.2.6 (dashed line) shows the normalised data misfit over iterations. Even though the overall model distance is increased the mismatch between the calculated and observed data decreases over iterations and reduces to less than a half of the initial misfit. In Fig. 6.2.7 the initial, observed and inverted seismograms are plotted upon each other for three different offsets. At 0 m offset (upper panel) there is no difference between the seismograms, only with further offsets the initial mismatch between the initial and observed seismograms become visible. The inverted seismogram fits quite nicely with the observed seismograms, especially in near to intermediate offsets. In farther offsets an increased mismatch between the inverted and observed seimograms can be seen, especially at later times (comp. Fig. 6.2.7, lower right panel, at 0.2 s and later). However the phases still fit and the mismatch is only due to the difference in amplitude.

$$model_{error} = \sqrt{\frac{\sum_{i=1}^{n}(m_i^{inv} - m_i^{true})^2}{\sum_{i=1}^{n} m_i^{true2}}} \cdot 100 \qquad (6.2.2)$$
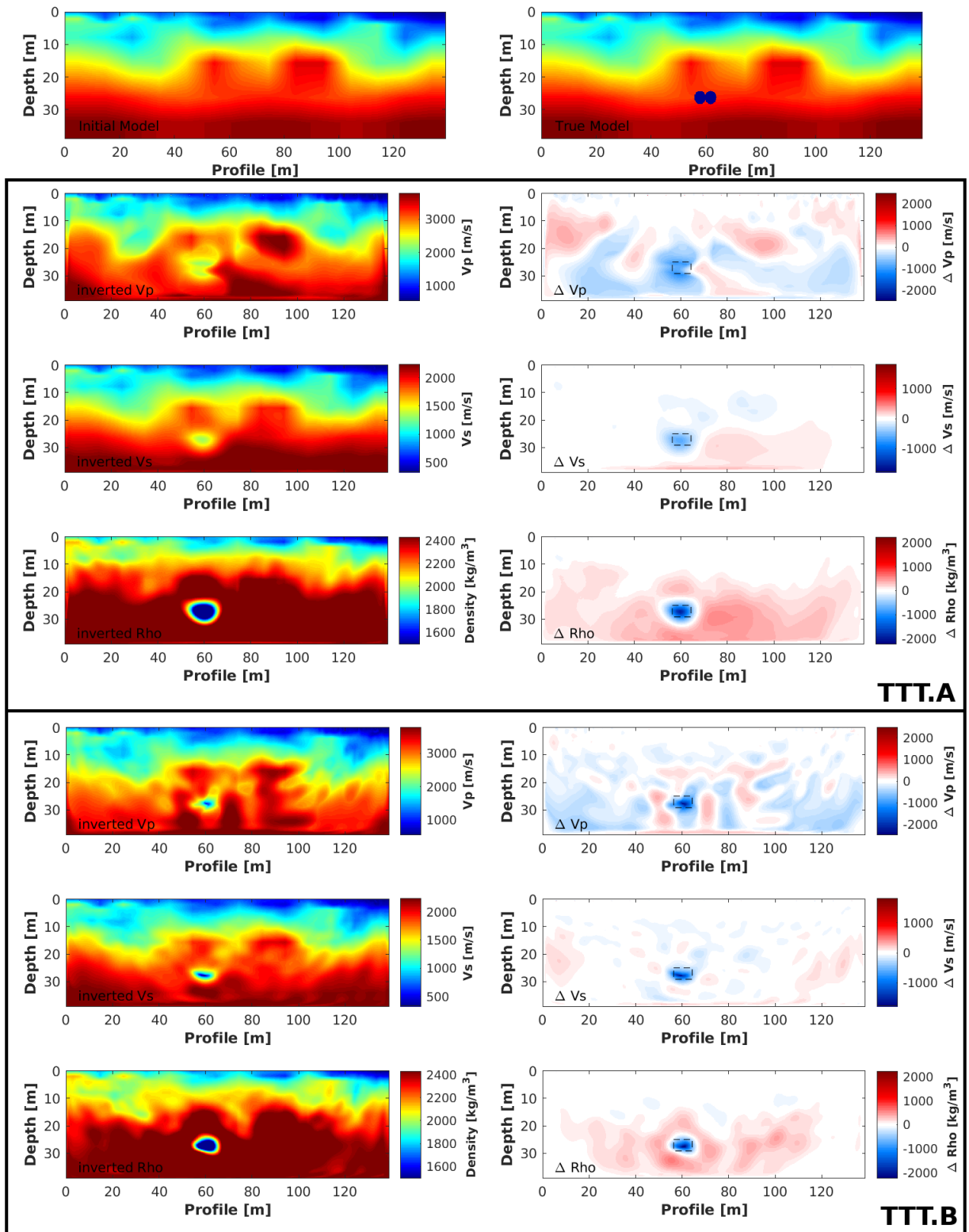
Figure 6.2.4: Initial (upper left) and true model (upper right) with inverted models (left panel) and difference models (right panels) for Vp (second panel), Vs (third panel) and density (lower panel) for the TTT model and inversion strategy A (upper black box) after 31 iterations and B (lower black box) after 63 iterations
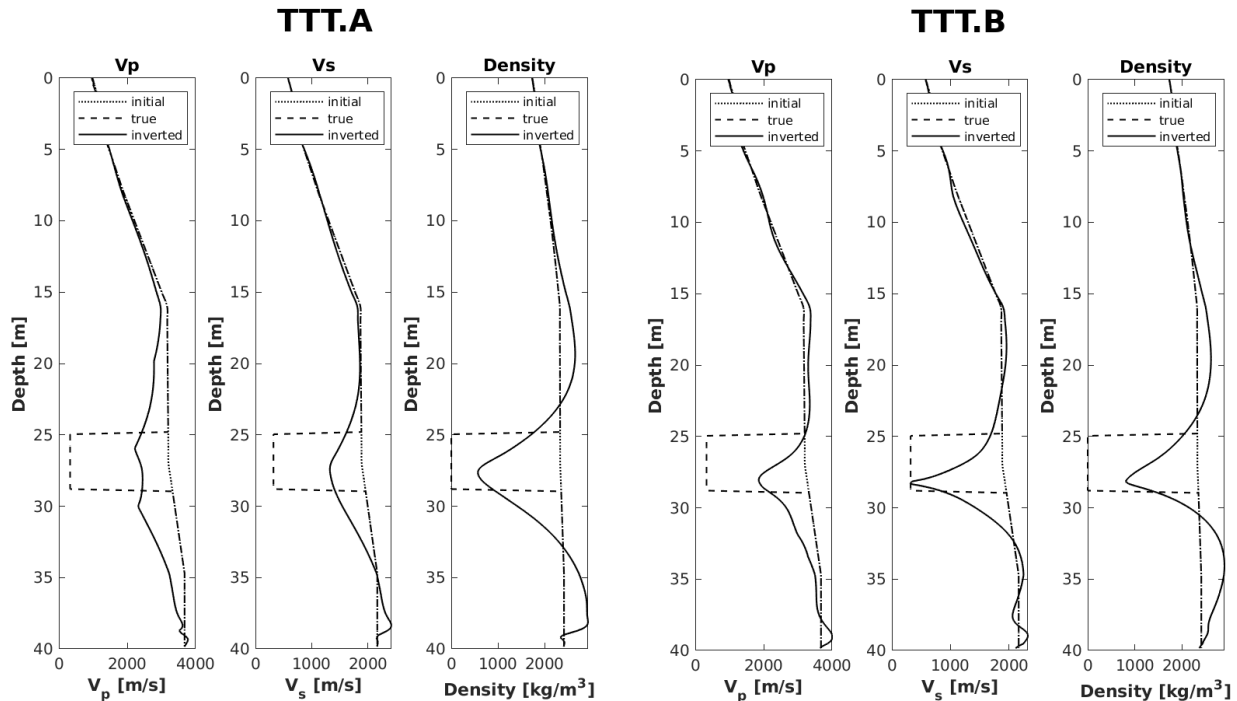
Figure 6.2.5: Depth profiles for Vp (left), Vs (middle) and density (right) at profile meter 63.68 m for the TTT model and inversion strategy A (left three panels) and B (right three panels)

TTT.B Since the background model is correct and the only feature to reconstruct is the cavity, it was tried to exclusively invert for the signals carrying the information of the cavity. Looking at the phase shifts plotted in Fig. 6.1.6 those signals are present in farther offsets and at higher frequencies. In this approach offsets smaller than 50 m were muted and additionally a LP-filtering between 200 and 400 Hz was applied (Actually it is some kind of mixture of BP- and LP-filtering, since a 200 Hz HP-filter is applied, but during the inversion just the upper-corner frequency is increased in 10 Hz steps, that is why it is referred to as LP-filtering). The inversion parameters are again summarise in Tab. 6.2.3.

Table 6.2.3: Parameter for inversion TTT.B

offset muting	yes
filtering	yes
taper	case 3.1
time windowing	no
STF inversion	no

The inversion results after 63 iterations are displayed in Fig. 6.2.4 (lower black box). It becomes obvious that the velocity and density reduction in the area of the cavity is more focused. The algorithm accomplishes a velocity reduction in P-wave of 2320 m/s, in S-wave of 1780 m/s and a reduction in density of 2250 kg/m^3, which is way better than in the previously discussed inversion run (TTT.A), which is also indicated by the Euclidean distance within
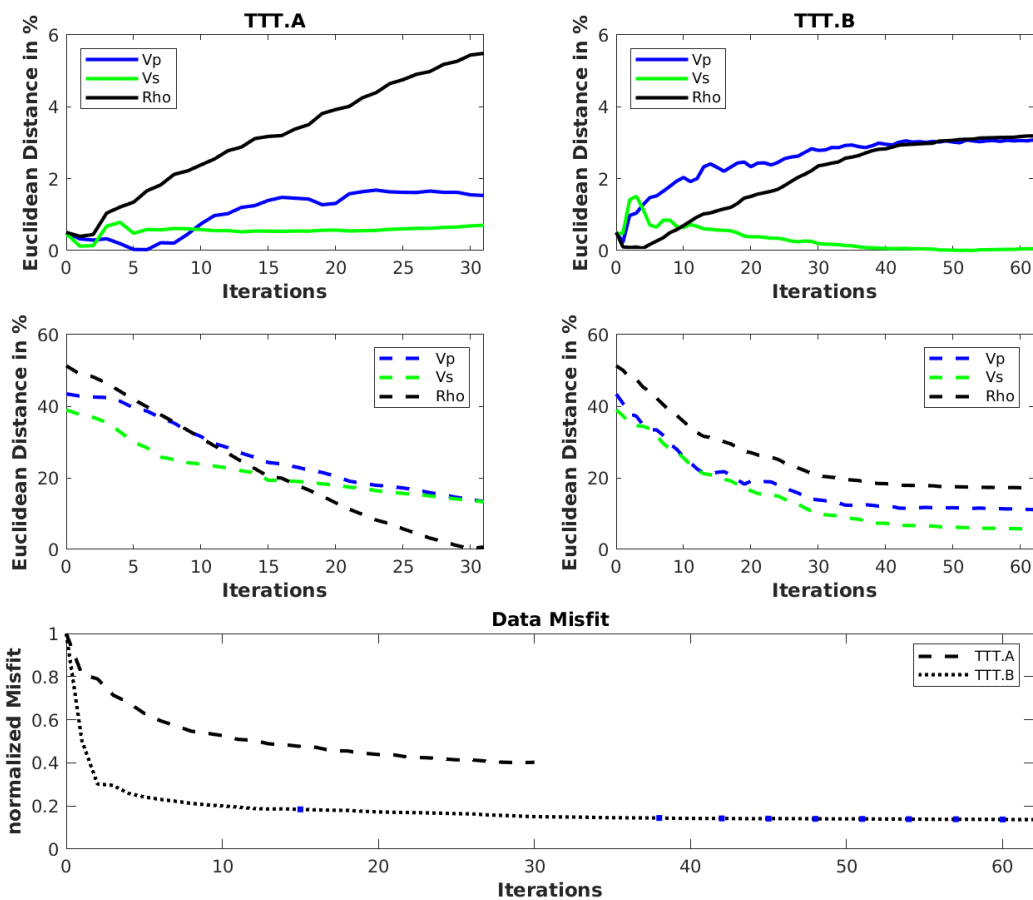
Figure 6.2.6: Upper panel: Euclidean distance of true and inverted models for TTT.A (left) and TTT.B (right); Middle panel: Euclidean distance of true and inverted models for TTT.A (left) and TTT.B (right) within the target area; Lower panel: normalised data misfit for TTT.A (dashed line) and TTT.B (dotted line); blue rectangles mark change in frequency band (note that this changes the misfit function each time the frequency band is changed)

the target area (right middle panel, Fig. 6.2.6). Also the introduced artefacts in the Vs and density background model are smaller. This becomes clearly visible when plotting the change of the Euclidean distance of the models over iterations (Fig. 6.2.6, upper right panel). The initial distance in the density model of 0.5% is now only six times increased to a value of 3.2% and not as high as in the previous test. The distance within the S-wave model is even reduced to a tenth of the initial distance to 0.05%. Only the P-wave model distance has worsen to a value of 3.1% and is now two times higher than in the previous inversion run and six times higher than the initial distance. Nevertheless the normalised data misfit displayed in Fig. 6.2.6 (lower panel) shows a misfit reduction to less than a fifth of the initial misfit and an overall smaller final misfit than in the previous inversion. The trace fit for example shot one is included in appendix C.

The plotted depth profiles in Fig. 6.2.5 show that the inverted S-wave model reaches the value of the (pseudo-)cavity in the true model and fits the background model quite well. Only
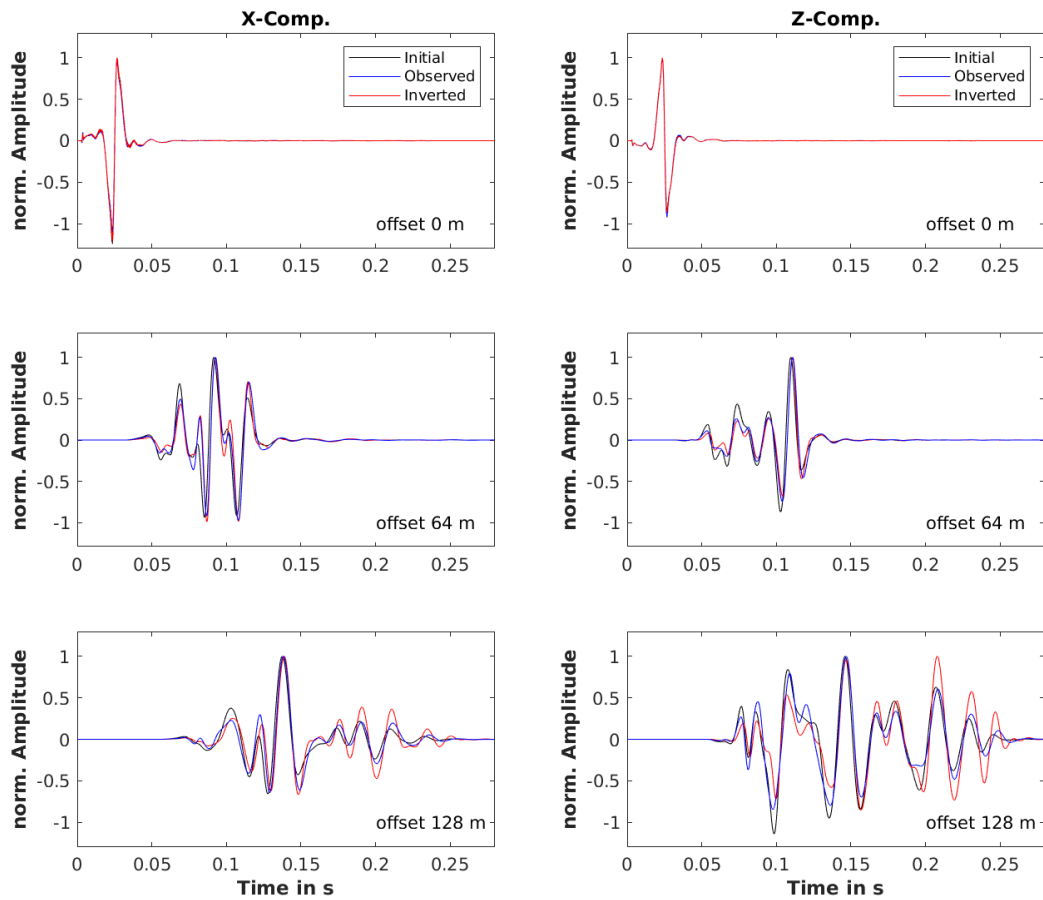
Figure 6.2.7: Initial (black), observed (blue) and inverted (red) x-(left panel) and z-component (right panel) seismograms of shot 1 plotted upon each other; the offset is indicated in the lower right corner

the inverted density is over-estimated around the cavity, compensating the density reduction within the area of the cavity.

TTT.C(P) & TTT.C(S)   The analysis of phase shifts in the time-domain (Fig.6.1.8) and their corresponding frequency-domain (Fig. 6.1.7) allows the specific inversion of those parts of the signal due to a correct time-windowing, offset selection and filtering. In the following two runs (TTT.C(P) and TTT.C(S)) the inversion was carried out once for the selected P-wave time window and once for the selected Surface-wave time window. In both cases an offset muting until 50 m was applied and a LP-filtering with lower and upper corner frequencies as they are suggested by the spectral phase shift displayed in Fig. 6.1.7, meaning a frequency range between 200 and 400 Hz for Vp and 160 to 300 Hz for Surface-waves (In fact the filtering procedure is the same as in the previous case TTT.B. First a HP-filter is applied and just the upper corner-frequency is increased in 20 Hz steps). Again the inverted and difference models after 82 and 67 iterations, respectively, are displayed in Fig. 6.2.8 and the inversion parameters are summarized in Tab. 6.2.4.

Table 6.2.4: Parameter for inversion TTT.C(P) and TTT.C(S)

offset muting	yes
filtering	yes
taper	case 3.1
time windowing	yes
STF inversion	no
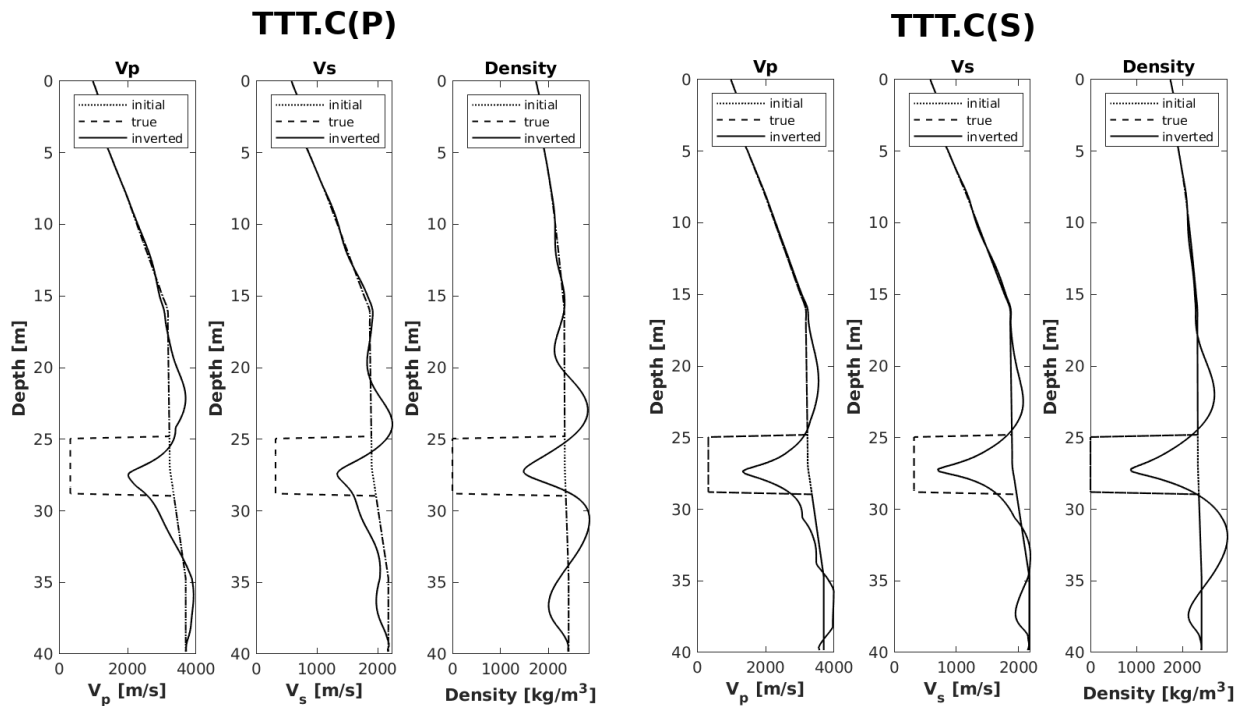
Figure 6.2.9: Depth profiles for Vp (left), Vs (middle) and density (right) at profile meter 63.68 m for the TTT model and inversion strategy C for P-waves (left three panels) and Surface-waves (right three panels)

Differently to the other two inversion approaches (TTT.A and TTT.B) the introduced artefacts within the background model are smaller and barley visible (note that the colour scale is equally standardised for all four inversion runs). This is also indicated by the overall Euclidean model distance depicted in Fig. 6.2.10 (upper panel), which slightly decreases for Vp and density and significantly for Vs. Concerning the target area the model misfit is minimized by 10 % for Vs and density, and even 20 % for Vp (TTT.C(P), left middle panel) in case a P-wave time window is applied and reduced by more than 20 % for all three parameters in case of an applied Surface-wave time window (TTT.C(S), right middle panel). The velocities and density are not as much decreased as in run TTT.B (offset muting and LP-filtering), but nevertheless the cavity is clearly visible and moreover the specific shape of the implemented cavity, meaning two circles next to each other, is indicated. In general the shape of the cavity is not as smeared as in the previous runs and the greater lateral extent compared to the horizontal extent of the cavity is nicely recovered. The data misfit is significantly decreased in both approaches down to 1 % in case of P-wave time windowing (dashed line in lower panel of Fig. 6.2.10) and to 2.5 % in case of Surface-wave

time-windowing (dotted line in lower panel of Fig. 6.2.10). Again the trace fits for eaxmple shot one are displayed in appendix C. The depth profiles shown in Fig. 6.2.9 again clearly show the reduction of velocity and density in the area of the implemented cavity, but also an overcompensation above and below the cavity, especially when a P-wave time windowing was applied (left three columns).

6.2.4   Perturbed Travel-Time Tomography Model

The previous starting model (TTT model) is unfortunately not a realistic case, since it is considered perfect except the implemented cavity. Therefore another starting model is introduced, where the model obtained by the travel-time tomography is perturbed in parts and the P-wave velocity ranges between $\pm\,3\,\%$ (Fig. 6.2.11). These perturbations are added to the TTT model, the S-wave and density models are then obtained as previously explained, by dividing the P-wave velocity by a factor of $\sqrt{3}$ and applying Gardner's rule, respectively. This procedure ensures that the perturbations are in the same realistic ranges for each elastic parameter and the Vp-Vs-ratio is not violated. The previously discussed inversion strategies A-C are again applied in order to obtain the implemented cavity.
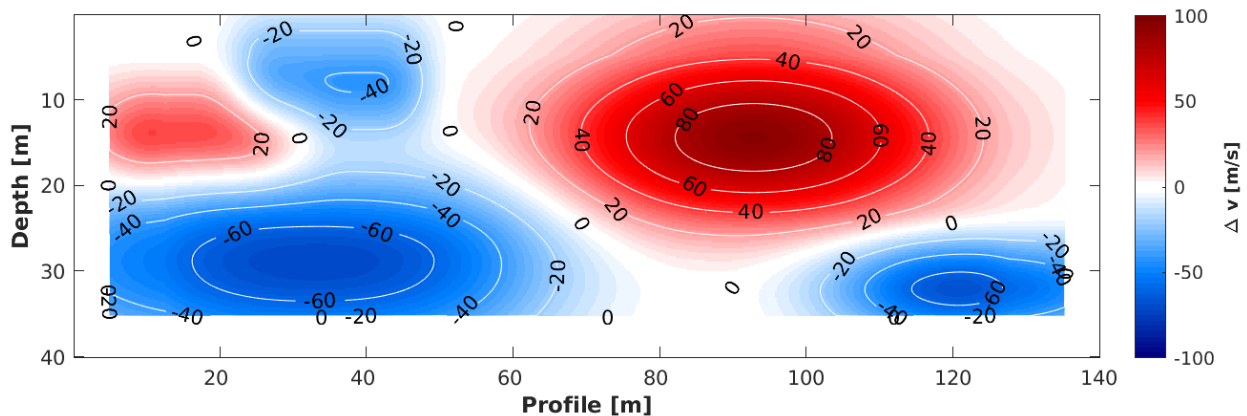
Figure 6.2.11: P-wave velocity perturbations added to the TTT model; white lines mark velocity contour lines, black numbers display amount of perturbation in m/s

PERT.A   The first run PERT.A depicted here was again performed without any data filtering, but with trace killing (see inversion parameters in Tab. 6.2.5). Differently to the inversion TTT.A a shallow taper was applied. In the previous inversion TTT.A the background model was perfect and there was no need for a correction of velocities in the very shallow part of the model. In this inversion approach the background velocities are not correct and have to be corrected. Therefore a shallow taper is applied, allowing the algorithm to correct shallow surface velocity and density perturbations. Looking at Fig. 6.2.12 (upper black box) shows the inversion result (left panel) for Vp, Vs and density and beside the difference models (right panel) after 21 iterations. The cavity is reconstructed in Vs and density, but only indicated in Vp. The S-wave decrease within the area of the implemented

cavity is about -230 m/s, whereas the velocity is not significantly over- or underestimated above or beyond the cavity (comp. Fig. 6.2.13, left three panels). The density reduction is in the range of roughly $625 \, kg/m^3$. In the case of density inversion the algorithm over-estimates the density right above and below the cavity, meaning the density is increased, even though this is not true (comp. Fig. 6.2.13). Looking at the results for the P-wave inversion, the velocity is decreased in the area of the cavity of about 280 m/s, but not well defined as for the other two parameters. In Vp it seems more like a big low velocity zone than a well defined and sharp cavity.

Table 6.2.5: Parameter for inversion PERT.A

offset muting	yes
filtering	no
taper	case 3.2
time windowing	no
STF inversion	no
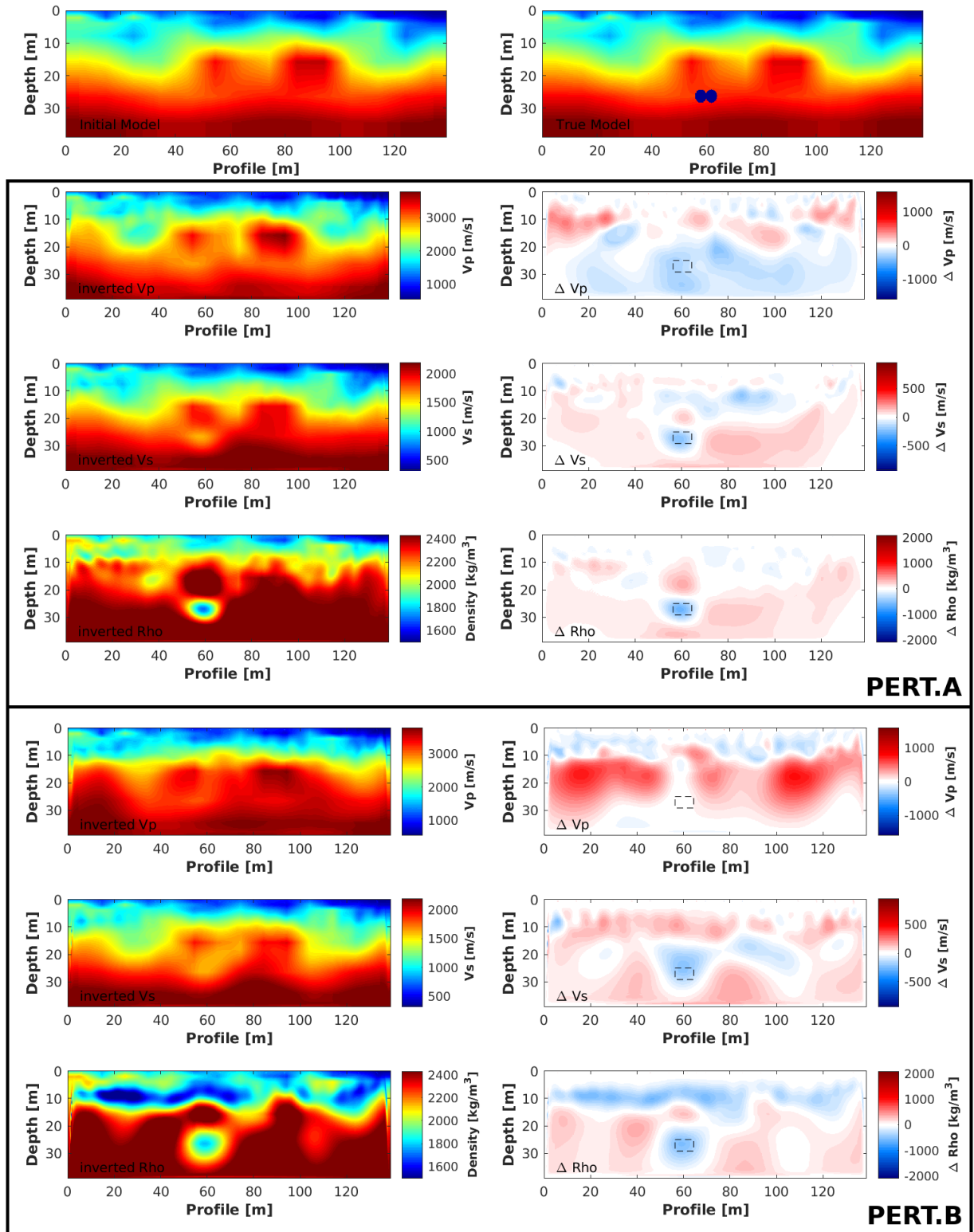
Figure 6.2.12: Initial (upper left) and true model (upper right) with inverted models (left panel) and difference models (right panels) for Vp (second panel), Vs (third panel) and density (lower panel) for the PERT model and inversion strategy A (upper black box) after 21 iterations and B (lower black box) after 92 iterations
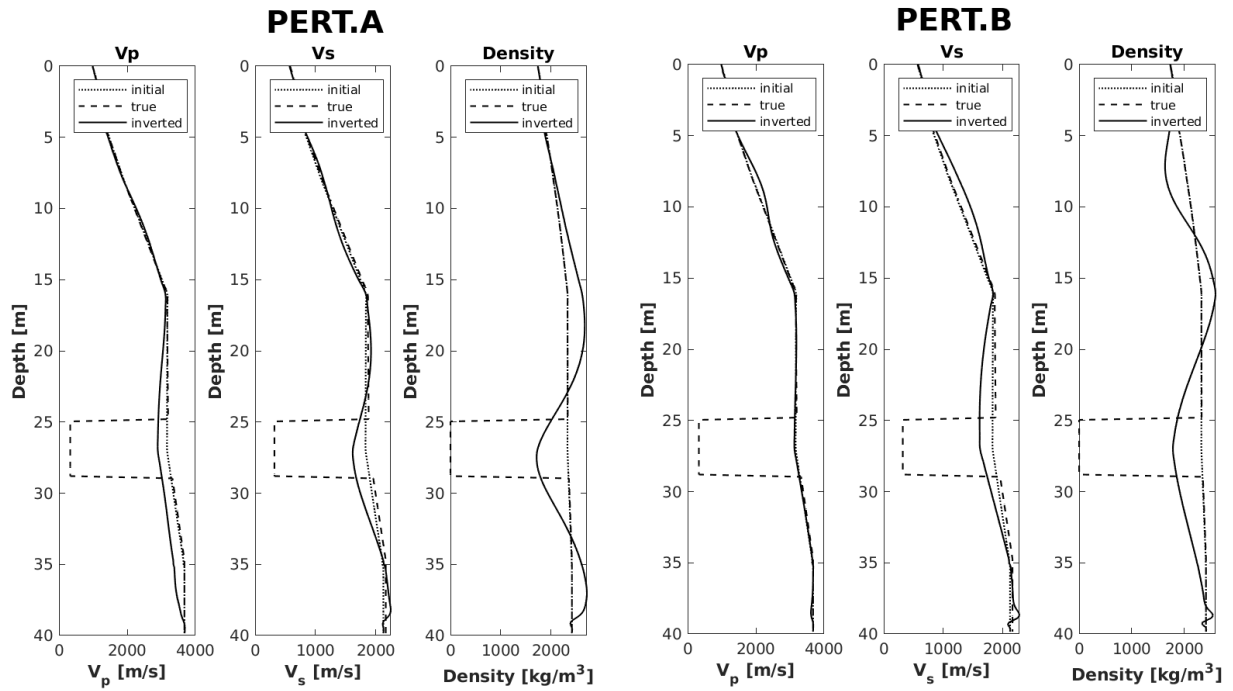
Figure 6.2.13: Depth profiles for Vp (left), Vs (middle) and density (right) at profile meter 63.68 m for the PERT model and inversion strategy A (left three panels) and B (right three panels)
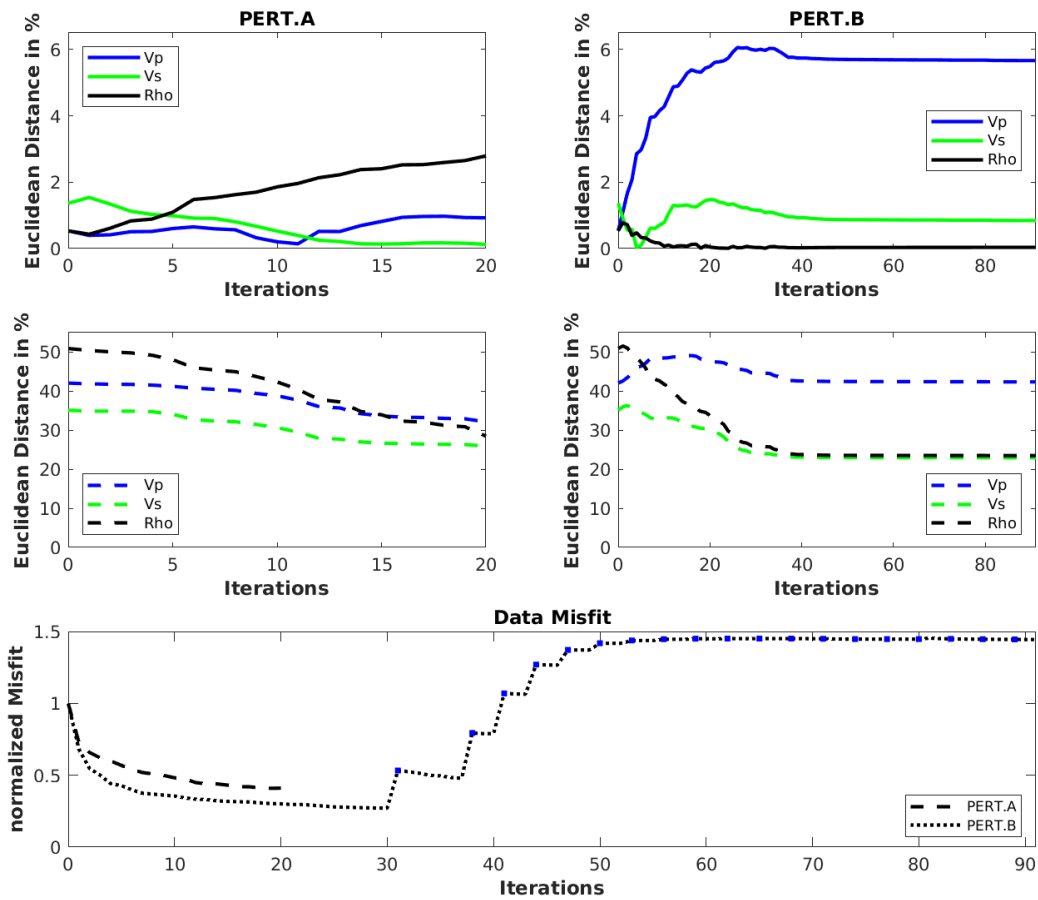
Figure 6.2.14: Upper panel: Euclidean distance of true and inverted models for PERT.A (left) and PERT.B (right); Middle panel: Euclidean distance of true and inverted models for PERT.A (left) and PERT.B (right) within the target area; Lower panel: normalised data misfit for PERT.A (dashed line) and PERT.B (dotted line); blue rectangles mark change in frequency band (note that this changes the misfit function each time the frequency band is changed)

The overall Euclidean model distance displayed in Fig. 6.2.14 (upper left) shows an increase for Vp and density, but an decrease in Vs. Comparing the difference models of Fig. 6.2.12 (right panel within upper black box) with the perturbations displayed in Fig. 6.2.11 shows no clear correlation of velocity or density correction. Only in Vs it seems that the algorithm compensates the big high velocity perturbation to some extent. This would explain why the overall Euclidean distance increases for Vp and density. Still looking at the model distance at the target area (Fig. 6.2.14, middle left) it is quite clear that all three parameters are decreased by at least 10 %. The data misfit plotted in Fig. 6.2.14 (lower panel, dashed line) shows a decrease to below 50 % of the normalized initial misfit. Plots displaying the trace fits of initial, observed and inverted seismograms for shot one are shown in appendix C.

PERT.B   To further investigate the effect of filtering inversion strategy B, including a LP-filtering, is applied to the perturbed initial model. Here the upper corner-frequency is

increased by 20 Hz steps if the misfit could not further be decreased. The outcome of the inversion after 92 iterations are shown in Fig. 6.2.12 (lower black box) (trace comparisons are shown in appendix C). In Vs and density the cavity is again well reconstructed with its circular shape and velocity and density reduction. However in Vp the velocity decrease is not as defined and strong as for the other two parameters (comp. Fig. 6.2.13, right Vp panel). In fact, the P-wave velocity is only decreased by 40 m/s, which is nearly nothing compared to the velocity changes within the rest of the model. Looking at the inverted model for Vp only, it is not possible to reliably locate the cavity. This is only possible by considering Vs and density too. Also the background perturbations are bigger leading to a significantly increased overall Euclidean model distance (comp. Fig. 6.2.14, upper right), especially for Vp. In case of Vs and density the model distance is moderately till significantly decreased, respectively. In case of S-wave the Euclidean model distance is reduced by 40 % and even further by nearly 90 % in case of density. Looking specifically at the Euclidean distance of the target area (6.2.14, right middle panel) the decrease of Vs and density is in the range of 10 to 25 %, respectively, and nearly zero in case of P-wave velocity. Noticeable is the steady trend of the overall and specific Euclidean distance for all three parameters, which appears after roughly 37 iterations. Here the distance is not further decreased and remains the same, only the data misfit (Fig. 6.2.14, lower panel, dotted line) rises. At iteration 37 the upper corner frequency changes from 40 to 60 Hz, which might be an indication that the inversion of the cavity is mostly driven by the low-frequency surface waves and higher-frequency phases do not contribute to the cavity reconstruction.

PERT.C(P) & PERT.C(S) Since the inversion results of the previous approaches PERT.A and PERT.B are not as clear as for TTT.A and TTT.B, the selective inversion by choosing the appropriate time windows is repeated and also applied to the perturbed initial model, meaning that the inversion was once carried out for the P-wave time window and once for the Surface-wave time window, respectively, and their corresponding frequencies.

Table 6.2.6: Parameter for inversion PERT.C(P) and PERT.C(S)

offset muting	yes
filtering	yes
taper	case 3.1
time windowing	yes
STF inversion	no

The results for a selective P-wave time window inversion after 111 iterations is depicted in Fig. 6.2.15 (upper black box). The cavity is clearly reconstructed in all three parameters and can be very well distinguished from other parameter changes within the background model. The velocity decrease is in the range of 1260 m/s for Vp and 780 m/s for Vs and therefore by far more than in PERT.A and PERT.B. Also the density reduction is much bigger with a value of 1400 kg/m^3. Again the shape of the cavity is very well recovered and not as smeared

and vague as in the previous runs. The decrease of the elastic properties is even bigger in case of an appropriate Surface-wave time-windowing (comp. Fig. 6.2.15, lower black box). Here the velocity and density decrease is in the range of $1600\,\mathrm{m/s}$ for Vp, $940\,\mathrm{m/s}$ for Vs and $2060\,kg/m^3$ for density and therefore by far more significant than in all three inversion approaches (PERT.A, PERT.B and PERT.C) before. This is also indicated by the depth profiles in Fig. 6.2.16. The velocity and density reduction is concentrated in the area of the cavity, but an over-compensation of all three parameters above and below the cavity is introduced by the algorithm. However looking at the overall Euclidean distance shows an increase for Vp and density and a slightly decrease in Vs for both types of time-windowing, indicating that the algorithm focuses on the cavity reconstruction and less on the correction of perturbations within the background model. The data misfit plotted in Fig. 6.2.17 (lower panel) is significantly decreased for both inversion approaches to less than $10\,\%$. In appendix C the fit between initial, observed and inverted traces is shown for shot one.
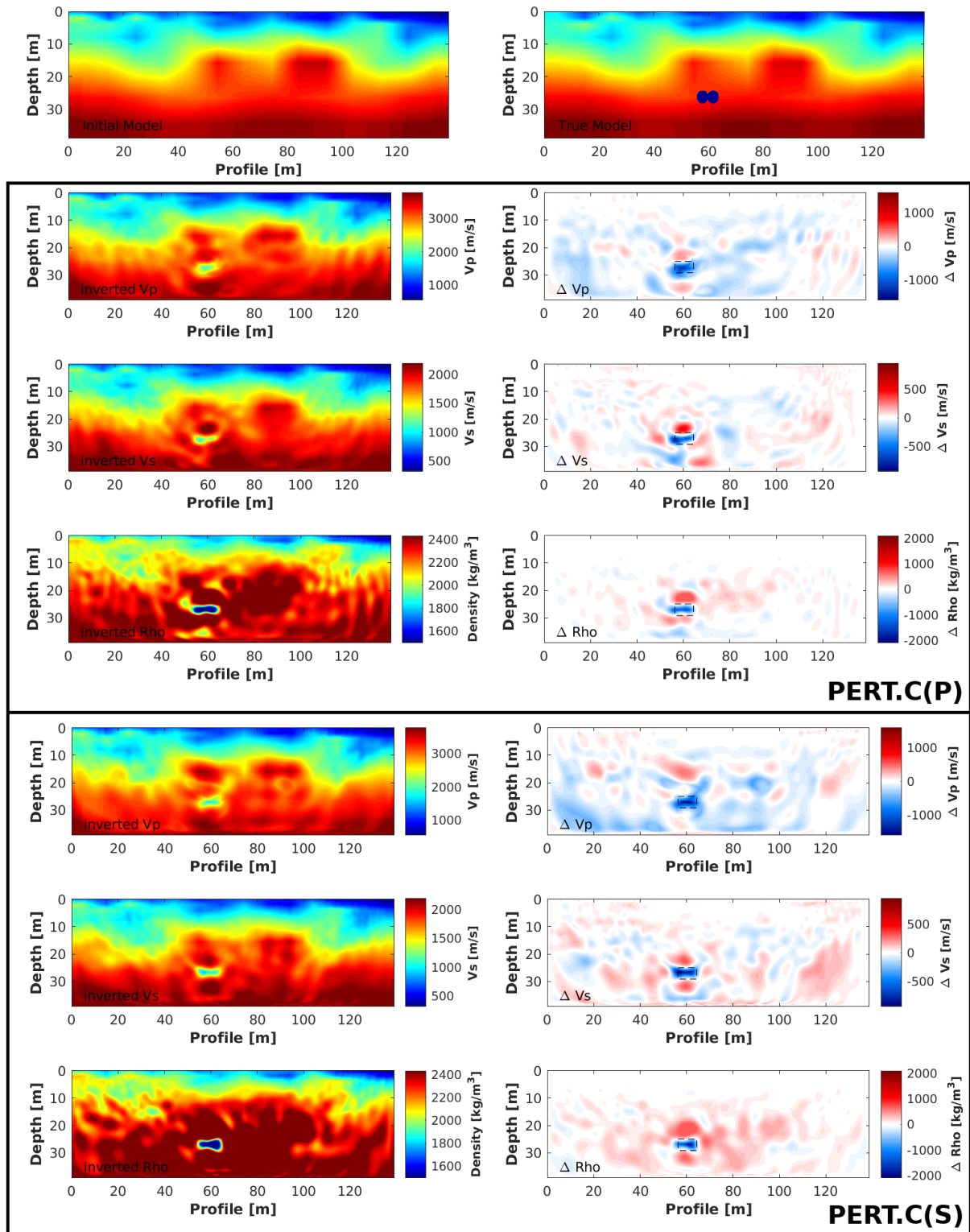
Figure 6.2.15: Initial (upper left) and true model (upper right) with inverted models (left panel) and difference models (right panels) for Vp (second panel), Vs (third panel) and density (lower panel) for the PERT model and inversion strategy C for P-wave time-windowing (upper black box) after **111** iterations and S-wave time-windowing (lower black box) after **73** iterations
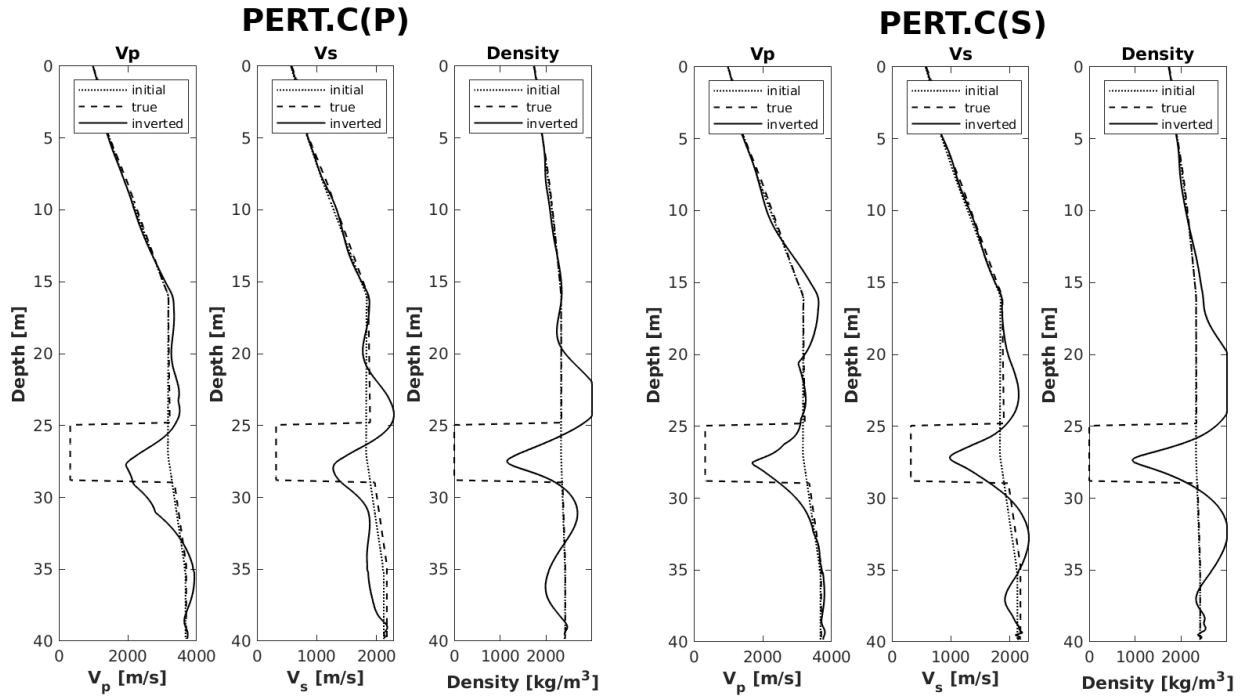
Figure 6.2.16: Depth profiles for Vp (left), Vs (middle) and density (right) at profile meter 63.68 m for the **PERT** model and inversion strategy **C** P-wave time-windowing (left three panels) and S-wave time-windowing (right three panels)
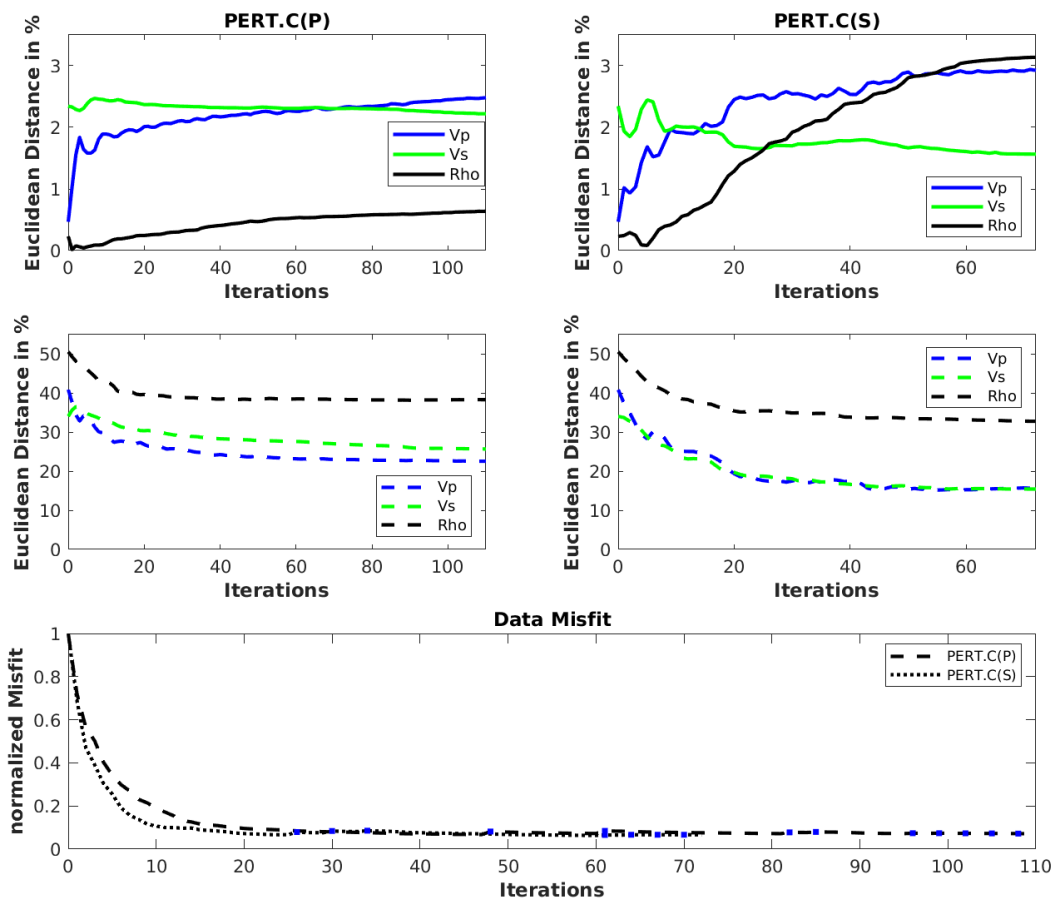
Figure 6.2.17: Upper panel: Euclidean distance of true and inverted models for **PERT.C(P)** (left) and **PERT.C(S)** (right); Middle panel: Euclidean distance of true and inverted models for **PERT.C(P)** (left) and **PERT.C(S)** (right) within the target area; Lower panel: normalised data misfit for **PERT.C(P)** (dashed line) and **PERT.C(S)** (dotted line); blue rectangles mark change in frequency band (note that this changes the misfit function each time the frequency band is changed)

6.2.5   Discussion and Conclusion of the Synthetic Inversion

The overall reconstruction of the cavity in the synthetic study worked very well. The cavity could clearly be reconstructed in all parameters in terms of size, shape and position in mostly all inversion approaches, except for Vp in case PERT.B. In this specific case a cavity location is not possible if only the P-wave inversion model is provided, but could be argued when considering Vs and density as well. Nevertheless the Euclidean distance within the target area is decreased in all cases and in all elastic parameters. Also the data misfit could be significantly decreased to at least but mostly more than 45 % of the initial misfit, except for the already mentioned case of PERT.B. When applying a specific time-windowing for P- or Surface-waves the specific shape of the cavity is indicated more clearly as in the other approaches. Here the greater lateral extent compared to the horizontal extent of the cavity is recovered as well, additionally to the size and position. On the other side the algorithm over-compensates the

Table 6.2.7: Summary of synthetic inversion results

Runs	max. decrease at target area			final misfit	L at target area [%]		
	Δ Vp [m/s]	Δ Vs [m/s]	$\Delta\rho[kg/m^3]$	[%]	Vp	Vs	Density
TTT.A	-1000	-600	-1940	40	-30	-25	-50
TTT.B	-2320	1780	-2250	14	-30	-30	-30
TTT.C(P)	-1240	-630	-1050	11	-20	-10	-10
TTT.C(S)	-2060	-1260	-1670	25	-20	-25	-20
PERT.A	-280	-230	-625	40	-10	-10	-20
PERT.B	-40	-220	-545	(+)45	0	-10	-25
PERT.C(P)	-1260	-780	-1400	7	-20	-10	-10
PERT.C(S)	-160	-940	-2060	6	-25	-20	-20

elastic properties above and below the cavity and therefore introduces artefacts that are not real and that are not as significant in the other two approaches. Analysing the TTT model exclusively, the greatest velocity and density reduction was achieved by inversion strategy B where an offset muting and LP-filtering was applied to the whole data set without any time-windowing. Generally the velocity decrease is better for time-windowed data (strategy C) than for the whole data set without any filtering (strategy A), whereas the density reduction is greater when the whole data is used instead of just P- or Surface-waves. Also the background artefacts are less for the time-windowed data, indicating that the algorithm is detained by making any changes that are not present within the P- or Surface-phase. In case of the perturbed model the biggest velocity and density reduction is achieved when a time-windowing is applied, namely a Surface-wave time window. The worst inversion results are obtained by the approaches without any time-windowing but with LP-filtering (TTT.B). Even though the cavity can confidently be identified within S-wave velocity and density, this is not true for P-wave velocity. The fact that the P-wave velocity is not changed at the position of the implemented cavity whereas in the rest of the model Vp is changed and additionally considering Vs and density allows the possibility of the presence of a cavity. In general, considering all synthetic inversion results, the cavity reconstruction worked best in density, since the cavity is clearly visible in all inversion approaches no matter what strategy is applied. Without doubt the cavity can be identified in all inverted density models, whereas it is sometimes difficult (e.g. Vs PERT.B) or not possible (e.g. Vp TTT.B) within the inverted velocity models. A discussion about density inversion is carried out in the later section 7.3.
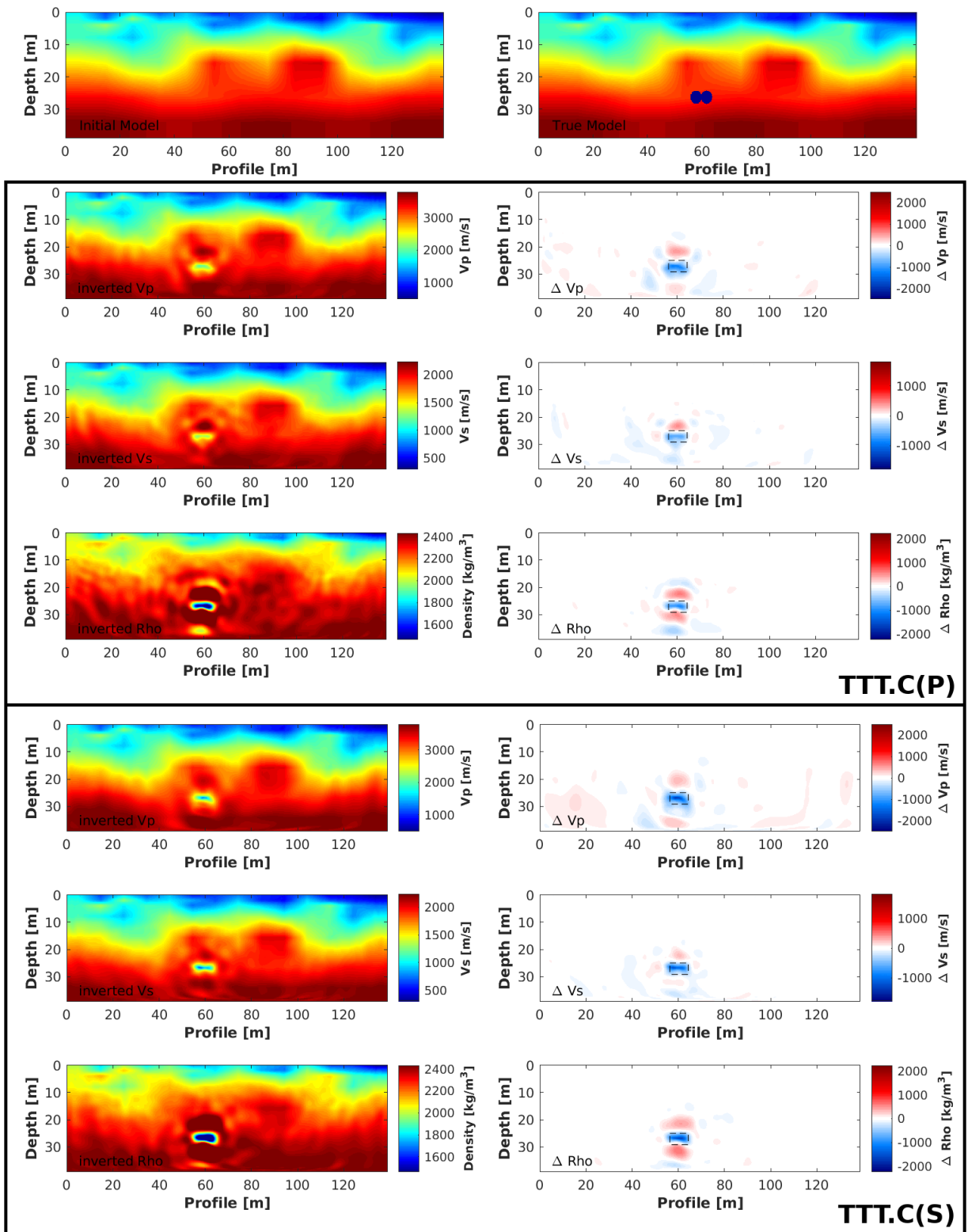
Figure 6.2.8: Initial (upper left) and true model (upper right) with inverted models (left panel) and difference models (right panels) for Vp (second panel), Vs (third panel) and density (lower panel) for the TTT model and inversion strategy C for P-waves (upper black box) after 82 iterations and Surface-waves (lower black box) after 76 iterations

110
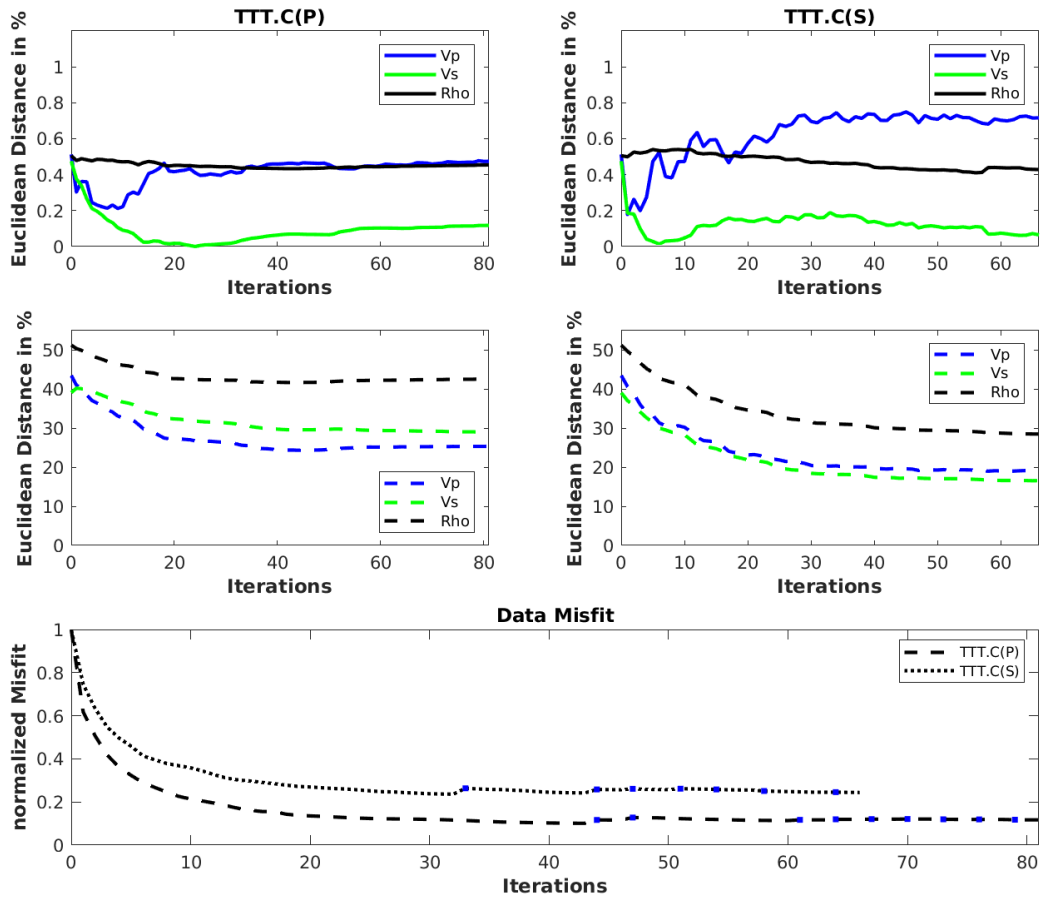
Figure 6.2.10: Upper panel: Euclidean distance of true and inverted models for **TTT.C(P)** (left) and **TTT.C(S)** (right); Middle panel: Euclidean distance of true and inverted models for **TTT.C(P)** (left) and **TTT.C(S)** (right) within the target area; Lower panel: normalised data misfit for **TTT.C(P)** (dashed line) and **TTT.C(S)** (dotted line); blue rectangles mark change in frequency band (note that this changes the misfit function each time the frequency band is changed)

Chapter 7

Elastic Parameter Inversion

7.1 Data Preparation

The observed data are recorded with 3-component geophones, measuring the seismic data in 3-dimensions, in-line, cross-line and vertical. Since the inversion code used is coded in 2-dimensions, the vertical and in-line components of the data are used for the inversion only. Thus, the amplitude decay with increasing offset due to geometrical spreading has to be considered and corrected for a 2-dimensional case. Therefore the real data were 3d-to-2d transformed by multiplying the data with the factor $\sqrt{t}$, were t is the travel time.

Additionally a removal of noise peaks appearing in the amplitude spectra of the data were removed. Looking at Fig. 4.3.4 in section 4.3.2 two distinct amplitude peaks in the noise spectra, but also in the amplitude spectra of the data in offset ranges 4 and 5 can be seen. The z-component amplitude spectra of offset range 5 without the noise spectra is once again displayed in Fig. 7.1.1 (left panel). Here the two peaks at 133.3 Hz and 266.6 Hz are marked by the black arrows. Since the frequency of the second peak is exactly two times the frequency of the first peak, the second peak is caused by a harmonic. As explained in section 4.3.1 the construction site of the ZAB is nearby and the construction work was in full progress at the time the survey was conducted. Since those outbursts are defined peaks, it is very unlikely that those peaks were caused by heavy machinery like dredgers or excavators, which would cause noise of a broader frequency range and no harmonic. It is more likely that those amplitude peaks are caused by some kind of machinery with constant rotation, like motors for poker vibrators or else. No matter where the noise comes from, it was filtered out by a Notch filter. The filtered amplitude spectra of the same offset range is displayed in the right panel of Fig. 7.1.1. The 3d-to-2d transformed, Notch filtered data are now used for the elastic parameter inversion.
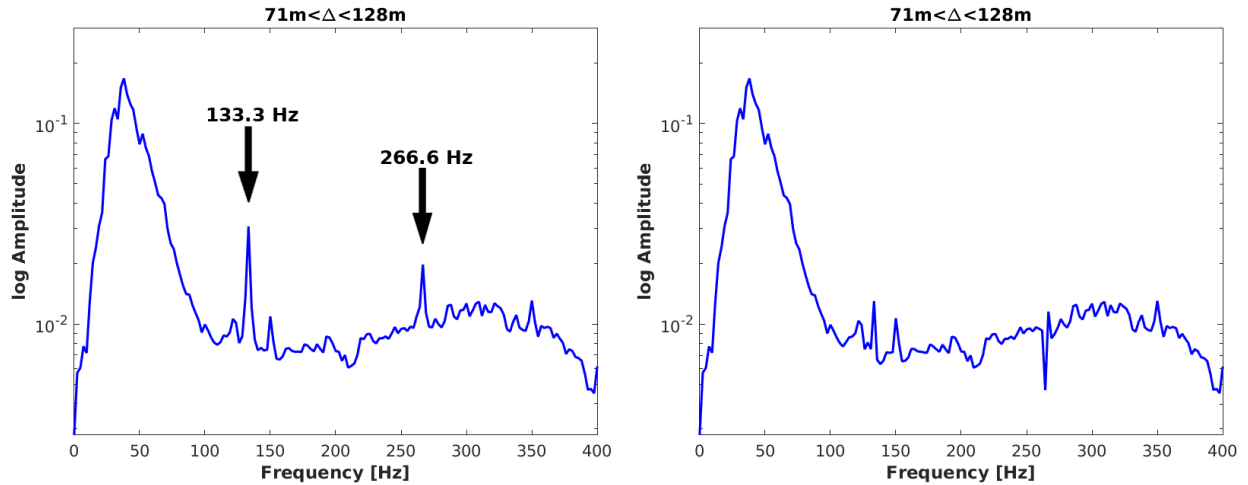
Figure 7.1.1: Unfiltered (left) and Notch filtered (right) z-component amplitude spectra of offset range 5; black arrows indicate frequency peaks within the spectra

7.2 Elastic Parameters Inversion of measured Field Data

In the following the inversion strategies B and C derived and tested in the previous synthetic study are applied to the real data measured in the field. Consequently the inversion runs will be referred to as REAL.B, REAL.C(P) and REAL.C(S). Additionally a third inversion strategy D is tested, which includes the band-pass filtering (BP-filtering) of the data. Also an inversion for the source time function is carried out, which was not necessary in the synthetic study, since the source wavelet is exactly known. The theory about the source time function inversion is summarised in appendix D, where also the inverted source time functions for each case are shown and discussed.

REAL.B In this inversion approach a LP-filtering between 1 and 400 Hz is applied, meaning that the upper corner-frequency is increased by 10 Hz steps each time the inversion algorithm cannot further decrease the data misfit more then 1 %, but is forced to try it al least two times within each frequency band. Again the inversion parameters are summarized in Tab. 7.2.1. The results of this inversion after 129 iterations are shown in Fig. 7.2.1 in the same manner as in the previous synthetic study. In the left panel, the initial and inverted models are displayed for Vp (second), Vs (third) and density (fourth), respectively, whereas on the right side the difference models between the initial and inverted models are plotted in the same order. Differently to the synthetic inversion of the TTT model or PERT model the cavity is not clearly reconstructed here. In fact in place of the suspected cavity (marked by the black dashed triangle) the P-wave and S-wave velocities are not changed compared to the rest of the model. The high velocity zone in Vp is concentrated to the right of the suspected cavity and the velocity increase in Vs is concentrated above. However in density the reduction at the position of the suspected cavity is in the range of -25 kg/m^3, which is not much compared to the overall density decrease of -590 kg/m^3 in the upper part of the

model (at roughly profile meters 10 and 115 m). Nevertheless it is eye-catching that in Vs as well as in density the increase of both parameters spares the region of the suspected cavity, leading to a convex structure. The data misfit is displayed in Fig. 7.2.2. Here the misfit is normalized by the initial misfit within the whole frequency band width and each cross marks the change in the upper frequency-corner. An example of trace fit is displayed in Fig. 7.2.3. One can see that the inverted and measured data fit quite nicely for the first arrivals within offset ranges 20 to 72 m in the x-component data and 8 to 112 m for the z-component data, respectively. Generally the data seem to fit better for the z-component.

Table 7.2.1: Parameter for inversion REAL.B

offset muting	yes
filtering	yes
taper	case 3.2
time windowing	no
STF inversion	yes
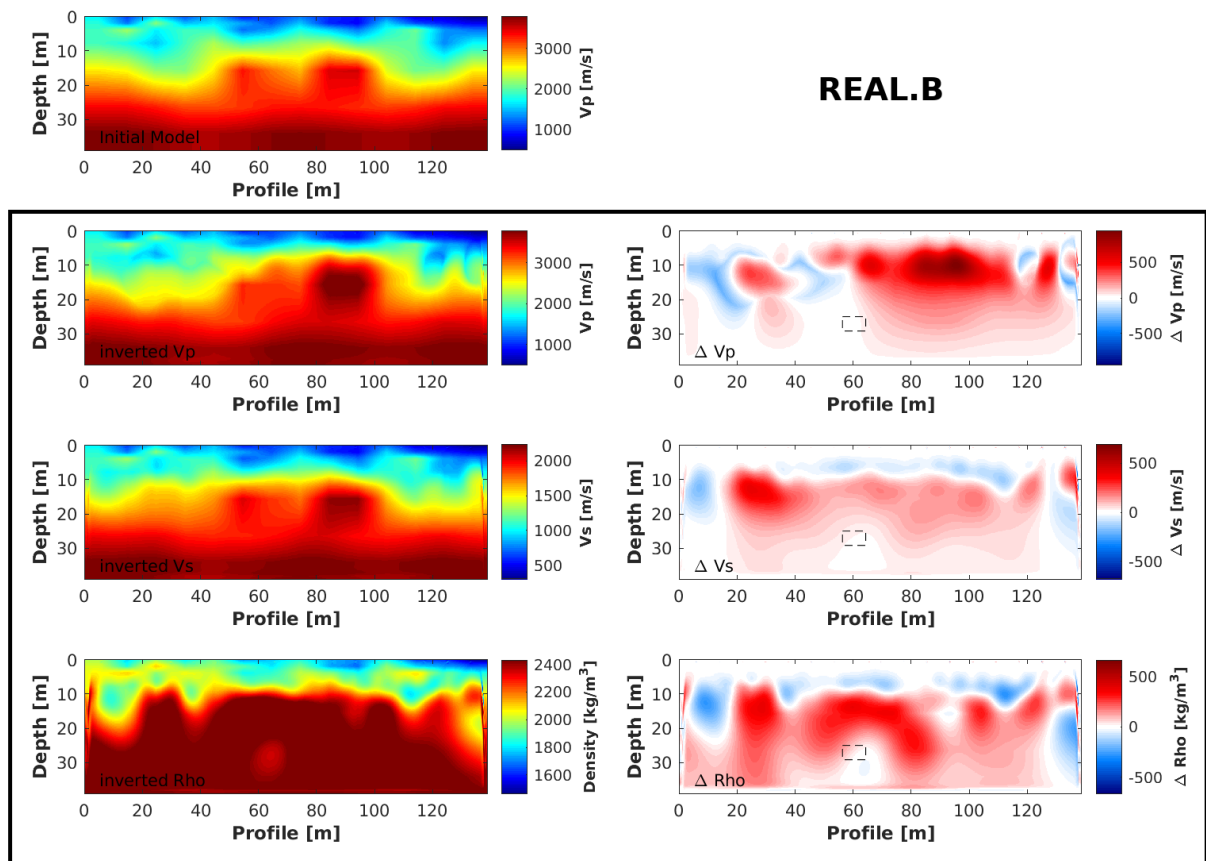
Figure 7.2.1: Initial (upper left), inverted (left panel) and difference models (right panels) for Vp (second panel), Vs (third panel) and density (lower panel) inversion strategy B after 129 iterations; the black dashed rectangle indicates the position of the suspected cavity
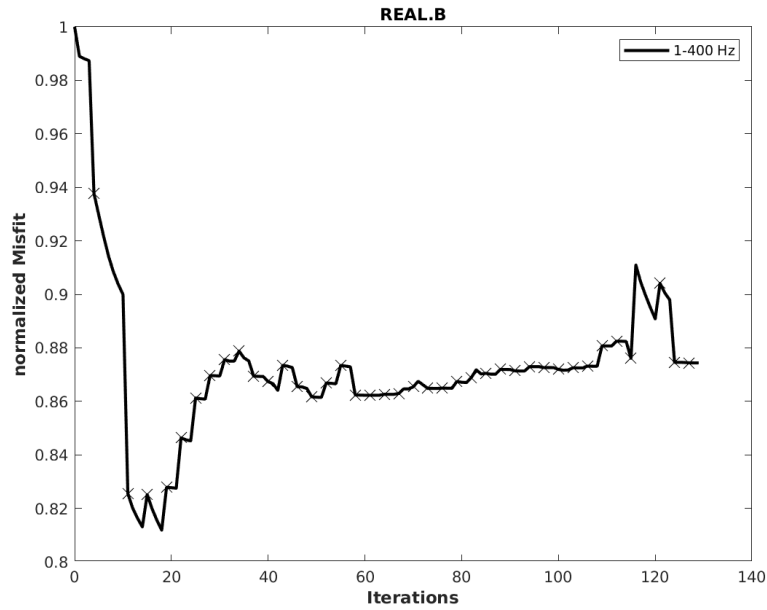
Figure 7.2.2: Misfit curve over iterations, crosses mark change of frequency band, the misfit is normalized to the initial misfit in the whole band width

Figure 7.2.3: Inverted (red) and measured field data (black) plotted upon each other for x-(left) and z-component (right), every second traces is shown

REAL.C(P) & REAL.C(S)   The same approach of time-windowing as it was defined as inversion strategy C is applied to the real data. As it is shown in the synthetic study, a significant phase shift caused by the cavity is present between 200 and 350 Hz within the P-wave time window and between 160 and 300 Hz in the Surface-wave time window. To verify if the sig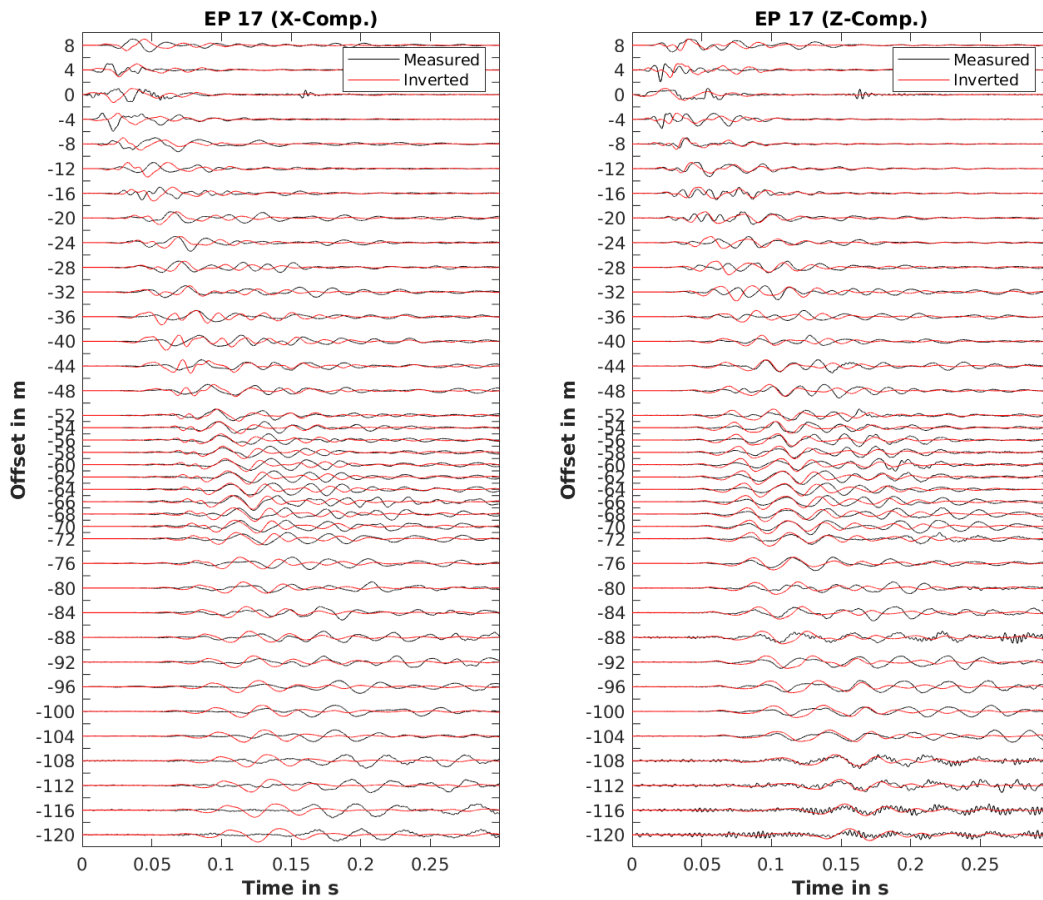nal is still strong enough within those frequency ranges, the amplitude spectra for the specific time windows is again plotted together with the noise spectra and shown in Fig. 7.2.4. In case of P-wave time-windowing the signal is very well separated from the noise for offsets smaller than 70 m, but falls within the noise range for offsets greater than that and frequencies above 200 Hz. This is crucial since the desired offset and frequency ranges for the targeted inversion of P-wave time windows lays just in these ranges (offset larger 50 m and frequencies higher than 200 Hz). The same can be seen for Surface-wave time-windowed data (right side of Fig. 7.2.4). Here the signal of the x-component data, which theoretically is dominated by S-waves, is in the same range as the noise level for offsets greater 30 m and frequencies higher than 320 Hz, which would be sufficient for the inversion. However, in the desired offset range, namely greater than 70 m, the signal is already in the same range as the noise at frequencies above 200 Hz. For that reason, the upper corner-frequency for the LP-filtering is once set to 60 Hz, 100 Hz, 150 Hz and 200 Hz for the P-wave inversion and to 20 Hz and 160 Hz for the Surface-wave inversion (Again a mixture of BP-filtering and LP-filtering is applied. However since the upper corner-frequency is increased only, the filtering is referred to as LP-filtering). The lowest corner-frequencies of 60 and 20 Hz, respectively, are determined by twice the lengths of the smallest time window applied. The corner-frequencies of 100 and 150 Hz are trials, since the phase shift displayed in Fig. 6.1.6 reaches nearly the critical threshold of 30° at those frequencies. Finally the highest starting corner-frequencies of 200 and 160 Hz, respectively, are determined by the phase shift displayed in Fig. 6.1.7. Since only a subset of shots is used (shots 1-6 and 13-18), which show phase shifts in the time-domain, the inversion was carried out with a deep taper (comp. case 3.1 in Fig. 6.2.1), to avoid model updates too close to the surface. This is a reasonable approach, because as it was analysed by the time-shift study, only shots with deep penetration depths show the influence of the cavity and therefore an update in the very shallow part of the model is not required. Tab. 7.2.2 summarized the inversion parameters used.

Table 7.2.2: Parameter for inversion REAL.C(P) and REAL.C(S)

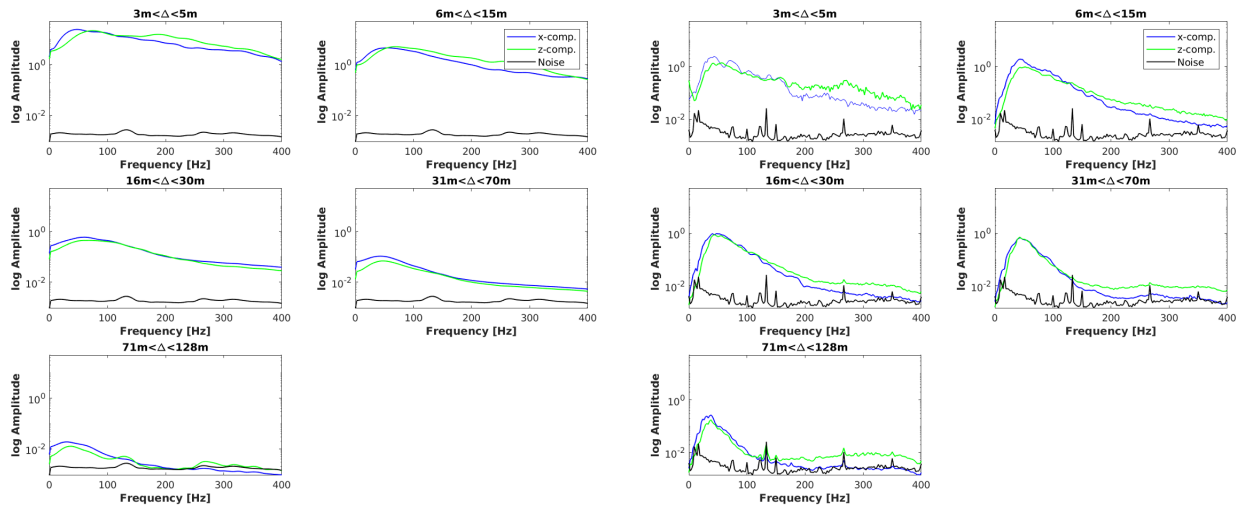|	
offset muting	yes
filtering	yes
taper	case 3.1
time windowing	yes
STF inversion	yes

Figure 7.2.4: Amplitude spectra for x-(blue) and z-component (green) data organised in five offset bins indicated on top of each sub-figure; left: P-wave time-windowed data; right: Surface-wave time-windowed data; note that the P-wave noise level is different to the Surface-wave noise level since the noise before the P-onset was considered

The inversion results for the P-wave time-windowing are displayed in Fig. 7.2.5. Looking at the upper left black box (frequency band between 60 and 350 Hz) a reduction in Vp and density at the position of the suspected cavity is visible. The velocity reduction in Vp is in the same range of the highest Vp reduction in the whole model, which is -430 m/s, and reaches a value of -380 m/s. Again a big area of increased P-wave velocity is introduced in the right part of the model, as it is seen in REAL.B. Also the velocity decrease at profile meter 50 in the upper parts of model REAL.B is here visible, but advances further down, towards the area of the suspected cavity. The density reduction reaches its maximum of -270 kg/m^3 closely below the dashed rectangle and therefore below the suspected cavity. This reduction is clearly visible within the inverted model and not only in the difference model. Overall the difference models show more small-scale variations, because the low-frequency content is missing. Those features of an indicated cavity get lost when higher starting corner-frequencies are applied. The velocity and density variations become smaller and have a higher amplitude (note that a standardized colour scale is used for all difference models). There is no structure recognisable any longer, leading to the assumption that for higher frequency-ranges only the noise is fitted by the algorithm, what was feared already by the spectral analysis of the signal and noise content of the P-wave time window. The normalised misfit over iterations is shown in Fig. 7.2.6. Again an example of data fit is displayed in Fig. 7.2.7 for the inverted and measured data with the frequency band of 60 to 350 Hz. Here the data fit better for later arrivals, especially in the x-component data within 16 to 88 m offsets, and in the z-component data within 28 to 54 m offsets, respectively. Nevertheless there are also phases that do not match at all, e.g. in the x-component data between 96 and 104 m and 0.2 to 0.27 s.
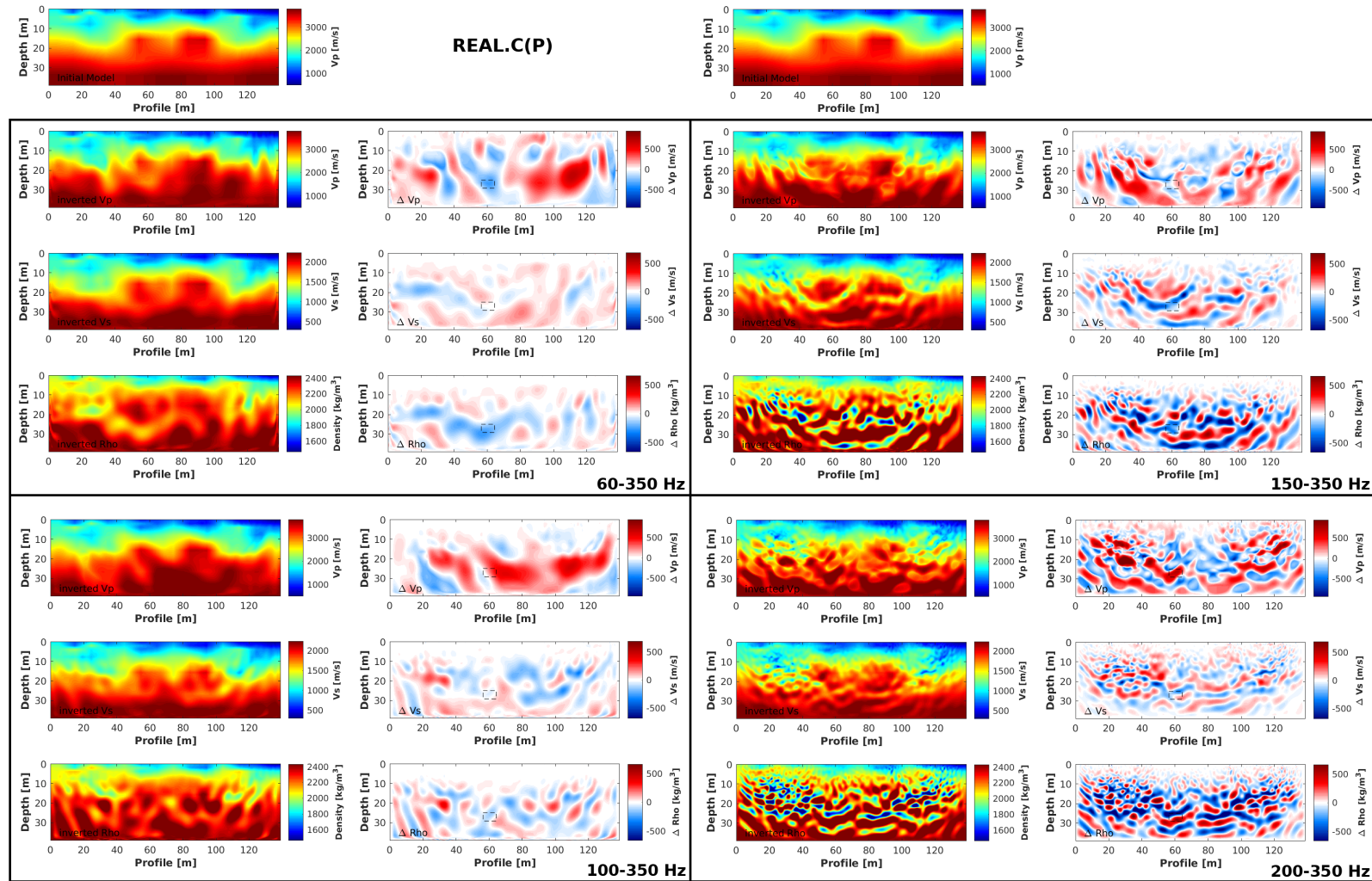
Figure 7.2.5: Upper panel: starting models, first and third column: inverted models for Vp (upper panel), Vs (second panel) and density (lower panel) within each black box; second and fourth column: difference models of the same order; frequency ranges are indicated in the lower right corner of each black box; upper left: P-wave time window inversion between 60 and 350 Hz after 89 iterations; lower left: P-wave time window inversion between 100 and 350 Hz after 81 iterations; upper right: P-wave time window inversion between 150 and 350 Hz after 60 iterations; lower right: P-wave time window inversion between 200 and 350 Hz after 81 iterations; the black dashed rectangle indicates the position of the suspected cavity
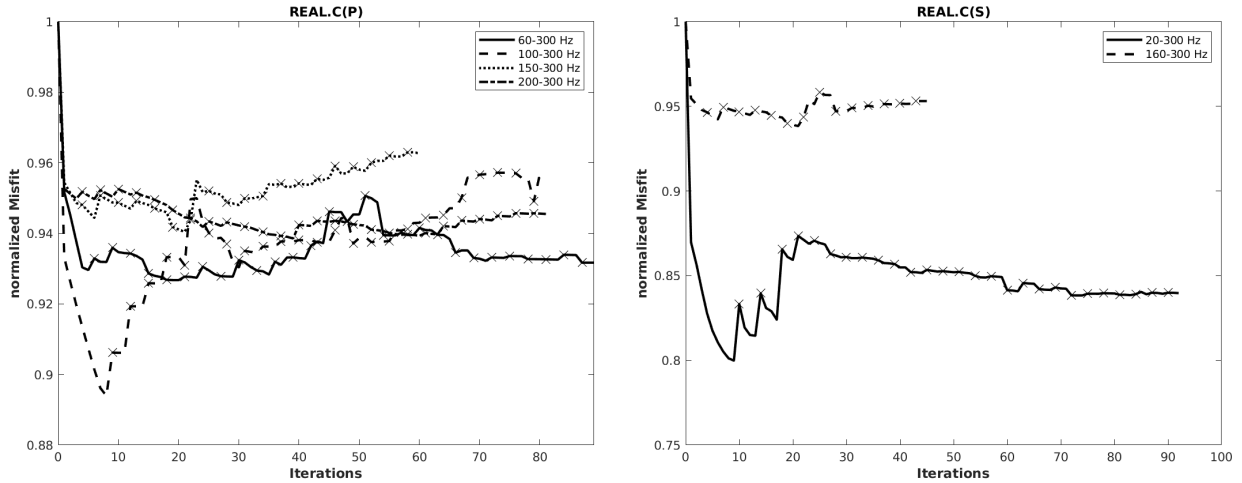
Figure 7.2.6: Misfit curve over iterations for P-wave time windowed data (left) and Surface-wave time-windowed data (right), crosses mark change of frequency band, the misfit is normalized to the initial misfit in the whole band width

Figure 7.2.7: Inverted (red) and measured field data (black) plotted upon each other for x-(left) and z-component (right) and frequency band of 60 to 350 Hz, every second traces is shown

The same strategy was applied to the Surface-wave time-windowed data. Once the frequency

range was chosen to be between 20 to 300 Hz and once between 160 to 300 Hz. The inversion outcome after 92 and 45 iterations is displayed in Fig. 7.2.8. In case of the lower starting frequency (upper black box) the only decrease in parameters at the position of the assumed cavity is indicated in Vp (difference model right). Here the velocity reduction is in the range of -250 m/s. However another Vp decrease of the same range of reduction is present right next to the assumed cavity between profile meters 80 to 100. Since both velocity reductions are nearly in the same range and show the same appearance it is not possible to locate the expected cavity unambiguously. Considering only that Vp difference model, the cavity could also be right next to the indicated position. No other inversion outcome of REAL.C(S) supports the identification of a cavity, since in both other properties, Vs and density, the values are increased. The inversion starting at higher frequencies displayed in the lower black box also suffers from fitting the noise instead of the actual signal as it was already the problem of P-wave time-windowed data and higher frequencies. This is also indicated by the misfit curve displayed in Fig. 7.2.6 (right), which is not significantly reduced. However the data fit of REAL.C(S) in Fig. 7.2.9 for a frequency range of 20-300 Hz shows quite a good match for later phases in the x-component data and offset ranges -16 to -78 and early phases in the z-component data for offset ranges greater than -80 m.

Figure 7.2.8: Upper panel: starting model, first column: inverted models for Vp (upper panel), Vs (second panel) and density (lower panel); second column: difference models of the same order; upper black box: results after 92 iterations for the frequency band 20-300 Hz; lower black box: results after 45 iterations for frequency band 160-300 Hz the black dashed rectangle indicates the position of the suspected cavity
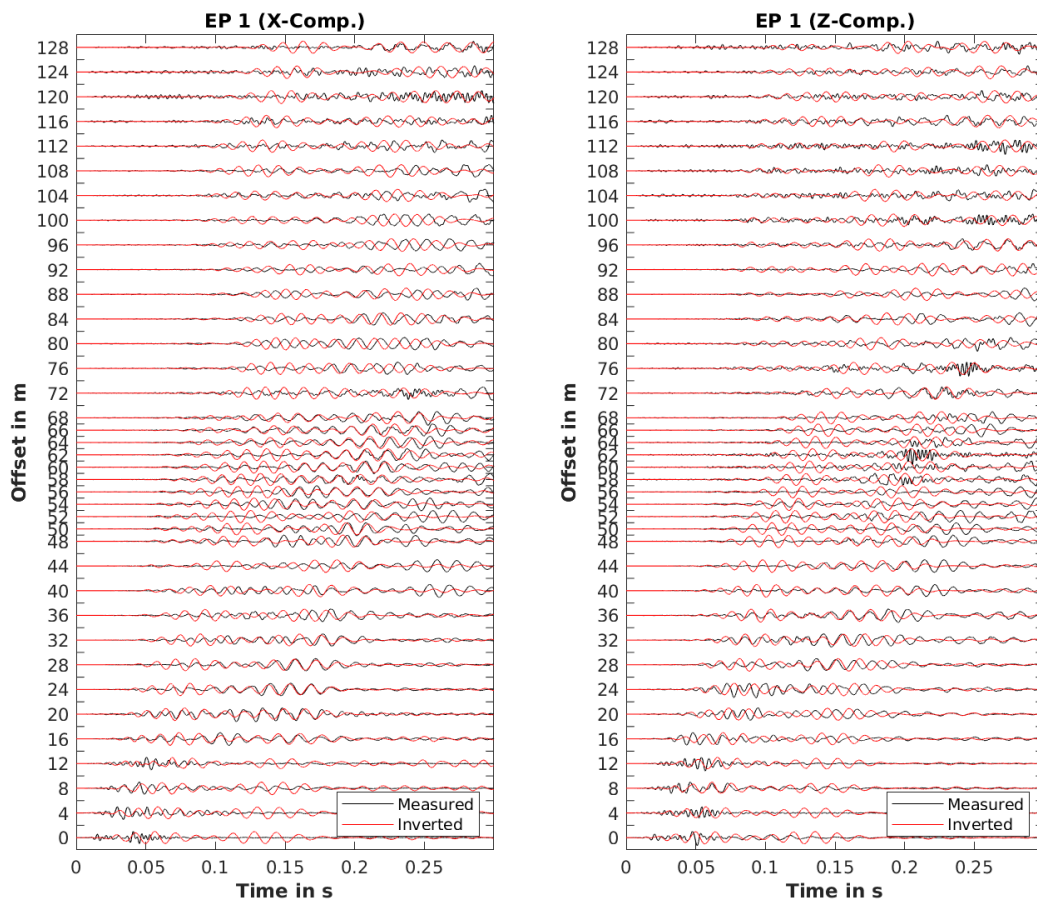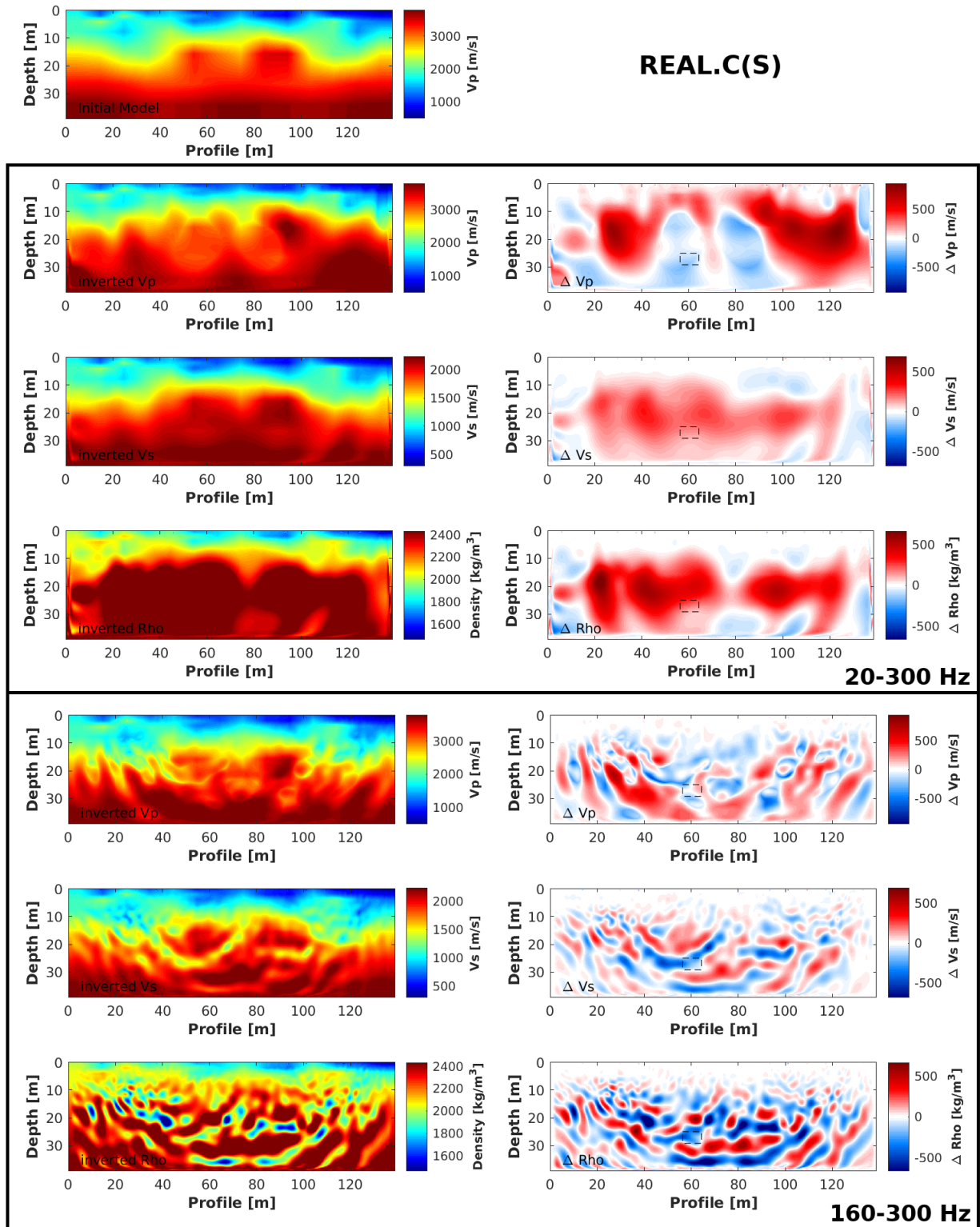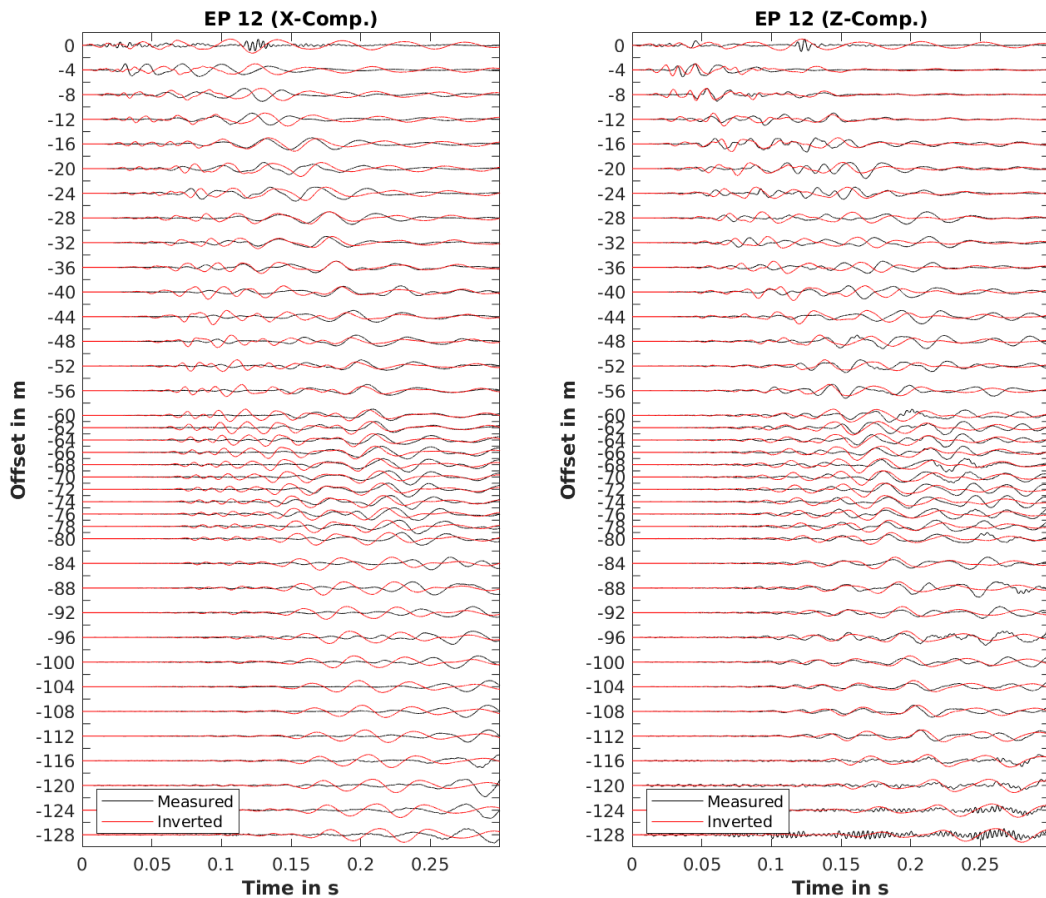
Figure 7.2.9: Inverted (red) and measured field data (black) plotted upon each other for x-(left) and z-component (right) and frequency band of 20 to 300 Hz, every second traces is shown

REAL.D As already mentioned a fourth inversion approach was applied to the measured field data (Tab. 7.2.3), which includes beside trace killing a BP-filtering of the data (Brossier et al. (2009)), meaning that the frequency bands were inverted successively, starting with a frequency range of 1-10 Hz and ending with the highest frequency range of 390 to 400 Hz. If the algorithm was not able to decrease the misfit any further within on frequency band, the next higher frequency was chosen. The inversion results are again depicted in Fig. 7.2.10. What is quite eye-catching is the density reduction, that is clearly visible in the inverted model, as well as in the difference model. The density decrease is in the range of -300 kg/m^3 and nearly exactly at the location of the suspected cavity marked by the black dashed rectangle. At the same position, Vs shows a reduction too, which is in the range of -122 m/s and therefore not as clearly and distinct as in density. However the position of velocity decrease in S-waves perfectly coincides with the location of density reduction, slightly shifted to the right of the marked area. Unfortunately the velocity reduction is not present in Vp, but even contrary the P-wave velocity is increased by 180 m/s at the position of the suspected cavity. Looking at the data misfit in Fig. 7.2.11 makes clear that the misfit reaches nearly

the value of the initial misfit after 80 iterations. The algorithm is not able to decrease the misfit any further, which coincides with frequency bands higher than 240 Hz. Fig. 7.2.12 shows an example of trace fit for shot 14 within the frequency band of 120-130 Hz. As in the previous runs, there are parts were the fit is quite good, e.g. in the z-component data (right) between offset ranges 8 to 28 m or -52 to -80, or in the x-component data (left) for offset ranges greater -76 m, but also areas were the data do not fit (e.g. in the x-component data at offset ranges -24 to -64 m for the first arrivals).

Table 7.2.3: Parameter for inversion REAL.D

offset muting	yes
filtering	yes
taper	case 3.2
time windowing	no
STF inversion	yes
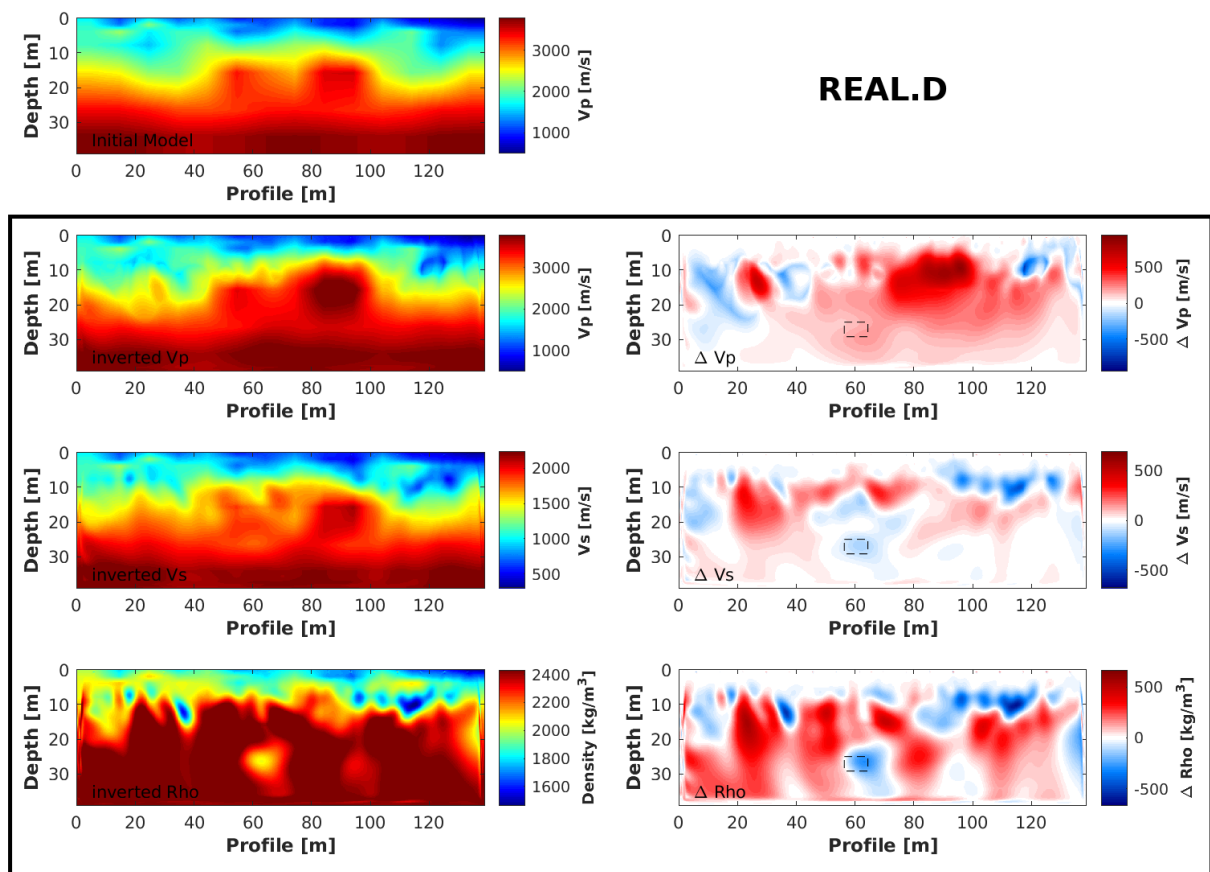
Figure 7.2.10: Upper panel: starting model, first column: inverted models for Vp (upper panel), Vs (second panel) and density (lower panel) after 128 iterations; second column: difference models of the same order; the black dashed rectangle indicates the position of the suspected cavity
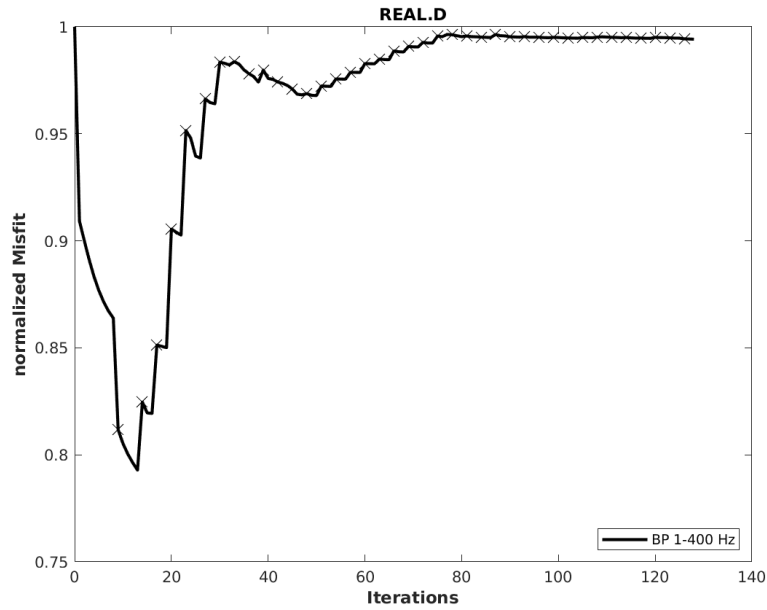
Figure 7.2.11: Misfit curve over iterations for REAL.D, crosses mark change of frequency band, the misfit is normalized to the initial misfit in the whole band width
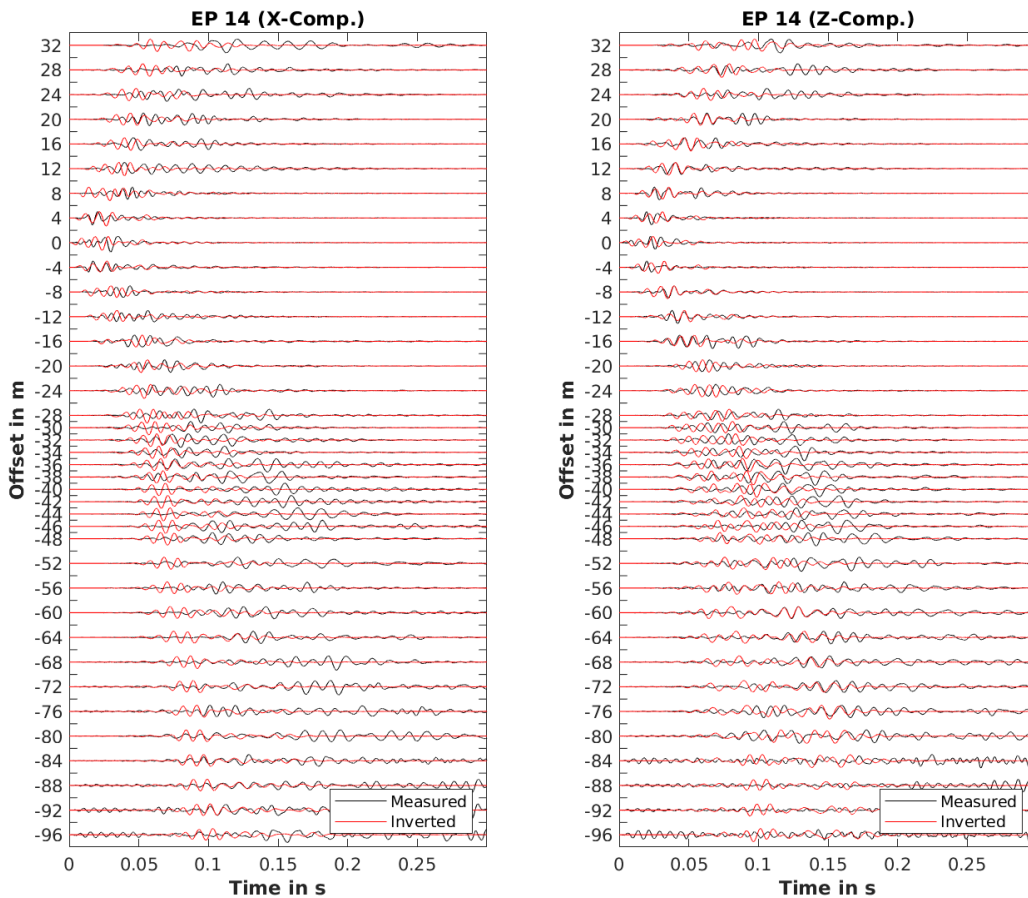
Figure 7.2.12: Inverted (red) and measured field data (black) plotted upon each other for x-(left) and z-component (right) and frequency band of 120 to 130 Hz, every second traces is shown

125

7.3 Discussion and Conclusion of the elastic Parameters Inversion

The inversion strategies derived from the synthetic study were applied to the measured field data more or less successfully. Inversion strategies B and D included all shots, a trace killing of near-offset traces and a LP-filtering or BP-filtering, respectively. Strategy C included an offset muting of the first 50 m, a time-windowing of P- or Surface-waves and a LP-filtering with the possible frequency band. All inverted P-wave models increased the velocity in the right part of the model between profile meters 80 to 100 and in 10 to 20 m depth. Generally the P-wave models seem more heterogeneous in the left part of the model. The decrease of velocity in the very left between 0-20 m is also recovered in all inversion outcomes and also in all three parameters. The inversion results for S-waves and density look quite similar for all inversions except REAL.C(P). Vs and density are increased throughout the whole model, except in the very shallow parts, on the sides and in cases REAL.B and REAL.D in the area of the suspected cavity. Here both properties are decreased, or do not change significantly. The suspected cavity could not clearly be identified in all three parameters within one single inversion approach. It is indicated either by Vs and density or by Vp alone, except for REAL.C(P) were it is indicated in Vp and density. The P-wave velocity reduction at the area of the suspected cavity is in the ranges of -380 m/s (REAL.C(P)) and -250 m/s (REAL.C(S)) and only indicated if a time-windowing is applied to the data. However the shape is not well defined and the indicated cavity appears as an extensive, smeared low-velocity zone. Also the velocity decrease in the area of the suspected cavity is not unique, since other parts of the Vp models were decreased as well and those reductions are in the same range as at the supposedly cavity position. A targeted inversion of P- ans Surface-wave time-windowed data for higher frequencies has failed, since the signal-to-noise ratio is not sufficient enough and the algorithm fitted the noise instead of the signal. Surprisingly the cavity is not indicated in the S-wave model when a targeted inversion of Surface-waves is carried out, but is indicated in all other approaches by a velocity decrease (REAL.C(P) and REAL.D) or by not changing at all even if everywhere else in the model the velocity is changed (REAL.B). The reduction of Vs is in the range of -122 m/s in REAL.D, which is not much, but noticeable since the velocity is increased in the vicinity. The same applies for REAL.B. Here the velocity decrease is in the range of several m/s, but it seems that the velocity increase spares the region of the suspected cavity. The most eye-catching inversion result is present in REAL.D, which is the density reduction of $300 \, kg/m^3$ and therefore introducing a clearly visible low-density area in the inverted model and that at the position of the suspected cavity. Also noteworthy is the appearance of that low-density feature, which is very well defined in a circular form. This characteristic can also be detected in REAL.B, where the density is slightly reduced, by just about -25 kg/m^3, but again the density increase in the vicinity spares exactly the position of the suspected cavity. The decrease of density in REAL.C(P) is nearly in the same range as

in REAL.D, but here the shape is not as well defined as in REAL.D.

The inversion of density has broadly been discussed over the last few years by different authors. The impedance, the product of P-wave velocity and density, determines the amplitudes of seismic waves. Both types of perturbations, pure velocity or pure density perturbation, cause the scattering of wavefields, but the amplitudes caused by a pure density anomaly decrease from small to large angles and offsets (Bai and Yingst (2014)). Keeping density fixed or neglecting it during the inversion process, projects all perturbations into the P-velocity model. Several authors already showed that neglecting density in the inversion process leads to distorted velocity results (e.g. Przebindowska et al. (2011) and Bai and Yingst (2014)). An extensive and detailed study of the role of density in the inversion process was conducted by Blom (2018). In her PhD studies she tested different inversion approaches, e.g. updating all three parameters (Vp, Vs, density), neglecting density and just invert for Vp and Vs, scaling density to Vs, including velocity models that exhibit only a specific amount of velocity structure, invert for density exclusively and keeping Vp and Vs fixed, adding noise to the inversion and many more. All inversion tests led to the conclusion that neglecting or fixing density during the inversion introduces more or less severe artefacts with the inverted density model, but also in velocity. She also concluded that the strength of density perturbation plays an important role on the recovery of that perturbation, if the perturbation is strong, the recovery is better than for a weaker perturbation. In our case, the cavity would possess the greatest density perturbation possible. Noise plays also a big role in the reliability of (velocity and) density reconstruction, since a high noise level deteriorates the parameter recovery and introduces artefacts (as seen in inversions REAL.C(P) and REAL.(S) for higher frequencies). Her conclusion was that it is indeed possible to recover density as an independent parameter in 2-dimensional waveform tomography. The recovery strongly depends on the low-frequency content of the data. In Fig. 7.3.1 the reduction of density at the position of the suspected cavity is plotted over iterations. It becomes obvious that the density reduction is strongest in the first several iterations and stops after roughly 55 iterations in REAL.B, which corresponds to an upper LP-corner-frequency of 160 Hz, after 35 iterations in REAL.C(P) and therefore at an upper corner-frequency of 170 Hz and after 47 iterations in REAL.D, corresponding to a frequency range of 120-130 Hz. After those thresholds the density is not significantly decreased any further.

Looking at one inversion outcome alone does not allow a reliable and unambiguous location of the suspected cavity. However considering all inversion results, there might be an indication of a cavity, of course only if a priori knowledge of a cavity is available.
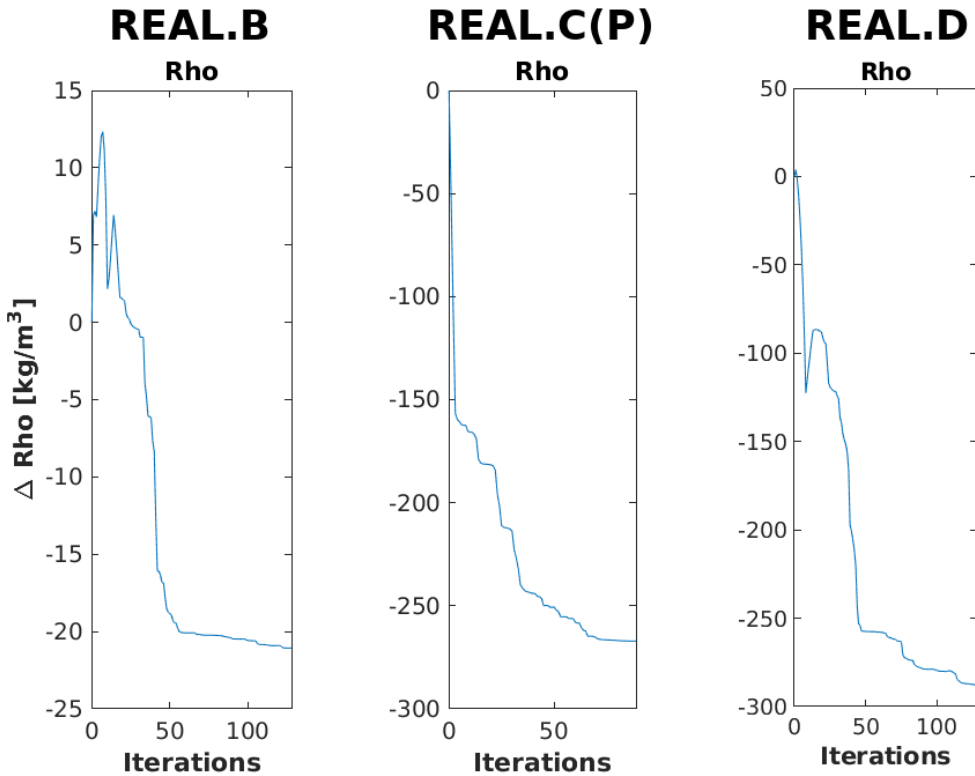
Figure 7.3.1: Density reduction plotted over iterations at the position of the suspected cavity for REAL.B (left), REAL.C(P) (middle) and REAL.D

Chapter 8

Conclusion and Outlook

In this thesis two different inversion algorithms were applied to a simple cross-hole configuration, whereby both of these algorithms shows a very good reconstruction of the implemented velocity anomaly. this reconstruction is meant in terms of position, size and sign of perturbation, whether the anomalies for Vp and Vs were placed at coinciding positions or not. The convergence of both algorithms is fast and could reduce the data misfit over the first several iterations significantly. The newly developed inversion algorithm viselawi2d should be tested in further works with the application of more complex model, for example the Marmousi model. Further the acquisition and data processing of two data sets at the test site of Mt. Erzberg where old mine maps indicate an abandoned tunnel in 25 m depth and a diameter of 4 m, were described. In survey one, hammer strikes were used as sources and in survey two, explosives were used, whereas the former source type resulted in unsatisfactory signal-to-noise ratio. Nevertheless the data processing shows that a proper normalisation, stacking routine and rotation can further increase the signal quality. However the data acquired with the explosives is considered for a travel-time tomography resulting in a sophisticated starting model for synthetic studies on the behaviour of the wavefield in the presence of a subsurface cavity. It is shown that the cavity causes phase shifts in the wavefield for shots at the beginning or end of the profile and therefore for shots with great penetration depths. Three main inversion strategies are determined by the synthetic study: strategy A, including a trace killing and no filtering; strategy B, including a trace killing and a LP-filtering and strategy C, including an offset mute, a LP-filtering and a time-windowing of P- and Surface-waves, respectively. The synthetic inversion tests are performed taking the travel-time tomography model and a perturbed version of the tomography model into consideration. The synthetic inversion results show a very satisfying reconstruction of the implemented cavity in nearly each inversion approach and elastic parameter. With that knowledge the inversion strategies are applied to the measured field data of the second survey, additionally applying a fourth strategy C, including trace killing and a BP-filtering of the data. Unfortunately, the suspected cavity could not be reliably and undoubtedly be reconstructed as in the synthetic case. Considering all inversion results and applying a priori knowledge, the cavity could be argued as indicated

at best. Since the overall signal-to-noise ratio of the data from the second survey is quite satisfactory, that does not account for the signal-to-noise ratio in case a time-windowing is applied. The inversion of higher frequencies was not possible and the algorithm fitted the noise instead of the signal. Here one point of improvement would be to used another type of source for the data acquisition, like a vibration source. Such kind of source would generate low to high frequencies and depending on the sweep time, the signal could be strong enough to exceed the noise level even for higher frequencies.

Chapter 9

Acknowledgement

Bibliography

1000things (2018). Bird's Eye View of Erzberg. `https://www.1000things.at/info/abenteuer-erzberg/`. Accessed: 17.01.2019.

Andreichuk, V., Eraso, A., and Dominguez, M. (2000). A large sinkhole in the Verchnekamsky potash basin in the Urals. *Mine Water and the Environment*, 19; p. 2–18.

Aster, R. C., Borchers, B., and Thurber, C. H. (2013). *Parameter Estimation and Inverse Problems*, volume 2. Elsevier.

Bai, J. and Yingst, D., editors (2014). *Simultaneous inversion of velocity and density in time-domain fill waveform inversion.*

Berkhout, A. J. (1984). Multidimensional linearized inversion and seismic migration. *Geophysics*, 49; p. 1881–1895.

Bleibinhaus, F. (2014). Simul Code Family.

Bleibinhaus, F., Lester, R. W., and Hole, J. A. (2009). Applying waveform inversion to wide-angle seismic surveys. *Tectonophysics*, 472; p. 238–248.

Bleibinhaus, F. and Rondenay, S. (2009). Effects of surface scattering in full-waveform inversion. *Geophysics*, 74; p. 69–77.

Blom, N. (2018). *Towards imaging density using waveform tomography*. PhD thesis, University Utrecht.

Brossier, R., Operto, S., and Virieux, J. (2009). Seismic imaging of complex onshore structures by 2D elastic frequency-domain full-waveform inversion. *Geophysics*, 74; p. 105–118.

Bryda, G., van Husen, D., Kreuss, O., Koukal, V., Moser, M., Pavlik, W., Schönlaub, H. P., and Wagreich, M. (2013). *Geologische Karte der Republik Österreich 1:50000, Erläuterungen zu Blatt 101 Eisenerz*. Geologische Bundesanstalt, Neulinggasse 38 1030 Wien.

Bunks, C., Saleck, F. M., Zaleski, S., and Chavent, G. (1995). Multiscale seismic waveform inversion. *Geophysics*, 60; p. 1457–1473.

Cardarelli, E., Cercato, M., Cerreto, A., and Filippo, G. D. (2009). Electrical resistivity and seismic refraction tomography to detect buried cavities. *Geophysical Prospecting*, 58; p. 685–695.

Courant, R., Friedrichs, K., and Lewy, H. (1928). Über die partiellen Differenzialgleichungen der mathematischen Physik. *Mathematischen Analen*, 100; p. 32–74.

Crase, E., Pica, A., Noble, M., McDonalds, J., and Tarantola, A. (1990). Robust elastic nonlinear waveform inversion: Application to real data. *Geophysics*, 55; p. 527–538.

DMT (2017). *SUMMIT X ONE - Operation manual*. DMT GmbH & Co. KG, Am Technologiepark 1 45307 Essen Germany.

Driad, L. and Piwakowski, B. (2014). Detection and characterization of underground cavities using high resolution seismic reflection (HRSR). In *8th Meeting Environmental and Engineering Geophysics*.

Erzberg, V. A. (2018a). Chronicle of ore production at Mt. Erzberg. `http://www.vaerzberg.at/unternehmen/chronik.html`. Accessed: 26.09.2018.

Erzberg, V. A. (2018b). Geology of Mt. Erzberg. `http://www.vaerzberg.at/erzproduktion/geologie.html`. Accessed: 27.09.2018.

Evans, J. R., Eberhart-Phillips, D., and Thurber, C. H. (1994). User's manual for SIMULPS12 for imaging vp and vp/vs: A derivative for the "Thurber" tomographic inversion SIMUL3 for local earthquakes and explosions. Technical report, U.S. Department of the Interior, U.S. Geological Survey.

Fichtner, A. (2011). *Full Seismic Waveform Modelling and Inversion*, volume 1 of *Advances in Geophysical and Environmental Mechanics and Mathematics*. Springer.

Fiore, V. D., Angelino, A., Passaro, S., and Bonanno, A. (2013). High resolution seismic reflection methods to detect near surface tuff-cavities: a case study in the neapolitan area, Italy. *Journal of Cave and Karst Studies*, 75; p. 51–59.

Flajs, G. and Schönlaub, H. P. (1976). Die biostratigraphische Gliederung des Altpaläozoikums am Polster bei Eisenerz (Nördliche Grauwackenzone, Österreich). *Verh. Geol. B.-A.*, 2; p. 257–303.

Forbriger, T. (2014). soutifu and libstfinv. `https://www.opentoast.de/Data_analysis_code_soutifu_and_libstfinv.php`. Accessed: 20.08.2020.

Galler, R. (2016). Research@ZaB- Start of construction of the "ZaB-Zentrum am Berg" research and development, training and education centre. *Geomechanics and Tunnelling*, 6; p. 715–725.

Galloway, D., Jones, D. R., and Ingebritsen, S. (1999). Land subsidence in the United States. Technical report, UGSG.

Gardner, G. H. F., Gardner, L. W., and Gregory, A. R. (1974). Formation velocity and density - the diagnostic basics for stratigraphic traps. *Geophysics*, 39; p. 770–780.

Gauthier, O., Virieux, J., and Tarantola, A. (1986). Two-dimensional nonlinear inversion of seismic waveforms: Numerical results. *Geophysics*, 51; p. 1387–1403.

Giorgi, L. D. and Leucci, G. (2014). Detection of Hazardous Cavities Below a Road Using Combined Geophysical Methods. *Surv Heophys*, 35; p. 1003–1021.

Grandjean, G. and Leparoux, D. (2004). The potential of seismic methods for detecting cavities and buried objects: experimentation at a test site. *Journal of Applied Geophysics*, 56; p. 93–106.

Groos, L. (2013). *2D full waveform inversion of shallow seismic Rayleigh waves*. PhD thesis, Karlsruher Institut für Technologie.

Hewitt, E. and Hewitt, R. E. (1979). The Gibbs-Wilbraham Phenomenon: An Episode in Fourier Analysis. *Archive for History of Exact Sciences*, 21; p. 129–160.

Hirzbauer, G., Stromberger, A., Schulz, O., and Vavtar, F. (1991). Neuerkenntnisse über das tektonische Gefüge des Steirischen Erzberg. *Archiv für Lagerstättenforschung*, Band 13; p. 51–85.

Hole, J. A. (1992). Nonlinear High-Resolution Three-Dimensional Seismic Travel Time Tomography. *Journal of Geophysical Research*, 97; p. 6553–6562.

Hole, J. A. and Zelt, B. C. (1995). 3-D finite-difference reflection traveltimes. *Geophys. J. Int.*, 121; p. 427–434.

Igel, H., Djikpéssé, H., and Tarantola, A. (1996). Waveform inversion of marine reflection seismograms for P impedance and Poisson's ratio. *Geophys. J. Int.*, 124; p. 363–371.

Kelly, K. R., Ward, R. W., Treitel, S., and Alford, R. (1976). Synthetic Seismograms: A finite-difference Approach. *Geophysics*, 41; p. 2–27.

Köhn, D. (2011a). IFOS2D User Manual.

Köhn, D. (2011b). *Time Domain 2D Elastic Full Waveform Tomography*. PhD thesis, Christian-Albrechts-Universität.

Komatitsch, D. and Martin, R. (2007). An unsplit convolutional perfectly matched layer improved at grazing incidence for the seismic wave equation. *Geophysics*, 72; p. 155–167.

Krebs, J. R., Anderson, J. E., Hinkley, D., Neelamani, R., Lee, S., Baumstein, A., and Lacasse, M.-D. (2009). Fast full-wavefield seismic inversion using encoded sources. *Geophysics*, 74; p. 177–188.

Kurzmann, A., Köhn, D., Przebindowska, A., Nguyen, N., and Bohlen, T. (2008). Performance of acoustic full waveform tomography for different acquisition geometries. Technical report, TU Freiberg, Germany.

Levander, A. R. (1988). Forth-order finite-difference P-SV seismograms. *Geophysics*, 53; p. 1425–1436.

Martin, R. and Komatitsch, D. (2009). An unsplit conventional perfectly matched layer technique improved at gazing incidence for the viscoelastic wave equation. *Geophys. J. Int.*, 179; p. 333–344.

Menke, W. (2012a). Chapter 3 - solution of the linear, gaussian inverse problem, viewpoint 1: The length problem. In Menke, W., editor, *Geophysical Data Analysis: Discrete Inverse Theory (Third Edition)*, pages 39 – 68. Academic Press, Boston, third edition edition.

Menke, W. (2012b). Chapter 7 - applications of vector spaces. In Menke, W., editor, *Geophysical Data Analysis: Discrete Inverse Theory (Third Edition)*, pages 123 – 148. Academic Press, Boston, third edition edition.

Miller, R. D. and Steeples, D. W. (1991). Detecting voids in a 0.6 m coal seam, 7 m deep, using seismic reflection. *Geoexploration*, 28; p. 109–119.

Mora, P. (1987). Nonlinear two-dimensional elastic inversion of multioffset seismic data. *Geophysics*, 52; p. 1211–1228.

Mora, P. (1988). Elastic wave-field inversion of reflection and transmission data. *Geophysics*, 53; p. 750–759.

Operto, S., Ravaut, C., Improta, L., Virieux, J., Herrero, A., and Dell'Aversana, P. (2004). Quantitative imaging of complex structures from dense wide-aperture seismic data by multiscale traveltime and waveform inversions: a case study. *Geophysical Prospecting*, 52; p. 625–651.

Paschke, M. (2016). Part 1: Mathematical Theory.

Paschke, M., Krause, M., and Bleibinhaus, F. (2016). Visco-elastic controlled-source full waveform inversion without surface waves. In *Proceedings of 78th EAGE Conference and Exhibition 2016*. European Association of Geoscientists and Engineers.

Peterie, S. L. and Miller, R. D. (2015). Near-surface scattering phenomena and implications for tunnel detection. *Interpretation*, 3; p. 43–54.

Pratt, R. G. (1990). Inverse Theory applied to multi-source cross-hole Tomography. Part 2: Elastic wave-equation Method. *Geophysical Prospecting*, 38; p. 311–329.

Pratt, R. G. and Worthington, M. H. (1990). Inverse Theory applied to multi-source cross-hole Tomography. Part 1: Acoustic wave-equation Method. *Geophysical Prospecting*, 38; p. 287–310.

Przebindowska, A., Kurzmann, A., Köhn, D., and Bohlen, T., editors (2011). *The role of density in acoustic full waveform inversion of marines reflection seismics*.

Pullan, S. E. and MacAulay, H. A. (1987). An in-hole shotgun source for engineering seismic surveys. *Geophysics*, 52; p. 985–996.

Quanyuan, W., Jiewu, P., Shanzhong, Q., Yiping, L., Congcong, H., Tingxiang, L., and Limei, H. (2009). Impacts of coal mining subsidence on the surface landscape in Longkou city, Shandong Province of China. *Environ Earth Sci*, 59; p. 783–791.

Robertsson, J. A. (1996). A numerical free-surface condition for elsatic/viscoelastic finite-difference modelling in the presence of topography. *Geophysics*, 61; p. 1921–1934.

Robertsson, J. O. A., Blanch, J. O., and Symes, W. W. (1994). Viscoelastic finite-difference modelling. *Geophysics*, 59; p. 1444–1456.

Romdhane, A. and Querendez, E. (2014). CO2 characterization at the Sleipner field with full waveform inversion: application to synthetic and real data. *Energy Procedia*, 63; p. 4358–4365.

Schmelzbach, C., Sollberger, D., Greenhalgh, S., Horstmeyer, H., Maurer, H., and Robertsson, J. (2016). 9C seismic data acquisition for near-surface applications: recording, waveform reciprocity and 4C rotation. In *78th EAGE Conference & Exhibition 2016 - Workshop Programme*.

Schön, J. H. (2011). *Physical Properties of Rocks*, volume 8 of *Handbook of Petroleum Exploration and Production*. Elsevier B. V.

Schönlaub, H. P. (1982). Die Grauwackenzone in den Eisererzer Alpen (Österreich). *Jahrb. Geolog*, Band 124, Heft 2; p. 361–423.

Schönlaub, H. P., Flajs, G., and Thalmann, F. (1980). Conodontenstratigraphie am Steirischen Erzberg (Nördliche Grauackenzone). *Jahrb. Geol. B.-A.*, Band 123, Heft 1; p. 169–229.

Schulz, O., Vavtar, F., and Dieber, K. (1997). Die Siderit-Erzlagerstätte Erzberg: Eine geowissenschaftliche Studie, mit wirtschaftlicher und geschichtlicher Betrachtung. *Archiv für Laergstättenforschung der geologischen Bundesanstalt*, 20; p. 65–178.

Schuster, G. T. (2017). *Seismic Inversion*, volume 1. Society of Exploration Geophysicists.

Shao, G. Z., Tsoflias, G. P., and jiang Li, C. (2016). Detection of near-surface cavities by generalized S-transform of Rayleigh waves. *Journal of Applied Geophysics*, 129; p. 53–65.

Sheriff, R. E. and Geldart, L. P. (1995). *Exploration Seismology*. Cambridge University Press.

Shin, C., Koo, N.-H., Cha, Y. H., and Park, K.-P. (2010). Sequentially ordered single-frequency 2-D acoustic waveform inversion in the Laplace-Fourier domain. *Geophys. Int. J.*, 181; p. 935–950.

Shin, C. and Min, D.-J. (2006). Waveform inversion using a logarithmic wavefield. *Geophysics*, 71; p. 31–42.

Shin, C., Yoon, K., Marfurt, K. J., Park, K., Yang, D., Lim, H. Y., Chung, S., and Shin, S. (2001). Efficient calculation of a partial-derivative wavefield using reciprocity for seismic imaging and inversion. *Geophysics*, 66; p. 1856–1863.

Sirgue, L. and Pratt, R. G. (2004). Efficient waveform inversion and imaging: A strategy for selecting temporal frequencies. *Geophysics*, 69; p. 231–248.

Sladky, T. (2018). Geophysikalische Hohlraumerkundung am Steirischen Erzberg. Master's thesis, Montanuniversitaet Leoben.

Sloan, S. D., Nolan, J. J., Broadfoot, S. W., McKenna, J. R., and Metheny, O. M. (2013). Using near-surface seismic refraction tomography and multichannel analysis of surface waves to detect shallow tunnels: A feasibility study. *Journal of Applied Geophysics*, 99; p. 60–65.

Stockwell, J. (2016). Complete listing of cwp free program self-documentations. Technical report, Colorado School of Mines.

Tarantola, A. (1984a). Inversion of seismic reflection data in the acoustic approximation. *Geophysics*, 49; p. 1259–1266.

Tarantola, A. (1984b). Linearized inversion of seismic reflection data. *Geophysical Prospecting*, 32; p. 998–1015.

Tarantola, A. (1986). A strategy for nonlinear elastic inversion of seismic reflection data. *Geophysics*, 51; p. 1893–1903.

Tarantola, A. (2005). *Inverse Problem Theory and Methods for Model Parameter Estimation*, volume 1. Siam.

USGS (2000). Land subsidence in the United States.

Vidale, J. (1988). Finite-Difference Calculation of Travel Times. *Bulletin of the Seismological Society of America*, 78; p. 2062–2076.

Vidale, J. E. (1990). Finite-difference calculation of traveltimes in three dimensions. *Geophysics*, 55; p. 521–526.

Virieux, J. (1984). SH-wave propagation in heterogeneous media: Velocity-stress finite-difference method. *Geophysics*, 49; p. 1933–1957.

Virieux, J. (1986). P-SV wave propagation in heterogeneous media: Velocity-stress finite-difference method. *Geophysics*, 51; p. 889–901.

Warner, M., Ratcliffe, A., Nangoo, T., Morgan, J., Umpleby, A., Shah, N., Vinje, V., Stekl, I., Guasch, L., Win, C., Conroy, G., and Bertrand, A. (2013). Anisotropic 3D full-waveform inversion. *Geophysics*, 78; p. 59–80.

Whyatt, J. and Varley, F. (2008). Catastrophic Failures of Underground Evaporite Mines. Technical report, NIOSH - Spokane Research Laboratory.

Xiao, W., Hu, Z., Chugh, Y. P., and Zhao, Y. (2014). Dynamic subsidence simulation and topsoil removal strategy in high groundwater table and underground coal mining area: a case study in Shandong Province. *International Journal of Mining*, 28; p. 250–263.

Appendix

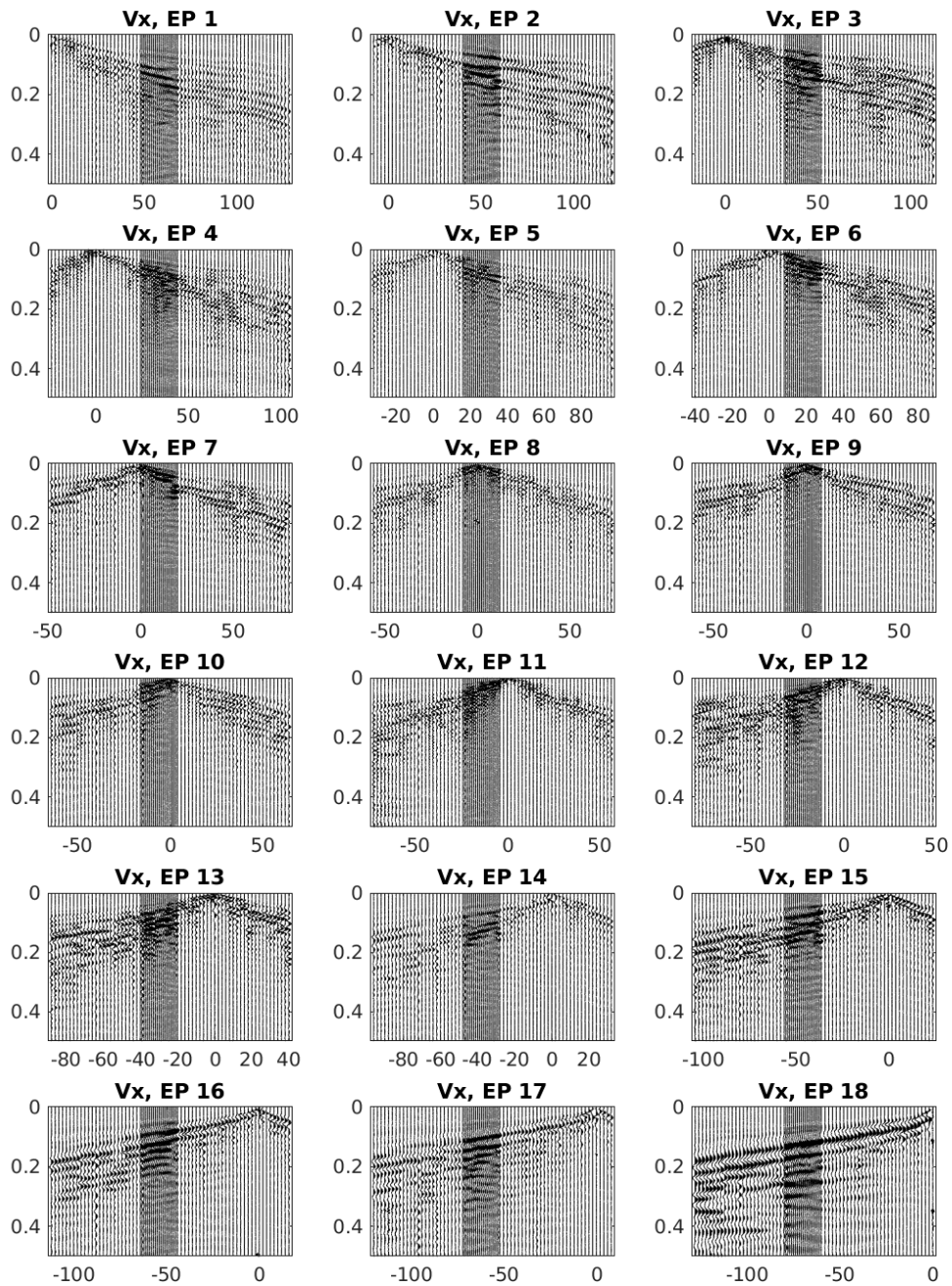## A   Data Acquisition

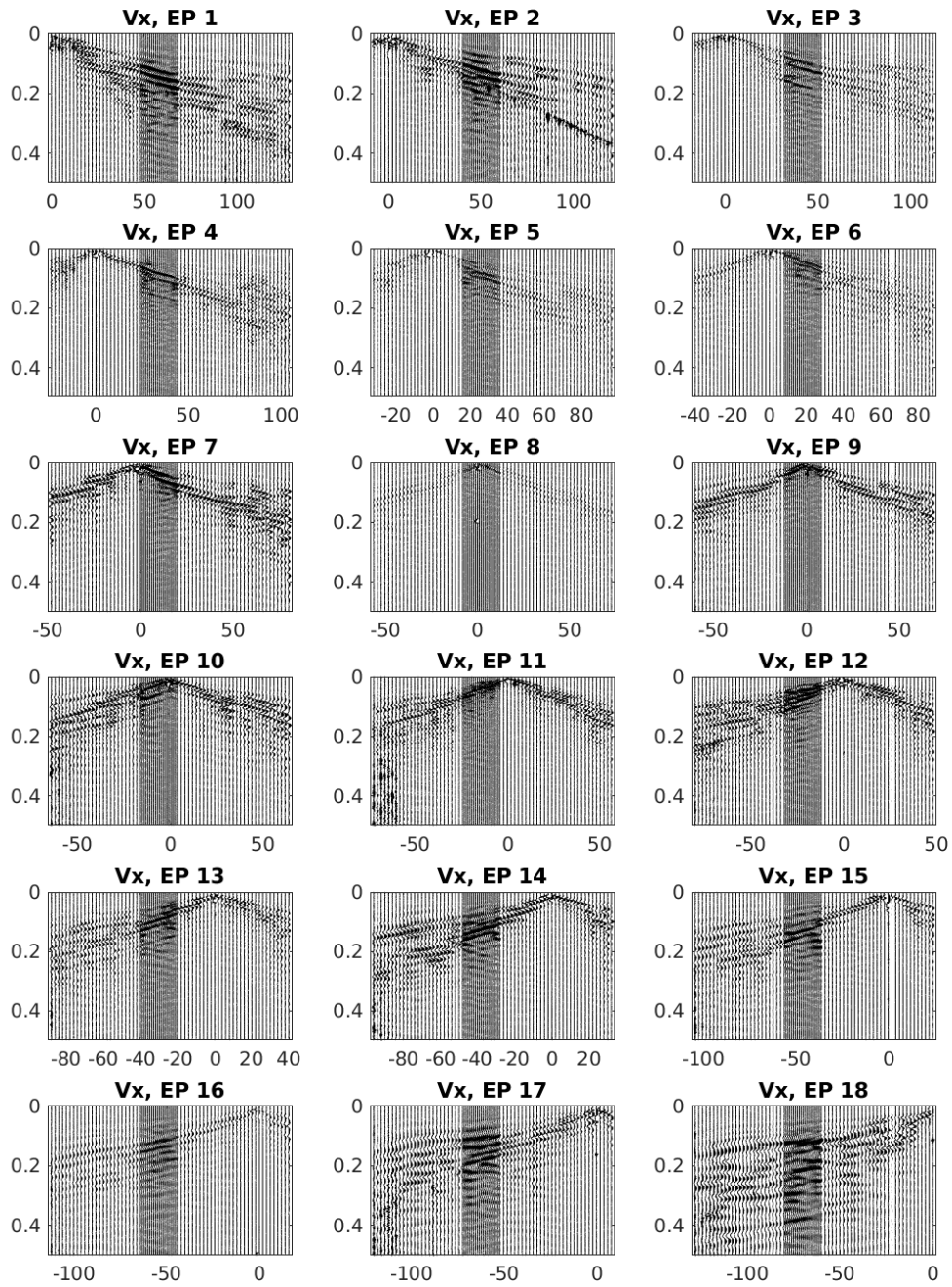**Measured Data**

Figure A1: X-component measured data

Figure A2: Z-component measured data

B   Travel-Time Tomography

Table B1: Picked arrival times for shots 1-18 in s

Trace	1	2	3	4	5	6	7	8	9	10	11	12	13	14	15	16	17	18
1	0	0.006	0.016	0.014	0.018	0.024	0.029	0.033	0.036	0.037	0.041	0.041	0.044	0.045	0.048	0.052	0.056	0.058
2	0.002	0.005	0.01	0.013	0.018	0.022	0.028	0.033	0.036	0.036	0.04	0.042	0.043	0.045	0.047	0.051	0.056	0.056
3	0.003	0.005	0.009	0.013	0.017	0.021	0.028	0.032	0.035	0.036	0.038	0.041	0.043	0.044	0.047	0.050	0.055	0.055
4	0.004	0.002	0.008	0.012	0.016	0.021	0.027	0.032	0.034	0.035	0.038	0.041	0.041	0.043	0.046	0.050	0.054	0.056
5	0.005	0	0.006	0.011	0.015	0.02	0.026	0.032	0.033	0.034	0.037	0.04	0.04	0.043	0.046	0.049	0.052	0.056
6	0.006	0.003	0.005	0.01	0.014	0.019	0.024	0.03	0.032	0.033	0.034	0.038	0.04	0.042	0.045	0.048	0.051	0.055
7	0.008	0.004	0.003	0.01	0.013	0.017	0.023	0.029	0.031	0.031	0.033	0.037	0.041	0.041	0.044	0.047	0.049	0.053
8	0.008	0.004	0.002	0.008	0.012	0.016	0.022	0.028	0.03	0.03	0.031	0.036	0.039	0.041	0.043	0.046	0.048	0.052
9	0.009	0.006	0	0.006	0.011	0.015	0.02	0.027	0.028	0.029	0.03	0.034	0.038	0.04	0.042	0.046	0.048	0.052
10	0.011	0.008	0.002	0.004	0.009	0.014	0.019	0.026	0.027	0.028	0.03	0.034	0.037	0.039	0.04	0.045	0.048	0.053
11	0.012	0.009	0.003	0.002	0.008	0.013	0.018	0.024	0.026	0.027	0.029	0.033	0.036	0.038	0.04	0.043	0.047	0.053
12	0.013	0.01	0.005	0.002	0.007	0.012	0.017	0.023	0.025	0.026	0.029	0.032	0.035	0.037	0.039	0.043	0.046	0.053
13	0.014	0.011	0.006	0	0.007	0.011	0.016	0.022	0.024	0.025	0.027	0.031	0.034	0.036	0.038	0.042	0.046	0.052
14	0.015	0.012	0.007	0.002	0.004	0.01	0.015	0.021	0.023	0.024	0.026	0.031	0.034	0.036	0.037	0.041	0.045	0.052
15	0.016	0.013	0.008	0.003	0.003	0.009	0.014	0.02	0.023	0.024	0.025	0.03	0.033	0.035	0.035	0.04	0.044	0.051
16	0.017	0.015	0.009	0.005	0.002	0.008	0.013	0.019	0.022	0.023	0.024	0.029	0.033	0.034	0.035	0.039	0.043	0.051
17	0.018	0.016	0.011	0.007	0	0.006	0.012	0.018	0.021	0.022	0.024	0.028	0.032	0.033	0.035	0.038	0.042	0.051
18	0.02	0.018	0.012	0.008	0.002	0.005	0.011	0.017	0.02	0.021	0.023	0.028	0.031	0.032	0.034	0.037	0.042	0.05
19	0.021	0.019	0.013	0.01	0.004	0.003	0.01	0.016	0.019	0.02	0.023	0.027	0.03	0.032	0.034	0.037	0.041	0.049
20	0.022	0.02	0.014	0.011	0.005	0.001	0.009	0.015	0.018	0.02	0.023	0.027	0.03	0.032	0.033	0.037	0.041	0.049
21	0.024	0.021	0.015	0.011	0.006	0	0.007	0.013	0.016	0.019	0.021	0.026	0.029	0.031	0.033	0.036	0.04	0.048
22	0.025	0.022	0.016	0.012	0.008	0.002	0.005	0.012	0.015	0.017	0.02	0.025	0.029	0.03	0.032	0.036	0.04	0.048
23	0.026	0.023	0.017	0.013	0.009	0.002	0.004	0.011	0.014	0.016	0.019	0.025	0.028	0.03	0.032	0.036	0.04	0.047
24	0.028	0.024	0.018	0.015	0.011	0.004	0.003	0.01	0.013	0.016	0.019	0.024	0.028	0.03	0.032	0.035	0.039	0.047
25	0.029	0.026	0.02	0.016	0.012	0.005	0	0.008	0.011	0.014	0.019	0.024	0.028	0.03	0.031	0.035	0.039	0.046
26	0.029	0.026	0.021	0.017	0.013	0.006	0.002	0.007	0.01	0.014	0.018	0.023	0.027	0.03	0.031	0.035	0.039	0.045
27	0.029	0.027	0.021	0.017	0.014	0.007	0.003	0.006	0.01	0.013	0.017	0.023	0.027	0.029	0.03	0.035	0.038	0.045
28	0.03	0.028	0.022	0.018	0.014	0.008	0.004	0.005	0.009	0.012	0.017	0.023	0.027	0.029	0.03	0.035	0.038	0.045
29	0.03	0.028	0.022	0.019	0.015	0.008	0.004	0.004	0.008	0.011	0.016	0.022	0.026	0.028	0.03	0.035	0.038	0.045

30	0.031	0.029	0.022	0.02	0.016	0.009	0.005	0.003	0.007	0.01	0.016	0.021	0.026	0.028	0.029	0.035	0.037	0.045
31	0.032	0.03	0.023	0.02	0.016	0.01	0.006	0.003	0.006	0.009	0.015	0.021	0.025	0.027	0.029	0.034	0.037	0.044
32	0.033	0.03	0.024	0.021	0.017	0.011	0.007	0.002	0.005	0.008	0.014	0.02	0.025	0.027	0.029	0.034	0.036	0.044
33	0.033	0.031	0.025	0.022	0.018	0.012	0.008	0	0.004	0.007	0.012	0.019	0.024	0.027	0.028	0.033	0.036	0.043
34	0.034	0.032	0.025	0.022	0.018	0.013	0.009	0.001	0.002	0.006	0.012	0.019	0.023	0.026	0.027	0.032	0.035	0.043
35	0.034	0.032	0.026	0.023	0.019	0.014	0.01	0.001	0.002	0.005	0.011	0.018	0.023	0.026	0.027	0.032	0.035	0.043
36	0.035	0.032	0.026	0.023	0.019	0.015	0.01	0.002	0.001	0.004	0.01	0.017	0.022	0.025	0.026	0.031	0.035	0.042
37	0.036	0.033	0.027	0.024	0.02	0.016	0.011	0.003	0	0.003	0.009	0.017	0.021	0.025	0.026	0.031	0.034	0.042
38	0.036	0.034	0.027	0.024	0.021	0.016	0.012	0.004	0.001	0.003	0.009	0.016	0.021	0.024	0.025	0.03	0.034	0.041
39	0.037	0.034	0.027	0.025	0.021	0.017	0.013	0.005	0.003	0.002	0.009	0.016	0.021	0.024	0.025	0.03	0.033	0.041
40	0.037	0.034	0.028	0.025	0.022	0.018	0.014	0.006	0.003	0.001	0.008	0.015	0.02	0.023	0.025	0.029	0.032	0.04
41	0.037	0.034	0.029	0.026	0.022	0.018	0.014	0.007	0.004	0	0.007	0.014	0.019	0.023	0.025	0.029	0.031	0.039
42	0.038	0.035	0.029	0.026	0.022	0.019	0.015	0.009	0.005	0.001	0.007	0.013	0.019	0.022	0.024	0.028	0.032	0.039
43	0.038	0.035	0.029	0.026	0.023	0.019	0.016	0.01	0.006	0.002	0.006	0.012	0.019	0.022	0.024	0.028	0.031	0.039
44	0.039	0.036	0.029	0.026	0.023	0.02	0.017	0.011	0.007	0.003	0.004	0.012	0.018	0.021	0.023	0.027	0.031	0.039
45	0.039	0.036	0.029	0.026	0.023	0.02	0.018	0.011	0.008	0.004	0.003	0.011	0.017	0.021	0.022	0.027	0.031	0.039
46	0.04	0.036	0.029	0.026	0.024	0.021	0.018	0.012	0.009	0.005	0.002	0.009	0.016	0.02	0.022	0.027	0.03	0.038
47	0.04	0.037	0.03	0.027	0.024	0.021	0.019	0.013	0.009	0.007	0	0.007	0.015	0.019	0.021	0.026	0.03	0.037
48	0.041	0.038	0.031	0.029	0.025	0.022	0.02	0.015	0.012	0.01	0.002	0.006	0.014	0.019	0.02	0.026	0.029	0.036
49	0.04	0.039	0.032	0.029	0.026	0.023	0.02	0.016	0.014	0.011	0.004	0.004	0.012	0.017	0.02	0.025	0.029	0.036
50	0.04	0.04	0.033	0.03	0.027	0.024	0.022	0.018	0.015	0.012	0.004	0.002	0.011	0.017	0.02	0.025	0.029	0.036
51	0.041	0.04	0.034	0.031	0.028	0.025	0.023	0.02	0.017	0.015	0.006	0	0.009	0.016	0.02	0.024	0.029	0.036
52	0.042	0.04	0.035	0.031	0.029	0.026	0.025	0.021	0.018	0.016	0.008	0.002	0.006	0.015	0.018	0.024	0.028	0.035
53	0.042	0.04	0.036	0.032	0.03	0.027	0.026	0.022	0.019	0.017	0.011	0.004	0.004	0.013	0.017	0.023	0.027	0.034
54	0.043	0.041	0.037	0.033	0.031	0.028	0.027	0.023	0.021	0.018	0.012	0.006	0.002	0.011	0.016	0.022	0.026	0.033
55	0.044	0.041	0.037	0.034	0.031	0.028	0.028	0.024	0.022	0.019	0.013	0.008	0	0.007	0.015	0.021	0.025	0.032
56	0.045	0.042	0.038	0.035	0.032	0.029	0.029	0.025	0.023	0.021	0.015	0.01	0.003	0.006	0.013	0.019	0.023	0.031
57	0.045	0.043	0.038	0.036	0.032	0.03	0.029	0.026	0.024	0.022	0.017	0.013	0.004	0.004	0.011	0.017	0.021	0.029
58	0.045	0.044	0.038	0.036	0.033	0.031	0.029	0.027	0.024	0.022	0.018	0.015	0.006	0.002	0.008	0.015	0.019	0.027
59	0.045	0.044	0.039	0.036	0.033	0.031	0.03	0.027	0.025	0.022	0.019	0.016	0.008	0	0.007	0.013	0.018	0.026
60	0.045	0.045	0.04	0.036	0.033	0.031	0.03	0.027	0.025	0.023	0.019	0.017	0.01	0.002	0.006	0.012	0.016	0.025

| 61	0.046	0.046	0.04	0.037	0.034	0.032	0.031	0.027	0.025	0.023	0.02	0.019	0.013	0.005	0.005	0.011	0.015	0.024
62	0.048	0.046	0.04	0.037	0.034	0.033	0.031	0.028	0.026	0.024	0.021	0.02	0.014	0.006	0.003	0.01	0.015	0.023
63	0.048	0.047	0.041	0.038	0.035	0.033	0.032	0.028	0.027	0.025	0.022	0.021	0.016	0.008	0	0.009	0.015	0.022
64	0.051	0.048	0.042	0.038	0.036	0.033	0.032	0.03	0.028	0.026	0.023	0.022	0.017	0.009	0.003	0.007	0.014	0.022
65	0.052	0.049	0.043	0.039	0.036	0.034	0.033	0.03	0.029	0.027	0.023	0.023	0.018	0.01	0.004	0.005	0.013	0.021
66	0.053	0.05	0.045	0.04	0.036	0.035	0.034	0.031	0.03	0.028	0.025	0.024	0.02	0.012	0.006	0.003	0.011	0.019
67	0.054	0.051	0.046	0.041	0.037	0.036	0.035	0.032	0.031	0.028	0.026	0.024	0.021	0.014	0.008	0	0.011	0.018
68	0.055	0.051	0.047	0.042	0.039	0.037	0.035	0.033	0.032	0.029	0.027	0.025	0.022	0.015	0.01	0.004	0.009	0.017
69	0.055	0.052	0.048	0.043	0.04	0.038	0.036	0.035	0.033	0.03	0.028	0.027	0.023	0.016	0.012	0.006	0.008	0.017
70	0.055	0.052	0.049	0.044	0.041	0.039	0.037	0.036	0.033	0.031	0.029	0.029	0.025	0.018	0.014	0.009	0.005	0.015
71	0.057	0.052	0.049	0.045	0.042	0.040	0.038	0.037	0.035	0.032	0.03	0.029	0.026	0.019	0.015	0.012	0	0.013
72	0.058	0.054	0.05	0.045	0.043	0.041	0.04	0.038	0.036	0.033	0.031	0.03	0.027	0.02	0.016	0.014	0.004	0.011
73	0.058	0.055	0.052	0.046	0.044	0.042	0.042	0.039	0.038	0.035	0.032	0.032	0.028	0.022	0.018	0.016	0.006	0.008
74	0.058	0.056	0.052	0.047	0.045	0.043	0.043	0.041	0.04	0.037	0.034	0.034	0.03	0.024	0.019	0.017	0.009	0.005
75	0.058	0.056	0.052	0.048	0.045	0.044	0.045	0.043	0.042	0.038	0.036	0.036	0.032	0.026	0.02	0.018	0.011	0

Ray Paths
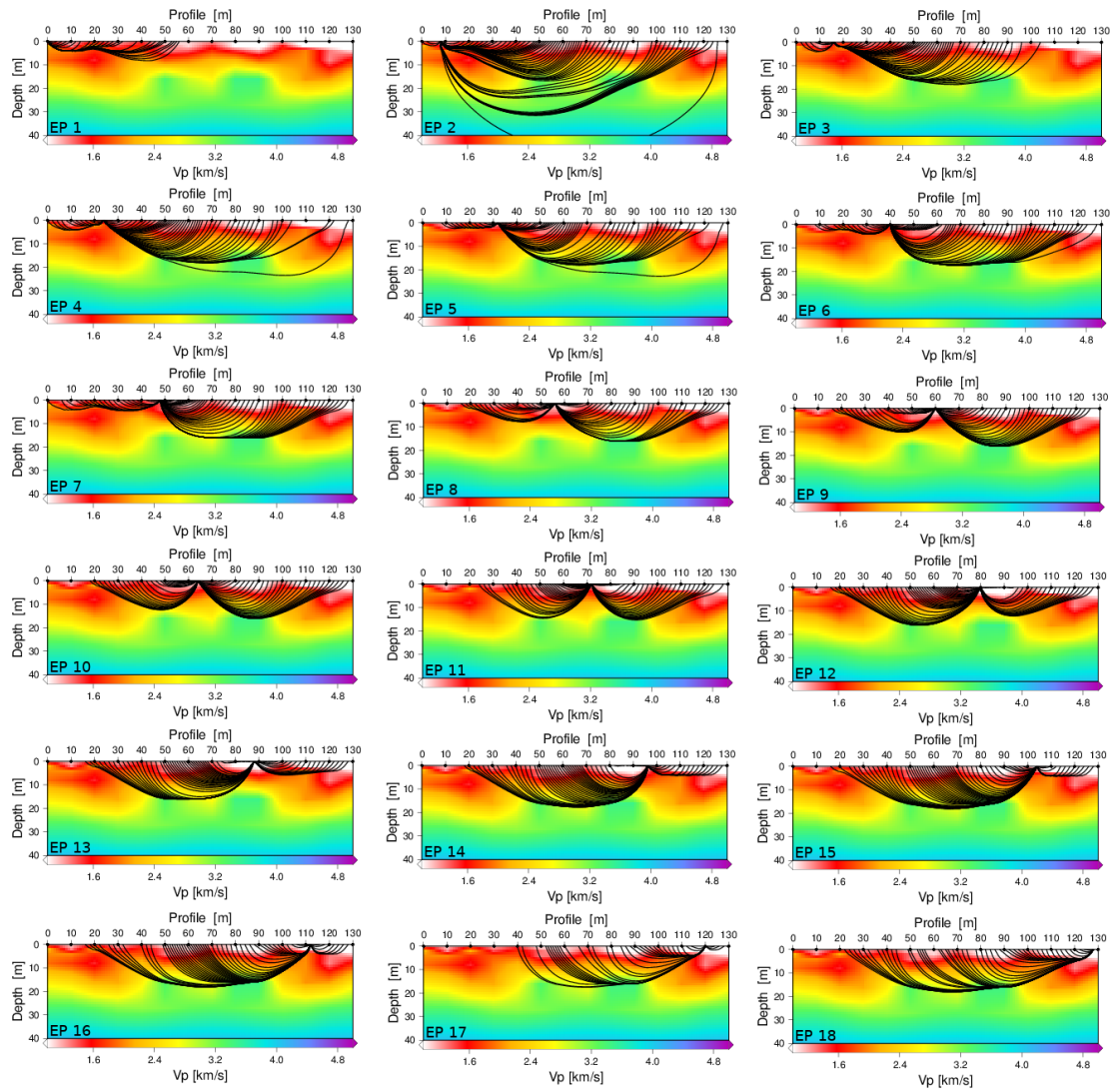
Figure B1: Black lines indicate ray paths through P-wave travel-time tomography model (comp. 5.5.1)

C Synthetic Studies
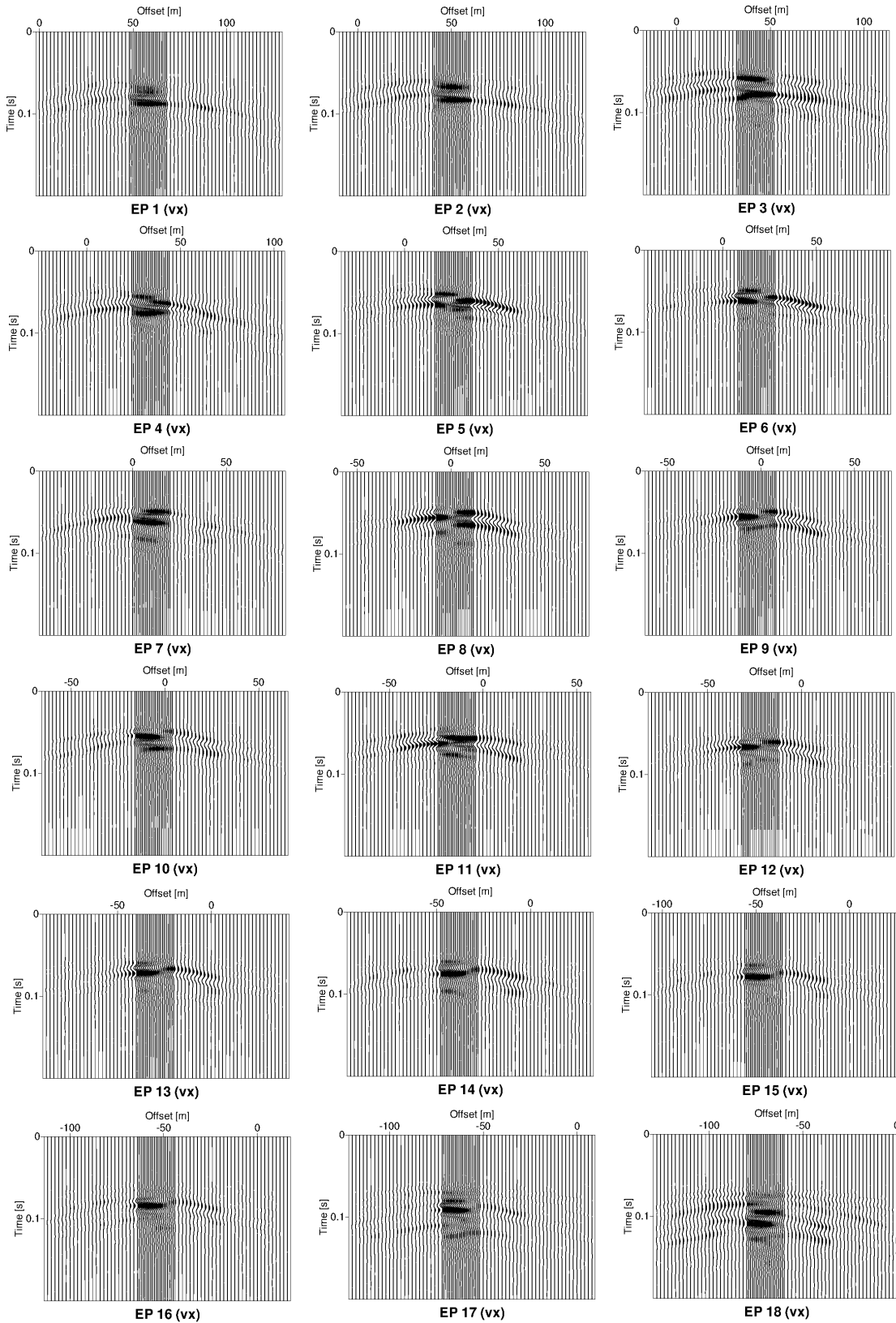
Difference Plots

Figure C1: X-component difference seismograms of synthetics without and with a cavity
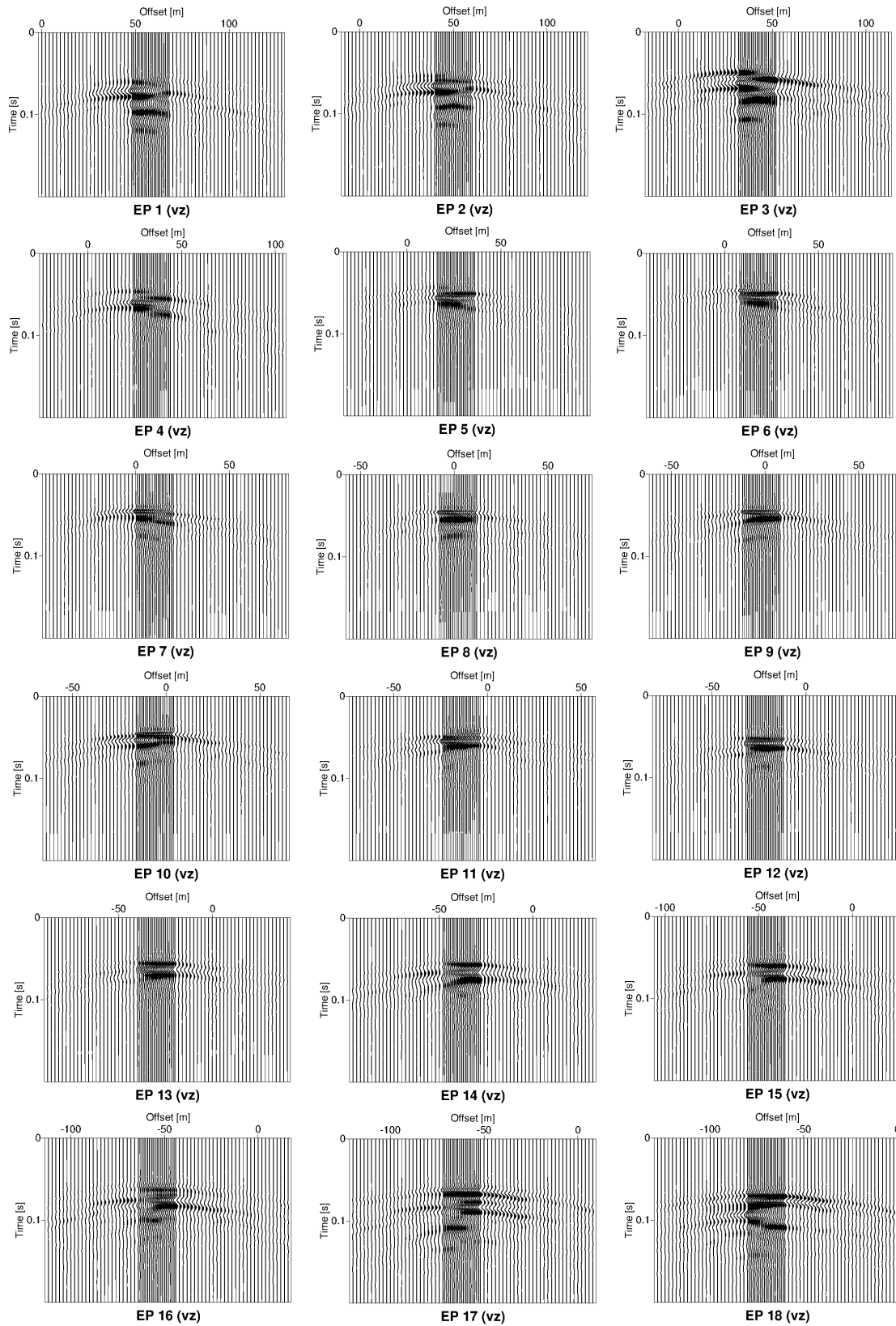
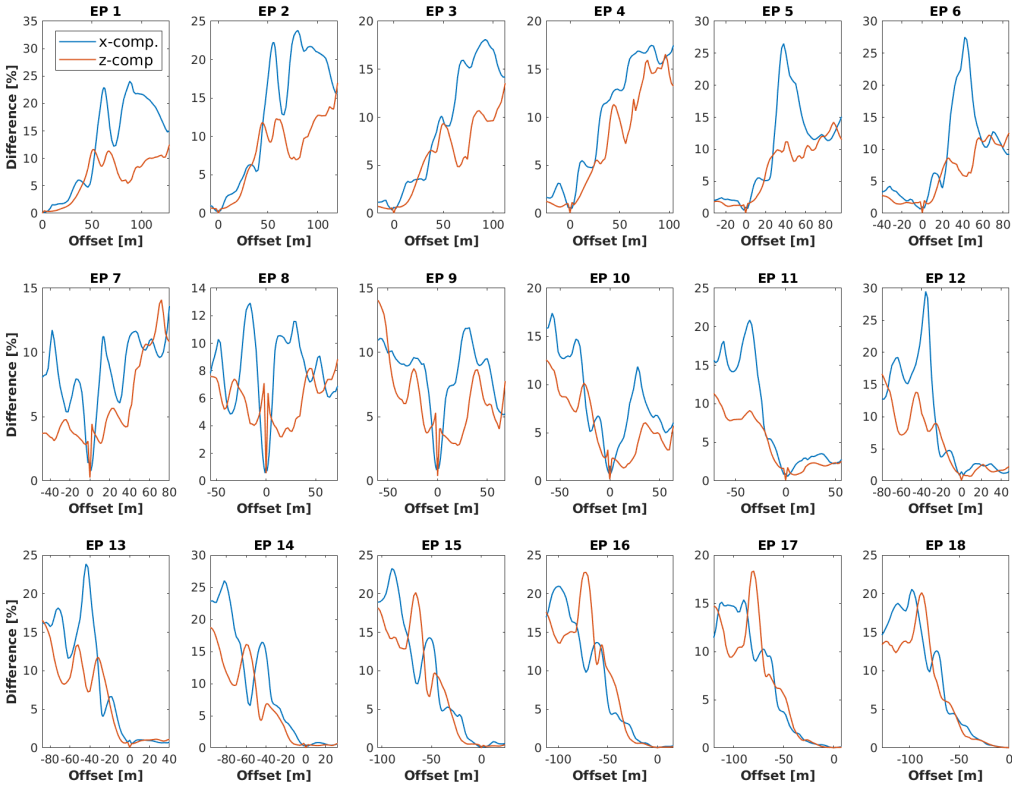**Figure C2: Z-component difference seismograms of synthetics without and with a cavity**

Figure C3: Percentage of difference amplitudes compared to the initial complete wavefield
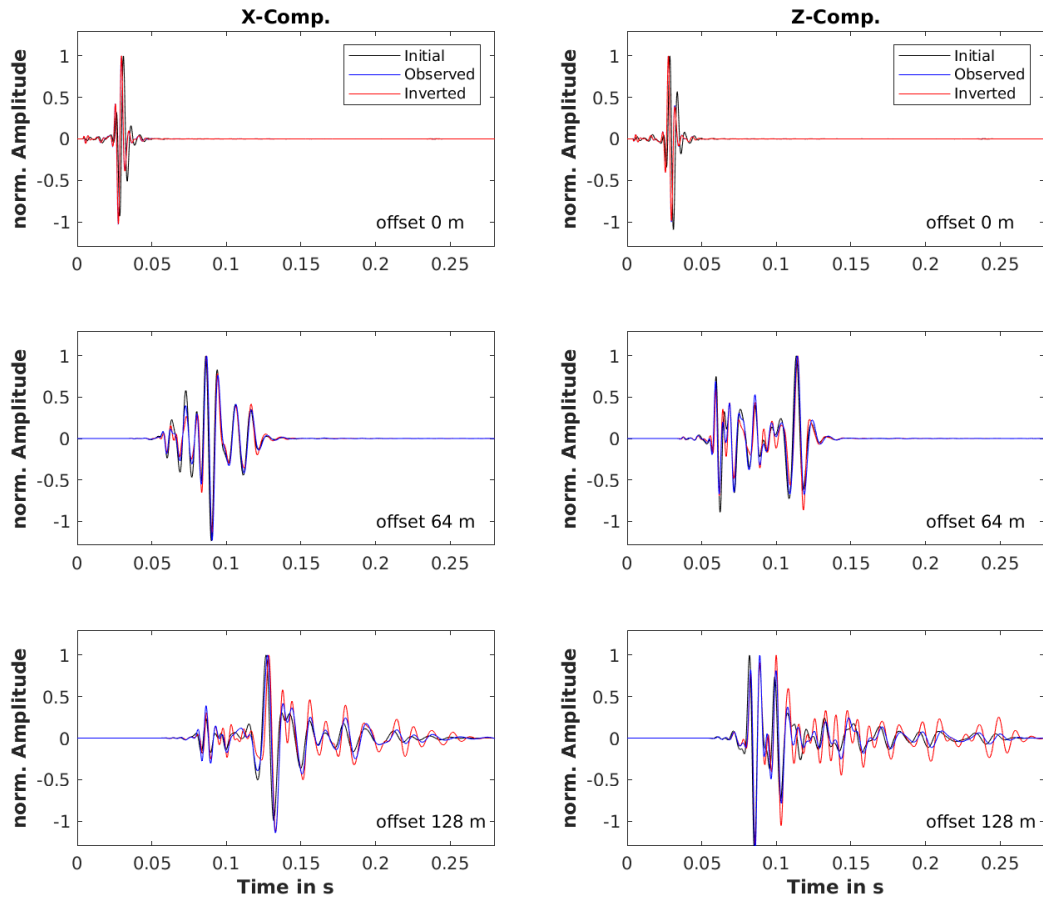
Example Trace Fits of synthetic Inversions

Figure C4: TTT.B: Initial (black), observed (blue) and inverted (red) x-(left panel) and z-component (right panel) seismograms of shot 1 plotted upon each other; the offset is indicated in the lower right corner
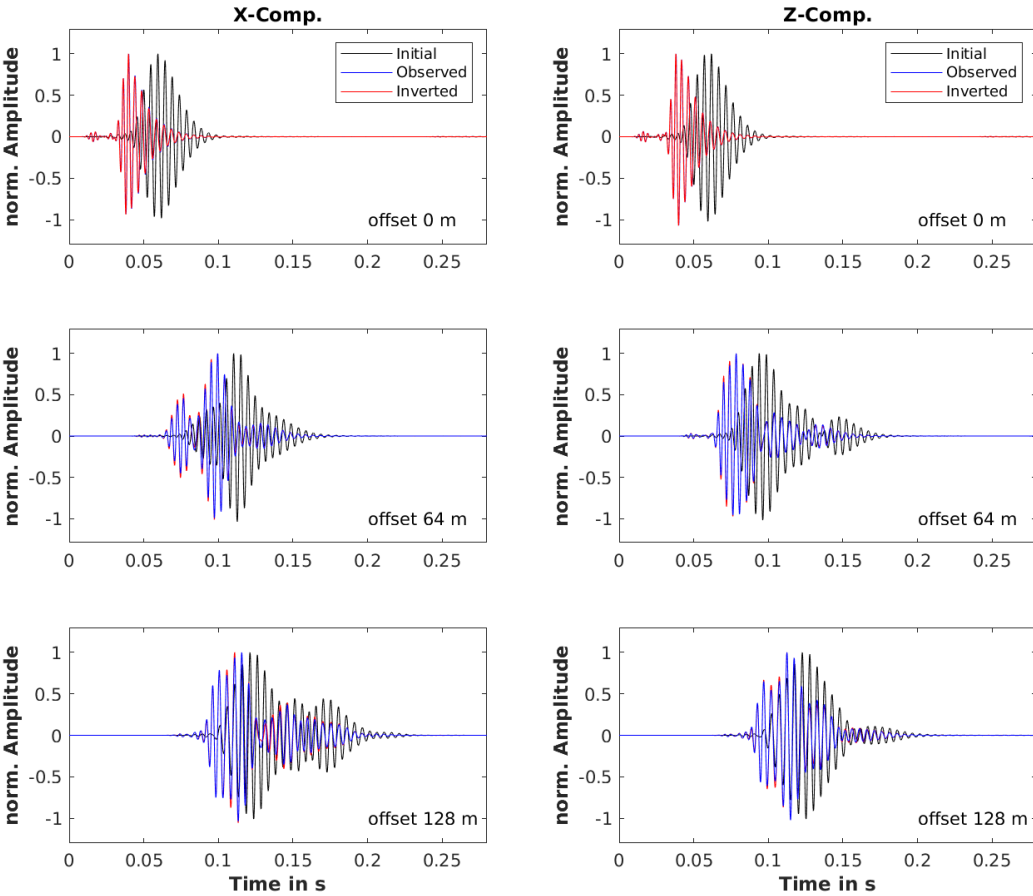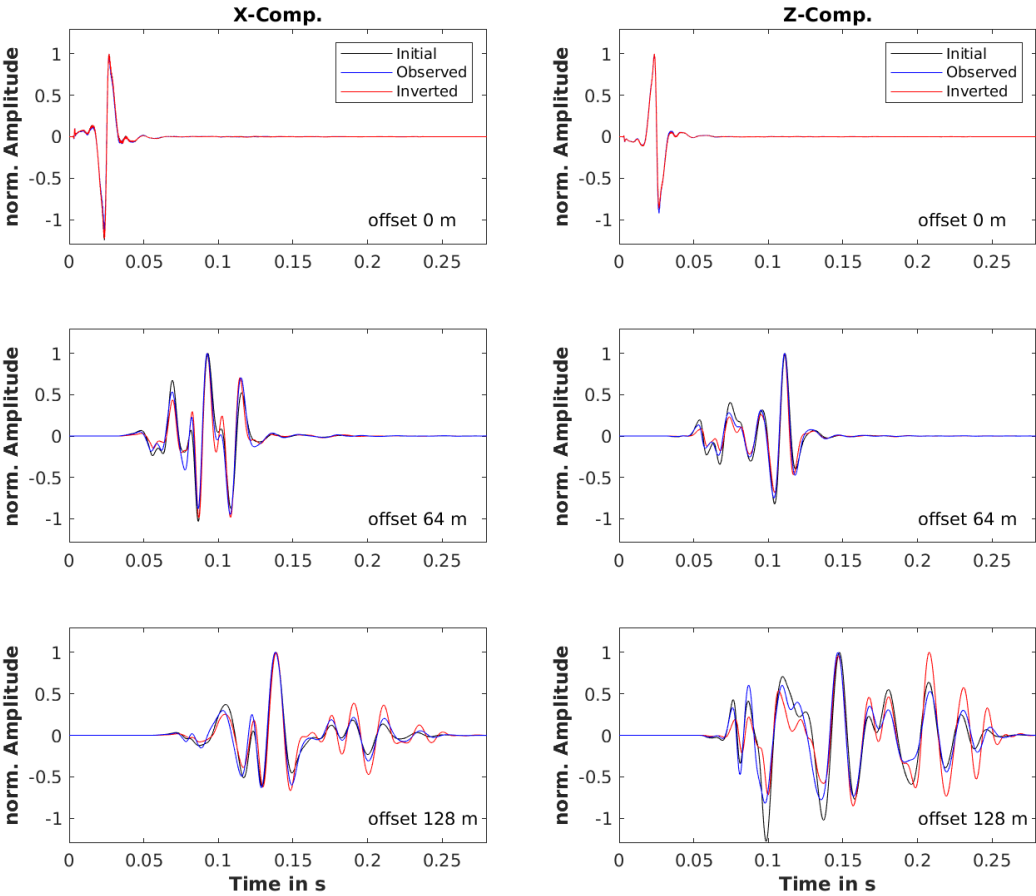
Figure C5: TTT.C(P): Initial (black), observed (blue) and inverted (red) x-(left panel) and z-component (right panel) seismograms of shot 1 plotted upon each other; the offset is indicated in the lower right corner
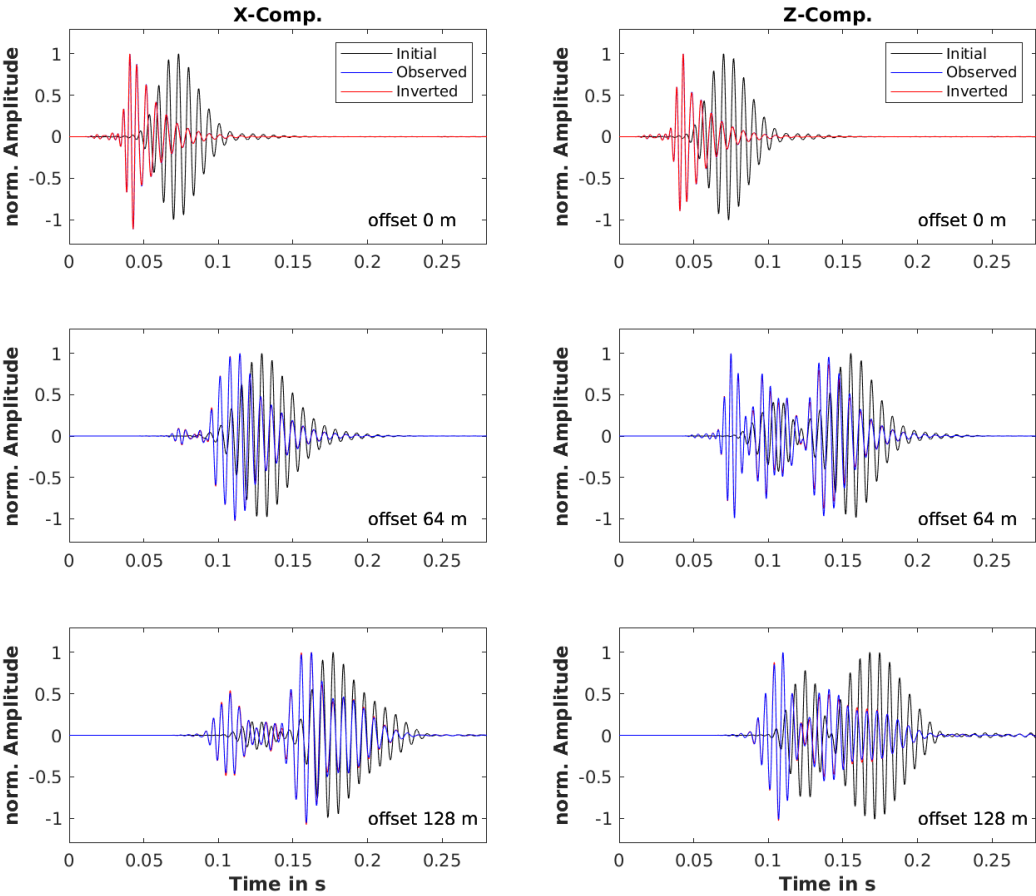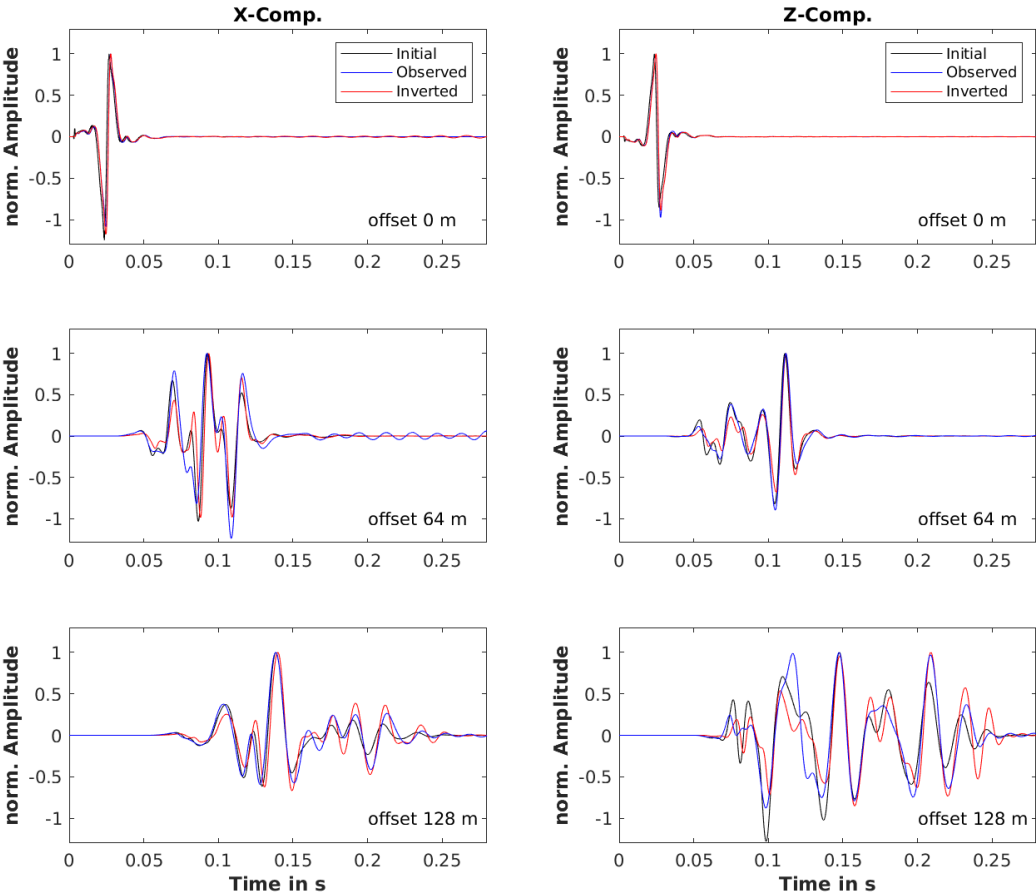
Figure C6: TTT.C(S): Initial (black), observed (blue) and inverted (red) x-(left panel) and z-component (right panel) seismograms of shot 1 plotted upon each other; the offset is indicated in the lower right corner
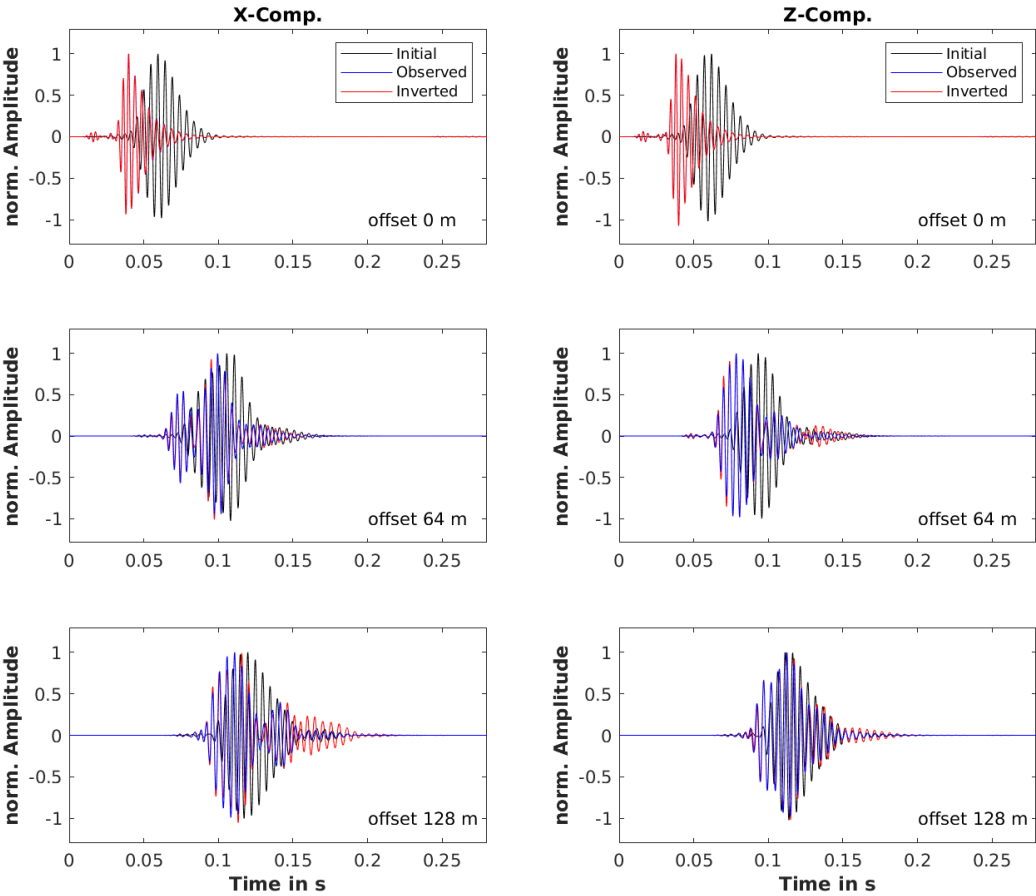
Figure C7: PERT.A: Initial (black), observed (blue) and inverted (red) x-(left panel) and z-component (right panel) seismograms of shot 1 plotted upon each other; the offset is indicated in the lower right corner

Figure C8: PERT.B: Initial (black), observed (blue) and inverted (red) x-(left panel) and z-component (right panel) seismograms of shot 1 plotted upon each other; the offset is indicated in the lower right corner
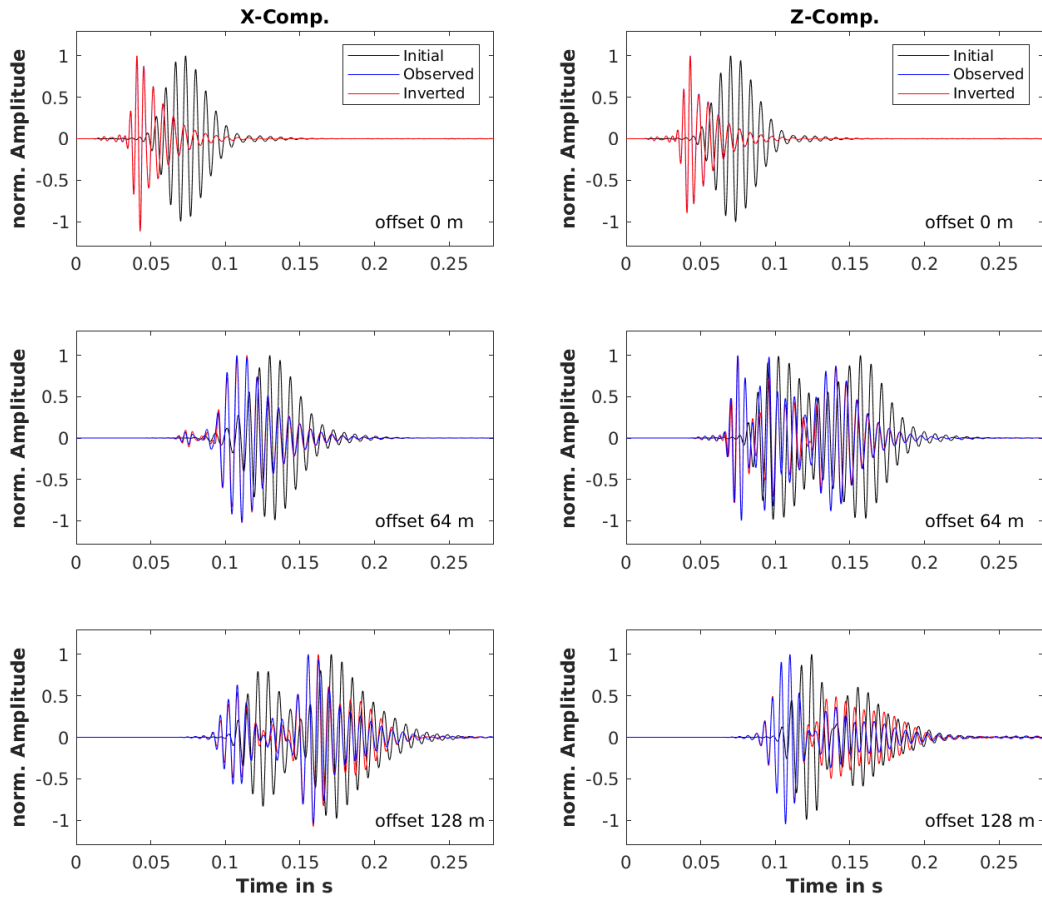
Figure C9: PERT.C(P): Initial (black), observed (blue) and inverted (red) x-(left panel) and z-component (right panel) seismograms of shot 1 plotted upon each other; the offset is indicated in the lower right corner

Figure C10: PERT.C(S): Initial (black), observed (blue) and inverted (red) x-(left panel) and z-component (right panel) seismograms of shot 1 plotted upon each other; the offset is indicated in the lower right corner

D   Inversion for Source Time Functions

Theory of Source Time Function Inversion

Another important unknown within the process of resolving the subsurface besides the model is the source time function. The source wavelet is often unknown and varies with each shot location. This is true especially for hammer blows or explosives. Several reasons could influence the characteristics of the source time function, for instance the coupling of the source, the strength or directivity of the explosion or hammer strike, but also laterally varying lithologies and therefore varying physical properties, just to name a few of them. An incorrectly assumed source time function used for the forward modelling in the inversion process would deteriorate the results, because the errors of the source wavelet propagate into the synthetic seismograms. To avoid this systematic inaccuracy, an inversion for the source time function has to be carried out as well. The inversion code IFOS2D by KIT uses the library *libstfinv* from Thomas Forbriger (Forbriger (2014)). The basic idea is to obtain

a source wavelet correction filter which minimises the misfit of the synthetic and observed seismograms by convolving the synthetic seismograms with this filter. Fourier coefficients of synthetic and observed seismograms are calculated in way a that the residuals of those coefficients after the application of this correction filter are minimised in a least-squares sense. The objective function which is minimised in the process is

$$E = \sum_{l,k} |\eta f_k(d_{lk} - s_{lk}q_l)|^2 + \sum_l \lambda^2 |q_l|^2 \tag{D1}$$

where η and f_k are specific weighting factors, d_{lk} and s_{lk} are Fourier coefficients of observed and synthetic data at frequency f_l and receiver k, respectively, q_l is the coefficient of the sought source wavelet and λ a damping factor. Demanding that the deviation of this objective function with respect to the sought source wavelet should be zero and rearranging eq. D1 yields

$$q_l = \frac{\eta^2 \sum_k f_k^2 s_{kl}^* d_{kl}}{\lambda^2 + \eta^2 \sum_k f_k^2 s_{kl}^* s_{kl}}. \tag{D2}$$

η and λ are used to balance the regularization and a water level as a fraction of the energy of synthetic data is sought. Choosing

$$\frac{\lambda^2}{\eta^2} = \frac{\epsilon^2}{N\eta^2} = \frac{\epsilon^2}{N} \sum_k f_k^2 \sum_{l=0}^{N-1} |s_{lk}|^2 \tag{D3}$$

and applying Parceval's Theorem to calculate signal energy gives

$$\sum_k f_k^2 \sum_{l=0}^{N-1} |s_{lk}|^2 = N \sum_k f_k^2 \sum_{j=0}^{2N-1} |S_{jk}|^2. \tag{D4}$$

Inserting eq. D3 and D4 into eq. D2 yields the final solution

$$q_l = \frac{\sum_k f_k^2 s_{lk}^* d_{lk}}{\epsilon^2 \sum_k f_k^2 \sum_{j=0}^{2N-1} |S_{jk}|^2 + \sum_k f_k^2 s_{lk}^* s_{lk}} \tag{D5}$$

with the water level parameter ϵ. For a more detailed deviation of those equations the reader is referred to Forbriger (2014) and Groos (2013).

Inverted Source Time Functions

In this section the inverted source time functions for the inversion approaches shown in chapter 7 are displayed and discussed. All inversions of the source time functions are carried out by applying a frequency-domain least-squares approach, an offset weighting w_k (Eq. D6), a water level of 0.01 and a selected offset range of 6-15 m, which corresponds to the same offset range two with which the source wavelet in section 6.1.2 is estimated.

$$w_k = \left(\frac{r}{1\,m}\right)^a \tag{D6}$$

REAL.B

The inverted source time function displayed in Fig. D1 look quite coherent. However the different complexity of the inverted model (Fig. 7.2.1) between the left and right side of the model is also reflected in the inverted source time functions. Traces 7 to 18 seem more coherent with each other than compared to traces 3 to 6. Also these traces, 7 to 18, seem to have longer wavelengths, which would fit with the introduced high-velocity area in the P-wave inversion model. The increased heterogeneity of the subsurface in the left part of the profile (the beginning of the profile) could be due to the construction works, which took place right before the measurements. As mentioned previously, the tier was shorten in order to introduce a support floor between the Schuchard tier and Dreikönige. This shortening was done at the beginning of the profile, so that the starting point in the second survey had to be shifted around several meters inline compared to the first survey. The excavation process during the construction of the support floor could have changed the stress regime in that area and therefore leads to a more heterogeneous velocity distribution. Another reason could simply be a complex geology with different lithologies as it is indicated in Fig. 4.1.6.
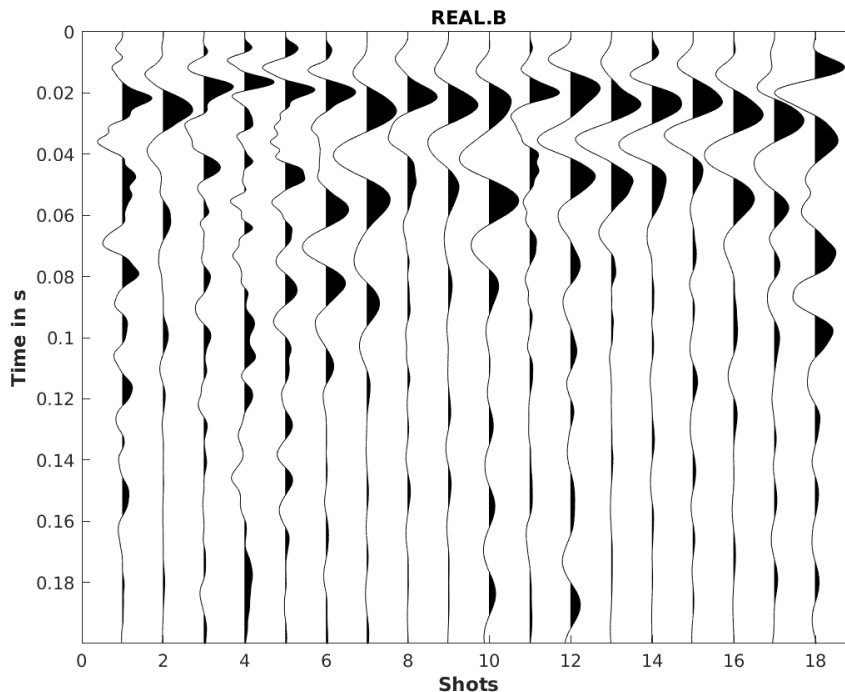

Figure D1: Inverted source time functions for REAL.B

REAL.C(P) and REAL.C(S)

The inverted source time functions for REAL.C(P) (Fig. D2) and REAL.C(S) (Fig. D3) look quite different. In fact they possess sever ringing, which is due to the time-windowing applied. If the windowing is done like a sharp cut in the time-domain it causes ringing effects in the frequency-domain and since the source time function inversion is done in the frequency-domain, those ringing is projected into the inverted source time functions. This phenomenon is commonly known as Gibbs phenomenon (Hewitt and Hewitt (1979)) and can be overcome by an adequate choice of time damping. Looking at Fig. D2 (right) the actual source time function is marked by the blue rectangle, the phases afterwards are ringing. Some traces in Fig. D2 and Fig. D3 are polarity reversed compared to their neighbouring traces and reversed in the right panels to increase coherence (of course just for the purpose of display). The inversions are again carried out with a much higher damping. The damping is done in the way

$$damping = \exp^{-\gamma \cdot t} \tag{D7}$$

where γ is a factor chosen by the user. Fig. D4 and D5 show the inverted source time functions for a chosen $\gamma = 100$ instead of previously used 1. It becomes obvious, that the ringing is significantly minimised and the source time functions look more coherent and well defined. However, the polarity reversal of some traces is still present and might be an indication that the source time function inversions are not as stable. The corresponding inverted models which resulted in the differently damped time windows are plotted in Fig. D6. Again there is no clear indication of a subsurface cavity. In case of a P-wave time-windowing (upper black box) a horizontally elongated low-velocity and low-density zone in Vs and density, respectively, is introduced in the depth of the assumed cavity. In the Surface-wave time-windowed inversion results (lower black box) the S-wave velocity and density decrease is vertically elongated, but not as far down to the expected cavity in case of the S-wave model. There is no indication of reduced P-wave velocity at the position of the assumed cavity, neither in the P-wave time-windowed data nor in the Surface-wave time-windowed data.
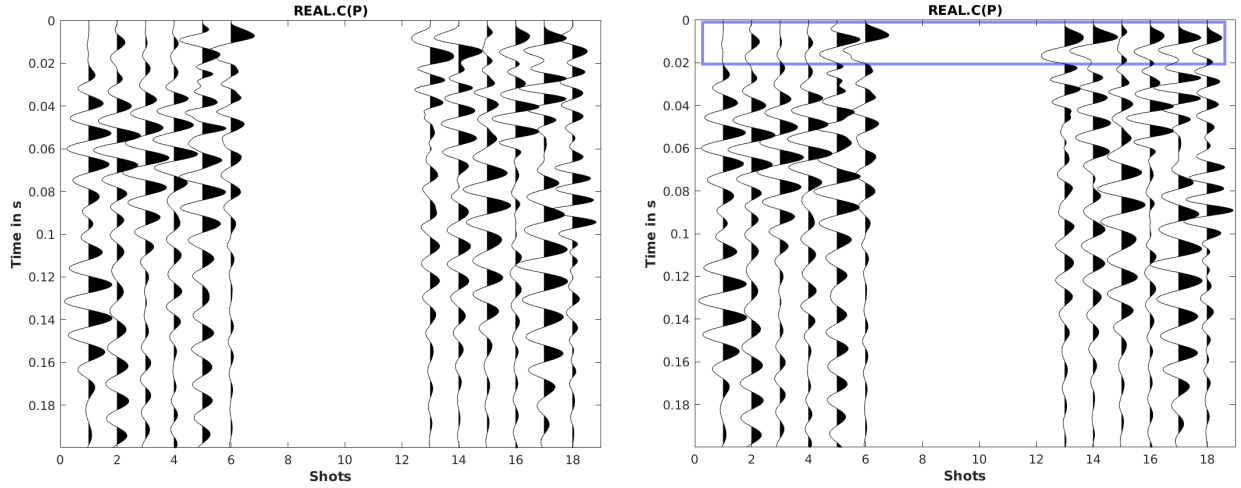
Figure D2: Inverted source time functions for REAL.C(P); left: not reversed; right: trace reversed to enhance coherence; blue rectangle marks the actual source time functions
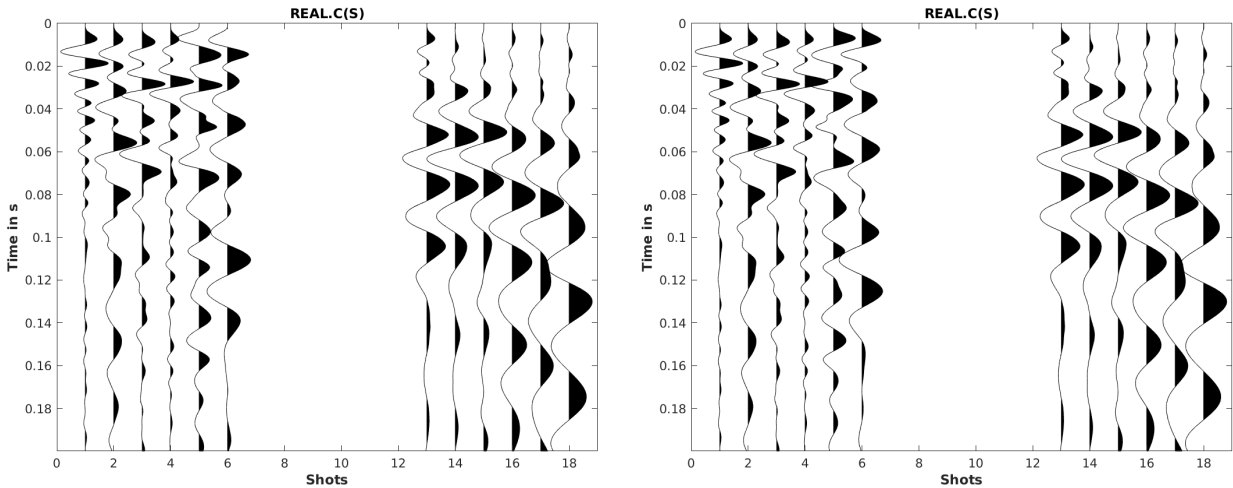

Figure D3: Inverted source time functions for REAL.C(S); left: not reversed; right: trace reversed to enhance coherence

REAL.D

The inverted source time functions for REAL.D are displayed in Fig. D7. The source time functions look very coherent, except in the middle part (traces 8 to 11). Again the polarity reversal is apparent, which is introduced for frequency bands higher than 100 Hz and therefore with iterations greater than 38. However the Vs and density reduction at the position of the assumed cavity (comp. Fig. 7.2.10) is already significant before 38 iterations (comp. Fig. 7.3.1) and therefore is no artefact by unstable source time function inversions.
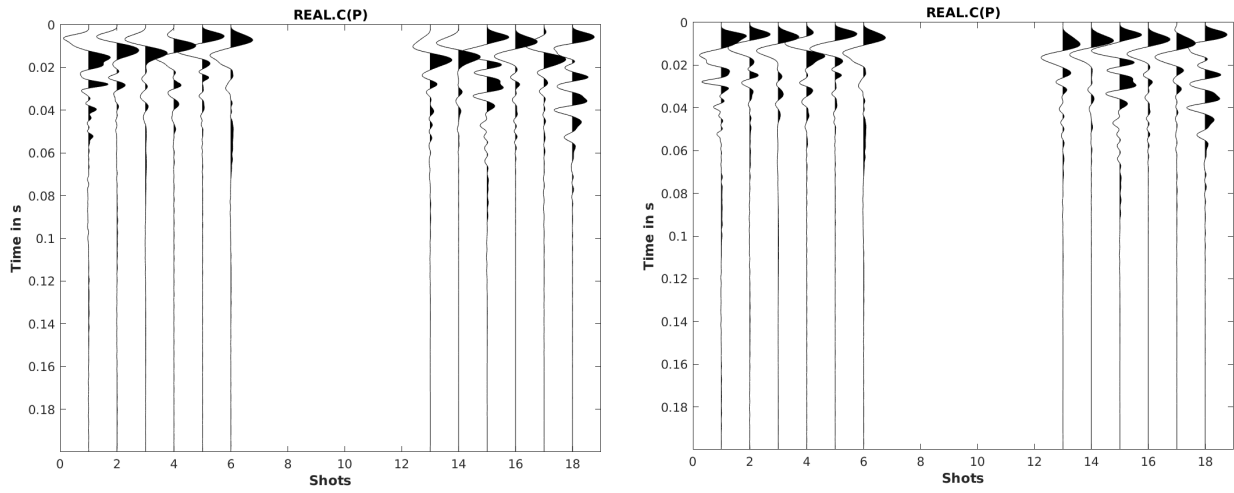
Figure D4: Inverted source time functions for REAL.C(P), but with different damping; left: not reversed; right: trace reversed to enhance coherence
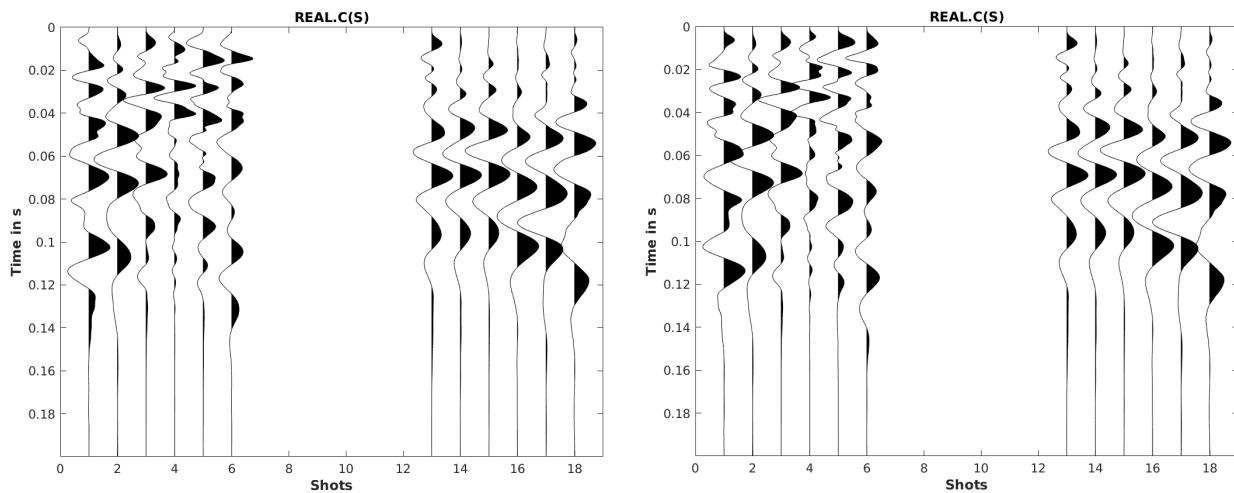

Figure D5: Inverted source time functions for REAL.C(S), but with different damping; left: not reversed; right: trace reversed to enhance coherence
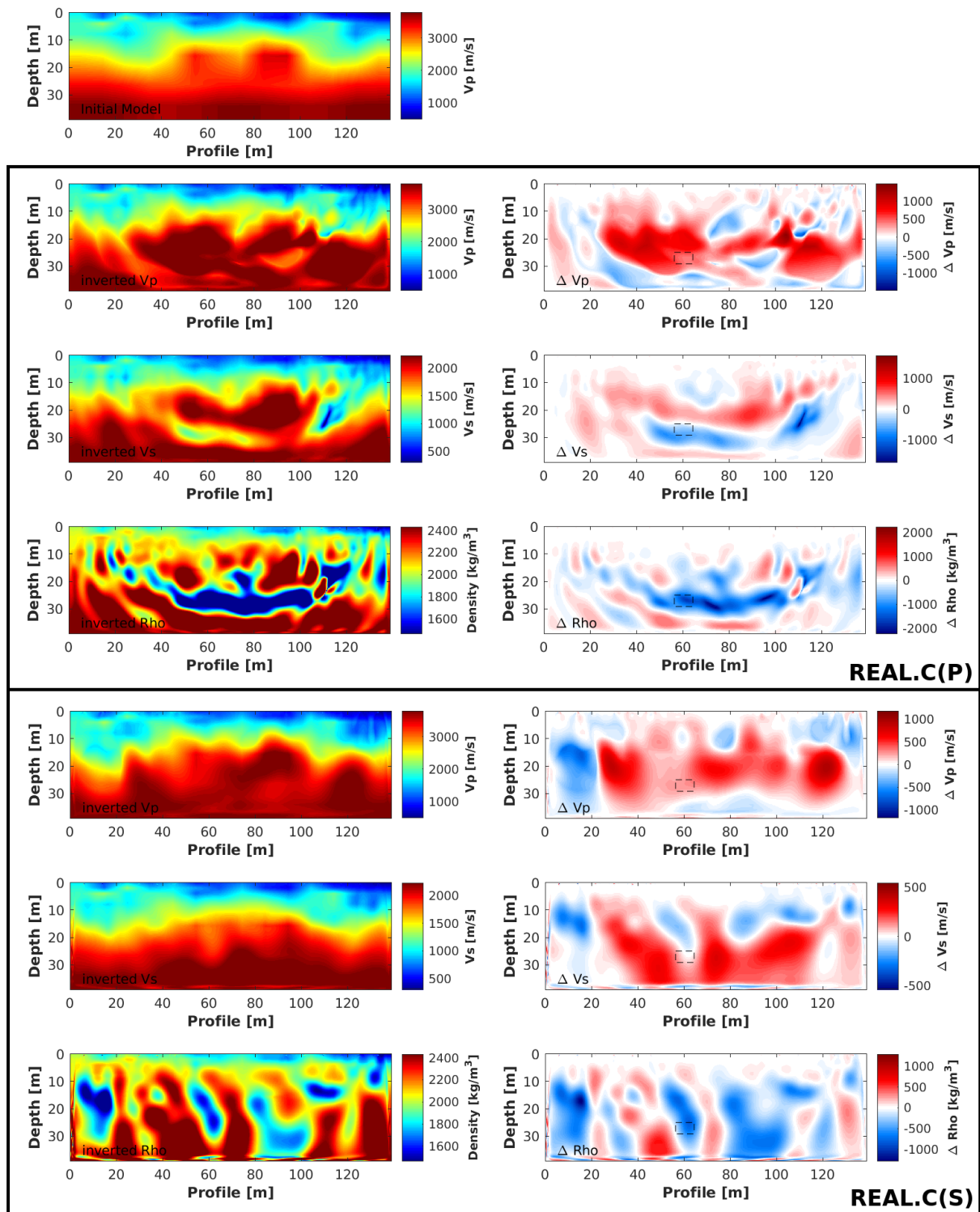
Figure D6: Upper panel: starting model, first column: inverted models for Vp (upper panel), Vs (second panel) and density (lower panel); second column: difference models of the same order; upper black box: results for REAL.C(P) after 88 iterations; lower black box: results for REAL.C(S) after 97 iterations; the black dashed rectangle indicates the position of the suspected cavity
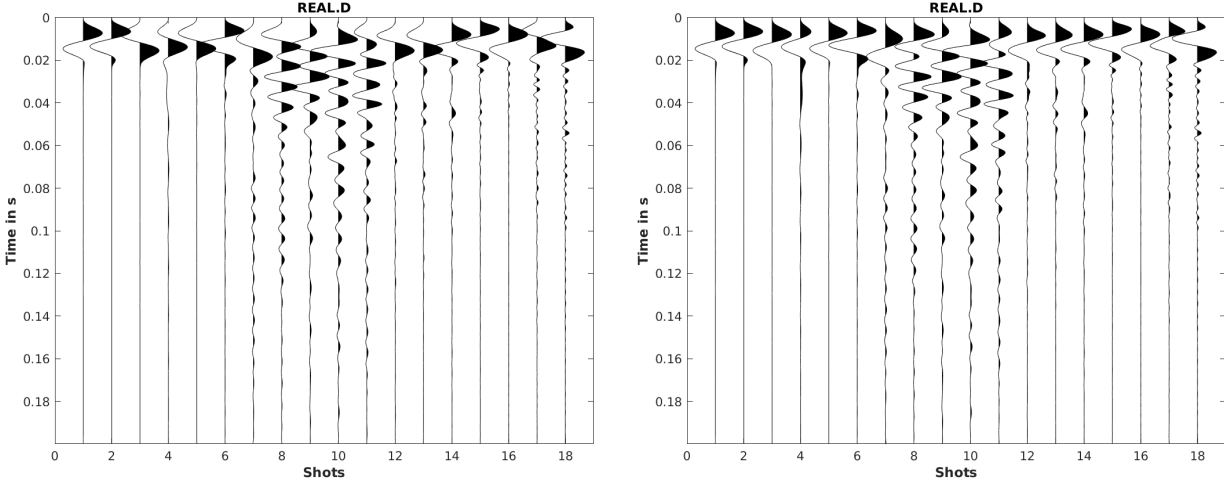
Figure D7: Inverted source time functions for REAL.D